SYNTHESIS, CHARACTERIZATION AND PROCESSING OF POWDERS, DENSIFICATION BEHAVIOR, MICROSTRUCTURE, AND PROPERTIES FOR SILICA / SILICON NITRIDE PREPARED FROM MICROCOMPOSITE PARTICLES

By

RAMESH RAGHUNATHAN

A DISSERTATION PRESENTED TO THE GRADUATE SCHOOL
OF THE UNIVERSITY OF FLORIDA IN PARTIAL FULFILLMENT
OF THE REQUIREMENTS FOR THE DEGREE OF
DOCTOR OF PHILOSOPHY

UNIVERSITY OF FLORIDA

1997

ACKNOWLEDGMENTS

I am grateful to Dr M.D Sacks for his invaluable guidance and support. I am thankful to Drs. R.T DeHoff, B.V Sankar, J.H Simmons, and E.D Whitney for their helpful suggestions I would like to thank Drs. F Ebrahimi, D.E. Clark, B.M. Moudgil, and M.J Kaufman for allowing me to use various analytical instruments

I would also like to thank G W Scherffele, S.D Vora, A.E Bagwell, A. Ulleny, D Parker N. Bozkurt, Y.J Lin, K Wang, D Kisailus, M Saleem, P Krishnan, M Randall, R. Crockett, A. Morrone, S Vemgalla, S Jayashankar, T.J Williams, G Klempel, and U Mahajan for their assistance in carrying out various experiments in this study Special thanks go to T.J Williams, G W Scherffele, G Staab, M. Saleem, J S Huffman, V Sheney, U Shenoy, R. Bandale, P Bendale, and U Mahajan for their timely help and encouragement especially during the final stages of preparing this document.

Finally, I would like to thank my brother Partha for his encouragement and support without which this dissertation would not have been possible

TABLE OF CONTENTS

ACKNOWLEDGMENTS ii

LIST OF TABLES vi

LIST OF FIGURES xi

ABSTRACT xxvi

CHAPTERS

1 INTRODUCTION 1

2 BACKGROUND 3

2.1 Introduction 3
2.2. Low-Dielectric Constant Glass-Matrix Composites 3
2.2.1 Potential Applications 3
2.2.2 Processing Considerations 8
2.3 Incorporation of Controlled Porosity in Glass/Ceramic Matrices. 11
2.4 Synthesis and Characterization of Composite Powders 13
2.5 Sintering of Particulate Composites. 20
2.5.1 Introduction 20
2.5.2 Analytical Models 21
2.5.3 Experimental Data Analysis. 27

3 EXPERIMENTAL PROCEDURE 40

3.1 Synthesis of Particles 40
3.1.1 Core Particles and Microcomposite Particles 40
3.1.2 SiO_2 Particles 44
3.1.3 Polystyrene (PS) Particles 49
3.2 Characterization of Particles 49
3.2.1 Core Particles and Microcomposite Particles 49
3.2.2. Characterization of PS Particles. 69
3.3 Suspension Preparation and Characterization. 69
3.3.1 Series I Composite Powder and Mixed Powder Suspensions 69
3.3.2 PS and Series II Composite Powder Suspensions. 70

3.3.3 Series III Composite Powder, SiO_2 Powder, and Mixed Powder Suspensions 71
3.4 Consolidation and Characterization of Green Compacts 72
3.4.1 Consolidation 72
3.4.2 Characterization of Green Compacts 76
3.5 Sintering 77
3.6 Microstructural Characterization 87
3.7 Physical Property Measurements 90
3.7.1 Dielectric Properties 90
3.7.2 Flexural Strength 93
3.7.3 Hardness and Toughness 95
3.8 Compression Creep Measurements 96

4 RESULTS AND DISCUSSION 104

4.1 Preliminary Investigations 104
4.1.1 Characterization of Particles 104
4.1.2 Effect of Spatial Distribution of Phases 122
4.2 Processing and Properties of Bulk Composites with Low Dielectric Constant 134
4.2.1 Characterization of Particles 135
4.2.2 Suspension and Green Compact Characterization 140
4.2.3 Sintering and Microstructure Evolution 162
4.2.4 Dielectric Properties 169
4.2.5 Mechanical Properties 175
4.3 Effect of Composition on Densification and Creep Behavior 182
4.3.1 Characterization of Particles 182
4.3.2 Estimation of Composite True Densities 238
4.3.3 Constant Heating Rate (CHR) Sintering Studies 240
4.3.4 Isothermal Sintering Studies 251
4.3.5 Compression Creep Studies 275
4.3.6 Rigidity Threshold in Composite Powder Compacts 297
4.3.7 Comparison of Experimental Data with Theoretical Models 305
4.3.8 An Empirical Model for Densification of Composite Powder Compacts 313

5 SUMMARY 323

6 SUGGESTIONS FOR FUTURE WORK 328

APPENDICES

A FRACTIONATION OF Si_3N_4 POWDER 331

B COATING OF Si_3N_4 POWDER WITH SiO_2 336

C SYNTHESIS OF POLYSTYRENE (PS) PARTICLES 342
D PHYSICAL PROPERTY MEASUREMENTS 344
E ARCHIMEDES DENSITY RESULTS 361
F DATA ANALYSIS FOR RHEOLOGICAL MEASUREMENTS 372
G POROSIMETRY ON SiO_2/PS COMPACTS 375
H DILATOMETRY RAW DATA 379
I X-RAY PHOTOELECTRON SPECTROSCOPY (XPS) PLOTS 386
J NITROGEN GAS ADSORPTION AND DESORPTION ISOTHERMS 392
K PARTICLE SIZE DISTRIBUTION PLOTS 403
L BOROSILICATE GLASS / ALUMINA COMPOSITES 409
M OXIDATION OF Si_3N_4 COMPACTS 421
N HIGH TEMPERATURE HEAT TREATMENT OF SiO_2/Si_3N_4 COMPACTS 440
REFERENCES 458
BIOGRAPHICAL SKETCH 471

LIST OF TABLES

Table	Page
2.1 Physical Properties of Some Glasses and Glass-Ceramics Used in Microelectronic Packaging Applications	6
2.2 Advantages and Disadvantages of Four Candidate Radome Materials	8
3.1 Amounts of Components in the Coating Experiments	43
3.2. Amounts of NH_4OH Used to Prepare Various Sizes of SiO_2 Powder	44
3.3 Parameters for Particle Size Analysis for Series I Powders	52
3.4 Parameters for Particle Size Analysis for Series II Powders	52
3.5 Parameters for Particle Size Analysis for Series III Powders	53
3.6 List of Calculated q_c, E_L, and μ_L Values for Various Powders	62
3.7 Calculated k Values for Samples Used for Dilatometry	82
3.8 Calculated k Values for 60/40 SiO_2/Si_3N_4 Samples Sintered to 1200°C in a Tube Furnace	83
3.9 Archimedes Density Results for Samples used for Dielectric Constant Measurements	91
3.10 Archimedes Density Results for Samples used for Flexure Strength Measurements	94
3.11 Thermal Histories of Samples used for Compression Creep Experiments	97
3.12 Strain Rate and Stress Data for 50/50 sample creep-tested at 1250°C	103
4.1 Electrophoretic Mobility and Zeta Potential Data for Batch I SiO_2 powder	115
4.2 Electrophoretic Mobility and Zeta Potential Data for Lot1 Si_3N_4 powder	115

4.3 Electrophoretic Mobility and Zeta Potential Data for Series I 60/40 Composite Powder..... 116

4.4 Specific Surface Areas of Core and Composite Powders..... 120

4.5 Densification Data for 60 vol% Si_3N_4 + 40 vol% Si_3N_4 Particle Mixture Samples..... 125

4.6 Densification Data for 60/40 SiO_2/Si_3N_4 Composite Powder Samples..... 126

4.7 Isothermal Densification Data at 1300°C for 60 vol% SiO_2 + 40 vol% Si_3N_4 Particle Mixture Samples..... 132

4.8 Isothermal Densification Data at 1300°C for 60/40 SiO_2/Si_3N_4 Composite Powder Samples..... 134

4.9 Electrophoretic Mobility and Zeta Potential Data for PS Particles..... 135

4.10 Results from Hg Penetration Porosimetry on Pre-Sintered Compacts..... 150

4.11 Density and Porosity Values Determined by the Archimedes Displacement Method Using Different Media..... 154

4.12 Density and Porosity Values for SiO_2 and Al_2O_3 Determined by Hg Porosimetry and Archimedes Displacement Method..... 161

4.13 Loss Tangent (tan δ) Values for SiO_2 and 60/40 SiO_2/Si_3N_4 Samples..... 173

4.14 Mechanical Properties of SiO_2 and 60/40 SiO_2/Si_3N_4 Samples..... 178

4.15 Comparison of Calculated and Expected Values of $\bar{V}_{max}$ for Composite Powders..... 198

4.16 Estimated Values of "Average" Core Diameter, D..... 208

4.17 BET Specific Surface Areas of Composite Powder Batches..... 211

4.18 Results from Surface Area and Pore Size Measurements on Calcined Series III Composite Powders..... 219

4.19 Calculated Vol% Porosity in the Coating and Composite Powder Volumes..... 222

4.20 Electrophoretic Mobility and Zeta Potential Data for Series III Composite Powders at pH Values in the Range of ~8.0 - 8.7..... 224

4.21 Electrophoretic Mobility and Zeta Potential Data for Calcined 30/70 Composite Powders at pH Values in the Range of ~9.0 - 9.3 224

4.22. Calculated Values of ψ_d for Different Values of the Shift in Shear Plane (Δ) 228

4.23 Summary of Results from ICP Analysis. 235

4.24 Calculated Weights of Different Components in the Composite Powders 235

4.25 Calculated Weight Percent of the Components in the Composite Powders 237

4.26 Calculated Volume Fractions of Components in the Composite Powders. 237

4.27 Estimated Powder True Densities Determined by Three Different Methods 239

4.28 Table of Sintered Densities Determined by Dilatometry and by Archimedes Measurements. Samples were Heated at ~11°C/min to ~1500°C. 242

4.29 List of Temperatures (T_{max}) Corresponding to the Densification Rate Maxima in the Plots Shown in Figure 4.51 243

4.30 Activation Energy Estimates for Densification of 60/40 SiO_2/Si_3N_4 Samples. 246

4.31 Summary of Particle Sizes, Pre-Sintering Conditions, and Pre-Sintered Densities for SiO_2 Compacts, 85/15 SiO_2/Si_3N_4 Composite Powder Compacts and SiO_2+Si_3N_4 Mixed Powder Compacts with 15 vol% Si_3N_4 259

4.32 Density Results for Samples Heated at 1500°C for 2 h. 259

4.33 Results from Quantitative Microscopy on Sintered (1225°C-24h) Samples. 274

4.34 List of n Values as a Function of Test Temperature for SiO_2 and Composite Samples 280

4.35 List of Activation Energies (E) at Various Compressive Stresses (σ), for SiO_2 and Composite Samples 280

4.36 Comparison of Viscosities Measured by Creep Experiments with Values Determined by Vora [Vor90] and Sacks and Tseng [Sac84b] 287

4.37 Calculated Values of Vol% Si_3N_4 in Bulk Volume of Creep Tested Samples 292

4.38 Density Data for Sintered Samples Used for Creep Testing 294

4.39 Density Data for Samples Creep Tested at 1275°C. 294

4.40 Pre-sintered Densities for Mixed Powder Compacts 304

4.41 Sintered Densities for Mixed Powder Compacts 304

B-I Amounts of Constituents Used for the Coating Process. 341

D-I. Archimedes Density Results for 60/40 SiO_2/Si_3N_4 Samples Containing Controlled Pores Created by Pyrolysis of PS 355

D-II Four-Point Bend Test Results for Dense SiO_2 Samples. 355

D-III Four-Point Bend Test Results for Dense 60/40 SiO_2/Si_3N_4 Samples. 356

D-IV Four-Point Bend Test Results for 60/40 SiO_2/Si_3N_4 Samples Containing Controlled Pores Created by Pyrolysis of PS 356

D-V Results from Fracture Toughness Measurements for dense SiO_2 Samples. 358

D-VI Results from Fracture Toughness Measurements for dense 60/40 SiO_2/Si_3N_4 Samples 358

D-VII Relative Dielectric Constants and Loss Tangents for Selected SiO_2 and 60/40 SiO_2/Si_3N_4 Samples 360

E-I Densification Data for Series II 60/40 SiO_2/Si_3N_4 Samples Without the Controlled Pores. 361

E-II Densification Data for Series II 60/40 SiO_2/Si_3N_4 Samples With the Controlled Pores 362

E-III Green Density Data for Pre-Sintered (800°C, 2 h) Series III Rod-Shaped Samples Used for Dilatometer Experiments. 363

E-IV Green Density Data for Pre-Sintered (800°C, 2 h) Series III Disk-Shaped Samples Used for Isothermal Sintering Experiments at 1225°C. 364

E-V Densification Data for Batch 3 SiO_2 Disk-Shaped Samples Sintered at 1225°C in Flowing Nitrogen. 365

E-VI Densification Data for Series III 85/15 SiO_2/Si_3N_4 Disk-Shaped Samples Sintered at 1225°C in Flowing Nitrogen 366

E-VII Densification Data for Series III 60/40 SiO_2/Si_3N_4 Disk-Shaped Samples Sintered at 1225°C in Flowing Nitrogen. 367

E-VIII Densification Data for Series III 50/50 SiO_2/Si_3N_4 Disk-Shaped Samples Sintered at 1225°C in Flowing Nitrogen. 368

E-IX. Densification Data for Series III 40/60 SiO_2/Si_3N_4 Disk-Shaped Samples Sintered at 1225°C in Flowing Nitrogen. 369

E-X. Densification Data for Series III 30/70 SiO_2/Si_3N_4 Disk-Shaped Samples Sintered at 1225°C in Flowing Nitrogen. 370

E-XI Densification Data for Disk-Shaped 85 vol% SiO_2 + 15 vol% Si_3N_4 Particle Mixture Samples Sintered at 1225°C in Flowing Nitrogen. 371

L-I Table of Sintered Densities for BSA/Al_2O_3 Samples. 415

M-I Density Results for 800°C (2 h) Pre-Sintered Si_3N_4 Compact 423

M-II Density Results for 1200°C Oxidized Si_3N_4 Compacts 427

M-III Density Results for Oxidation-Derived Composite Compacts Sintered at Various Temperatures 429

M-II Density Results for 1200°C Oxidized Si_3N_4 Compacts. 427

N-I Sample Weights and Densities for Heat-Treated 36/64 Composite Compacts 443

N-II Estimated and Measured Densities for Heat-Treated 36/64 Composite Compacts 443

N-III List of XRD Peaks for 36/64 Composite Sample Heated at 1300°C 451

N-IV List of XRD Peaks for 36/64 Composite Sample Heated at 1400°C 452

N-V List of XRD Peaks for 36/64 Composite Sample Heated at 1500°C 453

N-VI. List of XRD Peaks for 36/64 Composite Sample Heated at 1650°C 454

N-VII List of XRD Peaks for 36/64 Composite Sample Heated at 1750°C 455

N-VIII List of XRD Peaks for 36/64 Composite Sample Heated at 1800°C. 456

LIST OF FIGURES

Figure page

2.1 Empirical Relation between the thermal conductivity and dielectric constant for several dielectric materials of interest, including SiO_2 and Al_2O_3 [Gup96] 5

2.2 Schematic illustration of two types of powder compacts. (a) compact is formed by mixing A and B particles, and (b) compact is formed by using composite particles composed of cores of B particles and outer coatings of the A phase 10

2.3 Schematic illustration of incorporation of a closed, isolated pore in a SiO_2/Si_3N_4 matrix. 12

2.4 Electrophoretic mobility curves for various particles (•) $TEOS/Fe_2O_3$ molar ratio = 1.0, and (a). $TEOS/Fe_2O_3$ molar ratio = 0.1 [Azu92] 16

2.5 N_2 sorption isotherms for (a) the uncoated and (b) silica-coated α-Fe_2O_3 particles [Sun96] 18

2.6 In the self-consistent calculation, the region of matrix within the dashed circle is regarded as an isolated island surrounded by an infinite continuum (the composite) with a slower densification rate. Similarly, any of the inclusions (solid circles) can be treated as being isolated in the continuum [Sch87] 25

2.7 Relative density of a packing of coated particles as a function of normalized time $\tau' = (3/4\pi)^{1/3} \tau\gamma/[\eta(R+t)]$ for different coating thicknesses, and for the Mackenzie-Shuttleworth model [Jag94] (τ is the time, γ is the surface tension of the coating phase, η is the viscosity of the coating phase, R is the radius of the core particle, and t is the coating thickness.) 28

2.8 Density as a function of time for ZnO containing different volume fractions of SiC [Dej86] 31

2.9 Relative density of the composite vs. temperature for the die-pressed composites containing 0-22.5 vol% ZrO_2 inclusions (size 14μm) during constant-heating-rate sintering at 4°C/min to 1200°C [Fan92] 31

2.10 Linear strain rates of a polycrystalline ZnO matrix composite and a glass-matrix composite relative to the strain rate of the free matrix versus inclusions volume fraction. The dashed line represents the predictions of the rule-of-mixtures [Dut92] 32

2.11 Comparison of the experimental results for the linear strain rate of the composite normalized by the strain rate from the rule-of-mixtures, vs. relative density of the matrix ρ_m with the predictions of Scherer's model for the indicated volume fractions of inclusions, F [Rah87] (● ■) experimental values; (----)· predicted values 34

2.12 Linear strain rate of the composite referred to the strain rate from the rule-of-mixtures, vs relative density of the matrix for (•,—)0.15, and (o,—)0.30, platelet volume fractions. The symbols and lines represent experimental and predicted values, respectively [Boc94] 34

2.13 Data for the densification rate of the composite containing 20 vol% inclusions, relative to that of the free matrix, as a function of the matrix density compared with the predictions of Scherer's SC model using (a) the measured values for G_c, and (b) the Hashin-Shtrikman lower bound [Dut92] 37

2.14 Matrix relative density vs. temperature for the composite formed from the coated inclusion particles (20 vol% inclusions) compared with the data for a composite formed from conventionally mixed powders [Hu92] 39

3.1 Plots of cumulative volume percent vs. Stokes diameter for as-received, Lot1 and Lot2 Si_3N_4 powders 41

3.2 Plots of cumulative mass percent vs. Stokes diameter for (A) batch 1, (B) batch 2, and (C) batch 3 SiO_2 powders. 46

3.3 SEM micrograph of PS particles 50

3.4 Histogram plot of particle diameter distribution for PS particles 51

3.5 Schematic showing the pore geometry assumed for calculation of pore size distributions by nitrogen gas adsorption. 56

3.6 Schematic showing the image parameters that were measured. P and A denote perimeter and area, respectively, of the particle. (SN=core particle and C=composite particle) 64

3.7 Heating schedule for the pre-sintering of Series II powder compacts 74

3.8 Configuration for dilatometry experiments 79

3 9 Temperature profile in the tube furnace used for isothermal sintering experiments Inset shows the region up to 2 inches from the center 87

3 10 Schematic showing the electrode structure for the non-contacting electrode method for dielectric constant measurements 92

3 11 The four-point bend test configuration 95

3 12 Schematic illustrating the Knoop indentor geometry 96

3 13 The compression creep test configuration 99

3 14 Displacement vs. time plots for 50/50 sample creep-tested at 1250°C 101

3 15 Creep strain vs time plots for 50/50 sample creep-tested at 1250°C 102

4 1 SEM micrographs of (A) Si_3N_4 and (B) 60/40 microcomposite particles 105

4 2 Bright-field TEM images of (A) Si_3N_4, (B) 40/60, (C) 60/40 and (D) 85/15 particles 106

4.3 Micrographs illustrating problems observed for extreme compositions (A) SEM of 85/15 powder showing SiO_2 particles and (B) TEM of 30/70 powder showing a composite particle agglomerate 107

4 4 HRTEM image of a microcomposite particle from the 40/60 powder batch The lattice fringes on the left side represent crystal planes in Si_3N_4 109

4 5 Powder XRD patterns for Si_3N_4 and 80/20 composite powders 110

4 6 XPS plots for Lot1 Si_3N_4 fractionated powder (A=Auger peak) 112

4 7 XPS plots for Series I 60/40 SiO_2/Si_3N_4 composite powder (A=Auger peak) 113

4 8 XPS plots for Si_3N_4 and 60/40 composite powders for binding energies in the range of 300 - 600 eV 114

4 9 Zeta potential vs. pH plots for SiO_2, Si_3N_4 and 60/40 powders 117

4 10 Particle size distribution plots for Lot1 Si_3N_4, 60/40, and 80/20 powders 119

4 11 Particle size distribution plots for ~60 vol% SiO_2 + ~40 vol% Si_3N_4 mixed powder and 60/40 SiO_2/Si_3N_4 composite powder, respectively 123

4.12 Plots of (a) bulk density vs. temperature and (b) open porosity vs temperature for 60/40 SiO_2/Si_3N_4 samples prepared from (i) a mixture of SiO_2 particles and Si_3N_4 particles and (ii) SiO_2-coated Si_3N_4 microcomposite particles 127

4.13 Plots of relative density vs. sintering temperature for 60/40 SiO_2/Si_3N_4 samples prepared from (i) a mixture of SiO_2 particles and Si_3N_4 particles and (ii) SiO_2-coated Si_3N_4 microcomposite particles 128

4.14 Plots of (a) bulk density vs. time and (b) open porosity vs. time, at 1300°C for 60/40 SiO_2/Si_3N_4 samples prepared from (i) a mixture of SiO_2 particles and Si_3N_4 particles and (ii) SiO_2-coated Si_3N_4 microcomposite particles 130

4.15 Plots of relative density vs. sintering time at 1300°C for 60/40 SiO_2/Si_3N_4 samples prepared from (i) a mixture of SiO_2 particles and Si_3N_4 particles and (ii) SiO_2-coated Si_3N_4 microcomposite particles 131

4.16 SEM micrographs of polished and etched 60/40 SiO_2/Si_3N_4 samples prepared from (A) a mixture of SiO_2 particles and Si_3N_4 particles and (B) SiO_2-coated Si_3N_4 composite powder. Samples were sintered for 2 h at 1300°C 133

4.17 Plots of zeta potential vs. pH for polystyrene (PS) and 60/40 microcomposite particles 136

4.18 Plots showing (a) TGA and (b) DTA curves for PS particles heated at 3°C/min in nitrogen. 138

4.19 Plots showing (a) TGA and (b) DTA curves for PS particles heated at 3°C/min in air 139

4.20 Plots of (a) shear stress vs. shear rate and (b) viscosity vs. shear rate for PS suspension (~21 vol% solids) and 60/40 SiO_2/Si_3N_4(~36 vol% solids) suspensions, respectively at pH~9.2 141

4.21 Plots of (a) shear stress vs. shear rate and (b) viscosity vs. shear rate for 60/40 SiO_2/Si_3N_4(~30 vol% solids) suspensions with and without PS respectively, at pH~9.2 143

4.22 SEM micrographs of green compacts prepared by slip-casting (A) 60/40 SiO_2/Si_3N_4 composite powder and (B) a mixture of 60/40 SiO_2/Si_3N_4 microcomposite particles and PS particles 146

4.23 TGA plots for 100°C vacuum dried 60/40 SiO_2/Si_3N_4 compacts prepared with and without PS particles. 147

4.24 Plots of (a) pore volume and (b) specific volume frequency versus pore diameter obtained by mercury porosimetry for pre-sintered (800°C) 60/40 SiO_2/Si_3N_4 samples cast with and without PS particles 149

4.25 Adsorption and desorption isotherm plots for 800°C pre-sintered 60/40 SiO_2/Si_3N_4 compacts with PS-derived pores 153

4.26A Plots of (a) pore volume and (b) specific volume frequency vs pore diameter obtained by nitrogen adsorption for a pre-sintered (800°C) 60/40 SiO_2/Si_3N_4 sample with PS particle-derived pores. 155

4.26B Plots of (a) pore volume and (b) specific volume frequency (dV/dD) versus pore diameter obtained by nitrogen gas adsorption for 60/40SiO_2/Si_3N_4 composite powder and powder compact 156

4.27 Plots of bulk density vs. temperature for 60/40 SiO_2/Si_3N_4 samples prepared with and without PS particles 163

4.28 Plots of open porosity vs temperature for 60/40 SiO_2/Si_3N_4 samples prepared with and without PS particles 164

4.29 Plots of relative density vs temperature for 60/40 SiO_2/Si_3N_4 samples prepared with and without PS particles. 165

4.30 SEM micrograph of a fracture surface of a 60/40 composite powder sample (sintered at 1300°C, 2h) showing PS-derived pores 168

4.31 SEM micrograph of a polished and etched surface of a 60/40 composite powder sample (sintered at 1300°C, 2h) processed with PS particles 168

4.32 Plots of dielectric constant vs frequency for fully dense and porous SiO_2 and SiO_2/Si_3N_4 samples 170

4.33 Plots of dielectric constant vs frequency for 60/40 SiO_2/Si_3N_4 samples with varying amounts of porosity 172

4.34 Plots of dielectric constant vs porosity for 60/40 SiO_2/Si_3N_4 samples showing comparisons with theoretical predictions of equations 4.3 and 4.4 174

4.35 SEM micrographs of fracture surfaces showing controlling flaws in flexure-tested SiO_2 samples (A) Sample #3 and (B) Sample #8 176

4.36 SEM micrographs of a polished surface of a 60/40 sample showing a typical crack path at (A) a low magnification and (B) a high magnification The crack was produced by Vicker's indentation and the surface was etched with HF solution 177

4 37 SEM micrographs of a fracture surface of a 60/40 sample (sintered at 1300°C 2h) (A) Low magnification micrograph shows the mirror-mist-hackle pattern (B) Higher magnification micrograph shows the fracture origin which is a large processing defect (powder agglomerate) 179

4.38 SEM micrographs of a fracture surface of a 60/40 sample (sintered at 1300°C 2h) with PS-derived pores (A) Low magnification micrograph shows the mirror-mist-hackle pattern (B) Higher magnification micrograph shows the flaw (powder agglomerate) causing failure 180

4 39 Bright field TEM images of 50/50 microcomposite particles with (A) relatively smaller and (B) relatively larger core particles. The coating thickness is ~28nm for both particles. 183

4 40 Bright-field TEM images of 60/40 microcomposite particles with (A) relatively smaller and (B) relatively larger core particles The coating thickness is ~38nm for both particles 184

4 41 Bright-field TEM images of 85/15 microcomposite particles with (A) relatively smaller and (B) relatively larger core particles The coating thickness is ~110nm for both particles. 185

4 42 Plot of area-based coating thickness vs Si_3N_4 core particle diameter determined on composite powder with an overall composition of 30/70 SiO_2/Si_3N_4 186

4 43 Plot of area-based coating thickness vs Si_3N_4 core particle diameter determined on composite powder with an overall composition of 40/60 SiO_2/Si_3N_4 187

4 44 Plot of area-based coating thickness vs Si_3N_4 core particle diameter determined on composite powder with an overall composition of 50/50 SiO_2/Si_3N_4 188

4 45 Plot of area-based coating thickness vs. Si_3N_4 core particle diameter determined on composite powder with an overall composition of 60/40 SiO_2/Si_3N_4 189

4 46 Plot of area-based coating thickness vs Si_3N_4 core particle diameter determined on composite powder with an overall composition of 85/15 SiO_2/Si_3N_4 190

4 47 Plot of average coating thickness vs. average volume percent SiO_2 for SiO_2/Si_3N_4 microcomposite particles 192

4 48 Plot of volume fraction Si_3N_4 in coated particle vs Si_3N_4 particle diameter determined on composite powder with an overall composition of 30/70 SiO_2/Si_3N_4 193

4 49 Plot of volume fraction Si_3N_4 in coated particle vs Si_3N_4 particle diameter determined on composite powder with an overall composition of 40/60 SiO_2/Si_3N_4 194

4 50 Plot of volume fraction Si_3N_4 in coated particle vs. Si_3N_4 particle diameter determined on composite powder with an overall composition of 50/50 SiO_2/Si_3N_4 195

4 51 Plot of volume fraction Si_3N_4 in coated particle vs Si_3N_4 particle diameter determined on composite powder with an overall composition of 60/40 SiO_2/Si_3N_4 196

4.52 Plot of volume fraction Si_3N_4 in coated particle vs. Si_3N_4 particle diameter determined on composite powder with an overall composition of 85/15 SiO_2/Si_3N_4 197

4 53 Plot of percent reduction in shape factor after coating vs shape factor of core particle for composite powder with an overall composition of 30/70 SiO_2/Si_3N_4 200

4 54 Plot of percent reduction in shape factor after coating vs shape factor of core particle for composite powder with an overall composition of 40/60 SiO_2/Si_3N_4 201

4 55 Plot of percent reduction in shape factor after coating vs shape factor of core particle for composite powder with an overall composition of 50/50 SiO_2/Si_3N_4 202

4 56 Plot of percent reduction in shape factor after coating vs shape factor of core particle for composite powder with an overall composition of 60/40 SiO_2/Si_3N_4 203

4 57 Plot of percent reduction in shape factor after coating vs. shape factor of core particle for composite powder with an overall composition of 85/15 SiO_2/Si_3N_4 204

4 58 Plot of percent reduction in shape factor after coating vs shape factor of core particle for composite powders with overall compositions of 30/70, 40/60, and 50/50 SiO_2/Si_3N_4 205

4 59 Plot of percent reduction in shape factor after coating vs. shape factor of core particle for composite powders with overall compositions of 60/40 and 85/15 SiO_2/Si_3N_4 206

4 60 Particle size distribution plots for SiO_2/Si_3N_4 composite powders. 210

4 61 Plots of (a) pore volume and (b) specific volume frequency (dV/dD) vs. pore diameter obtained from nitrogen gas desorption isotherms for 30/70 composite powders calcined at various temperatures. 213

4 62. Plots of (a) pore volume and (b) specific volume frequency (dV/dD) vs pore diameter obtained from nitrogen gas desorption isotherms for 40/60 composite powders calcined at various temperatures. 214

4 63 Plots of (a) pore volume and (b) specific volume frequency (dV/dD) vs. pore diameter obtained from nitrogen gas desorption isotherms for 50/50 composite powders calcined at various temperatures 215

4 64 Plots of (a) pore volume and (b) specific volume frequency (dV/dD) vs pore diameter obtained from nitrogen gas desorption isotherms for 60/40 composite powders calcined at various temperatures 216

4 65 Plots of cumulative desorption pore volume vs pore diameter obtained from nitrogen gas desorption isotherms for 85/15 composite powders calcined at 200°C for 6 h. 217

4 66 Plots of (a) pore volume and (b) specific volume frequency (dV/dD) vs pore diameter obtained from nitrogen gas desorption isotherms for 30/70 40/60 and 60/40 composite powders calcined at 200°C for 6 h 221

4 67 XPS plot for Si_3N_4 powder showing the presence of oxygen on the surface. 229

4 68 XPS plot for 30/70 composite powder showing the absence of any nitrogen peaks 230

4 69 XPS plot for 40/60 composite powder showing the absence of any nitrogen peaks 231

4 70 XPS plot for 50/50 composite powder showing the absence of any nitrogen peaks 232

4 71 XPS plot for 60/40 composite powder showing the absence of any nitrogen peaks 233

4 49 Plots of bulk density vs. temperature for SiO_2/Si_3N_4 samples heated at 11°C/min. 241

4 73 Plots of relative density vs temperature for SiO_2/Si_3N_4 samples heated at 11°C/min 244

4 74 Plots of composite densification rate vs temperature for SiO_2/Si_3N_4 samples heated at 11°C/min 245

4 75 Plots of relative density vs temperature for 60/40 SiO_2/Si_3N_4 samples heated at three different heating rates (a)~6°C/min, (b)~11°C/min, and (c)~19°C/min 247

4 76 Plots of densification rate vs temperature for 60/40 SiO_2/Si_3N_4 samples heated at three different heating rates (a)~6°C/min, (b)~11°C/min, and (c)~19°C/min 248

4 77 Arrhenius plots for 60/40 SiO_2/Si_3N_4 samples at four different values of composite relative densities (a) 75%, (b) 75%, (c) 82%, and (d) 87% 249

4 78 Plots of bulk density vs temperature for microcomposite powder compacts with Si_3N_4 contents in the range of 30-70 vol%. 252

4 79 Plots of % open porosity vs temperature for microcomposite powder compacts with Si_3N_4 contents in the range of 30-70 vol% 253

4 80 Plots of bulk density vs temperature for SiO_2 and SiO_2/Si_3N_4 samples 254

4 81 Plots of % open porosity vs temperature for SiO_2 and SiO_2/Si_3N_4 samples. 255

4 82 Plots of composite relative density vs sintering time for composite powder compacts with Si_3N_4 contents in the range of 15-70 vol%. The compacts were sintered isothermally in nitrogen at 1225°C 256

4 83 Plots showing the data in Figure 4 82 at sintering times in the range of 0-600 min 257

4 84 Plots of relative density vs. sintering time for SiO_2 and SiO_2/Si_3N_4 compacts sintered isothermally in nitrogen at 1225°C 258

4 85 Plot of maximum relative density vs amount of Si_3N_4 for composite powder compacts. 261

4 86 XRD plots for SiO_2/Si_3N_4 samples heated at 5°C/min to 1500°C and soaked for 2h. The crystalline peaks (marked α) for all the samples correspond to α-Si_3N_4 262

4.87. Plots of compact densification rate vs. matrix relative density for SiO_2 compacts and composite powder compacts with Si_3N_4 contents in the range of 15-50 vol% 265

4.88. Hydrostatic stress in the matrix normalized by the sintering pressure, σ_m/Σ, vs matrix relative density, ρ_m, for the indicated volume fractions of Si_3N_4 268

4.89. Hydrostatic stress in the matrix normalized by the sintering pressure, σ_m/Σ, vs matrix relative density, ρ_m, for composite powder compacts and particle mixture compacts. 269

4.90. SEM micrographs of polished and etched samples prepared from composite powders with different SiO_2/Si_3N_4 volume ratios (A) 85/15, (B) 60/40, (C) 50/50 and (D) 40/60. Samples were sintered at 1225°C for 24h 271

4.91. High-resolution transmission electron micrograph of a 40/60 sample sintered at 1400°C for 2h. The lattice fringes depict adjacent Si_3N_4 particles while the thin (~5nm) layer separating the two particles is amorphous SiO_2 273

4.92. Plots of strain rate vs. stress for compression creep of SiO_2 samples at temperatures in the range of 900-1100°C 276

4.93. Plots of strain rate vs. stress for compression creep of 85/15 SiO_2/Si_3N_4 samples at temperatures in the range of 1100-1200°C 277

4.94. Plots of strain rate vs. stress for compression creep of 60/40 SiO_2/Si_3N_4 samples at temperatures in the range of 1200-1275°C 278

4.95. Plots of strain rate vs. stress for compression creep of 50/50 SiO_2/Si_3N_4 samples at temperatures in the range of 1250-1325°C 279

4.96. Plots of creep strain rate as a function of inverse temperature for SiO_2 samples. 282

4.97. Plots of creep strain rate as a function of inverse temperature for 85/15 SiO_2/Si_3N_4 samples 283

4.98. Plots of creep strain rate as a function of inverse temperature for 60/40 SiO_2/Si_3N_4 samples 284

4.99. Plots of creep strain rate as a function of inverse temperature for 50/50 SiO_2/Si_3N_4 samples. 285

4.100. Plots of strain rate vs. stress for 60/40 SiO_2/Si_3N_4 samples showing the effect of sintering temperature on the creep behavior 289

4.101 Plots of strain rate vs. stress for the compression creep of composite samples with SiO_2/Si_3N_4 ratios of 30/70, 40/60, 50/50, and 60/40, respectively, at 1275°C 290

4.102 XRD plots for SiO_2/Si_3N_4 samples compression creep tested at 1275°C. The crystalline peaks (α) for both samples correspond to α-Si_3N_4. 298

4.103 Schematic showing the formation of a rigid network of Si_3N_4 particles at the threshold concentration (rigidity threshold). 300

4.104 Plot of Si_3N_4 in the bulk volume at the maximum sintered density vs. Si_3N_4 content in solids. The rigidity threshold value is ~49 vol%. 302

4.105 Comparison plots of the normalized linear strain rate of the composite vs. the relative density of the matrix, for SiO_2/Si_3N_4 composites containing 85 vol% SiO_2 307

4.106 Comparison plots of relative density vs. normalized time $\tau = (3/4\pi)^{1/3} \tau\gamma/\eta R$, for composite powder compacts used in this study and simulations of Jagota [Jag94]. 312

4.107 Plots of equivalent viscosity (from eq. 4.32) vs. relative density for SiO_2 and composite powder compacts. 315

4.108 Plots of normalized viscosity vs. normalized separation distance for composite samples. 319

4.109 Plots of normalized viscosity vs. Si_3N_4 volume fraction for the composite samples. The symbols represent the experimental data whereas the solid line depicts the Dougherty-Krieger equation. 321

B-1 Plots of cumulative mass percent vs. Stokes diameter for Lot2 Si_3N_4 powder in different media. 338

D-1 Plots of load vs. displacement for dense 60/40 SiO_2/Si_3N_4 samples. 345

D-2 Plots of load vs. displacement for porous 60/40 SiO_2/Si_3N_4 samples. 347

D-3 Plots of load vs. displacement for dense SiO_2 samples. 351

F-1 Plots of shear stress vs. shear rate for PS. Series II SiO_2/Si_3N_4, and mixed particle suspensions in the range of 10 - 100 s^{-1}. The solid lines are the curves fit to the experimental data. 373

F-2 Plots of shear stress vs shear rate for PS, Series II SiO_2/Si_3N_4 and mixed4particle suspensions in the range of 100 - 1000 s^{-1} The solid lines are the curves fir to the experimental data. ..372

G-1 Plots of pora volume vs pore radius obtained by mercury porosimetry for dried aod pre-sintered (800°C) 60/40 samples cast with PS particles ..377

H-1 Plots of corrected axial shrinkage vs temperature for two independent 30/70 composite samples heated at ~11°C/min in the dilatometer .. 380

H-2 Plots of corrected axial shrinkage vs temperature for two independent 40/60 composite samples heated at ~11°C/min in the dilatometer ..381

H-3 Plots of corrected axial shrinkage vs. temperature for two independent 50/50 composite samples heated at ~11°C/min in the dilatometer ..382

H-4 Plots of corrected axial shrinkage vs temperature for two independent 60/40 composite samples heated at ~11°C/min in the dilatometer 384

H-5 Plots of corrected axial shrinkage vs temperature for two independent 60/40 composite samples heated at ~6°C/min in the dilatometer ..385

H-6 Plots of corrected axial shrinkage vs. temperature for two independent 60/40 composite samples heated at ~19°C/min in the dilatometer ..386

I-1 XPS plot for Si_3N_4 powder showing the presence of oxygen on the surface 387

I 2 XPS plot for 30/70 composite powder showing the absence of any nitrogen peaks. 388

I-3 XPS plot for 40/60 composite powder showing the absence of any nitrogen peaks 389

I-4 XPS plot for 50/50 composite powder showing the absence of any nitrogen peaks 390

I 5 XPS plot for 60/40 composite powder showing the absence of any nitrogen peaks 391

J-1 Plots of adsorption and desorption isotherms for Series III 30/70B powder heated for 2 h at 100°C in vacuum (degassed for ~6 h at 200°C in nitrogen) 393

J-2 Plots of adsorption and desorption isotherms for Series III 30/70B powder heated for 6 h at 400°C in air (degassed for ~6 h at 200°C in nitrogen) 394

J-3 Plots of adsorption and desorption isotherms for Series III 30/70B powder heated for 6 h at 600°C in air (degassed for ~6 h at 200°C in nitrogen) ... 395

J-4 Plots of adsorption and desorption isotherms for Series III 30/70B powder heated for 6 h at 800°C in air (degassed for ~6 h at 200°C in nitrogen) ... 396

J-5 Plots of adsorption and desorption isotherms for Series III 40/60B powder heated for 2 h at 100°C in vacuum (degassed for ~6 h at 200°C in nitrogen) ... 397

J-6 Plots of adsorption and desorption isotherms for Series III 40/60B powder heated for 6 h at 600°C in air (degassed for ~6 h at 200°C in nitrogen) ... 398

J-7 Plots of adsorption and desorption isotherms for Series III 50/50B powder heated for 6 h at 400°C in air (degassed for ~6 h at 200°C in nitrogen) ... 399

J-8 Plots of adsorption and desorption isotherms for Series III 50/50B powder heated for 6 h at 600°C in air (degassed for ~6 h at 200°C in nitrogen). ... 400

J-9 Plots of adsorption and desorption isotherms for Series III 60/40B powder heated for 2 h at 100°C in vacuum (degassed for ~6 h at 200°C in nitrogen) ... 401

J-10 Plots of adsorption and desorption isotherms for Series III 60/40B powder heated for 6 h at 600°C in air (degassed for ~6 h at 200°C in nitrogen) ... 402

K-1 Particle size distribution plots (two independent samples) for Series III 30/70 composite powder ... 404

K-2 Particle size distribution plots (two independent samples) for Series III 40/60 composite powder ... 405

K-3 Particle size distribution plots (two independent samples) for Series III 50/50 composite powder ... 406

K-4 Particle size distribution plots (two independent samples) for Series III 60/40 composite powder ... 407

K-5 Particle size distribution plots (two independent samples) for Series III 85/15 composite powder ... 408

L-1 Plots of (a) bulk density vs. temperature and (b) open porosity vs. temperature for ~39/61 BS/Al_2O_3 and ~39/61 SiO_2/Al_2O_3 [Sac91a] compacts prepared from microcomposite particles ... 419

M-1 Plots of (a) temperature vs time (i.e. the temperature profile) and (b) weight gain vs temperature for Si_3N_4 compact ... 424

M-2 XRD plots for (A) 45/55 and (B) 50/50 SiO_2/Si_3N_4 samples formed by oxidizing Si_3N_4 compacts at 1200°C in oxygen ... 426

M-3 SEM micrographs (270x magnification) of polished cross-sections of the oxidation-derived 45/55 sample sintered at 1350°C for 2 h (A) (B) and (C) denote fields in the "top", "middle", and "bottom" regions, respectively (This notation is based on the as-cast configuration For e g , "top" denotes the region of the cross-section near the top of the cast sample) ... 432

M-4 SEM micrographs (270x magnification) of polished cross-sections of the oxidation-derived 50/50 sample sintered at 1350°C for 2 h (A) and (B) denote fields in the "top" and "middle regions, respectively ... 433

M-5 SEM micrographs (4000x magnification) of polished cross-sections of the oxidation-derived 45/55 sample sintered at 1350°C for 2 h. (A), (B) and (C) denote fields in the "top", "middle", and "bottom" regions, respectively ... 434

M-6 SEM micrographs (4000x magnification) of polished cross-sections of the oxidation-derived 50/50 sample sintered at 1350°C for 2 h. (A), (B) and (C) denote fields in the "top", "middle" and "bottom" regions, respectively ... 435

M 7 SEM micrographs (25 000x magnification) of polished cross-sections of the oxidation-derived 45/55 sample sintered at 1350°C for 2 h (A) (B) and (C) denote fields in the "top", "middle" and bottom" regions, respectively ... 438

M-8 SEM micrographs (25 000x magnification) of polished cross-sections of the oxidation-derived 50/50 sample sintered at 1350°C for 2 h (A), (B) and (C) denote fields in the "top", "middle", and "bottom" regions respectively ... 439

N-1 XRD plots for 36/64 SiO_2/Si_3N_4 composite powder compact sintered at 1400°C for 2 h in nitrogen ... 445

N-2 XRD plots for 36/64 SiO_2/Si_3N_4 composite powder compact sintered at 1500°C for 2 h in nitrogen ... 446

N-3 XRD plots for 36/64 SiO_2/Si_3N_4 composite powder compact sintered at 1600°C for 2 h in nitrogen ... 447

N-4 XRD plots for 36/64 SiO_2/Si_3N_4 composite powder compact sintered at 1650°C for 2 h in nitrogen ... 448

N-5 XRD plots for 36/64 SiO_2/Si_3N_4 composite powder compact sintered at 1750°C for 2 h in nitrogen ... 449

N-6 XRD plots for 36/64 SiO_2/Si_3N_4 composite powder compact sintered at 1800°C for 2 h in nitrogen 450

Abstract of Dissertation Presented to the Graduate School
of the University of Florida in Partial Fulfillment of the
Requirements for the Degree of Doctor of Philosophy

SYNTHESIS CHARACTERIZATION, AND PROCESSING OF POWDERS, DENSIFICATION BEHAVIOR MICROSTRUCTURE AND PROPERTIES FOR SILICA / SILICON NITRIDE PREPARED FROM MICROCOMPOSITE PARTICLES

By

Ramesh Raghunathan

May 1997

Chairman Dr Michael D Sacks
Major Department. Materials Science and Engineering

A novel process was used to synthesize submicrometer composite particles ('microcomposite particles") containing inner cores of Si_3N_4 and outer coatings of amorphous SiO_2. Microcomposite particles with overall SiO_2/Si_3N_4 volume ratios ranging from 30/70 to 85/15 were prepared Quantitative microscopy showed that for any given powder batch, the average area-based thickness of the coating on each composite particle was independent of the core particle size Since the core particles had a size distribution the smaller composite particles had relatively higher concentrations of SiO_2 and larger composite particles had relatively lower concentrations of SiO_2 The surface area varied between powder batches of samples with the same overall composition due to the presence of varying amounts of nano-sized porosity in the coating These pores were generally eliminated upon calcination at ~600°C However, samples with extremely thin (~12nm) coatings retained significant amounts of porosity after heating under the same conditions For powders with overall SiO_2 contents ≥ 40 vol%, the zeta potentials of the

composite particles were found to be similar to that of SiO_2. In contrast, for powders with an overall SiO_2/Si_3N_4 volume ratio of 30/70, the zeta potentials were significantly lower. Further, the zeta potential increased as the powder was calcined at progressively higher temperatures. Bulk compacts were prepared by slip-casting well-dispersed, aqueous composite powder suspensions. Powder compacts prepared with the composite powders showed enhanced densification compared to compacts prepared from a mixture of SiO_2 and Si_3N_4 powders. Electron microscopy observations on sintered composites revealed that densification in the mixed powder samples was constrained by the development of rigid networks of "non-sinterable" Si_3N_4 particles. In contrast, the controlled spatial distribution of the phases (core + coating) in the microcomposite particles inhibited the formation of Si_3N_4 particle-particle contacts during sintering. Compacts with Si_3N_4 contents below a threshold value (defined as the "rigidity threshold") of ~49 vol% could be sintered to full density (i.e., zero porosity) at temperatures ≤ 1300°C. The low sintering temperature was attributed to densification by viscous flow of the SiO_2 coatings. This was consistent with the activation energy values obtained from constant-heating-rate sintering experiments (~550 - 616 kJ/mol) and with the activation energies of deformation obtained from compressive creep experiments (529 - 579 kJ/mol) on dense composite samples with 60-85 vol% SiO_2. It was shown by a geometrical analysis that the "rigidity threshold" is numerically equal to the green compact density for ideal systems. The "rigidity threshold" for the SiO_2/Si_3N_4 composite powder compacts was significantly lower than the theoretical value of ~60 vol%, presumably due to the experimental non-uniformities resulting from the phase composition distribution in the composite powders. The densification data did not follow the predictions of existing theoretical models (such as Scherer's self-consistent model and Jagota's finite-element model). An empirical model based on an "effective viscosity" of the solid material for densification was formulated to predict the densification behavior. Composite powder compacts with ~9-10 vol% closed, isolated, spheroidal pores (~1-9 μm dia.) were

prepared by using a mixture of microcomposite particles and polystyrene (PS) particles. The incorporation of microporosity resulted in a lower dielectric constant (~4.4 at 1 MHz) compared to a fully dense sample (~4.9 at 1 MHz) with the same SiO_2/Si_3N_4 volume ratio (~60/40). The samples had the same loss tangent (2×10^{-4}) and average flexural strength (183 MPa) values. SEM observations of fracture surfaces suggested that the strength values for these samples could be increased by reducing the concentration of large processing related flaws (e.g., powder agglomerates).

CHAPTER 1
INTRODUCTION

Reinforcement of ceramic matrices with second-phase particulates can result in significant improvements in properties (e.g., mechanical, electrical, thermal, etc.) [Bet84, Bet86a, Bet86b, Bet90, Cer90, Che92, Ult88]. However, it is sometimes difficult to fabricate such composites using conventional powder processing and pressureless sintering methods. This is because densification of a powder matrix is usually inhibited by the addition of rigid ("non-sinterable") inclusions. Furthermore, the densification rate will be controlled primarily by the inclusions when the volume fraction is sufficient to establish a contiguous network (i.e., percolation path). In the case of equal-sized spheres that are randomly mixed, the threshold concentration for percolation occurs at only ~16 vol% inclusions [Zal83].

An alternative processing approach which can lead to enhanced densification and controlled microstructure development is based on using submicrometer composite particles. These "microcomposite" particles consist of inner cores of the rigid (inclusion) phase and outer coatings of the sinterable (matrix) phase. The structure prevents the formation of inclusion-inclusion contacts in the green compacts, regardless of the inclusion volume fraction. During sintering, however, the matrix phase is redistributed and the inclusion particles approach one another as the compact shrinks. A contiguous network of the inclusion phase may develop prior to full densification if the matrix/inclusion volume ratio is too low. Nevertheless, bulk composites with considerably higher inclusion contents can usually be fabricated by pressureless sintering of coated powders instead of random powder mixtures. Previous studies have shown that

rigid inclusions inhibit densification to a lesser extent when the matrix phase sinters by viscous flow. Thus, a particularly effective method for enhancing densification is based on using composite particles in which the outer coating is an amorphous material.

In recent years, there has been increasing interest in developing low dielectric constant glass/ceramic formulations for high performance applications such as high-speed microelectronics packaging [Tum91] and hypersonic radar guidance systems [Kou92, Fra92]. Composite materials containing SiO_2 and/or Si_3N_4 have been identified as candidate materials for these applications [Tum91, Fra92]. In the present study SiO_2/Si_3N_4 composites were prepared from composite particles consisting of crystalline Si_3N_4 cores and amorphous SiO_2 coatings.

The objectives of this study were as follows: (1) to perform detailed characterization of the SiO_2/Si_3N_4 microcomposite particles, (2) to carry out an investigation of the densification behavior and microstructure evolution during the sintering of the composite powder compacts, (3) to study the high-temperature deformation behavior of sintered composites, and (4) to evaluate the room temperature electrical and mechanical properties of selected sintered samples.

In chapter 2, a general background relevant to this investigation is presented. In chapter 3, detailed experimental procedures are described. The results and discussion are detailed in chapter 4. The results are summarized in chapter 5 and suggestions for future work are given in chapter 6.

CHAPTER 2
BACKGROUND

2.1. Introduction

A review of the processing of glass/ceramic composites will be described in this chapter. The potential applications and the processing considerations for the preparation of low-dielectric constant composites will be discussed. This will be followed by a discussion on the preparation of composites with controlled porosity. Previous research on the synthesis and characterization of composite powders related to this study will then be reviewed. Finally, some of the existing sintering models will be described and they will be compared to results from various experimental investigations.

2.2. Low-Dielectric Constant Glass-Matrix Composites

2.2.1. Potential Applications

There is increasing interest in developing advanced low dielectric constant materials for high performance applications such as high-speed microelectronics packaging and hypersonic radar guidance systems. The substrate materials used in microelectronics packaging applications must have low dielectric constant (in order to increase signal propagation speed) and low loss tangent, coefficient of thermal expansion (CTE) match with chip and/or metallizing materials, good corrosion resistance (e.g. to moisture), and adequate mechanical properties (strength, fracture toughness) to withstand stresses imposed

during fabrication and handling of the package The most widely used packaging material is alumina, which has a dielectric constant of ~9 Since the signal propagation speed is inversely proportional to the square root of the dielectric constant, the speed of propogation of a signal in alumina is only 1/3 times that in the material with the lowest possible dielectric constant (= 1), i.e., in vacuum. In contrast, SiO_2 and silicate glasses have dielectric constants of ~4– 5 The use of these materials represents an increase in signal speed of ~50%, i.e., from that of 1/3 to 1/2 times that in vacuum In recent years, many investigations have been directed toward the development of glass/ceramic materials with co-firing compatibility with lower resistivity metals such as copper, silver etc (in order to produce packages with higher circuit density) [Tum91] Figure 2.1 shows an empirical relation between thermal conductivity and dielectric constant for several dielectric materials of interest, including SiO_2 and Al_2O_3 [Gup96] It is clearly evident that the SiO_2-based glass, glass/ceramic, and ceramic formulations have lower moduli, lower strengths, and lower thermal conductivities, compared to Al_2O_3. Therefore, the packages built with these materials must be provided with external thermal and/or mechanical management systems [Tum91] The physical properties of some of the candidate glass and glass/ceramic materials developed for microelectronic packaging applications are summarized in Table 2.1

The desired material properties for advanced missile radomes in radar guidance systems include high melting point (>1000°C) high strength and high fracture toughness, low CTE, corrosion and impact resistance (against rain drops), and low and stable dielectric constant at radio frequencies. The most prevalent materials for existing missile radomes are slip-cast fused silica (SCFS) and Pyroceram 9606 (MgO-Al_2O_3-SiO_2 ceramic) [Kou92,

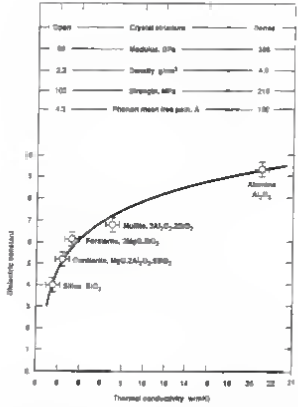

Figure 2.1 Empirical relation between thermal conductivity and dielectric constant for several dielectric materials of interest, including SiO_2 and Al_2O_3 [Gup96]

Table 2.1 Physical Properties of Some Glasses and Glass-Ceramics Used in Microelectronic Packaging Applications

Material*	Dielectric Constant[†]	tan δ[†]	Vicker's Hardness (GPa)	Flexural Strength (MPa)	Reference
40 vol% borosilicate glass/ 60 vol% silica glass	4.0	0.0025		85 - 105	[Gup96]
15 wt% quartz glass/65 wt% borosilicate glass/20 wt% α-cordierite	4.2	0.0020	12	128	[Kat92]
15 wt% quartz glass/65 wt% borosilicate glass/20 wt% α-cordierite with ~13 vol% PS-derived closed porosity	3.4	0.0026	7.8	85	[Kat92]
$2MgO\text{-}2Al_2O_3\text{-}5SiO_2$ glass-ceramic[†] (primary crystalline phase: α-cordierite)	5	0.0010		200	[Kum92]
20 wt% MgO/20 wt% Al_2O_3/60 wt% SiO_2 (cordierite) glass	6.8	0.0020			[Tho91]
Magnesium SiAlON glass	6.7	0.0080			[Tho91]
Mullite (crystalline thin film)	6.8		10	302	[Kur90]
Lead borosilicate glass	4.5 - 5.2	0.0030			[Sha88]
55 wt% (Na,K) aluminosilicate glass/45 wt% alumina	7.4	0.0026		245	[Bab88]
55 wt% borosilicate glass/45 wt% α-cordierite	5.0	0.0050		147	[Sha87]
60 wt% CAS (crystalline)/ 40 wt% borosilicate glass	7.7	0.0003		196	[Nis85]
45 wt% lead borosilicate glass/55 wt% alumina	7.5	<0.0038			[Sha83]
Boron-doped (2% B) sol-gel silica	4.2	0.0005		66	[San89]
Fused silica	3.8		7		[Kur95]

* Thermal properties of these glass compositions (or relative densities) were not determined on these samples. However, in most cases, the materials were reported to be "dense."
Composition or concentration of ceramic phase not reported.
† Reported at 1MHz.

Fra92] Although SCFS has excellent radar transmission qualities (e.g., stable and low dielectric constant of ~4, low CTE of ~0.5ppm/°C, etc.), it has relatively poor mechanical properties (room temperature design tensile strength is ~28 MPa [Kou92]). Due to the lower strengths, greater wall thicknesses are required and this may compromise radar transmission. A qualitative comparison [Kou92, Fra92] of four candidate materials with respect to six performance criteria desirable for good radome design is given in Table 2.2. A rating system from poor to excellent is used in the table. All ratings above "poor" signify that the material will perform adequately under ideal conditions (no erosion environment or nuclear blast). A rating of "fair" suggests that the material may not be adequate under adverse flight conditions. A "good" rating indicates that the material will perform satisfactorily under adverse flight conditions, except on rare occasions. Ratings above "good" mean that the material will perform well even under adverse conditions. Based on the data presented in Table 2.2, recent investigations [Kou92] are being directed toward producing glass/ceramic formulations such as SiO_2-matrix composites with inclusions (alumina, silicon nitride, boron nitride, etc.) and SiO_2 containing crystalline ceramics (e.g., celsian and cordierite).

Glass/ceramic compositions can be generally classified into two types: (i) "glass-ceramic" materials in which the glass powder compacts are sintered to high relative density (low porosity) and can be subsequently crystallized to nearly glass-free materials and (ii) "glass + ceramic" composites in which powder compacts prepared with mixtures of glass and crystalline ceramic particles are sintered to high relative density. The crystalline components usually have higher dielectric constant than the glassy phases, but they also improve mechanical and thermal properties of the material. A difficulty in processing

"glass + ceramic" composites is that powder compact densification rates usually decrease as the volume fraction of crystalline ceramic particles increases [Ran93 Rah87a, K. Wang and M D Sacks, personal communication, 1996] Composite densification may be severely impeded when the concentration of the "non-sinterable" inclusions is sufficient to form a connected particulate network (i.e., percolation path) Thus, it may be necessary to limit the amount of crystalline phase in the powder mixture. This approach has been effective in producing hermetic composites with high relative density, but it imposes compositional constraints which limits the range of physical properties that can be achieved Therefore, there is a need for alternate processing methods.

Table 2.2 Advantages and Disadvantages of Four Candidate Radome Materials.

Performance Criterion	Slip-Cast Fused Silica	Celsian	Pyroceram 9606	Reaction Bonded Si_3N_4
Maximum Temperature	Good	Fair	Fair	Good
Thermal Shock Resistance	Excellent	Fair	Good	Fair
Maneuvering Capability	Fair	Good	Good	Good
Radar Transmission	Excellent	Very Good	Good	Good
Rain and Dust Erosion	Fair	Fair	Good	Very Good
Ease of Manufacture	Very Good	N/A	Very Good	Fair

2.2.2. Processing Considerations

Two different approaches are used to form "glass + ceramic" composites In one case, a conventional processing method is utilized in which green compacts were formed from mixtures of amorphous matrix (A) and crystalline inclusion (B) powders A schematic illustration of a green compact formed from a mixture of powders is shown in Figure 2.2(a)

Another approach involves processing of microcomposite particles which consist of inner cores of B particles and outer coatings of the A phase. As illustrated in Figure 2.2(b), the formation of a contiguous network of the "non-sinterable" B inclusions can be avoided by controlling the spatial distribution of the phases using the microcomposite particles. By maintaining the more sinterable amorphous phase (A) as an outer coating, compacts can be densified by the viscous flow mechanism. This approach would not only facilitate sintering at relatively low temperatures, but would also allow the development of microstructures in which a high concentration (i.e. above the percolation threshold [Zal83]) of the B phase could be dispersed in the A matrix as isolated inclusions.

Sacks and co-workers [Sac91a, Sac91b, Sac92, Sac93] have demonstrated the advantage of this approach using microcomposite powders in which amorphous silicate coatings (SiO_2, B_2O_3-SiO_2) were deposited on a variety of crystalline core particles (Al_2O_3, Si_3N_4, SiC, ZrO_2). Glass-matrix composites with high volume fractions of crystalline inclusions were prepared at relatively low sintering temperatures. In addition, glass-free crystalline ceramics and ceramic-ceramic composites (e.g., with mullite and SiAlON matrices) were fabricated by reacting the core material with the amorphous matrix phase at elevated temperatures [Sac92, Sac93]. Other researchers have prepared crystalline-matrix composites without chemical reactions by using composite powders in which both the cores and the coatings were crystalline [Hu92, Hu94]. In such composites, densification is improved compared to using conventional powder mixtures if the coating phase is more sinterable than the core materials [Hu92, Hu94].

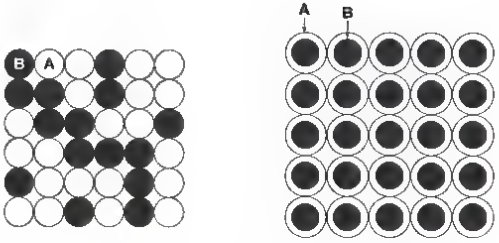

Figure 2 2 Schematic illustration of two types of powder compacts (a) compact is formed by mixing amorphous A and crystalline (B) particles, and (b) compact is formed using microcomposite particles containing inner cores of B particles and outer coatings of the A phase

2.3. Incorporation of Controlled Porosity in Glass/Ceramic Matrices

Isolated, closed pores can be incorporated in a composite matrix by using green compacts prepared from a mixture of composite powder and relatively large polymer particles (schematically illustrated in Figure 2.3). Pyrolysis of the polymer particles at relatively low temperatures (i.e., significantly below sintering temperatures) would result in a powder compact with a bimodal distribution of pores: (i) larger voids created by pyrolysis of the polymer particles and (ii) smaller pores associated with the microcomposite particle packing arrangement. This compact could be heated at higher temperatures to densify the matrix (i.e., eliminate the fine interparticle pores). As densification of the powder matrix occurred, the larger voids would begin to close (and become less accessible to infiltration from the surface). Furthermore, if the concentration of the polymer particles was below the percolation threshold and they were homogeneously dispersed in the compact, they would be "non-touching" before pyrolysis. Consequently the PS-derived pores would remain isolated from each other even after the matrix had densified.

PS particles have also been used by other researchers [Kat92, Ran93, Sac93] to introduce controlled isolated porosity in glass/ceramic matrices. Kata et al. [Kat92] demonstrated that very high loadings of PS (>25 vol% in solids) in the green compact can lead to residual open porosity. They determined the limiting value of closed porosity (without the presence of any open pores) that can be achieved using this approach to be ~13 vol%. Some workers [Kel87, Ver85] have used an alternate approach to produce porous materials which involved using mixtures of hollow SiO_2 microspheres and glass-ceramic powders. This approach allowed the development of microstructures in which a high concentration (i.e., above the percolation threshold) of the pore phase could be incorporated

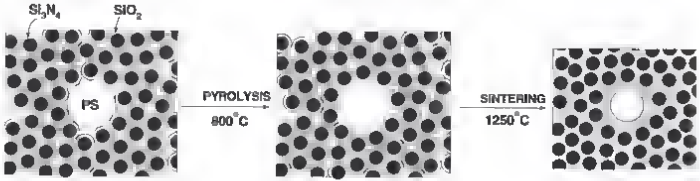

Figure 2.3 Schematic illustration of incorporation of a controlled pore in a SiO_2/Si_3N_4 powder matrix. Green compact prepared from a mixture of SiO_2/Si_3N_4 microcomposite particles and PS particles can be heated to relatively low temperatures to pyrolyze the PS and subsequently sintered at higher temperatures to eliminate porosity associated with the packing of the microcomposite particles

as isolated, closed pores (For example, Kellerman [Kel87] has fabricated bulk glass-ceramics with as high as ~50 vol% isolated, closed porosity.)

2.4. Synthesis and Characterization of Composite Powders

The composite particles pertinent to this study consist of inner cores of a crystalline (inclusion) phase and outer coatings an amorphous (matrix) phase. The potential advantages of using this approach are: (1) increased threshold concentration of percolation of the inclusion particles and (2) the absence of packing heterogeneities in the matrix phase immediately surrounding the inclusion particles.

Controlled hydrolysis of metallorganic precursors has been utilized to synthesize composite particles with amorphous coatings. Composite particles with inner cores Al_2O_3 and outer coatings of SiO_2 have been synthesized using tetraethyl orthosilicate (TEOS) as the precursor. Sheu [She86] and Agrawal et al. [Agr90] have prepared SiO_2 gel-coated α-Al_2O_3 particles by adding a mixture of ethanol, TEOS, water, and HCl, to a suspension of submicrometer size Al_2O_3 particles. It was demonstrated in both studies that the formation of the SiO_2 coating changes the zeta potential of the particles with time from the value corresponding to an alumina surface to the value for a SiO_2 surface. Furthermore, it was argued by Agrawal et al. [Agr90] that since the TEOS solution did not show gelation without the presence of the Al_2O_3 particles and since an incubation time was associated with the precipitation process, the coating process followed a nucleation-and-growth type of reaction kinetics. Sando et al. [San90] synthesized SiO_2-coated α-Al_2O_3 particles using a slightly different technique. The Al_2O_3 powder was first placed in a high humidity vessel till a uniform layer of adsorbed water was formed on the particle surface. This powder was

dispersed in a hydrophobic solution which contained a mixture of n-hexane, TEOS, and a surfactant (sorbitan monostearate). Hydrolysis of the TEOS was catalyzed by additions of stearic acid or stearylamine. TEM observations were used to demonstrate the presence of the SiO_2 coatings on the Al_2O_3 particles. Zeta potential-pH characteristics of the coated powder varied from "Al_2O_3-like" to "SiO_2-like" as the SiO_2 content increased from 0.9 wt% to 8.5 wt%.

Sacks et al. prepared SiO_2-coated "microcomposite" particles (with submicrometer size) comprising crystalline cores such as α Al_2O_3 [Sac91a, Sac92, Sac91b, K. Wang and M.D. Sacks, personal communication, 1996], SiC [Sac91b], ZrO_2 [Sac91b], and Si_3N_4 [Sac91b, Sac92, Sac93]. The synthesis procedure involved two steps: (1) mixing a TEOS/ethanol solution and a suspension of the core particles in ethanol; and (2) precipitating a SiO_2 coating by the addition of ammoniated water (~30 wt% NH_3). Bright field TEM and high-resolution TEM (HRTEM) images were used to demonstrate the presence of the amorphous SiO_2 coating on the core particles [Sac91b, Sac93, K. Wang and M.D. Sacks, personal communication, 1996]. The surface properties of SiO_2-coated Al_2O_3 composite particles were analyzed using various techniques [K. Wang and M.D. Sacks, personal communication, 1996]. XPS analysis of the composite powders showed that Al was not present on the composite powder surface. The electrophoretic mobility vs. pH behavior for the composite particles were similar to that for SiO_2 particles. These results indicated that the core particle surface was completely covered by SiO_2. Preliminary analysis of results from Wang's study [K. Wang and M.D. Sacks, personal communication, 1996] indicated that the surface area of the composite particles was not reproducible. For

example, the different batches of composite powders with an overall composition of ~74 wt% Al_2O_3/ ~26 wt% SiO_2 and surface areas in the range of ~22-30 m^2/g. Although the use of relatively fresh source of TEOS and the coarse filtration of composite particle suspension after coating were found to reduce the surface area, the exact reasons for the lack of reproducibility were not established [K. Wang and M.D. Sacks, personal communication, 1996].

Azuma et al. [Azu91] coated ferric oxide particles with SiO_2 by hydrolysis of TEOS using ammoniated water. It was shown that when the TEOS concentration became too high, some SiO_2 precipitated as independent particles in the solution. A linear relationship was found between the limiting concentration of TEOS (C_T) and the concentration of the dispersed ferric oxide (C_F). For example, for NH_3 and H_2O concentrations of 2.0 mol/l and 7.9 mol/l, respectively, C_T increased linearly from ~0.02 mol/l to ~0.05 mol/l as C_F increased from ~0.0025 mol/l to ~1.0 mol/l. XRD analysis showed that the the intensity of the ferric oxide peaks decreased steadily as the coating thickness of SiO_2 increased. The electrophoretic mobility-pH curve for the coated particles were found to be in excellent agreement with that for SiO_2 particles (Figure 2.4). Based on these results, it was speculated that the core particles were completely covered with SiO_2. TEM observations were also used to demonstrate the presence of the SiO_2 coating on the ferric oxide particles.

Hwang et al. [Hwn93] prepared SiO_2 and TiO_2-coated α-Al_2O_3 powders by hydrolysis of TEOS and titanium isopropoxide respectively, using aqueous ammonia. Shyu and Chen [Shy95] prepared SiO_2-coated α-Al_2O_3 and zircon ($ZrSiO_4$) powders by hydrolysis of TEOS using pH~11 water. Chen and Yen [Che94] used the method of Sacks

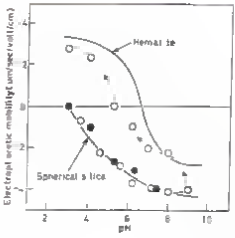

Figure 2.4 Electrophoretic mobility curves for various particles (•) TEOS/Fe_2O_3 molar ratio = 1 0, and (o) TEOS/Fe_2O_3 molar ratio = 0 1 [Azu92]

et al. [Sac91a] to prepare amorphous SiO_2-coated SiC whiskers and α-Al_2O_3. Giesche and Matijevic [Gie94] prepared SiO_2-coated yttrium basic carbonate by the controlled hydrolysis of TEOS using an aqueous ammonia solution. The aforementioned studies used TEM images of selected composite particles to illustrate the presence of the coating on the core particle surface. The studies conducted by Chen and Yen [Che94] and Giesche and Matijevic [Gie94] also demonstrated that the zeta potential-pH behavior for the coated particles were similar to that for SiO_2 particles.

Sun et al. [Sun96] coated porous α-Fe_2O_3 powders (needle-like morphology with ~20nm radius, ~1μm length, and a specific surface area of ~130 m^2/g) with SiO_2 by hydrolysis of TEOS using distilled water. The powders were sintered in the temperature range of 800-900°C and the surface area and pore sizes were determined by nitrogen sorption. Figures 2.5 (a) and 2.5(b) show the nitrogen gas adsorption isotherms for the coated and uncoated samples. The isotherms exhibit apparent characteristics of Type II and Type IV, according to the Brunauer-Emmett-Teller (BET) classification [Gre82]. The sorption volume increased by ~20 times after the coating process, indicating that the sample became more porous after the deposition of the SiO_2 layer. The hysteresis was attributed, in part, to the presence of an "ink-bottle" type pore structure in the composite particles. The presence of a broad peak centered at $2\theta \approx 22°$ in the XRD pattern for the coated samples demonstrated the presence of the amorphous SiO_2 in the composite particles. High-resolution TEM (HRTEM) analysis of composite powders also confirmed the presence of the amorphous SiO_2 coating on the Fe_2O_3 particles. SEM observations on 800°C heated

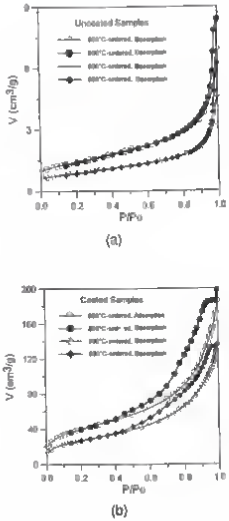

Figure 2.5 N_2 sorption isotherms for (a) the uncoated and (b) silica-coated α-Fe_2O_3 particles [Sun96]

powder samples showed that the coating consisted of a packing of numerous SiO_2 particles (<100 nm) on the Fe_2O_3 grains

Composite particles with inner cores of amorphous SiO_2 and outer coatings of yttrium-doped ZrO_2 [Hir91] or TiO_2 [Par93] have also been prepared by controlled hydrolysis of metallorganic precursors. The former particles were prepared by suspending the SiO_2 particles in an alcohol solution of zirconium and yttrium isopropoxide, and subsequently precipitating the coating by the addition of water to the mixture. The latter particles were synthesized by hydrolyzing an ethanolic solution of titanium isopropoxide in the presence of SiO_2 particles, by the addition of water. Partch et al. [Par93] demonstrated that the dependence of electrophoretic mobility on pH for pure TiO_2 particles and for SiO_2 particles coated with TiO_2 were essentially the same

Composite powders with crystalline cores and crystalline coatings, such as Al_2O_3-coated SiC [Mit95, Hu93], hematite-coated TiO_2 [Ghe86], ZnO-coated ZrO_2 [Hu92], and $CaAl_2O_4$-coated Al_2O_3 [Des95] have been prepared by forced hydrolysis of metal salt solutions in the presence of core particles. Powders with multiple coatings have also been synthesized. Jang [Jan95] prepared composite powders consisting of cores of α-cordierite, inner coatings of aluminum hydroxide, and outer coatings of ZrO_2, by sequential hydrolysis of metal salt solutions (aluminum nitrate and zirconium oxychloride for the two coatings, respectively). However, the composite particles prepared in the aforementioned studies were characterized only by SEM and/or TEM observations

It is noted that although the synthesis methods of composite powders have been extensively described in literature, very few studies [Gie94, Azu91, K. Wang and M.D

Sacks, personal communication, 1996] have involved particle characterization in any significant detail. However, it is important to realize that rigorous particle characterization is essential to completely understand the sintering and microstructure development of bulk compacts derived from these powders.

2.5. Sintering of Particulate Composites

2.5.1. Introduction

Ceramic particulate composites may offer considerable improvement in various properties compared to single phase ceramics. In the formation of these composites, however, the presence of rigid (non sintering, incompressible) inclusions can cause substantially reduced densification rates in the composite matrix. The potential for improved properties is hence offset by the increased difficulty in forming the composites with the required high density and controlled microstructure by conventional, pressureless sintering. Considerable efforts have therefore been made over the past 5-10 years to understand the factors that retard the conventional sintering of ceramic composites so that the sintering process can be better applied to the formation of these materials.

It is now widely recognized that rigid inclusions induce differential sintering rates which in turn produce transient stresses during sintering. These stresses not only retard the rate of densification but can generate flaws that reduce the strength of the final body [Hsel86]. Almost all the composite sintering studies therefore involve the determination of these stresses using analytical and experimental approaches. Although the effect of rigid inclusions on the densification of polycrystalline ceramic-matrix composites has been a

subject of much debate in recent years, it has been possible to model the sintering stresses in glass-matrix composites through experimental and theoretical studies.

2.5.1. Analytical Models

A number of explanations, based on theoretical models or microstructural observations, have been put forward to explain the significant reduction in the sintering rates of glass-matrix composites. The early analyses [Hse86, Dej86] involved using a viscoelastic approach to analyze problems of constrained sintering. However, it was established later [Sch87, Rah87a] that some of the assumptions made were unrealistic and that the predicted stresses were too small to account for the significant reduction in densification rates. Scherer [Sch87] has modelled the effect of rigid inclusions on sintering and applied the theory to the case of viscous sintering. The self-consistent (SC) approach used by Scherer is the most widely accepted analytical model for viscous sintering of glass-matrix composites containing rigid inclusions.

Constitutive behavior

To predict stresses, it is essential to know the constitutive equation (i.e., equation relating the applied stresses and resulting strains) for the matrix. For an isotropic, linearly elastic material, the constitutive relation is given by the expression [Tim70]

$$\varepsilon_x = \varepsilon_f + \frac{1}{E}[\sigma_x - \nu(\sigma_y + \sigma_z)] \qquad (2.1)$$

where ε_x is the strain in the x-direction, ε_f is the free strain, E is the Young's modulus, ν is Poisson's ratio, and σ_i ($i = x,y,z$) are the principal stresses. For an isotropic, linearly viscous material, the viscous analogy [Sch91] can be applied where, in eq. (2.1) strain rates replace

strains, ν becomes ½ (because the liquid is incompressible) and E is replaced by 3η, where η is the shear viscosity of the liquid, so

$$\dot{\varepsilon}_x = \dot{\varepsilon}_f + \frac{1}{3\eta}\left[\dot{\sigma}_x - \frac{1}{2}(\sigma_y + \sigma_z)\right] \qquad (2.2)$$

where the superscript dot indicates the derivative with respect to time. This is valid only for a dense material since porous bodies are compressible in nature. Therefore for a porous viscous material such as a sintering matrix, eq (2.2) must be modified to account for the compressibility of the pores [Sch79]

$$\dot{\varepsilon}_x = \dot{\varepsilon}_f + \frac{1}{E_m}\left[\dot{\sigma}_x - \nu_m(\sigma_y + \sigma_z)\right] \qquad (2.3)$$

where E_m is the "apparent Young's modulus" (uniaxial viscosity) of the porous matrix, and ν_m is "apparent Poisson's ratio". As the porosity goes to zero (i.e., as the matrix relative density goes to 1), $E_m \to 3\eta$ and $\nu_m \to ½$, so eq (2.3) reduces to eq (2.2). In place of ε_f, some workers [Raj82] have made use of the "sintering pressure" or "sintering stress" that drives densification. If the applied stress is hydrostatic, $\sigma_x = \sigma_y = \sigma_z = P$, then eq (2.3) becomes

$$\dot{\varepsilon}_A - \dot{\varepsilon}_f + \frac{P}{E_m}(1 - 2\nu_m) = \dot{\varepsilon}_f + \frac{P}{3K_m} \qquad (2.4)$$

where K_m is the "apparent bulk modulus" defined by

$$K_m = \frac{E_m}{[3(1 - 2\nu_m)]} \qquad (2.5)$$

by analogy of the elastic bulk modulus. Since K_m is not a true modulus and it represents the viscous response of a porous body to a hydrostatic stress, it can be termed as the bulk viscosity of the porous matrix. As expected, K_m becomes infinite (i.e., the matrix is

incompressible) when there is no more porosity ($\nu_m = ½$). If P is equal to and opposite to the sintering stress, Σ, then densification is arrested ($\varepsilon_a = 0$), according to eq. (2.4) this happens when $P = -3K_m \varepsilon_f$, so

$$\Sigma = 3K_m \varepsilon_f \qquad (2.6)$$

This pressure has a complex dependence on local forces which do not produce hydrostatic compression at the interparticle neck. The more fundamental quantity, which is predicted by theory and determined experimentally, is the free strain rate.

The viscous response can therefore be described by two independent functions. The constitutive equation can be written in terms of E_m and ν_m as in eq. (2.3), or equivalent relations can be obtained in terms of K_m and the "apparent shear modulus", G_m.

$$G_m = \frac{E_m}{[2(1 + \nu_m)]} \qquad (2.7)$$

G_m represents the viscous response of the porous material to a shear stress, so it may be termed as the shear viscosity of the porous matrix. As porosity approaches zero, $E_m \to 3\eta$ and $G_m \to \eta$ (i.e., they are finite), while the bulk viscosity (K_m) diverges.

In this analysis, the properties ε_f, E_m, and ν_m are assumed to be isotropic. The assumptions of linearity and isotropy may cease to be valid towards the final stages of sintering when the inclusions will inhibit shrinkage in the circumferential, but not in the radial, direction. However, these effects are more pronounced in polycrystalline materials and the present analysis is consistent with the experimental results for composites with non-crystalline matrices [Schi87].

Some workers [Hse86 Raj84] have used a viscoelastic approach to analyze problems of constrained sintering. Unlike in the case of viscous analysis, viscoelastic stresses rise to their maximum values during a transient period. However, the transient is orders of magnitude shorter than the total sintering time, and the maximum stresses are identical to those predicted by the viscous analysis. Since the viscous analysis predicts the maximum stresses that will occur, there is no practical advantage of using the more complicated viscoelastic approach. Moreover, it has been established [Bor88] that sintering materials are not linearly viscoelastic, so the usual methods of viscoelastic analysis are not applicable.

Self-consistent calculation

The self-consistent (SC) model focuses attention on a microscopic region within the matrix (Figure 2.6). That region can be treated as an island of sintering material in a continuum (the composite) that is contracting at a slower rate. In other words, that region constitutes the "core" of an infinite composite sphere whose cladding is the composite consisting of the matrix plus inclusions. The mismatch in the shrinkage rates of the island and the continuum imposes tensile stresses on the core of the matrix material. The hydrostatic tensile stress in the island of matrix can be calculated using Selsing's solution [Sel61] for the stress in an isolated inclusion. The stress in the matrix (which is equal in the radial and circumferential directions) is

$$\sigma_m = (\varepsilon_c - \varepsilon_{fm}) \left[\frac{1}{3K_m} + \frac{1}{4G_c} \right]^{-1} \qquad (2.8)$$

where ε_c is the linear contraction rate of the composite, ε_{fm} is the free strain rate of the matrix (i.e., the linear contraction rate of the unconstrained sintering material), K_m is the

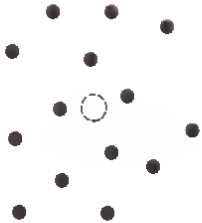

Figure 2.6 In the self-consistent calculation the region of matrix within the dashed circle is regarded as an isolated island surrounded by an infinite continuum (the composite) with a slower densification rate. Similarly, any of the inclusions (solid circles) can be treated as being isolated in the continuum [Sch87]

bulk viscosity of the matrix, and G_c is the shear viscosity of the composite. Eq. (2.8) indicates that the stress in the (island) of matrix is proportional to the difference between its free strain rate and the strain rate of the surrounding composite. The linear shrinkage rate of the composite, ε_c, is related to the densification rate of the matrix by

$$\varepsilon_c = -(1 - f)\frac{\rho_m}{3\rho_m} = (1 - f)\left[\varepsilon_{fm} + \frac{\sigma_m}{3K_m}\right] \tag{2.9}$$

where f is the instantaneous volume fraction of the inclusions, which increases as the volume of the void phase decreases (i.e., as the compact densifies). Substituting eq. (2.9) in eq. (2.8) and solving for σ_m we obtain

$$\sigma_m = -f\,K_{S\text{-}C}\,\varepsilon_{fm} \tag{2.10}$$

where

$$K_{S\text{-}C} = \left[\frac{1}{4G_c} + \frac{f}{3K_m}\right] \tag{2.11}$$

The S-C results should apply until f becomes so great that the inclusions form a contiguous network (i.e., corresponding to the percolation threshold) that prevents contraction of the composite. In such a case, $G_c \to \infty$, $\varepsilon_c \to 0$, and $\sigma_m \to \Sigma$.

Finite-element approach

Jagota [Jag94] modelled the sintering of coated particle compacts using a finite-element method (FEM). He considered two spherical particles consisting of rigid cores and uniform outer coatings of a glassy phase undergoing sintering. The rigid core was not modelled explicitly but velocities of all nodal points on the surface were constrained to be identical. It was found that the results from the numerical method was consistent with the kinetics of the flattening of a nearly plane solid due to capillarity.

The FEM simulations showed that during most of the sintering process, deformation is localized to the neck between the particles. Therefore, the sintering rate is almost independent of composition for compacts with relatively high amounts of the coating phase. In the later stages of sintering, the densification is controlled by lubrication flow in the narrow gap between the rigid cores. For samples with very thin coatings (i.e., low volume fractions of the coating phase), there exists a final stage of sintering where particle rearrangements result in internal changes in the microstructure without any overall shrinkage. Figure 2.7 shows the predicted change of relative density (from the numerical simulations) of a packing of coated particles as a function of time. Also shown are predictions for particles without a core and the Mackenzie-Shuttleworth (MS) model [Kin76] (based on spherical pores). These results were obtained by assuming that the initial packing fraction was 0.60 and that the macroscopic linear shrinkage of the packing equals that for every pair of particles. It was shown that for a core particle radius of R, a minimum coating thickness, t, of 0.186R (i.e., a minimum volume fraction of 0.4 for the coating in the coated particle) is required for an initial packing fraction of 0.6, to obtain full density. Figure 2.7 shows that with only a slightly thicker coating (t=0.20R) full density is achieved at a rate comparable to a packing that consists of particles without a rigid core.

2.5.3. Experimental Data Analysis

Calculation of parameters

This section describes the methodology used to convert experimentally measured parameters to those used in the SC model. While free sintering (under zero external load)

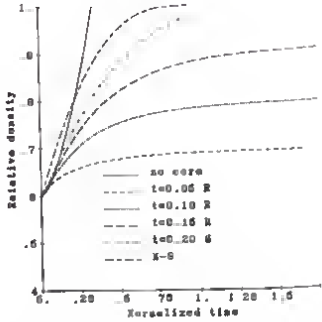

Figure 2.7 Relative density of a packing of coated particles as a function of normalized time, $\tau = (3/4\pi)^{1/3} \gamma t/[\eta(R+t)]$, for different coating thicknesses, and for the Mackenzie Shuttleworth model [Jag94] (τ is the time, γ is the surface tension of the coating phase η is the viscosity of the coating phase R is the radius of the core particle, and t is the coating thickness)

experiments may be used to determine densification rates, creep experiments (sintering under a controlled uniaxial stress) are done to determine viscosities

It would be instructive to normalize the strain rates with respect to that predicted by a rule-of-mixtures approach. It may be shown that [Sch87]

$$\frac{\dot{\varepsilon}_c}{\dot{\varepsilon}_c^{rm}} = [1 + f\frac{4G_c}{3K_m}]^{-1} \tag{2.12}$$

where $\dot{\varepsilon}_c^{rm}$ is the strain rate predicted by the rule-of-mixtures and is given by

$$\dot{\varepsilon}_c^{rm} = (1-f)\,\dot{\varepsilon}_m \tag{2.13}$$

under the assumption that the strain rate is zero for the densification of the inclusions The linear strain rate for a sintering body undergoing isotropic shrinkage is related to the densification rate by the expression

$$\frac{\dot{\rho}}{\rho} = -3\,\dot{\varepsilon} \tag{2.14}$$

where ρ and $\dot{\rho}$ are the density and the densification rate, respectively

The shear viscosity of the composite, G_c, may be estimated as the lower bound of the Hashin-Shtrikman equation [Has63], and is given by

$$\frac{4G_c}{3K_m} = \frac{4G_m}{3K_m}\left\{1 + \frac{15}{2}\frac{f}{(1-f)}\frac{(1-\nu_m)}{(4-5\nu_m)}\right\} \tag{2.15}$$

The ratio $4G_m/(3K_m)$ is related to Poisson's ratio of the matrix, ν_m, by

$$\frac{4G_m}{3K_m} = \frac{2(1-2\nu_m)}{(1+\nu_m)} \tag{2.16}$$

Poisson's ratio is related to the matrix density by [Sch79]

$$v_m \sim \frac{1}{2}\left[\frac{\rho_m}{(3 - 2\rho_m)}\right]^{1/2} \qquad (2.17)$$

Eqs (2.14) to (2.17) can be used to evaluate the theoretical values of $\frac{\varepsilon_c}{\varepsilon_c^{free}}$

Results from experimental investigations

The effect of rigid inclusions on the sintering of ceramic-matrix composites was studied by DeJonghe et al. [Dej86]. Figure 2.8 [Dej86] shows plots of bulk density vs. time for powder compacts containing particle mixtures of ZnO (matrix) and SiC (inclusions). It is evident there was a severe effect on the strain rate of the ZnO matrix even at low volume fractions of inclusions (<5 vol% SiC). Fan and Rahaman [Fan92] carried out similar experiments using mixed particle composites consisting of a fine-grained (0.3 μm average size) ZnO matrix and coarse (~14 μm size), rigid, inert particulate inclusions of ZrO_2. Figure 2.9 [Fan92] shows plots of composite relative density as a function of temperature for die-pressed composites containing 0-22.5 vol% ZrO_2 inclusions during constant-heating-rate sintering at 4°C/min to 1200°C. The unreinforced ZnO starts started densifying at ~650°C and reached almost full density at ~1000°C. As the volume fraction of the inclusions increased, the composite density (and hence the densification rate) at any given temperature decreased.

Dutton and Rahaman [Dut92] compared the sintering behavior for composites with polycrystalline and amorphous matrices. In contrast to a polycrystalline ZnO-matrix composite, a soda-lime glass-matrix composite, with SiC inclusions, followed closely the predictions of a rule-of-mixtures until ~15 vol% inclusions (Figure 2.10 [Dut92]). It was suggested [Rah90] that at >15 vol% inclusions, the percolation threshold is reached and a

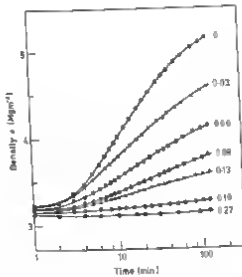

Figure 2.8 Density as a function of time for ZnO containing different volume fractions of SiC [Dej86]

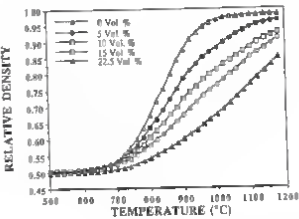

Figure 2.9 Relative density of the composite vs temperature for the die pressed composites containing 0-22.5 vol% ZrO_2 inclusions (size 14μm) during constant-heating rate sintering at 4°C/min to 1200°C [Fan92]

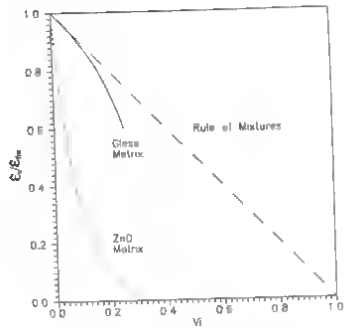

Figure 2.10 Linear strain rates of a polycrystalline ZnO matrix composite and a glass-matrix composite, relative to the strain rate of the free matrix, versus inclusions volume fraction. The dashed line represents the predictions of the rule-of-mixtures [Dut92]

contiguous network of inclusions is formed. Although the effect of rigid inclusions on the densification of polycrystalline-matrix composites has not been clearly understood yet, it has been possible to experimentally determine the various factors controlling densification of glass-matrix composites and verify the different analytical models describing their sintering kinetics

Rahaman and De Jonghe [Rah87] compared experimental data for the sintering rate of soda-lime glass-matrix (~4 μm average size) composite containing SiC inclusions (~35 μm average size) with the predictions of the self-consistent (SC) model In the analysis of Rahaman and De Jonghe, G_c was taken as the lower bound of the Hashin-Shtrikman equation calculated using eq (2.15) This equation was used in the absence of the measured values for G_c. Figure 2.11 [Rah87] shows plots of the experimental and predicted values of the normalized strain rate of the composite vs. the relative density of the matrix for composites with ~9 and ~17 vol% inclusions It is evident that the densification rates were in good agreement with Scherer's theory for an inclusion volume fraction of 0 09 For the sample with ~17 vol% inclusions, although there was good agreement with theory at relatively low matrix densities, significant deviations were evident above $\rho_m \sim 0\ 7$ At this value of ρ_m the inclusion volume fraction in the bulk was determined to be ~0 12 [Rah87] It was speculated that the significant deviations from theory at high volume fractions (i e., ≥ 0 12) of inclusions were a result of interactions between inclusions [Rah87]. Boccaccini [Boc94] studied the effect of Al_2O_3 platelet inclusions (major axes in the range of 5-25 μm) on the sintering behavior of aluminosilicate glass powder (~8μm mean particle size) matrices using a heating microscope at 850°C The data analysis was similar to those

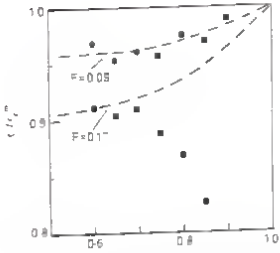

Figure 2.11 Comparison of the experimental results for the linear strain rate of the composite normalized by the strain rate from the rule-of-mixtures, vs relative density of the matrix ρ_m with the predictions of Scherer s model for the indicated volume fractions of inclusions, F [Rah87] (■ ■) experimental values· (----) predicted values

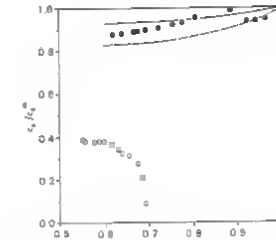

Figure 2.12 Linear strain rate of the composite referred to the strain rate from the rule-of mixtures, vs relative density of the matrix for (●—)0.15 and (▫,---)0.30 platelet volume fractions The symbols and lines represeot experimental and predicted values, respectively [Boc94]

described earlier for the study conducted by Rahaman and De Jonghe [Rah87]. Figure 2.12 [Boc94] shows plots of the experimental and predicted values of the normalized strain rate of the composite vs. the relative density of the matrix for composites with ~15 and ~30 vol% platelets. The experimental values were in good agreement with Scherer's model predictions for inclusion loadings of ≤15 vol%. The differences between the values for higher inclusion loadings was attributed to the interaction between the platelets since the inclusion volume fractions were above the percolation threshold [Boc94].

Scherer and Jagota [Sch91] have used numerical methods to explain the difference between the measured and calculated sintering rates as encountered by Rahaman and De Jonghe [Rah87]. Using this approach, the SC model was extended [Sch91] to take account of the properties of the inclusion-matrix contacts. The SC theory depends on the knowledge of the shear viscosity of the composite, and this was obtained directly from the simulation. It was found that Hashin-Shtrikman lower bound failed to account for the increase in shear viscosity near the percolation threshold, which was predicted by the numerical model. It was concluded that the SC model provides a good prediction of the sintering kinetics, if the shear viscosity of the composite is independently measured. Beyond the percolation threshold, however, the theoretical value of the sintering rate may be limited to the insight that the sintering rate is inversely related to the shear viscosity of the composite. Numerical simulations of the type discussed by Scherer [Sch91] are expected to be invaluable tools in the search of models predicting the rheology of percolating systems. Shear viscosities of glass powder compacts have been experimentally determined using loading dilatometry [Rah90, Dej84, Duc89, Boc92]. Dutton and

Raharan [Dut92] used a model composite system consisting a mixture of spherical soda-lime glass particles and spherical nickel inclusion particles to measure G_c and check the validity af the SC model It was observed that while the SC models and the Hashin-Shtrikman lower bound can describe the observed data for G_c for the composites with the coarser inclusions (150 - 300 μm) , they failed for the finer (6 - 10 μm) inclusions (Figure 2.13) The increase in viscosity of the composites with the finer inclusions showed trends similar to the numerical analysis of Scherer and Jagata [Sch91], but the magnitude of the observed increase (~ 50 times) was lower than that predicted by the modal (10^4), which assumed bonded contacts [Dut92] If the contacts were allowed to slip then the percolation threshold would not coincide with the rigidity threshold (where sintering essentially stops) and the predicted increase in G_c would be much lawer

Recently, Sacks and co-workers [Sac91a, Sac91b, Sac92, Sac93] developed a novel process to fabricate glass-matrix composites by sintering compacts comprising microcomposite particles. These particles consisted of outer coatings of a glassy phase (SiO_2 or B_2O_3-SiO_2), and inner cores of crystalline materials (i.e., Al_2O_3, Si_3N_4, ZrO_2, and/or SiC) Powder compacts prepared with the microcomposite particles showed enhanced densification. The increased densificatioo rate for the former sample was attributed to the fact that the formation of a contiguous network of rigid inclusions was avoided by encapsulating the crystalline particles with the siliceous phase [Sac91a, Sac93] Recent investigations by Raharan and co-workers [Fan92, Hu92] identified inclusion particle interactions and the packing of the matrix phase, especially in the regions immediately surrounding the inclusions as the main factors responsible for the reduced

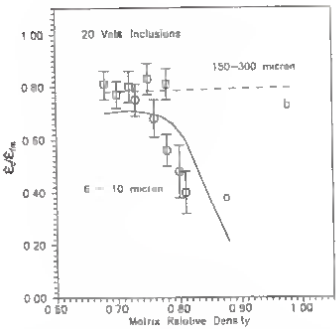

Figure 2.13 Data for the densification rate of the composite containing 20 vol% inclusions, relative to that of the free matrix, as a function of the matrix density, compared with the predictions of Scherer's SC model using (a) the measured values for G_e, and (b) the Hashin-Shtrikman lower bound [Dut92]

sinterability in polycrystalline matrix composites Hu and Rahaman [Hu92] synthesized coated ZrO_2 inclusion particles with a cladding of fine-grained, crystalline ZnO powder using a chemical precipitation technique. As expected, the use of coated particles led to a remarkable improvement in the sinterability of bulk composites (Figure 2.14 [Hu92]) Composites containing up to ~40 vol% inclusions were sintered to nearly full density This was a remarkable improvement over composites formed by conventional mixing where modest inclusion contents of ~10 vol% were found to lead to a severe reduction in the sinterability of the composite [Fan92]

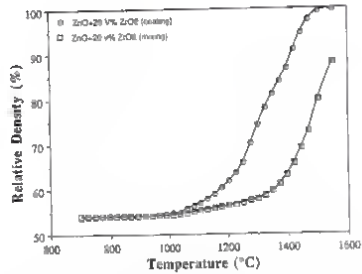

Figure 2.14 Matrix relative density vs temperature for the composite formed from the coated inclusion particles (20 vol% inclusions) compared with the data for a composite formed from conventionally mixed powders [Hu92]

CHAPTER 3
EXPERIMENTAL PROCEDURE

3.1 Synthesis of Particles

3.1.1. Core Particles and Microcomposite Particles

Microcomposite particles were prepared by precipitating a coating of amorphous SiO_2 on to Si_3N_4 core particles. Submicrometer core particles were desired for the coating process. High-purity α-Si_3N_4[1] (<1.5 wt% O) powder was fractionated using centrifugal and gravity sedimentation to remove the coarsest agglomerates from the as-received material. The procedure was based on the Stokes law for sedimentation of particles in a dilute aqueous suspension (~0.75 vol%). Powders (Lot 1) for a preliminary investigation (Section 4.1) were prepared by combining powders obtained from both gravity and centrifugal sedimentation experiments while the powders (Lot 2) used in more detailed studies (Sections 4.2 and 4.3) were obtained by gravity sedimentation alone. The detailed fractionation procedures are described in Appendix A. Figure 3.1 shows plots of cumulative volume percent vs. Stokes diameter for both the as-received and fractionated powders, which were determined using a centrifugal photosedimentation method[2] (see Section 3.2.2 for details). The as-received Si_3N_4 powder had ~9% particles with diameter greater than 1 μm and the median diameter was ~0.50 μm. In contrast, the particles in the

[1] SN-E-10, Ube Industries (America), Inc., New York, NY
[2] Model CAPA-700, Horiba Instruments, Inc., Irvine, CA

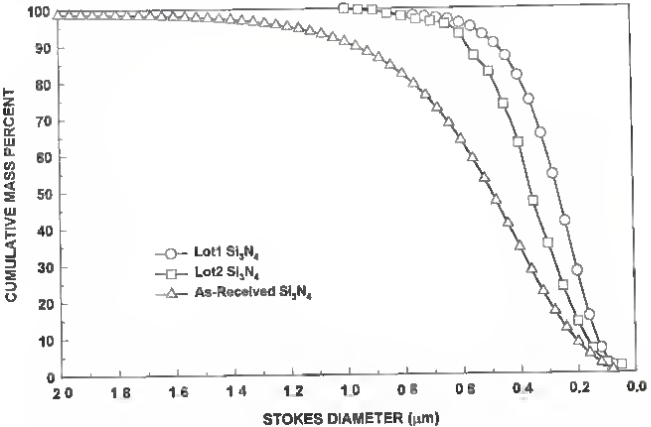

Figure 3 1 Plots of cumulative mass percent vs Stokes diameter for as-received, Lot1 and Lot2 Si_3N_4 powders

fractionated powders were submicrometer in size and the median particle diameters of Lot 1 and Lot 2 powders were ~0.27 μm and ~0.33 μm, respectively.

The SiO_2-coated microcomposite particles were synthesized using the fractionated core Si_3N_4 powder and tetraethyl orthosilicate (TEOS)[3] as starting materials. The detailed step-by-step procedure for the preparation of these powders is described in Appendix B. A dilute (~2 vol%) suspension of the core particles was prepared in ethanol[4] using styrene-maleic anhydride co-polymer[5] as the dispersant. A TEOS/ethanol solution was mixed into this suspension. Precipitation of the SiO_2 coating on the core particles was induced by the addition of concentrated (~30 wt% NH_3) ammonium hydroxide solution. Composite powders with different SiO_2 contents were prepared by varying the TEOS/Si_3N_4 ratio in the coating suspension. Table 3.1 lists the amounts of different components used in the coating experiments. After precipitation of the coating, the powders were washed with deionized water and pressure filtered using 0.22 μm nylon filter paper. The powders were oven-dried at ~80°C for 24 hours and then stored in a dessicator.

Three independent series of composite powders were prepared for the current investigation. For Series I, samples with overall SiO_2/Si_3N_4 volume ratios[6] of 40/60, 60/40, 80/20, and 85/15 were synthesized using Lot 1 Si_3N_4 core powder. Powders for Series II were prepared using Lot 2 Si_3N_4 core powder and they and overall compositions of 60/40

[3] Fisher Scientific, Fair Lawn, NJ
[4] Denatured, Fisher Scientific, Fair Lawn, NJ
[5] SMA 1440A, Arco Chemical Co., Hinsdale, IL
[6] The SiO_2/Si_3N_4 composite powders will henceforth be designated by their nominal SiO_2/Si_3N_4 volume ratios which were calculated from the amounts of the components used in the coating process, assuming that complete conversion of TEOS to SiO_2 had occurred.

and 85/15. For Series III, composite powders with overall compositions of 30/70, 40/60, 50/50, and 60/40 were prepared using Lot 2 Si_3N_4 core powder and ultra-high purity TEOS[7] as starting materials.

Table 3.1 Amounts of Components in the Coating Experiments

SiO_2/ Si_3N_4*	ml ethanol/ g TEOS	g TEOS/g Si_3N_4	ml NH_4OH/g TEOS
30/70	107.5	1.014	21.5
40/60	107.5	1.497	21.5
50/50	107.5	2.365	21.5
60/40	107.5	3.531	21.5
80/20	107.5	9.418	21.5
85/15	107.5	13.401	21.5

* volume ratio

It is important to note that the nominal volume ratios stated earlier were calculated based on the assumption that precipitation of SiO_2 occurred with 100% yield. It must also be noted that some siliceous species remain in solution and therefore SiO_2 concentration in the composite powder may be slightly lower than the calculated value. However, this effect may have been compensated for (at least partially) by the presence of SiO_2 [D. Kisailus and M.D. Sacks, personal communication, 1996] on the core Si_3N_4 particle surface. Since the density of the core powder (which contains SiO_2) was used for the calculation of volume ratios, these values actually correspond to SiO_2/core powder.

[7] 99.999%, Alfa Chemical, Ward Hill, MA

ratios and not to SiO_2/Si_3N_4 ratios. Experimental evidence (described in detail in Section 4.3.1) indicates that the SiO_2/core powder ratios were lower than the nominal values which seems to suggest that SiO_2 precipitation indeed did not occur with 100% yield.

3.1.2. SiO_2 Particles

The silica powders used in this study were prepared by the method of Stober et al [Sto68]. Batches of narrow size distribution powders were produced with median particle diameters in the range of 0.20 – 0.52 μm. Reagent grades of TEOS[8], ethanol[9], and concentrated (~30 wt% NH_3) NH_4OH solution[10] were used. 4.5 liters of ethanol and 234g TEOS (~250 ml) were used per batch (~70 grams) of SiO_2. The median particle size was varied by varying the amounts of NH_4OH solution (i.e., by varying the amount of water). Table 3.2 lists the amount of NH_4OH used to produce the various sizes of SiO_2 powders prepared in this study.

Table 3.2. Amounts of NH_4OH Used to Prepare Various Sizes of SiO_2 Powder

Batch No.	Median Particle Size (μm)	NH_4OH Solution (ml)
1	~0.25	275
2	~0.30	290
3	~0.52	350

Ethanol from a recently opened (i.e., less than two weeks after breaking the seal) container was filtered through a coarse filter paper[11] to remove any contaminant particles.

[8] Fisher Scientific Co., Fair Lawn, NJ
[9] Denatured, Fisher Scientific Co., Fair Lawn, NJ
[10] Fisher Scientific Co., Fair Lawn, NJ
[11] 541 Hardened Ashless, Whatman, Kent, UK

The measuring cylinders and erlenmeyer flasks used in the powder preparation were cleaned with soap solution[2], rinsed with deionized water (to remove the soap solution), and rinsed with filtered ethanol. The containers were then dried in a convection oven for ~6 hours at ~70°C in air. Finally, the mixing flask was rinsed with filtered ethanol and the measuring cylinders were rinsed with the corresponding chemicals viz., filtered ethanol, TEOS, and NH_4OH solution.

The chemicals were mixed using the following procedure. In a 6l erlenmeyer flask, 4500 ml of filtered ethanol was poured and the ethanol was kept stirring using a 2 in. magnetic stirrer. A concentrated NH_4OH (~30 wt% NH_3) solution was then added to the ethanol. After ~5 min, TEOS was quickly (in ~5 s) transferred to the alcohol-ammonia mixture. The onset of precipitation was determined by the change in color (from clear to translucent) of the solution. The SiO_2 particles began to precipitate within ~10 min and the mixture was stirred for an additional 45 min in an attempt to complete the reaction. The precipitated SiO_2 powder was removed from the alcohol solution using the same filtration procedure as that used for the composite powders (see Appendix B). The filtered cakes were dried at ~80°C for 6h and ground for ~10 min using an alumina mortar and pestle. The powders were then loosely packed in a high-purity alumina crucible[3] and calcined in air for 24 h at 200°C. Figures 3.2 A-C and Table 3.2 show the results from particle size distribution measurements on these powders. (The measurement method is similar to that described in Section 3.2.1.) The pH of the SiO_2 suspension was adjusted to ~8.0 and the density of the 200°C heat treated SiO_2 was assumed to be 2.06 g/cm^3 [Sac84a]).

[2] Alkanox, Fisher Scientific, Fair Lawn, NJ
[3] Coors Ceramic Co., Golden, CO

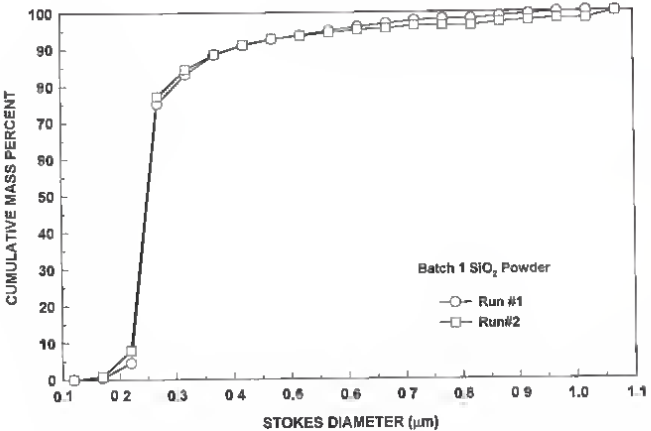

Figure 3 2A Plots of cumulative mass percent vs Stokes diameter for batch 1 SiO_2 powder

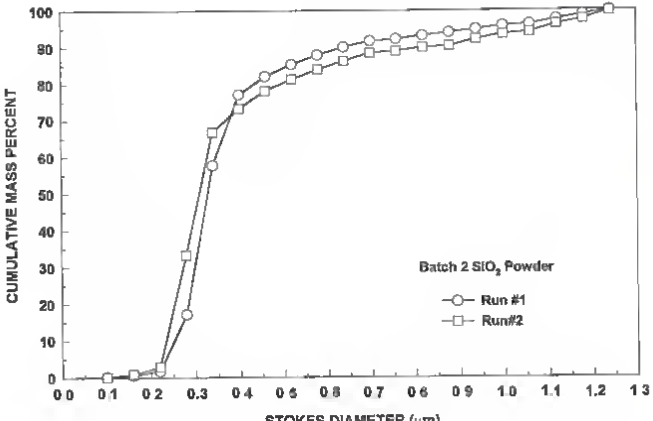

Figure 3 28 Plots of cumulative mass percent vs Stokes diameter for batch 2 SiO_2 powder

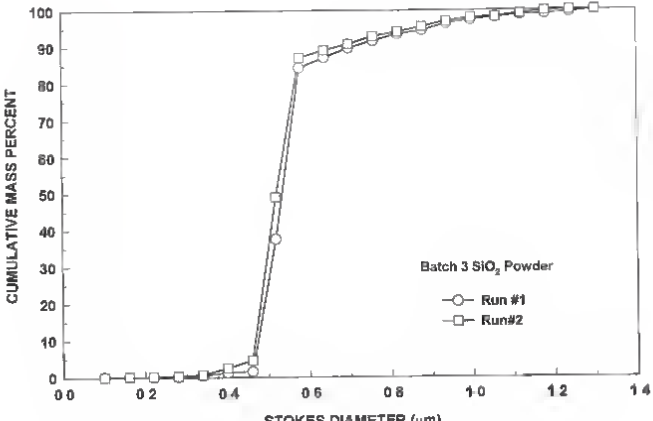

Figure 3 2C Plots of cumulative mass percent vs Stokes diameter for batch 3 SiO_2 powder

3.1.3. Polystyrene (PS) Particles

Polystyrene (PS) particles were synthesized by a dispersion polymerization technique developed by Lu et al. [Lu88]. The detailed synthesis procedure is provided in Appendix C. SEM observations (see Figure 3.3) on the PS particles prepared in this study showed that the particles were nearly spherical and monosized. The number based diameter distribution[14] of these particles is depicted by the histogram plot shown in Figure 3.4. The mean particle diameter was calculated to be 1.89 μm. The geometric standard deviation was 1.05.

3.2. Characterization of Particles

3.2.1. Core Particles and Microcomposite Particles

Particle size distribution analysis

Particle size distributions were measured using a centrifugal photo-sedimentation analyzer[15]. Suspensions with ~0.01 vol% powder were prepared by adding oven-dried (~80°C) powder to deionized water. Sufficient base (1N NH_4OH) was added to both as-received and fractionated Si_3N_4 suspensions to bring the pH in the range 9.6-10.0. The same base was also added to the microcomposite particle suspensions to bring the pH to 9.0-9.2. The electrostatically stabilized suspensions were ultrasonicated[16] for ~1 hour and

[14] SEM samples were prepared using the same procedure (Section 3.2.2.) as that used for the composite powders. Particle size was measured on enlarged (8.5 in. x 11 in.) prints using a digitizing tablet as described in Section 3.2.2. Measurements were carried out on ~300 particles and particle size histograms were generated from these measurements.

[15] Model CAPA 700, Horiba Instruments Inc. Irvine, CA

[16] All ultrasonication in the current study was carried out using a titanium-horn sonicator (Model W 375 Heat Systems-Ultrasonics, Inc. Farmingdale, NY).

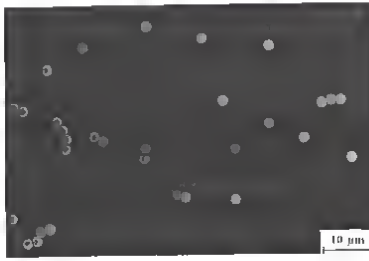

Figure 3 3 SEM micrograph of PS particles

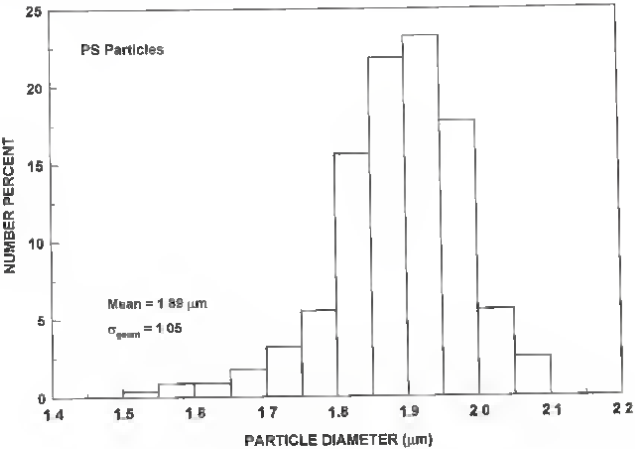

Figure 3.4 Histogram plot of particle diameter distribution for PS particles obtained by quantitative microscopy

the pH was re-checked prior to the particle size measurement. The various parameters used for the measurements are listed in Tables 3 3 through 3 5 Particle size analysis was performed twice on each powder to ensure that reproducible data was collected.

Table 3 3 Parameters for Particle Size Analysis for Series I Powders

	Si_3N_4 AR*	Si_3N_4 f**	60/40	80/20
Solvent Density 25°C (g/cm^3)	1 00	1 00	1 00	1 00
Solvent Viscosity 25°C (mPa•s)	0 89	0.89	0 89	0 89
Powder Density[17] (g/cm^3)	3 19	3 19	2 51	2.28
Maximum Particle Size (μm)	2.00	1.00	1 00	1 00
Minimum Particle Size (μm)	0 08	0 05	0 13	0 13

* AR=as-received** f=fractionated

Table 3 4 Parameters for Particle Size Analysis for Series II Powders

	Si_3N_4 f	60/40	85/15
Solvent Density 25°C (g/cm^3)	1 00	1 00	1 00
Solvent Viscosity 25°C (mPa•s)	0 89	0 89	0 89
Powder Density (g/cm^3)	3 19	2.51	2.22
Maximum Particle Size (μm)	1 00	1.20	1 20
Minimum Particle Size (μm)	0 05	0 10	0 10

[17] The powder densities were calculated assuming true densities of 3 19 and 2.05 g/cm^3 for Si_3N_4 and SiO_2, respectively The first value was determined by gas pycnometry on vacuum-dried (100°C) as-received powder [Rag92] The density of SiO_2 was based on the values obtained by Szoke and Tseng[Sac 84a] for TEOS-derived SiO_2 particles.

Table 3.5 Parameters for Particle Size Analysis for Series III Powders.

	30/70	40/60	50/50	60/40
Solvent Density 25°C (g/cm^3)	1.00	1.00	1.00	1.00
Solvent Viscosity 25°C (mPaes)	0.89	0.89	0.89	0.89
Powder Density (g/cm^3)	2.85	2.73	2.62	2.51
Maximum Particle Size (μm)	1.2	1.00	1.00	1.00
Minimum Particle Size (μm)	0.1	0.1	0.1	0.1

Surface area and surface porosity measurements

Surface area measurements on Series I powders were carried out on a nitrogen gas adsorption instrument[18] using the multipoint BET method. Approximately 1-2 g of vacuum oven dried (100°C, 4h) powder was used for the analysis. Prior to the measurement, the samples were outgassed in the measuring cell under flowing nitrogen for at least 4 hours at 150°C. Two separate measurements were conducted for each powder sample.

Series II and Series III powders were analyzed using an automated surface area and pore size analyzer[19]. Prior to the measurement, approximately 1-2 g of vacuum oven dried (100°C, 2h) or calcined (for 6h at temperatures in the range 200 - 800°C) powder was degassed under flowing nitrogen for ~6 hours at 200°C.. Only one powder sample was used for each composition investigated, i.e., data at different calcination temperatures was obtained on a single sample which was progressively calcined at increasing temperatures.

[18] Model QS-7. Quantachrome Corp. Syosset, NY.
[19] ASAP 2000. Micromeritics Instruments Corp. Norcross, GA.

In addition, for a given calcination temperature, only one measurement was carried out for each powder sample.

Nitrogen gas adsorption/desorption experiments were performed at 77K in the pressure range of 0-950 mm Hg. If v_g is the volume of gas adsorbed expressed in cm^3/g of the solid,

$$v_g = f(p/p^o)_T \qquad (3.1)$$

where p is the pressure of the gas (vapor), p^o is the saturation vapor pressure of the gas, T is the temperature, and $f(x)$ denotes a function of any given variable x. Adsorption and desorption isotherms were obtained as plots of v_g vs. p/p^o, for adsorption and desorption, respectively. Surface areas were measured using the 5-point BET method [Gre82], as described briefly below. The BET equation for gas adsorption is expressed as

$$(p/p^o) / [(1-p/p^o)(v_g)] = 1/(v_m C) + [(C-1)(p/p^o)] / (v_m C) \qquad (3.2)$$

where

v_m = volume of the monolayer adsorbed (in cm^3/g of the solid) and
C = a constant.

The values of v_g were collected at five nitrogen relative pressure values in the range of 0.16 to 0.28. A least squares fit was performed by an algorithm [Acc92] on the computed values of the term in the left hand side of eq. (3.2) plotted as a function of the relative pressure, p/p^o. Consequently, a slope, S, and a y-intercept, Y_{INT}, were obtained. The BET specific surface area, SA_{BET} (m^2/g), was then calculated as [Acc92]

$$SA_{BET} = [(CSA)(6.023\times10^{23})]/[(22414\ cm^3\ STP)(10^{18}\ nm^2/m^2)(S+Y_{INT})] \qquad (3.3)$$

where

CSA = nitrogen gas molecular cross-sectional area = 0.162 nm^2

The C value in the BET equation was calculated as

$$C = (S + Y_{INT})/(Y_{INT}) \quad (3.4)$$

Micropore (defined as pores < 17Å in diameter) calculations were made using the approach of Harkins and Jura [Grel82]. A thickness parameter, T, corresponding to a nitrogen relative pressure of p/p^o, was defined as [Grel82]

$$T = [\ 13.99/(0.034 - \log(p/p^o))\ ]^{0.5} \quad (3.5)$$

A least squares fit was performed on the measured values of the amount of gas adsorbed, v_g, plotted as a function of T. Accordingly, a slope, S_2, and a y-intercept, Y_2, were obtained. The external specific surface area (defined as the surface area of the primary particles excluding the area of any the pores within the primary particles which are termed as "internal" porosity or "micropores") SA_{EXT} (m^2/g) was then calculated as [Acc92]

$$SA_{EXT} = \{S_2\ cm^3/g\text{-Å STP})(10^{10}\ Å/m)(D\ cm^3\ liquid/cm^3\ STP)\} / [F(10^6\ cm^3/m^3)] \quad (3.6)$$

where

F = surface area correction factor = 1
D = density conversion factor = 1.546×10^{-3} cm^3 liquid/cm^3 STP

The micropore surface area, SA_{MP} (m^2/g), was calculated as [Acc92]

$$SA_{MP} = SA_{BET} - SA_{EXT} \quad (3.7)$$

The micropore volume was determined by [Acc92]

$$v_{MP} = (Y_2\ cm^3/g\ STP)(D\ cm^3\ liquid/cm^3\ STP) \quad (3.8)$$

In the current investigation, the measuring apparatus used an algorithm [Acc92] to determine the terms in eqs. (3.6) through (3.8).

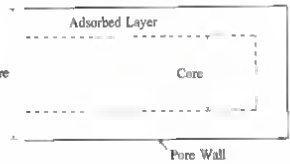

Figure 3.5 Schematic showing the pore geometry assumed for calculation of pore size distributions.

The desorption branch of the isotherm was used to relate the amount of adsorbate (nitrogen) lost in the desorption step to the average diameter of the pores emptied in the step. A pore (see schematic in Figure 3.5) loses its condensed liquid adsorbate (known as the "core" of the pore, at a particular relative pressure related to the "core" radius, r_c, by the Kelvin equation [Gre82]

$$\ln p/p^o = -(2\gamma V_L/RT)(1/r_c) \qquad (3.9)$$

where V_L is the molar volume and γ is the surface tension of the adsorbed liquid (nitrogen). After the core has evaporated, a layer of adsorbate remains on the wall of the pore. The thickness of this layer is given by the thickness equation, eq. (3.5) [Acc92]. This layer becomes thinner with successive decreases in pressure, so that the measured quantity of gas desorbed in a step (i.e., at any given p/p^o) is composed of a quantity equivalent to the liquid "cores" evaporated in that step plus the quantity desorbed from the walls of the pores whose "cores" have been evaporated in that and the previous steps (i.e., at higher p/p^o values during the desorption process). Barrett, Joyner and Halenda [Gre82] developed a detailed procedure (known as the BJH method) that incorporated this approach to calculate the pore

size distribution. In the current investigation, the measuring apparatus used a complex algorithm [Acc92] implementing the BJH method to determine the pore size distribution, i.e. the plots of cumulative pore volume (V_p, in cm^3/g) vs the pore diameter (D_p in nm). Differential volumes (with respect to diameter) dV/dD were then calculated as [Acc92]

$$(dV/dD)_i = V_{pi}/(D_{pi} - D_{pi+1}) \qquad (3\ 10)$$

where

V_{pi} = incremental pore volume for the Ith step (i.e., for a relative pressure of p_i/p^o)

D_{pi}, D_{pi+1} = pore diameters corresponding to Ith and (I+1)th steps, respectively

Electrophoretic mobility measurements

Electrophoretic mobilities were measured on the core and composite powders using a laser microelectrophoresis instrument[20]. Dilute (40-60 ppm) suspensions were prepared by adding a small amount of powder dried (24h at ~80°C in vacuum) to an aqueous KCl solution (10^{-3} M in deionized water). The suspension pH was varied using additions (ranging from 10^{-3} - 10^{-1} ml in 100ml of suspension) of 0.01N HNO_3 (for pH 2.0-6.0) or 0.01N NH_4OH (for pH 6.0-10.0). Prior to the mobility measurements, the suspension was placed in a low-shear tumbler for 18-24 hours to allow pH stabilization. For each powder electrophoretic mobilities were determined for two independent samples at the "top" and "bottom" stationary levels. (The observed particle velocity is the sum of the electrophoretic velocity of the particle relative to a stationary liquid and the electro-osmotic velocity of the liquid relative to the stationary capillary tube. Since the electrophoresis cell is a closed system during measurements, the liquid displaced by electro-osmotic flow must circulate

[20] DELSA 440, Coulter Electronics, Inc., Hialeah, FL

back in the opposite direction by Poisseville flow. There are certain locations in the cell in which the flow rates in the forward and backward directions are equal. These locations are termed as the "stationary levels" of the cell and they occur at 70.7% of the radial distance from the center of the cylindrical capillary. Experimentally, the "top" and "bottom" stationary levels are located at a distance 14.65% of the capillary diameter from the two capillary walls as viewed in cross-section. A particle tracked at these positions will have its true electrophoretic mobility, uncomplicated by electro-osmotic flow of the liquid [Roe88].

The suspensions were prepared in the KCl solution in order to maintain the ionic strength invariant. The ionic strength (I) of a solution is defined as,

$$I = 1/2 \; \Sigma z_i^2 M_i \qquad (3.11)$$

where,

z_i^2 – valancy of the ions of type i,
M_i = concentration of the ions of type i in solution (moles/l), and
Σ denotes summation over i

The ionic strength of the KCl solution can be calculated as $1/2*(1*10^{-3}+1*10^{-3}) = 10^{-3}$ moles/l. If 10^{-1} ml (the maximum amount used in the experiments) of 0.01N HNO_3 or 0.01 N NH_4OH is added to 100ml of the KCl solution, their concentration can be calculated as $(10^{-1}/1000)*0.01*(1000/100) = 10^{-5}$ moles/l. The total ionic strength then becomes $1/2*(1*10^{-3}+1*10^{-3}+1*10^{-5}+1*10^{-5}) = 1.01*10^{-3}$ moles/l. In other words, the change in ionic strength resulting from the addition of the acid or base results is only 1%. Therefore it is clear that the ionic strength remains almost constant with the additions of HNO_3 or NH_4OH. It is noted that when acid or base is added to the suspension, some of the H^+ and OH^- will adsorb on the particle surface. Therefore, the ionic strength of the solution may be slightly lower than the calculated value. In such a case, the increase in ionic strength due to acid or

base additions will be even lower than the calculated increase. Furthermore, it is noted that the solubility of the particles in suspension was neglected in the calculations. The solubility of the SiO_2 particles and the SiO_2 coatings in the composite particles are dependent on the pH of the suspension. At extreme pH values (i.e., typically, <4 and >8) the solubility is significant. However, since the suspensions used were very dilute, the solubility of SiO_2 is not expected to cause any significant errors in the calculation of the ionic strength values. For Si_3N_4 suspensions, it is presumed that the solubility is negligible and therefore, the associated error in the calculated ionic strength values is also negligible.)

In order to calculate zeta potentials it is necessary to determine the value of κR, where R is the particle radius (m) and κ (m^{-1}) is the Debye Huckel parameter, defined by,

$$\kappa^2 = (\epsilon^2 / \epsilon \varepsilon_o kT) \Sigma z_i^2 \bullet n_i \qquad (3\ 12)$$

where,

e = electron charge = 1.6×10^{-19} C,
k = Boltzmann constant = 1.38×10^{-23} J/K,
T = temperature = 298K, and
n_i = number of ions of type i ($/m^3$)
= $M_i N_A / 1000$, where N_A is the Avogadro's number

For symmetric electrolyte (i.e., for $z_+ = z_- = z$) solutions, eq (3.12) can be reduced to

$$\kappa\ (cm^{-1}) = 3.29 \times 10^7\ |z|\ M^{1/2} \qquad (3\ 13)$$

where, z is the valency and M is the molarity. For the KCl solution used in the current study, κ was calculated to be $1.04 \times 10^8\ cm^{-1}$ by using eq (3.13) and recognizing that z = 1 and $M = 10^{-3}$. Particle size measurements on composite powders (Figure 4.41) have shown that the median Stokes diameter of the Series II and Series III composite powders is in the range of 0.4 - 0.5 μm (i.e., the median radius is in the range of 0.20 - 0.25 μm). Based on

these values, the calculated values of κR range from ~21 26. The lot1 and lot2 Si_3N_4 core powders, Series I 60/40 composite powder and the batch1 SiO_2 powder had median Stokes diameters (obtained from centrifugal sedimentation measurements) of ~0 27, ~0 33, ~0 30 and ~0.25 μm, respectively The corresponding κR values were calculated to be ~14 ~16, ~17, and ~13, respectively

Zeta potentials can be calculated from electrophoretic mobilities using the Henry equation [Par81]

$$\zeta = \mu \eta / [f(\kappa R) \varepsilon \varepsilon_o] \qquad (3\ 14)$$

where ζ = zeta potential (V), μ = electrophoretic mobility ($m^2 \bullet s^{-1} \bullet V^{-1}$), η = solvent viscosity (0 89 x 10^{-3} Pa•s), ε = relative dielectric constant of liquid (~78), ε_o = permittivity of vacuum (8 854 x 10^{-12} F/m), and $f(\kappa R)$ is a complicated function of κR in which $f(\kappa R)$ varies from 2/3 to 1 as κR goes from 0 to ∞. (When $f(\kappa R)$=1, eq (3 14) reduces to the well-known Helmholtz-Smoluchowski equation [Par81]) Henry [Hen31] plotted $f(\kappa R)$ as a function of κR and it was deduced from this plot that $f(\kappa R)$ varied from 0 88 to 0 90 as κR varied from 21 to 26 (for calculation purposes $f(\kappa R)$ was assumed to be 0 89 for all the Series II and Series III composite powders). It was also deduced that the values of $f(\kappa R)$ for lot1 and lot2 Si_3N_4 core powders, Series I 60/40 composite powder and batch1 SiO_2 powder were ~0 86, ~0 87, ~0 87, and ~0 85, respectively For the polystyrene (PS) particles with a diameter of ~2 μm κR = 104 and therefore $f(\kappa R)$ = 1 was substituted in eq. (3 14) (i e., Helmholtz-Smoluchowski equation [Par81] was used)

Wiersema et al [Wie66] showed that for relatively low values of κR and for relatively high zeta potentials (typically >25 mV), relaxation effects become important and

that Henry s equation underestimates the zeta potential (Henry's treatment [Hen31] neglected relaxation effects.) Therefore, it is important to determine if Henry's calculations are valid for the powders used in the current study For this purpose, it is necessary to calculate two dimensionless parameters E and q_e using the following equations [Wie66]

$$E = 0.7503 \times \mu \tag{3 15}$$

$$q_e = 0.3289 \times 10^4 \ (M \bullet z_-)^{1/2} \ R \tag{3 16}$$

where μ is the electrophoretic mobility in $\mu m \bullet cm \bullet V^{-1} \bullet s^{-1}$, M is the electrolyte concentration in equivalents per liter (i.e the molarity of KCl = 10^{-3}) z_- is the valence of the anions (= 1), and R is the particle radius in μm. Wiersema et al [Wie66] determined that there was a limiting value of E (or the mobility) above which Henry s treatment was not applicable and that it was a function of q_e. The calculated value for q_e, the limiting value of E (E_L) and the limiting value of mobility (μ_L, calculated using eq (3 15)) for various powders are shown in Table 3 6 (The particle radius was determined as half the median Stokes diameter determined by centrifugal sedimentation measurements.) Henry's treatment is valid only when the absolute value of the mobility is smaller than μ_L. An inspection of Tables 4 1 – 4 3 and 4.20 4 21 reveals that most of the mobility values were higher than the critical required for the applicability of Henry s approach. In such cases, the zeta potentials were determined as follows. First, a dimensionless parameter, y_e, was determined for the E and q_e values (calculated from eqs. (3 15) and (3 16), respectively) using tables provided in the treatment of Wiersema et al [Wie66] Second, the zeta potential (ζ, in mV) was determined using the equation

$$\zeta = 25\ 69 \bullet y_e \tag{3 17}$$

Table 3 6 List of Calculated q_o, E_L, and μ_L Values for Various Powders

Powder	R (μm)	q_o	E_L	μ_L ($\mu m \cdot cm \cdot V^{-1} \cdot s^{-1}$)
Lot1 Si_3N_4	0 135	14	~1.5	~2 0
Lot2 Si_3N_4	0 165	17	~1 6	~2 1
Series I 60/40	0 150	16	~1.5	~2.0
batch1 SrO_2	0 125	13	~1.5	~2.0
Series III 30/70	0 195	20	~1 7	~2.3
Series III 40/60	0 210	22	~1 7	~2.3
Series III 50/50	0.225	23	~1 8	~2 4
Series III 60/40	0.240	25	~1 8	~2 4
Series II 85/15	0.260	27	~1 9	~2.5

X-ray photoelectron spectroscopy (XPS)

X-ray photoelectron spectroscopy (XPS) was carried out, using a spectrometer[21], on powders that were vacuum oven dried at 100°C for 24h A small quantity of powder (~0 1g) was evenly spread on a double-sided tape mounted on a stainless-steel sample holder Analysis was performed at binding energies in the range 0-1500 eV

X-ray diffraction

Powder X-ray diffraction (XRD) patterns were obtained using a diffractometer[22] with Ni filtered CuKα radiation and a scan rate of 3°/min Prior to the measurements ~0.5g of the dried (for 24h at 80°C in air) powder sample was firmly packed into an acrylic sample holder Data was collected in the 2θ range of 5° - 85°

[21] Model XSAM 800, Kratos Analytical Manchester U K
[22] Model APD 3720, Philips Electronic Instruments Co Mt Vernon, NY

Electron microscopy

Samples for scanning electron microscopy (SEM)[25] were prepared using dilute suspensions (~100 ppm) of the powder dried (for 24h at 80°C in air) in ethanol, which were initially ultrasonicated for 15 minutes to break down soft agglomerates. A clean glass substrate (~5mm x 5mm) was attached to an aluminum SEM mount with carbon paint. One drop of the suspension was deposited on the substrate and the solvent was allowed to evaporate. The sample and the mount were then sputter-coated with a thin (≈ 100 Å) gold-palladium film for SEM analysis. The aforementioned suspensions were also used to prepare samples for transmission electron microscopy (TEM)[26] and high-resolution TEM (HRTEM)[27] analyses. Approximately 1-2 drops of the suspension were pipetted on a Cu grid loosely placed on a glass slide and the solvent was allowed to evaporate. The TEM and HRTEM observations were made at magnifications in the ranges of 50,000-100,000x and 400,000-500,000x, respectively.

Quantitative stereological measurements

TEM samples were prepared by depositing one drop of a dilute (~100ppm) suspension of the composite particles in ethanol on to a Cu grid. After drying, random areas of the grid was sampled to obtain TEM images (15 - 25) of individual particles. The TEM pictures were scanned at a high resolution (at 450 dpi so that the two phases could be clearly distinguished) using a flat bed scanner[28] and a graphics software[29]. The contours of

[25] JSM 35-CF and JSM-6400, Japan Electron Optics Co. Ltd., Tokyo, Japan
[26] Model 200 CX, Japan Electron Optics Co. Ltd., Tokyo, Japan
[27] Model 400 CX, Japan Electron Optics Co. Ltd., Tokyo, Japan
[28] Model ENV 8100, Envision Solutions Technology
[29] Photoshop Version 2.5, Adobe Systems, Inc.

the core particle surface and the coating surface were traced (using a line thickness of 0.25 pts or ~0 08 mm) using a drawing software[28] The traces were then imported back to the graphics software. Quantitative analysis was carried out on the traced particles using an image analysis software[29] by the following procedure. First, the core particles were filled with black color and the perimeter (P_{SN}) and cross-sectional area (A_{SN}) of these particles were measured. Second, the entire composite was filled and the corresponding perimeter (P_C) and the cross-sectional area (A_C) of the composite were determined. Figure 3 6 schematically illustrates the parameters measured using the image analysis.

Figure 3 6 Schematic showing the image analysis parameters that were measured. P and A denote perimeter and area, respectively, of the particle (SN–core particle and C= composite particle)

Several physical quantities were calculated using the measured values of the areas and perimeters as described below:

Area based equivalent diameter of Si_3N_4 $d_{SN} = (4A_{SN} / \pi)^{1/2}$ (3 18)

Area based equivalent diameter of composite $d_C = (4A_C / \pi)^{1/2}$ (3 19)

[28] Intellidraw Version 2.01 Aldus Corp
[29] NIH Image Analyst

Area based volume fraction[30] of Si_3N_4 , $f_{SiN_4} = (A_{SN} / A_C)^{3/2}$ (3.20)

Area based average coating thickness , $t_a = (d_C - d_{SN}) / 2$ (3.21)

It follows from eq (3.21) that,

$$t_a = (A_C^{1/2} - A_{SN}^{1/2}) / \pi^{1/2} \quad (3.22)$$

Shape factor[31] of Si_3N_4 , $S_{SN} = P_{SN}^{\ 2} / (4\pi A_{SN})$ (3.23)

Shape factor of composite , $S_C = P_C^{\ 2} / (4\pi A_C)$ (3.24)

Inductively coupled plasma (ICP) analysis

Samples for ICP analysis were prepared using the following technique. ~0.25g of the composite powder was heated in a box furnace[32] at 450°C for 6h. When the furnace cooled to ~150°C the sample was quickly transferred to a vacuum desiccator and allowed to equilibrate at room temperature for ~6h. ~408g of a concentrated (~49 wt%) HF solution[33] was mixed with ~592g of deionized water to form a ~20 wt% HF solution. The dry powder was accurately weighed and then transferred to a clean 30 ml plastic bottle which was previously filled with 21.08g of the dilute HF solution. The suspension was mixed by manually shaking for ~2 min and placed in a constant temperature water bath at 18°C for ~4h to completely dissolve the SiO_2 coating. The etched powder suspension was then poured into 50 ml plastic centrifuge tubes. A centrifuge apparatus[34] was used to centrifuge the suspension at ~1800 rpm for ~20 min. ~15 ml of the clear supernatant was

---

[30] This is based on the conversion of areas to equivalent spherical volumes. For a perfect sphere of radius R, the area A is proportional to R^2. Since the volume is proportional to R^3 it is also proportional to $A^{3/2}$. The calculation implicitly assumes that for a given particle, both the core and the composite have similar shapes (which is not necessarily accurate).

[31] The shape factor is an indirect measure of the sphericity of the particle. In the case of a perfect sphere, the cross-section would be circular and the value of S would be equal to 1.

[32] Model DT-31, Deltech, Inc. Denver CO

[33] Fisher Scientific, Fair Lawn, NJ

[34] Model J2-21, Beckaman Instruments, Inc., Schaumburg, IL

transferred to a clean 30ml plastic bottle. To a 30 ml plastic bottle, 39g of deionized water and 1g of the clear supernatant were added and the resulting solution was shaken for ~2min and used for ICP analysis.

Silicon concentrations in solution were determined by an ICP apparatus[35] calibrated using a 50 ppm Si standard solution[36]. The compositions of the powders were determined using the following calculation procedure. If the measured silicon concentration is denoted by C_s (ppm), the total amount of silicon (W_1 g) in the analysis suspension (40 g total) is equal to $C_s \cdot 10^{-6} \cdot (40)$. Therefore 1g of the supernatant from centrifuging contained W_1 g of silicon. If W_2 is the weight of SiO_2 in this solution, then it can be expressed as, $W_2 = W_1 \cdot 60/28$ g. It follows that the ratio of the weights of SiO_2 and the HF solution in the supernatant solution is $W_2/(1-W_2)$. Since the total amount of HF solution used was 21.08g, the total amount of SiO_2 dissolved in this solution (W_3) is given by $21.08 \cdot W_2/(1-W_2)$.

In order to determine the relative amounts of the phases, powder true densities of SiO_2 and Si_3N_4 are necessary. The true density of SiO_2 and the core Si_3N_4 powders were assumed to be 2.15 g/cm^3 (~450°C heat treated [Sac84a]) and 3.19 g/cm^3 (100°C vacuum dried [Bag92]), respectively. The SiO_2 content in the Si_3N_4 powder was not determined in this study. However, another study [D. Kisailus and M.D. Sacks, personal communication, 1996] conducted on similar powders showed that ~2 vol% SiO_2 was present on the core Si_3N_4 surface. Therefore the assumed true density of the core powder is actually the density of a "composite" powder with a composition of ~2 vol% SiO_2 / ~98 vol% Si_3N_4. The true density of "pure" Si_3N_4 (i.e., without the surface SiO_2) was

[35] Model 11, Perkin Elmer
[36] Fisher Scientific, Fair Lawn, NJ

estimated by assuming that the fractionated Si_3N_4 core powder (which had a true density of 3.19 g/cm^3) contained 2 vol% SiO_2 and that the density of the SiO_2 was 2.20 g/cm^3 [Sac84a]. Based on these assumptions, the true density of "pure" Si_3N_4 was estimated as (3.19 − 0.02•2.20)/0.98 = 3.21 g/cm^3. The weight fraction of SiO_2 (f_S^{SN}) in the core powder can therefore be calculated as

$$f_S^{SN} = [\,1 - (0.98/3.21)/\{(0.98/3.21)+(0.02/2.20)\}\,] = 0.0289 \qquad (3.25)$$

Another important factor given consideration in the current data analysis is the contribution of the hydroxyl (OH) groups in the SiO_2 present in the composite powder. Sacks and Tseng [Sac84a] carried out weight loss studies for TEOS-derived SiO_2 powders. It was determined that the powder underwent ~11% and ~12.5% loss in weight when heated to temperatures of ~450 and ~1200°C, respectively. It can be deduced from these values that the weight fraction of residual OH groups in a ~450°C heat-treated SiO_2 powder was, $f_{OH} = (12.5-11)/(100-11) = 0.0168$. It was assumed that the same volume fraction of OH groups were present in the SiO_2 phase in the composite powders used in this study.

The total weight (W_T) of the composite powder can be divided into four parts: (1) W_{SN}, the weight of the Si_3N_4 phase (i.e., excluding the SiO_2 phase in the core powder), (2) W_S^{SN}, the weight of SiO_2 in the core powder = $[f_S^{SN}/(1-f_S^{SN})]\bullet W_{SN}$, (3) W_S^S, the weight of SiO_2 (i.e., excluding the OH groups in the coating), and (4) W_{OH}, the weight of the OH groups in the coating = $[f_{OH}/(1-f_{OH})]\bullet W_S^S$. Therefore the total weight is given by

$$W_T = W_{SN} + \{f_S^{SN}/(1-f_S^{SN})\}\bullet W_{SN} + W_S^S + \{f_{OH}/(1-f_{OH})\}\bullet W_S^S \qquad (3.26)$$

Recalling that the weight of the leached SiO_2 is W_S, it follows that

$$W_3 = [f_S^{SN}/(1-f_S^{SN})]\cdot W_{SN} + W_S^S \quad (3.27)$$

Using eq (3.27) to substitute for W_S^S in eq (3.23), we obtain

$$W_T = [1+f_S^{SN}/(1-f_S^{SN})]\cdot W_{SN} + [1 + f_{OH}/(1-f_{OH})]\cdot(W_3 - [f_S^{SN}/(1-f_S^{SN})]\cdot W_{SN}) \quad (3.28)$$

The value of W_T and W_3 from each measurement was substituted into eq (3.28) to calculate the value of W_{SN}. The value of W_S^S was then obtained by using this value in eq (3.27). From these two values, all the four terms in the right hand side of the equality in eq. (3.26) were computed. The weight percent of different components were calculated using the following expressions:

w_{SN} = weight percent Si_3N_4 in the OH free composite powder

$$= W_{SN}*100/(W_{SN} + W_S^{SN} + W_S^S) \quad (3.29)$$

w_S = weight percent SiO_2 in the OH-free composite powder

$$= 100 - w_{SN} \quad (3.30)$$

w_{core} = weight percent core Si_3N_4 particles in the OH-free composite powder

$$= (W_{SN} + W_S^{SN})*100/(W_{SN} + W_S^{SN} + W_S^S) \quad (3.31)$$

w_{coat} = weight percent TEOS-derived SiO_2 in the OH-free composite powder

$$= W_S^S*100/(W_{SN} + W_S^{SN} + W_S^S) = 100 - w_{core} \quad (3.32)$$

The volume percent of the various components were calculated as follows. The volume percent of the core particles and the coating (i.e., the TEOS-derived SiO_2) were calculated from the weight percent values by assuming their true densities to be 3.19 and 2.15 g/cm^3, respectively. The volume percent of Si_3N_4 phase was calculated from the weight percent by assuming the true densities of the Si_3N_4, TEOS-derived SiO_2 (the coating phase) and the SiO_2 in Si_3N_4 to be 3.21, 2.15 and 2.20 g/cm^3, respectively.

There are three possible sources of error in this analysis. First, incomplete dissolution of SiO_2 in the HF solution can lead to a lower measured value of the SiO_2 concentration. Second, the assumption that Si_3N_4 does not undergo any dissolution in the HF solution may not be rigorously correct. Third, the assumed true density values may not be accurate. Nevertheless, each of these sources of error is believed to be relatively small

3.2.2. Characterization of PS Particles

Electrokinetic measurements[37] were performed on aqueous suspensions of PS particles in the pH range of 2-10 The measurement procedure was identical to that described in the previous section. Differential thermal analysis (DTA) and thermal gravimetric analysis (TGA)[38] were carried out at a heating rate of 5°C/min in both flowing (~60 cm^3/min) nitrogen and air atmospheres.

3.3 Suspension Preparation and Characterization

3.3.1. Series I Composite Powder and Mixed Powder Suspensions

Two different suspensions were prepared using (1) a mixture of SiO_2 and Si_3N_4 particles and (2) SiO_2-coated Si_3N_4 particles In the first case, the starting powders were batch 1 SiO_2 and Lot 1 Si_3N_4 The powders were used to prepare individual concentrated (~25 vol%) aqueous suspensions The two suspensions were subjected to ultrasonication for ~2 h to break down powder agglomerates and pH adjustment (to ~9-10 using 3N NH_4OH solution) to achieve electrostatic stabilization. They were then mixed to form a co-

[37] Delta Model 440, Coulter Electronics Inc Hialeah, FL
[38] Netzsch STA409 Exton, PA

dispersed suspension containing a ~51/49 weight ratio of SiO_2 and Si_3N_4 (this proportion corresponds to a ~60/40 volume ratio in a sintered compact if the powder densities of SiO_2 and Si_3N_4 are assumed to be 2.20 and 3.19 g/cm^3, respectively). The mixed powder suspension was ultrasonicated for an additional 1h before consolidation.

The second type of suspension was prepared using Series I 60/40 composite powder. Suspension preparation was carried out in the same manner as described for the individual suspensions in the previous paragraph.

3.3.2. PS and Series II Composite Powder Suspensions

Separate well-dispersed aqueous suspensions of both PS and Series II 60/40 composite powders were initially prepared. The suspensions were stabilized against flocculation by adjusting the pH to ~9 (using a 3N NH_4OH solution) and ultrasonicating for ~2 hours to break down the agglomerates. Mixed suspensions with an overall solids concentration of ~30 vol% and with overall SiO_2/Si_3N_4 powder to PS powder volume ratios of 84/16, 86/14, and 88/12 were prepared by combining a ~36 vol% SiO_2/Si_3N_4 suspension, a ~21 vol% PS suspension, and deionized water in the ratios of 1 : 0.33 : 0.10, 1 : 0.28 : 0.12 and 1 : 0.23 : 0.13, respectively. SiO_2/Si_3N_4 suspensions with a solids concentration of ~30 vol% were used to prepare composite compacts which did not contain PS particles.

Suspension rheological flow characteristics (shear stress, τ versus shear rate, γ, behavior) were determined using a concentric cylinder viscometer[39]. Shear stresses were determined by conducting separate measurements in the shear rate ranges of 0 - 1000 s^{-1} and

[39] Model RV 100/CV-100 viscometer, Haake Inc., Saddle Brook, NJ.

0 100 s^{-1}, respectivaly. For each measurement, the shear rate was first increased to the maximum value in 2 min (to obtain the "up-curve") and subsequently reduced to zero in 2 min (to obtain the "down-curve"). The data from the two measurements were merged and fitted to smooth curves using a curve-fitting algorithm[46]. Viscosity values, η, were calculated from the flow curves using the equation:

$$\eta = \tau / \dot{\gamma} \qquad (3.33)$$

3.3.3. Series III Composite Powder, SiO_2 Powder, and Mixed Powder Suspensions

Series III powders were dispersed in water (at a solids concentration of ~30 vol%) using ultrasonication for ~2 h to break down agglomerates and pH adjustment (to ~9 using a 3N NH_4OH solution) to achieve electrostatic stabilization. Suspensions (~30 vol% solids) were also prepared from batch 2 and batch 3 SiO_2 powders in order to directly compare densification and creep behavior of microcomposite particle compacts with SiO_2 powder compacts. Well-dispersed suspensions were prepared in deionized water by adjusting the pH to ~8 (for electrostatic stabilization) using a 3N NH_4OH solution and ultrasonicating for ~2h to break down agglomerates.

In order to study the effect of phase distribution on densification kinetics, samples were also prepared from a mixture of batch 3 SiO_2 and Lot2 Si_3N_4 particles. Well-dispersed suspensions (~30 vol% solids, pH~9.0) of SiO_2 and Si_3N_4 were prepared separately using the same procedure that was used for the preparation of microcomposite particle suspensions. A co-dispersed suspension was prepared by mixing the two suspensions such

[46] TableCurve 2D, Jandel Scientific, San Rafael, CA

that the mixture had a SiO_2/Si_3N_4 ratio of 85/15. This suspension was mixed using a paint shaker[41] for ~5 min and ultrasonicated for ~15 min.

SiO_2 samples for dielectric and mechanical property measurements were prepared using batch 1 SiO_2 powder. In order to introduce controlled, closed pores in the samples, ~1 μm dia. spherical monosized PS particles that were synthesized by Amim and Sacks [M.M. Amim and M.D. Sacks, personal communication, 1990] were utilized. Separate well-dispersed aqueous suspensions of both PS and SiO_2 powders were initially prepared. The suspensions were then stabilized against flocculation by adjusting the pH to ~9 (using a 3N NH_4OH solution) and ultrasonicating for ~2 hours to break down the agglomerates. Mixed suspensions with an overall solids concentration of ~28 vol% and with overall SiO_2 powder to PS powder volume ratios of 95/5 and 85/15 were prepared by combining a ~35 vol% SiO_2 suspension, a ~25 vol% PS suspension, and deionized water in the appropriate ratio.

3.4. Consolidation and Characterization of Green Compacts

3.4.1. Consolidation

Slip-cast samples were prepared by pouring suspensions into molds set on porous plaster blocks[42]. A 0.22 μm cellulose filter paper[43] was placed between the molds and the plaster.

[41] Model 5400, Red Devil Equipment Co., Brooklyn Park, MN.
[42] Blocks were made by mixing a mixture of 2 parts plaster-of-paris powder (Bondex Corp., Montreal, Canada) to 1 part water into plastic blocks. Drying was carried out at ~50°C for ~48h.
[43] 0.22μm nylon, Fisher Scientific, Fair Lawn, NJ.

Green compacts having characteristics similar to those schematically depicted in Figure 2.1 were prepared using suspensions containing (1) a mixture of SiO_2 and Si_3N_4 particles and (2) SiO_2-coated Si_3N_4 particles. The suspensions (Section 3.3.1) were cast into acrylic rings (~20 mm in diameter). The samples were covered with a plastic cover and allowed to dry under ambient conditions for ~48 h. They were subsequently oven-dried (~80°C, 12 h), pre-sintered in a quartz tube furnace[44] at 600°C (heating rate ~2°C/min) for 2 h in ambient air, and stored in a vacuum dessicator. The cast samples were ~2-3 mm thick and weighed ~1 g after pre-sintering.

The suspensions described in Section 3.3.2 were poured into teflon rings (~20 mm in diameter) or rectangular molds (~30 mm length x ~6 mm width). Samples were placed in a controlled humidity chamber[45] (~90% relative humidity) for ~48 hours. The cast compacts were then dried under ambient conditions for ~24 hours and subsequently oven-dried at ~80°C for ~24 hours. The disk and bar samples were ~2-3 mm and ~4-5 mm thick, respectively, after drying. The oven-dried samples were heated to 575°C in air to pyrolyze the PS particles and then presintered at 800°C in nitrogen. The pre-sintering schedule is shown schematically in Figure 3.7.

For Series III powder samples, teflon molds were used to prepare disk-shaped compacts (~2-3 mm thick and ~19 mm diameter) for isothermal densification studies whereas polystyrene molds (~25 mm long pieces cut from polystyrene pipets[46]) were used to form rod-shaped compacts (~12 mm high and ~6 mm in diameter) for dilatometry and

[44] Model 59344, Lindberg Co., St. Waterton, WI
[45] Model 5851 National Appliance Co., Portland, OR
[46] Serological pipet, 5ml, Fisher Scientific, Fair Lawn, NJ

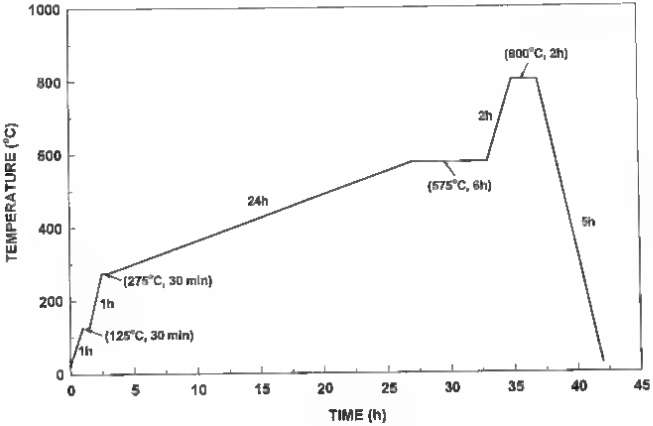

Figure 3 7 Heating schedule for pre-sintering of Series II powder compacts

creep experiments. The compacts were dried at ~80°C for 24 h in air and subsequently pre-sintered in nitrogen at 800°C (heating rate ~2°C/min) for 2 h. In order to produce cylindrical geometry, the top surfaces of the pre-sintered rod samples were ground[47] using 600 grit SiC grinding paper[48].

The batch 1 SiO_2/PS suspensions with overall SiO_2 powder to PS powder volume ratios of 95/5 and 85/15 were poured into teflon rings (~20 mm in diameter) to form 2-3 mm thick disk-shaped compacts. Some of the former suspension was poured into rectangular molds (~30 mm length x ~6 mm width) to form bar-shaped samples. The casting, drying, and pre-sintering conditions for these samples were similar to those used for the (SiO_2/Si_3N_4)/PS compacts except that the furnace atmosphere was flowing (~50 cm^3/min) air and that the final temperature was 700°C.

Batch 2 SiO_2 suspensions were used to form rectangular bars (~25 mm x 6 mm x 5 mm) for creep studies. After drying (at ~80°C in air), the compacts were pre-sintered in air (heating rate ~15°C/h) at 700°C for 6h. The rectangular bars were sintered in air (heating rate ~10°C/min) at 1150°C for 24 h after which they were nearly transparent and almost fully dense (i.e., no residual porosity). It is noted that the bars typically cracked into two pieces during sintering. The pieces that were >10 mm in length were cut into ~10 mm long specimens using a precision saw[49] and polished plane parallel (< 5% variation in length) using aqueous 600 grit SiC[50] slurry on a glass plate. Disk shaped compacts (~2-3 mm thick

[47] When a suspension is poured into a mold, it forms a curved surface (meniscus) on the top due to interfacial effects. Therefore, the top surface of the rod samples are curved (concave upward). This surface needs to be ground flat in order to obtain samples suitable for dilatometry and creep experiments.
[48] Buehler Ltd. Lake Bluff IL.
[49] Isomet, Buehler Ltd. Lake Bluff IL.
[50] Buehler Ltd. Lake Bluff IL.

and ~19 mm diameter) were also slip-cast from the ~85 vol% SiO_2 + ~15 vol% Si_3N_4 mixed powder suspension. The casting, drying, and heat-treatment procedures were identical to those used for the Series III composite powder compacts.

The batch 3 SiO_2 powder suspension was used to slip-cast disk-shaped compacts (~2-3 mm thick and ~19 mm diameter) for isothermal densification experiments.

3.4.2. Characterization of Green Compacts

Some of the pre-sintered samples were saturated with deionized water by placing in a boiling water bath for ~2 h and the bulk densities and open porosities of these samples were determined by the Archimedes displacement method.

Some of the pre-sintered (800°C) compacts were characterized by mercury porosimetry[51] to obtain pore-size information. The distribution of pore channel radii was determined by applying the Washburn equation [Ree88]:

$$R = -2\,\gamma \cos\theta / P \qquad (3.34)$$

where, R is the pore channel radius (in m), γ is the mercury surface energy (4.84 x 10^{-1} J/m^2), θ is the contact angle (140°), and P is the pressure (in Pa). The total volume percent of porosity, V_p, was obtained using the relation:

$$V_p = V_i / (W/\rho + V_i) \bullet 100 \qquad (3.35)$$

where W is the weight of the sample, V_i is the intruded volume, and ρ is the theoretical density of the powder. The powder densities of SiO_2 (heated to 800°C) and Si_3N_4 have been determined to be 2.20 g/cm^3 [Sac84a] and 3.19 g/cm^3 [Bag92], respecovely, by helium

[51] Model Autoscan 60, Quantachrome Corp., Syosset, NY

pycnometry These values were used to estimate by linear extrapolation, the theoretical densities for samples with different SiO_2/Si_3N_4 volume ratios

3.5 Sintering

The Series I powder and the ~60 vol% SiO_2 + ~40 vol% Si_3N_4 mixed powder compacts were sintered in an alumina tube furnace[52] in flowing (~50 cm^3/min) nitrogen One compact of each type was placed on an alumina sample holder and they were heated (together) sequentially at temperatures of 1000 1100 1200, 1250, 1275, 1300 and 1400°C The heating rate used was 10°C/min and the samples were held at the sintering temperature for 2 h. For isothermal sintering experiments, two similar compacts were heated together sequentially for different intervals of time, at 1300°C For each heat treatment, the heating rate used was 10°C/min and the total sintering time after a given sintering experiment was determined as the sum of the isothermal hold times used in all the experiments conducted to that point. Compact densities were determined by the Archimedes displacement method, as described in Section 3 4 2

The pre-sintered Series II disk-shaped compacts (prepared both with and without PS additions) were sintered in a tube furnace[53] in flowing (~60 cm^3/min) nitrogen at temperatures in the range 1000 1400°C for 2 h The pre-sintered bar shaped samples with and without the PS-derived pores were sintered under the same conditions for 2 h at 1250 and 1300°C, respectively One disk sample containing PS-derived pores (prepared with a composite powder/PS volume ratio of 84/16) was sintered for 2 h at 1250 °C. The bulk

[52] Netzsch STA409 Exton, PA
[53] Model 64259 Lindberg Co. St. Watertown, WI

density, apparent density, and open porosity values were determined on these samples using the Archimedes displacement method with deionized water as the liquid medium (as described earlier). Some measurements involved using ethanol or methanol as the medium. In such cases, samples were saturated for ~30 min with the liquid using vacuum impregnation. Total porosity was determined assuming a powder true density of 2.60 g/cm^3 for the 60/40 composite powder (see Section 4.3.1 for details). Closed porosity values were determined by subtracting the open porosity from the total porosity.

The batch 1 SiO_2 samples containing the PS-derived pores were heated in static air in a box furnace[54]. The samples prepared with overall SiO_2 powder to PS powder volume ratios of 95/5 and 85/15 were heated (heating rate ~10°C/min) for 24 h at 1150°C, and 2 h at 1100°C, respectively.

Constant-heating-rate (CHR) experiments were performed on pre-sintered Series III rod samples using a dilatometer[55] with a vertical alumina push-rod assembly (Figure 3.8).

The sample was placed between two small (~10 mm dia. x ~1 mm thick disks) pieces of dense alumina[56] and clamped between the push rod and the base of the mullite muffle. The weight of the push rod was balanced by the counterweight such that there was almost no load applied on the sample. The sample and the push rod assembly were enclosed in a mullite muffle which was isolated from the graphite furnace (heated by graphite heating elements). The mullite muffle and the furnace were individually evacuated.

[54] Model DT 31, Deltech, Inc.–Denver, CO.
[55] Unitherm Model 1251, Anter Corp.–Pittsburgh, PA.
[56] Disk-shaped (~12 mm dia. x ~2 mm thick) samples were slip-cast from well-dispersed (pH~4.8), concentrated (~35 vol% solids) suspensions of alumina (RCHP grade, Reynolds Corp.). The samples were sintered at 1500°C for 2 h in ambient atmosphere. They were then mounted on to a lapping fixture and ground plane-parallel (within ~±5% thickness variation).

(to ~100 μm Hg) using a mechanical vacuum pump[27]. The two regions were then purged for ~5 min with nitrogen and argon, respectively. This procedure was carried out three times to insure that no air remained in either region. The outlet pressures and flow rates of the two gases were then adjusted to ~1 psi and ~60 cm^3/min, respectively, and allowed to equilibrate for ~30 min.

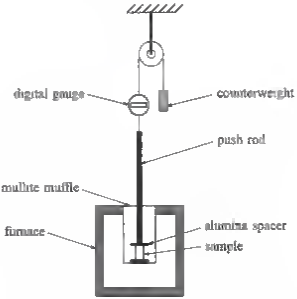

Figure 3.8 Configuration for dilatometry experiments.

The temperature of the sample was raised to 600°C in 15 min and held at that temperature for 10 min. Thereafter, one or more of three different heating rates, viz., ~6°C/min, ~11°C/min, and ~19°C/min were used to increase the temperature from ~600°C to ~1500°C. The experiments were terminated (i.e., the power to the furnace was cut) when

[27] Model Maxima D16A, Fisher Scientific, Fair Lawn, NJ

the temperature reached 1500°C. The axial displacement in the sample was measured in situ by means of a digital displacement gauge that had a least count of 0.001 mm (1 μm).

The thermal expansion of the alumina assembly was calibrated by reference runs using a dense sapphire[56] sample with similar dimensions (~6.5 mm dia. x ~12.5 mm length) as the test samples. Three reference runs were carried out for each heating rate and the plots of axial displacement vs. temperature were fitted (by the dilatometer software) to fourth order polynomial equations, i.e., of the form $Y = a_0 + a_1X + a_2X^2 + a_3X^3 + a_4X^4$, where Y is the expansion and X is the temperature. Each of the five coefficients (a_0 through a_4) obtained from the three runs were averaged. These coefficients were subtracted from book value coefficients (i.e., the standard values for the sapphire sample) to obtain the corrected coefficients. During the CHR experiments, the displacement of the test sample and the corresponding sintering temperature was recorded at intervals of 1 min. The system expansion was calculated at each temperature by using the corrected coefficients in the polynomial equation. This value was then subtracted from the measured displacement to obtain the corrected sample displacement. Measurements were carried out at ~11°C/min for pre-sintered Series III 30/70, 40/60, 50/50, and 60/40 composite powder compacts. Two independent samples were used for each composition and the average data was obtained by calculating the mean of the individual sample displacement values at each temperature. Measurements were also carried out at ~6 and ~19°C/min, respectively, for the 60/40 compacts. For these experiments, only one sample was used for each heating rate.

[56] Standard sample NBS SRM 732

The density of the samples was calculated from the displacement data using the following procedure Archimedes method (with deionized water as the medium) was used to determine the initial composite bulk density (i.e. green density), ρ_{cb} , and the final composite bulk density (after cooling to room temperature) ρ_{cf} The axial strain at any instant during the heat treatment is equal to $\Delta L/L_o$ where L_o is the initial sample length, and $\Delta L = L_o - L$, where L is the instantaneous sample length (ΔL is directly measured during dilatometry) The bulk density of the composite, ρ_c, at any instant can be calculated (assuming a right cylinder geometry) using the equation,

$$\rho_c = \rho_{cb} \left(1 - \frac{\Delta R}{R_o}\right)^2 \left(1 - \frac{\Delta L}{L_o}\right) \tag{3.36}$$

where R_o is the initial sample radius, and $\Delta R = R_o - R$, where R is the instantaneous sample radius It has been observed in various investigations [Rah87, Rah90, Dut92] that the axial and radial shrinkages are related by the expression,

$$\frac{\Delta R}{R_o} = k \frac{\Delta L}{L_o} \tag{3.37}$$

where k is a constant for a given experiment. The value of k can be obtained from $\Delta R/R_o$ and $\Delta L/L_o$ values measured at the end of the sintering experiment. Some workers [Rah90, Dut92] have performed intermittent sintering runs to measure axial and radial dimensions at various stages of sintering. The values obtained from these measurements have been used to check the linearity described in Eq. (3.37) and calculate the value of k. Though the value of k for a freely sintering body (pressureless sintering) has been observed to be almost 1,

significant deviations from unity are evident in samples sintered under a uniaxial stress [Dut92]. However, the linearity described in Eq. (3.37) was still maintained.

Table 3.7 lists the k values obtained for the dilatometery samples. The k values lie in the narrow range of 0.84 - 0.89 for the sintering experiments. Anisotropic shrinkage with k<1 is generally observed for samples subjected to a compression load (since the radial shrinkage is opposed by the expansion associated with creep). In order to check if the anisotropy in the current study was due to the load exerted by the push rod on the samples, two 60/40 samples were sintered in a tube furnace[39] and the k values for these samples are shown in Table 3.8.

Table 3.7 Calculated k Values for Samples Used for Dilatometry

SiO_2/Si_3N_4	Heating Rate (°C/min)	L_o (mm)	L_f (mm)	R_o (mm)	R_f (mm)	$\frac{\Delta L}{L_o}$	$\frac{\Delta R}{R_o}$	k
30/70	~11	11.17	10.38	5.79	5.43	0.071	0.062	0.88
30/70	~11	11.03	10.26	5.81	5.45	0.070	0.062	0.89
40/60	~11	10.57	9.36	5.77	5.10	0.114	0.102	0.89
40/60	~11	10.67	9.46	5.76	5.10	0.113	0.101	0.89
50/50	~11	11.68	9.84	5.73	4.93	0.158	0.140	0.89
50/50	~11	10.81	9.03	5.75	4.93	0.165	0.143	0.87
60/40	~11	11.11	9.21	5.66	4.85	0.171	0.143	0.84
60/40	~11	11.50	9.55	5.67	4.85	0.170	0.145	0.85
60/40	~7	11.96	9.98	5.69	4.87	0.166	0.144	0.87
60/40	~19	12.02	10.04	5.65	4.84	0.165	0.143	0.87

[39] Model 64259, Lindberg Co., Watertown, WI

Table 3 8 Calculated k Values for 60/40 SiO_2/Si_3N_4 Samples Sintered to 1200°C in a Tube Furnace

SiO_2/Si_3N_4	Heating Rate (°C/min)	L_o (mm)	L_f (mm)	R_o (mm)	R_f (mm)	$\frac{\Delta L}{L_o}$	$\frac{\Delta R}{R_o}$	k
60/40	~10	10.50	9 40	5 74	5 20	0 105	0 094	0 90
60/40	~10	9 60	8 65	5 72	5 22	0 099	0 087	0 88

Table 3.8 shows that the k values for the "free" sintering experiment were also <1 and were comparable to the values in Table 3 7 Therefore it was concluded that the slight anisotropy observed in the current investigation was probably due to a combination of viscous deformation under self-weight and any anisotropy that may exist in the green microstructure (e g , due to orientation of the particles which are relatively less equiaxed, lower packing density along the axial direction compared to the radial direction, etc).

It follows from eqs. (3.36) and (3 37) that the density of the composite is

$$\rho_c = \rho_{cti} (1 - k\frac{\Delta L}{L_o})^{-2} (1 \quad \frac{\Delta L}{L_o})^{-1} \tag{3 38}$$

Some theoretical treatments define a relative density of the matrix, ρ_m, as the ratio of the mass of the matrix phase to the sum of the volumes of the matrix and pore phases divided by the matrix powder true density In other words, it is assumed that all the porosity is associated with the matrix alone and that the inclusions are completely dense. The value of ρ_m at any time can be expressed as [Rah87a]

$$\rho_m = \frac{(\rho_{cti} - \rho_i f_o)\rho_c}{(\rho_{cti} - f_o\rho_c)} \tag{3.39}$$

where f_0 is defined as the volume fraction of the inclusion in the green compact and ρ_c is the density of the inclusion phase. The densification rate of the matrix, ρ_m is then obtained by analytically differentiating the expression in eq. (3.39) and can be written as

$$\rho_m = \rho_{m0}\rho_c \frac{(\rho_{c0} - f_0\rho_c)}{(\rho_{c0} - f_0\rho_c)^2} \qquad (3.40)$$

From eqs. (3.39) and (3.40), the volumetric strain rate of the matrix is

$$\frac{\dot{\rho}_m}{\rho_m} = \frac{\dot{\rho}_c}{\rho_c} \frac{\rho_{c0}}{(\rho_{c0} - f_0\rho_c)} \qquad (3.41)$$

As the pore phase reduces during sintering, the volume fraction of the inclusions, f, increases. Usually the volume fraction of the inclusions is calculated on the basis of the fully dense composite, denoted here by F. The instantaneous volume fraction of inclusions, f, at any matrix bulk density ρ_m is related to F by the equation [Rah87a]

$$f = \rho_m \left[\rho_m + \rho_{mt}\frac{(1 - F)}{F}\right]^{-1} \qquad (3.42)$$

where ρ_{mt} is the powder true density of the matrix.

Relative density values were calculated by dividing the bulk density values by the appropriate powder true density. The procedure used to determine powder true densities will be described in Section 4.3.2. Densification rates were calculated from the relative densities (ρ) as follows. Since shrinkage data was collected at intervals of 1 min, the corresponding relative density data was also calculated at the same intervals of time. The densification rate, $\frac{d\rho}{dt}$ (min^{-1}), was calculated by simply taking the difference between the adjacent density values and dividing by unity (or 1 min), i.e., no curve-fitting or

analytical differentiation was necessary The densification rate was converted to s^{-1} units prior to activation energy calculations.

The Arrhenius equation for the densification rate $\frac{d\rho}{dt}$, of green compacts can be expressed as,

$$\frac{d\rho}{dt} = A\ f(\rho\ G)\ \frac{e^{-Q/RT}}{T} \qquad (3\ 43)$$

where $f(\rho,G)$ is a function of density ρ and particle (or grain) size G, Q is the activation energy, R is the gas constant (8 314 J/mol•K) T is the absolute temperature, and A is a material parameter that is independent of T or ρ For amorphous matrices with a constant starting particle size, the term describing the dependence on particle size can be neglected and hence eq (3 43) reduces to,

$$\frac{d\rho}{dt} = A\ f(\rho)\ \frac{e^{-Q/RT}}{T} \qquad (3\ 44)$$

where $f(\rho)$ is a function only of density Taking logarithms of each side of eq (3 41), we obtain,

$$\ln\left(T\frac{d\rho}{dt}\right) = \ln A + \ln\left[f(\rho)\right] - \frac{Q}{RT} \qquad (3\ 45)$$

A plot of $\ln\left(T\frac{d\rho}{dt}\right)$ vs $\frac{1}{T}$ would be a straight line with a slope of -Q/R, provided that data points at constant ρ are used

The following pre-sintered disk samples were used for isothermal sintering studies SiO_2 batch3 compacts ~85 vol% SiO_2 + ~15 vol% Si_3N_4 mixed powder compacts, and Series III composite powder compacts Experiments were carried out in 1225°C in a

flowing (~60 cm^3/min) nitrogen atmosphere using a horizontal alumina tube furnace[60]. Prior to the sintering experiments, the temperature profile in the furnace was determined. The furnace was heated at 5°C/min to 1225°C and equilibrated for 1 h. Temperature readings were collected at different points in the furnace using a Type B (Pt -30% Rh / Pt - 6% Rh) thermocouple. The thermocouple was held at each point for ~3 min before recording the temperature. Figure 3.9 shows the measured temperature profile in the furnace tube. Since one end of the furnace was placed only 6 inches from a wall, it did not allow measurements on both sides of the center and therefore the plot in Figure 3.9 only shows the profile on one side. However, the sample loading and unloading was done from the same half of the tube wherein the temperatures were actually measured. Figure 3.9 (see inset plot) shows that the temperature across the tube was uniform (1223 ± 2°C) over a 2 inch distance. It was assumed that the temperature profiles were nearly symmetrical about the center so that the temperature was presumed to be uniform in a 4 inch range in the center of the tube. The samples were centered on the porous alumina substrate and the substrate was placed at the center of the tube during sintering. Since the samples occupied a maximum of only ~2.5 inch length, the sample temperature was expected to be uniform.

The "gas-inlet" end of the furnace was first sealed using a brass endcap and the nitrogen gas flow was set to ~60 cm^3/min using a flowmeter. The green samples were then arranged on the porous alumina substrate and the substrate was placed in the "gas-outlet" end of the furnace. This end was sealed using another brass endcap with a vacuum fitting[61]. A quartz (fused silica) rod was passed through this fitting such that it served as a pushrod

[60] Model 64259, Lindberg Co., St. Watertown, WI
[61] Ultratorr 1/8", Jax Valve and Fitting Co., Jacksonville, FL

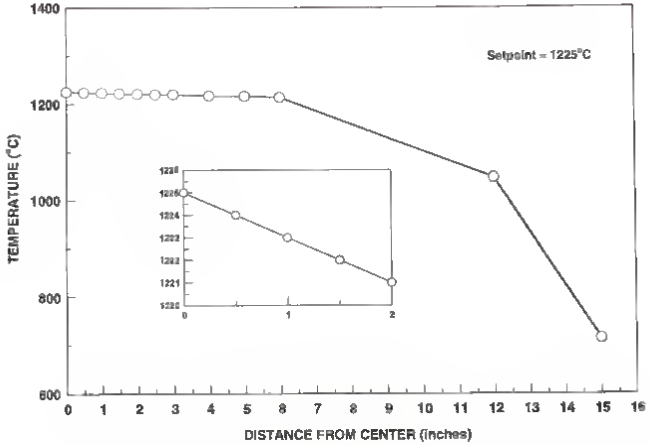

Figure 3 9 Temperature profile in the tube furnace used for isothermal sintering experiments Inset shows the region up to 2 inches from the center

for loading and unloading samples. The furnace was then heated to 1225°C and allowed to equilibrate for ~1 h. The substrate was pushed to the ~800°C point (~14 inches from the center, see Figure 3.9) within the tube and allowed to soak for ~2 min after which it was rapidly (in <10 s) inserted into the center of the tube. A digital stopwatch was used to accurately record the sintering time. After the sintering time had elapsed, the substrate was rapidly removed to the ~800°C point and after an additional ~1 min, it was withdrawn to the cool end of the tube. The furnace was then shut down and the samples were removed from the furnace tube when the furnace center had cooled to below ~300°C.

3.6 Microstructural Characterization

To study the microstructural features of sintered compacts and creep tested samples, polished sections were prepared by the following procedure. Small representative specimens were obtained by cutting the samples with a precision saw[42]. These samples were then glued with a commercial adhesive[43] to the bottom (the side to be polished facing down) of 20 ml glass vials[44] that were ~20 mm in diameter. A mixture of methyl methacrylate (MMA) monomer and methyl propionitrate (initiator) was prepared in the ratio of 5 ml monomer to 9 mg of initiator. The mixture was stirred for 5 min to ensure complete dissolution of the initiator in the monomer. This mixture (3 ml) was poured into the vials. The vials were sealed with a plastic cap lined with aluminum foil and placed in a convection oven at 65°C. After ~6 h, the monomer was completely polymerized (to PMMA) resulting in solid hard mounts. The vials were removed from the oven and ~5 ml

[42] Isomet, Buehler Ltd. Lake Bluff IL
[43] Super Glue, Loctite Corp. Cleveland, OH
[44] Fisher Scientific, Fair Lawn, NJ

of Quickmount[65] solution was added into each vial. The Quickmount solution solidified in ~1 h at room temperature after which the vials were broken to release the sample mounts. It is noted that PMMA infiltration was used to allow polishing of porous samples. For highly dense samples (i.e., with relative density >95%), the specimens were directly mounted using ~8 ml Quickmount solution (i.e. PMMA was not used).

The mounted samples were ground with SiC powder slurries on glass plates. The following grit sizes of powders were used in succession: 120, 180, 240, 320, 400, 600, and 1000. After fine grinding, samples were polished using an automatic polisher containing an iron oxide / silica suspension[66] on a polishing grade cloth[67]. The polishing step was typically carried out for 1-3 days. After polishing, the samples were cleaned in an ultrasonic cleaner with deionized water. Some of the polished samples were etched by dipping into a freshly prepared 0.5% HF solution for 2-3 min. (It was very important to carry out the etching prior to PMMA removal since the silica surrounding the pore regions tended to be over-etched if the pores were not infiltrated by PMMA.) The mounts were then placed in an oven at 200°C for 30 min to soften the mounts. Samples were removed from the mounts with a tweezer and the mounts were discarded. Finally, the samples were slowly (~5°C/min) heated to 600°C for 6 h in a box furnace[68] to remove the PMMA.

The polished sections were then cleaned in the ultrasonic cleaner with acetone and rinsed with deionized water. The samples were mounted on aluminum SEM specimen holders using thick carbon slurries[69]. All samples were coated with a thin gold-palladium

[65] Fulton Metallurgical Products Corp. Sassenburg, PA
[66] MasterPolish II, Buehler Ltd. Lake Bluff IL
[67] Pelanet, Buehler Ltd. Lake Bluff IL
[68] Model DT 31, Deltech, Inc. Denver CO
[69] #14825 Low resistance contact cement, Ernest F. Fullam, Latham, NY

coating prior to observation in the SEM. For quantitative microscopy, a minimum of 12 micrographs (scanned over the entire cross-section) were taken for each sample. Negatives of each micrograph were used to obtain enlarged (8.5 in. x 11 in.) prints for better accuracy during microstructure characterization.

Standard techniques [Deh68] of quantitative microscopy were used to obtain quantitative values of volume fraction of phases (i.e, porosity, SiO_2, and Si_3N_4) and average Si_3N_4 intercept sizes on selected sintered samples. A transparent plastic sheet with a 10 x 10 square grid (100 intersecting points) was overlaid on the enlarged prints. Points intersecting the different phases were counted. A total of of 25 - 40 different fields were measured. The average point fraction equals the volume fraction of the corresponding phase in the sintered sample.

A transparent plastic sheet with equally spaced parallel lines was overlaid on the enlarged prints. The length of every Si_3N_4 particle intercept was measured using a digitizing tablet interfaced with a personal computer[79]. Average Si_3N_4 particle intercept sizes were determined from the digitized measurements. A minimum of 600 intercept sizes were measured.

3.7 Physical Property Measurements

3.7.1 Dielectric Properties

Dielectric properties (dielectric constant and loss tangent) measurements were carried out on sintered samples described in Section 3.5.2 (0.8 – 1.5 mm thick). Table 3.9

[79] Model H-P 86, Hewlett-Packard

lists the results from Archimedes density measurements (using deionized water as the medium) for these samples. The "dense" and "porous" SiO_2 samples correspond to those prepared with overall SiO_2 (batch 1) powder to PS powder volume ratios of 95/5 and 85/15, respectively (sintered at 1150°C and 1100°C respectively). The "dense" and "porous" 60/40 samples correspond to compacts prepared with overall 60/40 SiO_2/Si_3N_4 (Series II) powder to PS powder volume ratios of 100/0 and 84/16, respectively (sintered at 1300°C and 1250°C, respectively).

Table 3.9 Archimedes Density Results for Samples Used in Dielectric Measurements.

Sample	ρ_{bulk} (g/cm^3)	Open Porosity (%)	$\rho_{apparent}$ (g/cm^3)	Relative Density (%)	Closed Porosity (%)
Dense SiO_2 #1	2.193	0.1	2.195	99.7	0.2
#2	2.194	0.2	2.198	99.7	0.1
Porous SiO_2 #1	2.008	0.4	2.016	91.3	8.3
#2	2.010	0.2	2.014	91.4	8.4
Dense 60/40 #1	2.601	0.0	2.601	100.0	0.0
#2	2.600	0.1	2.603	100.0	0.0
Porous 60/40 #1	2.360	0.4	2.369	90.4	9.2
#2	2.352	0.6	2.366	90.1	9.3

Samples were mounted on to a lapping fixture [Ran93] and polished plane parallel (<5% thickness variation) using aqueous SiC slurries in successive steps from 120 grit through 1000 grit. Prior to the measurements, samples were washed with acetone in an ultrasonic bath to remove alkali impurities[7] and water. The samples were then dried in a

[7] Alkali ions (singly charged) are highly mobile and therefore, their presence typically results in increased dielectric constant. The high mobility also leads to high DC conductivities which increases dielectric losses [Kin76]. Therefore, extreme caution was exercised during handling and processing to avoid alkali contamination (for e.g., use of gloves to prevent any contact with the skin which contains alkali ions).

vacuum oven at 100°C for ~ 24 h to remove the solvent and stored under vacuum in a desiccator The mean thickness of each sample was obtained by averaging 10 micrometer measurements

Dielectric measurements were carried out using a dielectric test fixture[72] (adapted for samples with ~10 mm diameter) attached to an LF impedence analyzer[73] A non-contacting electrode method [Hpp89] was used to measure the capacitance and loss tangents of the samples. The schematic electrode structure for this method is given in Figure 3.10

Figure 3 10 Schematic electrode structure for the non-contacting method for dielectric constant measurements

The relative dielectric constant (ε_r) and the loss tangent ($D = \tan \delta$) values for the test sample were obtained from the following equations [Hpp89]

$$\varepsilon_r = [1 - (1 - C_{s1}/C_{s2})(t_g/t_a)]^{-1} \quad (3\ 46)$$

and

$$D = D_2 + (\varepsilon_r)(D_2 - D_1)(t_g/t_a - 1) \quad (3\ 47)$$

where

C_{s1} = Series capacitance when the sample is not inserted (F)

[72] Model HP 16451B, Hewlett Packard Tokyo Japan
[73] Model HP 4192A, Hewlett-Packard, Tokyo, Japan

D_1 = dissipation factor when the sample is not inserted
t_s = average sample thickness (m)
C_{s2} = Series capacitance when the sample is inserted (F)
D_2 = dissipation factor when the sample is inserted
t_g = gap between the electrodes ≈ 10% of t_s (m)

Four independent capacitance measurements were made at each frequency. Relative dielectric constant values were determined at five frequencies- 1 1kHz, 10kHz, 100kHz, 1MHz, and 10MHz. Loss tangents (tan δ) values were collected at 1 MHz. (The values at other frequencies were found to be negative; i.e., out of the measurement range for the instrument)

3.7.2. Flexural Strength

Average flexural strength values were determined on 8-10 samples having dimensions of ~25 mm x ~5 mm x ~2 mm. Table 3.10 lists the results from Archimedes density measurements (using deionized water as the medium) for selected samples of each composition used for strength evaluation. The "dense" SiO_2 samples correspond to those prepared with overall SiO_2 (batch 1) powder to PS powder volume ratio of 95/5 (sintered for 24 h at 1150°C). The 'dense' and 'porous" 60/40 samples correspond to compacts prepared with overall 60/40 SiO_2/Si_3N_4 (Series II) powder to PS powder volume ratios of 100/0 and 88/12, respectively (sintered at 1300°C and 1250°C, respectively).

The faces of the bend test specimens were first ground with SiC powder[4] slurries on glass plates. The following grit sizes of powders were used in succession: 240, 320, 400, 600, and 1000. Minimal pressures were applied on the samples in order to minimize any

[4] Buehler Ltd. Lake Bluff, IL

damages/stresses introduced during the grinding steps After fine grinding, the faces were polished using aqueous ~0 3 μm γ-alumina slurry[35] and the tensile edges were beveled to eliminate stress concentrations and any large edge defects arising from the grinding steps.

Table 3 10 Archimedes Density Results for Samples Used in Strength Measurements

Sample	ρ_{bulk} (g/cm^3)	Open Porosity (%)	$\rho_{apparent}$ (g/cm^3)	Relative Density (%)	Closed Porosity (%)
Dense SiO_2 #1	2 198	0 1	2 200	99 9	0 0
#2	2 196	0 1	2 198	99 8	0 1
Dense 60/40 #1	2 600	0 1	2.603	100 0	0 0
#2	2 602	0 0	2.602	100 0	0 0
Porous 60/40 #1	2.380	0 1	2 382	91 5	8 4
#2	2 377	0.2	2.382	91 4	8 4

Flexural strength values were determined by performing four-point bend tests using a materials testing apparatus[36] The specimens were loaded by two bearings which were located 5 mm away from the outer two support bearings which were 20 mm apart (Figure 3 11). A cross-head speed of 0.5 mm/min was used and the load-displacement data was recorded at intervals of 0.5 *s* In order to prevent surface damage due to gauging dimension measurements were carried out after the failure of the specimens The formula [Mil83] used for the calculation of the flexural strength, σ_f (in MPa) was

$$\sigma_f = 3 F_f \cdot L / 4 w \cdot t^2 \qquad (3\ 48)$$

where F_f = fracture load (N)
L = outer span = 20 mm
w = specimen width (mm)

[35] Micropolish 3 Buehler, Lake Bluff IL
[36] MTS Systems Corp Eden Prairie, MN

t = specimen thickness (mm)

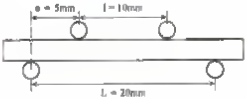

Figure 3 11 The four-point bend test fixture configuration

3.7.3. Hardness and Toughness

Vicker's hardness measurements were performed using a micro-hardness tester[77] under a load of 500 g for 20 seconds. Samples were polished using an aqueous ~0 3 μm γ-alumina slurry and cleaned with ethanol before the measurements Fracture toughness values were determined using the method developed by Anstis et al. [Ans81] The equation used to relate the elastic modulus, hardness, indentation load and crack length to fracture toughness, K_{Ic} (in $MPa \cdot m^{1/2}$) is

$$K_{Ic} = \psi (E/H)^{1/2} (P/c_0^{3/2}) \qquad (3\ 49)$$

where
ψ = constant = 0 016[78]
E = Young s modulus (GPa)
H = Vicker s Hardness (GPa)
P = indentation load = 4 905 x 10^{-6} MN
c_0 = equilibrium crack length (m)

[77] Micromet, Buehler Ltd

[78] Anstis et al [Ans81] equated the indentation toughness values of a variety of monocrystalline, polycrystalline, and amorphous ceramic materials (designated as "reference" serum us) to those measured by conventional means. Accordingly a value of α = 0 016± 0 004 was obtained by averaging over the data corresponding to these materials.

The crack generated by the indentations were sufficiently long (~2 times the indent size) for the validity of this equation [Ans81] It is noted that eq (3 49) implicitly predicts that the indentation fracture parameter, $P/c_o^{3/2}$ is independent of the indentation load. Although this was not directly confirmed in the current study, it has been established by Anstis et al [Ans81] that within experimental error $P/c_o^{3/2}$ was invariant with respect to load for various glasses, glass-ceramics, and crystalline ceramic materials

The E/H ratio in Eq 3 49 was determined from Knoop indentation measurements (indentor geometry schematically illustrated in Figure 3 12) using the relation [Mar82]

$$b'/a' = b/a - \alpha\,(H/E) \qquad (3\ 50)$$

where a', b' = diagonal indent dimensions
a, b = diagonal indentor dimensions
b/a = 1 / 7 11 from indentor geometry
α = dimensionless constant = 0 45

Figure 3 12 Schematic illustrating the Knoop indentor geometry

Some of the tested specimens were etched with dilute (~2 wt%) hydrofluoric acid solution for 10 – 30s to observe the crack paths using SEM

3.8 Compression Creep Measurements

Compression creep experiments were performed on sintered rod samples Prior to sintering, the top surface of the pre-sintered (800°C) composite powder compacts were

ground flat by gently grinding on a 600 grit SiC polishing paper[79]. However, the 85/15 pre-sintered samples tended to crack during the grinding due to inadequate green strength. Therefore, such samples were heated further to 1150°C for 2 h to provide the additional handling strength necessary for the machining operation. The 60/40 and 85/15 samples were then sintered to 1300°C for 2 h. The 30/70, 40/60, and 50/50 samples were sintered to 1400°C for 2 h. As described in Section 3.4, the SiO_2 compacts were sintered in static air at 1175°C for 24 h. Table 3.11 summarizes the thermal histories of all the samples used for the creep experiments.

Table 3.11 Thermal Histories of Samples Used for Compression Creep Experiments.

Sample	Powder Batch	Heat treatment(s)* prior to machining	Sintering Schedule*
SiO_2	Batch 2	15°C/h-700°C-6 h-static air	10°C/min-1150°C-24 h-static air
30/70	Series III	2°C/min-800°C-2 h-nitrogen	10°C/min-1400°C-2 h-nitrogen
40/60	Series III	2°C/min-800°C-2 h-nitrogen	10°C/min-1400°C-2 h-nitrogen
50/50	Series III	2°C/min-800°C-2 h-nitrogen	10°C/min-1400°C-2 h-nitrogen
60/40	Series III	2°C/min-800°C-2 h-nitrogen	10°C/min 1300°C-2 h-nitrogen
85/15	Series II	2°C/min-750°C-2 h-nitrogen + 10°C/min-1150°C-2 h nitrogen	10°C/min-1300°C-2 h-nitrogen

* Notation: (heating rate)-(setpoint temperature)-(dwell time at setpoint)-(atmosphere)

Creep behavior was determined by performing constant load compression tests on sintered samples using an MTS testing apparatus[80]. Steady-state creep rates, $\dot{\varepsilon}$, were

[79] Buehler Ltd., Lake Bluff, IL.
[80] MTS Systems Corp., Eden Prairie, MN.

determined as functions of stress, σ, in the range of 10 - 300 MPa by successively increasing the load on each sample. Experiments were carried out at temperatures in the range of 950-1325°C in argon atmospheres. Stress exponents, n, and the activation energies, Q, were determined from the data using the phenomenological relationship [Fer92]

$$\dot{\varepsilon} = A\left(\frac{\sigma}{G}\right)^{n} \exp\left(-\frac{Q}{RT}\right) \qquad (3.51)$$

where G is the shear modulus, R is the gas constant, T is the absolute temperature, and A is a constant with the units of inverse time.

The compression creep test configuration is shown in Figure 3.13. The sample was placed between two small square (~5 mm x 5 mm) pieces of grafoil[8] and clamped between two SiC platens such that the initial load was 5-10 lbs. The furnace chamber was evacuated (to ~100 microns vacuum) and backfilled with argon. This was carried out three times in order to remove any residual air in the chamber. The furnace was then heated to the test temperature at a rate of ~20°C/min and allowed to equilibrate for ~30 min. It is noted that the load was maintained constant (by using the "load control" setting on the instrument) during the heating and equilibration steps. Experiments were carried out under different compressive stresses by successively increasing the load on the sample at 5 lb/s and maintaining the load until steady state (explained later in the section) is attained. The axial displacement was recorded as a function of time at intervals of 30 or 60 s.

[8] UCAR, Cleveland, OH

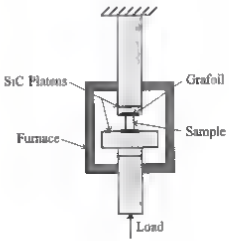

Figure 3.13 The compression creep test configuration

The engineering creep stress (s) and the engineering creep strain (e) can be expressed as [Tim70]

$$s = P / A_o \tag{3.52}$$

$$e = \Delta L / L_o \tag{3.53}$$

where P = compressive load

A_o = initial cross-sectional area of the specimen

$= \pi D_o^2 / 4$, for rod-shaped samples where,

D_o is the initial diameter of the specimen

or $w_o \bullet t_o$, for bar-shaped sample where,

w_o and t_o are the width and thickness, respectively

L_o = initial length of the specimen

ΔL = axial displacement

Assuming that the sample is incompressible[82] (i.e., there is no volume change during creep), the true compressive stress (σ) and the true compressive strain (ε) can be calculated using the following relations [Tim70]

[82] The porous 36/70, 40/60 and 50/50 composite compacts underwent some densification during the creep experiments. In such samples, the actual cross-sectional area was slightly higher and therefore the predicted stresses were slightly lower. However, as will be explained in Section 4.3.5, the densification strains are insignificant compared to the creep strains and hence the error in the calculated stress values is negligible.

$$\sigma_T = (1 - e)\sigma_E \tag{3.54}$$

$$\varepsilon = \ln (1 - e) \tag{3.55}$$

Eqs (3.52) - (3.55) were used to derive true stress and true strain values from the axial displacement data. Strain rates ($\dot{\varepsilon}$) were determined by calculating slopes of straight lines fitted to the steady-state portion of the displacement vs. time plots. The arithematic average stress over this range was used in the strain rate vs. stress plots.

A typical calculation procedure is illustrated by using the results obtained for a ~50/50 SiO_2/Si_3N_4 sample which was tested at 1250°C. Figures 3.14 and 3.15 show the plots of displacement vs. time and creep strain vs. time, respectively, for this sample. During the creep tests, temperature variations of up to ± 2°C were typically observed. These variations would lead to fluctuations in the measured displacement due to the differences in the thermal expansion coefficients of the SiC platens and the sample. The scatter in the data in Figure 3.15 may be attributed to this phenomenon. As seen in Figure 3.15, at each load, there are three stages of deformation: (1) an initial elastic stage, corresponding to the relatively rapid increase in strain resulting from the rapid increase in load, (2) an intermediate stage, i.e., the region where a gradual change in slope occurs, which represents a combination of both elastic and creep deformations, and (3) steady-state creep deformation stage, i.e., the region in which the strain increases almost linearly with time. Straight lines were fit to the last 10-15 data points (i.e., in the steady-state region) at each load in order to calculate strain rates. The average stress at each load was determined by the arithematic average of the individual stress values corresponding to these data points. Table 3.12 shows the calculated stresses and strain rates for this sample.

It is important to note that these experiments were carried out under constant-load conditions and not constant-stress conditions. When the sample deforms under a constant compressive load, due to volume conservation, the cross-sectional area increases gradually and this results in a steady reduction in stress. Consequently, the strain rate is

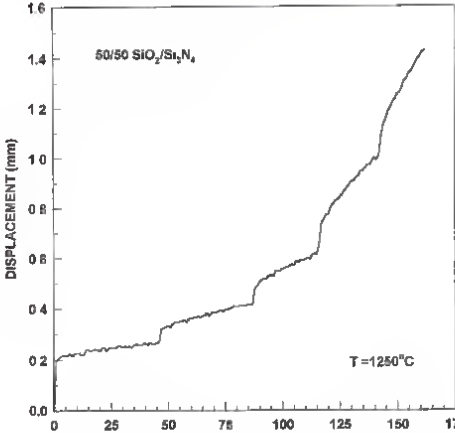

Figure 3.14 Plot of axial displacement vs. time for a 50/50 SiO_2/Si_3N_4 sample tested at 1250°C

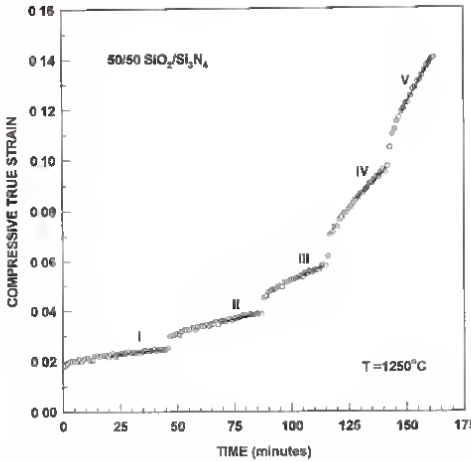

Figure 3.15 Plot of true strain vs time for a ~50/50 SiO_2/Si_3N_4 sample tested at 1250°C. The open circles depict the raw data whereas the solid lines represent the linear curve fit values.

not expected to reach a constant value at a given load However, as shown in Table 3 12, the standard deviation in the stress values are <1% in the range of loads used in this study Therefore it may be reasonable to fit linear curves to the strain vs. time data in order to determine the strain rates

Table 3 12 Strain Rate and Stress Data for a 50/50 Sample Creep-Tested at 1250°C

Strain Rate (s^{-1})	Stress (MPa)
1.34×10^{-6}	18.7 ± 0.0
3.44×10^{-6}	42.4 ± 0.1
6.71×10^{-6}	80.7 ± 0.1
1.66×10^{-5}	153.4 ± 0.6
2.55×10^{-5}	219.9 ± 1.5

CHAPTER 4
RESULTS AND DISCUSSION

4.1 Preliminary Investigations

The results pertaining to some of the preliminary experiments conducted using the Series I composite powders will be presented in this section. The results from the characterization of fractionated Lot1 Si_3N_4 batch 1 SiO_2, and Series I composite powders will be discussed in Section 4.1.1. In Section 4.1.2, the results from sintering experiments conducted to study the effect of spatial distribution of phases on the densification behavior will be described.

4.1.1. Characterization of Particles

Figures 4.1(A) and 4.1(B) show SEM micrographs of the fractionated Si_3N_4 and 60/40 composite powders, respectively. Figures 4.2 (A)-(D) show bright field TEM images of a Lot1 Si_3N_4 core particle and microcomposite particles from Series I powders with overall compositions of 40/60, 60/40, and 85/15, respectively.

At high concentrations (typically > 80 vol%) of SiO_2 in the composite powder, SiO_2 particles were usually observed in addition to the microcomposite particles. This is illustrated by SEM observations (Figure 4.3A) carried out on a Series I 85/15 composite

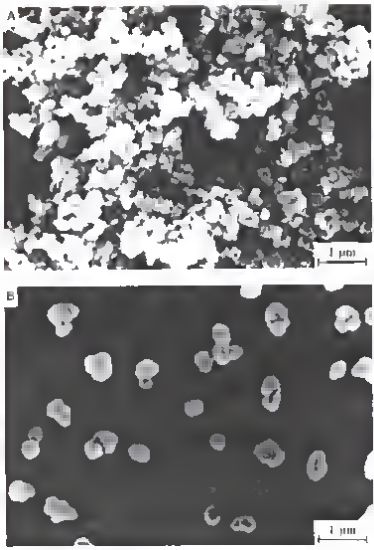

Figure 4.1 SEM micrographs of (A) Lot1 Si_3N_4 powder and (B) 60/40 composite powder

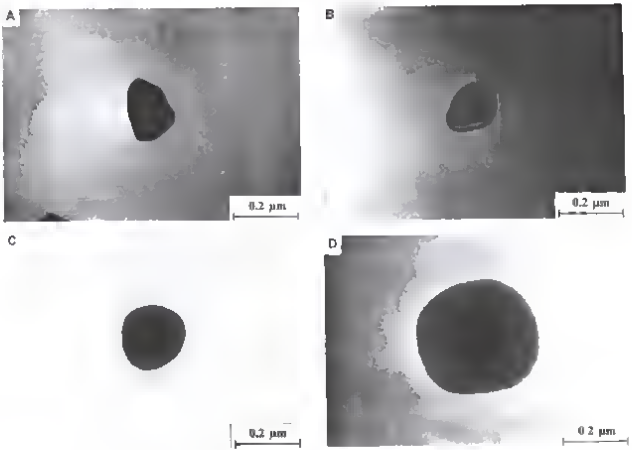

Figure 4.2 Bright-field TEM images of (A) Lot1 Si_3N_4 and (B) 40/60, (C) 60/40, and (D) 80/20 particles

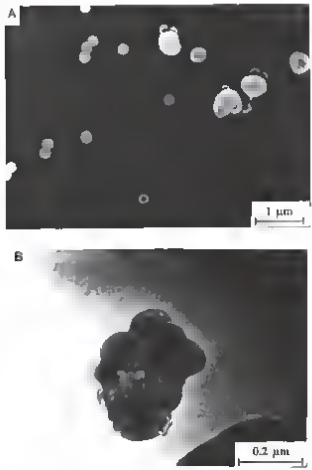

Figure 4.3 Micrographs illustrating problems associated with extreme compositions. (A) SEM of 85/15 powder showing free SnO_2 particles, and (B) bright field TEM image showing coated agglomerates in 30/70 powder

powder samples[83]. The SiO_2 particles have a monosized spherical morphology and, therefore, are easily distinguished from the relatively irregular microcomposite particles (Figure 4.3A). It must be noted, however, such SiO_2 particles were not consistently observed and the reasons for the homogeneous nucleation events are not known. Some sensitivity to the source, exposure to the atmosphere and aging of the TEOS has been observed. However, these factors were not investigated in any detail. Azuma et al. [Azu91] have also reported the formation of discrete SiO_2 particles during the synthesis of SiO_2-coated Fe_2O_3 composite powders using a technique similar to that described in this study. As reported in the current investigation, Azuma et al. [Azu91] observed SiO_2 particles when the concentration of the TEOS was high relative to the concentration of the seed (Fe_2O_3) particles.

During the synthesis of composite powders containing low concentrations (<40 vol%) of SiO_2, some (typically one out of every ~100 particles) large composite particles (typically ~0.3-1.0 μm diameter), each containing two or more core particles, have been observed in the TEM (e.g., Figure 4.3.B). It is not known if these are formed by (a) coating of "hard" or "soft" agglomerates composed of the core particles, and/or (b) agglomeration of individual coated particles.

Figure 4.4 shows a bright field image of a 40/60 microcomposite particle observed under the high-resolution transmission electron microscope (HRTEM). The lattice fringes on the left side of the image correspond to the crystalline Si_3N_4 core particle and the absence of crystal planes in the SiO_2 phase confirms its amorphous nature. The amorphous nature

[83] Two batches of Series I 85/15 powder were synthesized and SiO_2 particles were observed in both these batches. However, it should be noted that for Series II 85/15 powder SEM observations showed that three out of eight batches did not contain any SiO_2 particles. These batches were eventually used for sintering and creep experiments.

Figure 4 4 High resolution trasmission electron micrograph of a 40/60 particle. The lattice fringes on the left side depicts Si_3N_4 while the phase on the right side is amorphous SiO_2

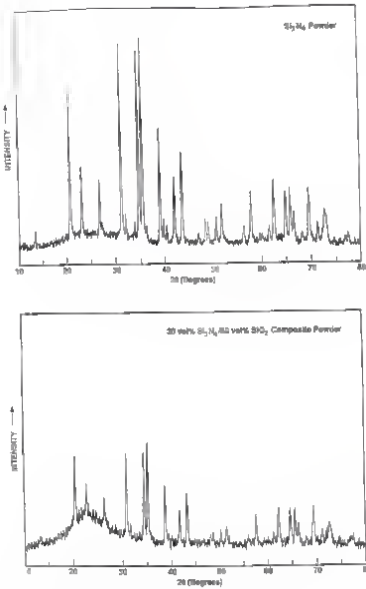

Figure 4.5 X-ray diffraction patterns for Lot1 Si_3N_4 and 80/20 composite powders. The amorphous peak at centered at $2\theta \approx 22^\circ$ is characteristic of amorphous SiO_2

of the coating was also confirmed using X-ray powder diffraction (XRD) analysis. Figure 4.5 shows the XRD patterns of the fractionated Si_3N_4 and 80/20 composite powders. The crystalline peaks in the XRD pattern of the 80/20 powder correspond to α-Si_3N_4 [JCP-pat] and the broad peak centered at $2\theta \approx 22^\circ$ is characteristic of amorphous SiO_2.

The bright field TEM analysis provided some evidence for the complete coverage of the core particle surface with the SiO_2 coating, i.e., no "bare" (uncoated) Si_3N_4 particles were observed. However, the TEM analysis involved a relatively small sampling (~100-200 particles) of the powder sample. Therefore techniques that assess a greater number of particles were necessary to study the surface coverage of the SiO_2 coating. Figures 4.6 and 4.7 show the XPS plots for the Lot1 Si_3N_4 and Series I 60/40 composite powders. Figure 4.8 shows a combination plot for the the two powders, at binding energies in the range of 300 - 600eV. It is clear from Figure 4.8 that both oxygen and nitrogen are evident on the Si_3N_4 surface whereas only oxygen is present on the composite powder surface. In addition to these elements, adventitious carbon was observed in both samples (peaks are shown in Figures 4.6 and 4.7). (It is noted that the secondary peaks adjacent to the main element peaks are satellite peaks which are characteristic of the XPS technique [Bar93].) The origin of the oxygen on the Si_3N_4 may be explained by (a) partial oxidation of the surface[86], and (b) presence of surface hydroxyl groups arising from the fractionation process. The absence of any nitrogen on the microcomposite powder surface suggests that there is complete coverage of the core particles by the SiO_2 coating.

---

[86] It is reported by the manufacturer that the as-received Si_3N_4 powder contains ~1.5 wt% O.

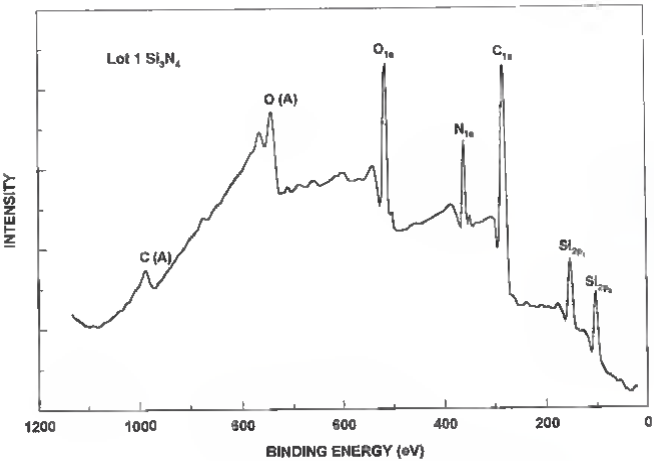

Figure 4 6 XPS plot for Lot1 Si_3N_4 fractionated powder (A = Auger peak.)

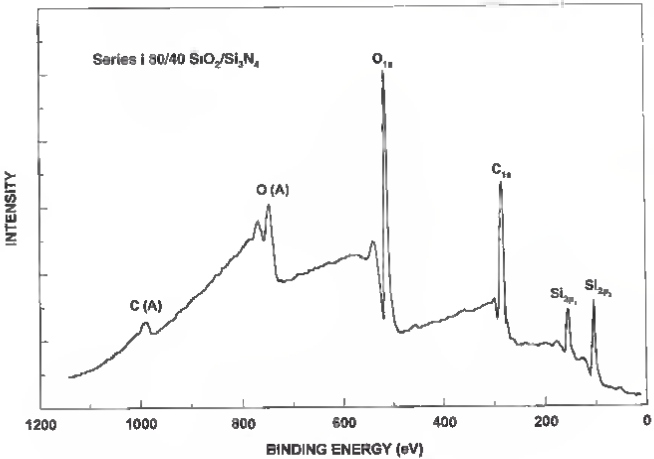

Figure 4.7 XPS plot for Series I 60/40 SiO_2/Si_3N_4 composite powder (A = Auger peak)

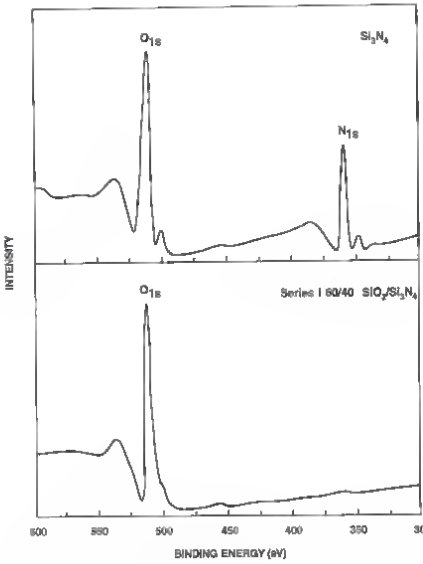

Figure 4.8 XPS plots for Si_3N_4 and 60/40 composite powders for binding energies in the range of 300 – 600 eV

Table 4.1 Electrophoretic Mobility* (μ) and Zeta Potential (ζ) Data for batch1 SiO_2 Powder

	μ μmesm Ves					average ζ
pH	T1	B1	T2	B2	average	(mV)
2.6	0.01	0.13	0.20	0.24	0.15±0.09	2.3
4.1	0.07	0.02	-0.30	-0.48	-0.17±0.23	-2.6
5.4	-1.40	-1.53	-1.97	-2.42	-1.83±0.40	-27.9
7.2	3.04	3.93	-3.70	-3.46	-3.53±0.33	-61.7
9.8	-4.92	-4.63	-4.53	-4.89	-4.74±0.17	-100.2

*T top stationary level, B bottom stationary level, 1 sample #1 and 2. sample #2.

Table 4.2. Electrophoretic Mobility* (μ) and Zeta Potential (ζ) Data for Lot1 Si_3N_4 Powder

	μ μmesm Ves					average ζ
pH	T1	B1	T2	B2	average	(mV)
2.0	3.91	3.23	3.50	2.83	3.37±0.39	56.5
3.9	3.31	3.52	4.21	3.91	3.74±0.35	69.4
6.6	0.22	1.44	0.71	1.56	0.98±0.55	14.8
7.1	-0.91	-0.30	-0.23	-1.50	-0.74±0.51	-11.2
9.9	-3.15	-1.51	-1.49	-1.70	-1.96±0.69	-29.6

*T top stationary level B bottom stationary level, 1 sample #1 and 2 sample #2

Table 4 3 Electrophoretic Mobility* (μ) and Zeta Potential (ζ) Data for Series 1 60/40 Composite Powder

	μ μmlcm/ V•s				average ζ
pH	T1	B1	T2	B2	average (mV)
2 0	-0 14	0 30	0 45	-0 23	0 10±0.29 1.5
3 9	-0 54	-0 64	-0 74	-1.03	-0 74±0 18 -11 0
5 9	-2 96	-2 74	-2 81	-3.22	-2 93±0 18 -51 4
7 8	-4 73	-4 06	-4 07	-4 42	-4 32±0.28 -77 0
9 9	-4 81	-5 55	-4 45	-6 10	-5.23±0.64 -105.3

*T: top stationary level B bottom stationary level, 1 sample #1 and 2 sample #2

Tables 4 1 – 4.3 list the measured mobilities and the calculated zeta potentials for batch 1 SiO_2, Lot1 Si_3N_4, and Series 1 60/40 composite powders, respectively Figure 4 9 shows the zeta potential vs. pH plots for these powders. It is evident from Figure 4 9 that the SiO_2 and SiO_2/Si_3N_4 composite powders exhibit essentially the same dependence of zeta potential on the suspension pH The isoelectric point of the pure Si_3N_4 is, however, higher (i e., the zeta potential curve is shifted to higher pH values) As mentioned in Section 2 4, the similarities in the zeta potential-pH dependence between the coating-phase particles and the corresponding coated particles have also been demonstrated for other composite powders such as SiO_2-coated Al_2O_3 [Arg90 Che94] Y_2O_3 [Gie94], SiC [Che94] and Fe_2O_3 [Azu91] and TiO_2-[Par93] and Y-doped ZrO_2- [Hir91] coated SiO_2

Figure 4 10 shows the plot of volume percent vs. Stokes diameter for the fractionated Si_3N_4 60/40, and 80/20 composite powders. It is evident form Figure 4 10 that the distribution shifts to higher particle sizes as the amount of SiO_2 coated on the Si_3N_4 cores increases. As discussed in detail later (see Section 4.3 1), smaller nanocomposite

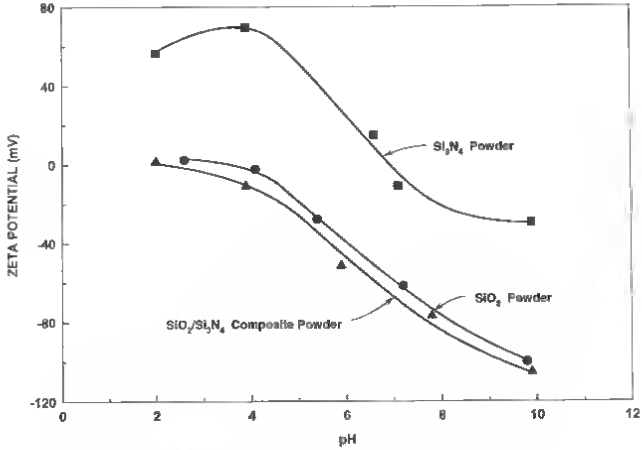

Figure 4 9 Zeta potential vs pH plots for batch1 SiO_2, Lot1 Si_3N_4, and Series 1 60/40 composite powders

particles contain larger amounts of of SiO_2 compared to the larger particles. Consequently the true densities of the former particles are lower, and those of the latter particles are higher than the overall powder density. Since the overall powder density is utilized in the particle size calculations, these density differences will result in errors in the calculated size distributions. According to the Stokes equation [Ree88] for sedimentation, for a given particle-liquid system, the predicted particle diameter is inversely proportional to the square root of the powder true density. Since the true densities of the smaller microcomposite particles are lower than the assumed (i.e., overall) value, smaller particle sizes will be predicted. Similarly, the larger microcomposite particles have densities higher than the assumed value and therefore larger sizes will be predicted for these particles. Therefore, it follows that broader size distributions will be predicted if the overall density is used in the particle size analysis. Detailed quantitative microscopy (TEM) may be necessary to accurately determine the particle size distribution of the microcomposite particles. Nevertheless, the data in Figure 4.10 is valid for qualitatively illustrating the shift to higher particle sizes that is associated with the precipitation of the coatings of varying average thickness.

Table 4.4 shows the measured BET specific surface areas of as-received and fractionated Si_3N_4, 60/40 and 80/20 powders. It also shows the calculated surface areas derived from the particle size distributions (Figure 4.10) assuming spherical geometry for the particles. The calculated specific surface area S_w (in m^2/g) was determined by an algorithm[11] using the following equation

---

[11] Version 5.2 Particle Analyzer Software, Horiba Instruments, Japan

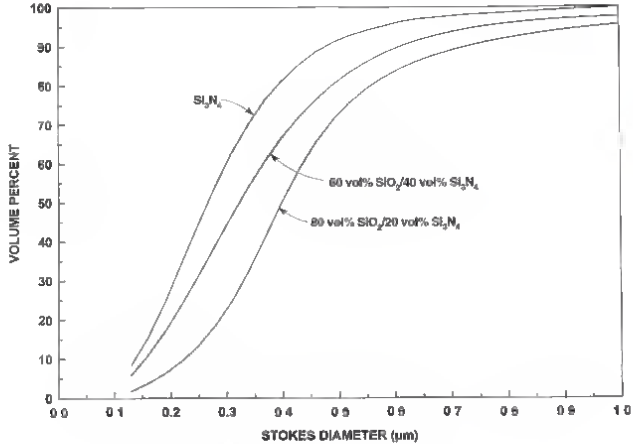

Figure 4.10 Particle size distribution plots for Lot1 Si_3N_4, 60/40 and 80/20 powders

$$S_w = (6/\rho) \bullet \Sigma(F_i / D_i) \qquad (4.1)$$

where, ρ is the density in g/cm^3, i is an interval in the distribution, F_i is the volume fraction of particles with diameter D_i (in μm) and Σ is the summation over i. The powder true densities were the same as those used for the particle size measurements (see Table 3.3).

Table 4.4 Specific Surface Areas of Core and Composite Powders.

	Measured Specific Surface Area* (m^2/g)	Calculated Specific Surface Area (m^2/g)
Si_3N_4 as-received	10.7 (10.6, 10.8)	4.9
Si_3N_4 fractionated	14.9 (14.8, 15.0)	8.5
60/40	15.3 (15.2, 15.4)	9.4
80/20	8.0	7.5

* Numbers in parentheses represent values obtained from two independent measurements

The fractionated Si_3N_4 powder exhibits a higher specific surface area than the as-received powder. This is expected since the relatively coarse aggregates are removed by fractionation which results in a reduction in the average particle size. When a SiO_2 coating is deposited on the core particle surface, two consequent factors affect the surface area: (1) the reduction in solid density and (2) the increase in the average particle size. While the former factor leads to an increase in the specific surface area, the latter causes a reduction in the surface area value. The calculated values of the surface area show that for the 60/40 powder the reduction in solid density is the dominant factor, which results in an increase (from 8.5 to 9.4 m^2/g) in specific surface area. In contrast, the increase in particle size is the controlling factor for the 80/20 powder which results in an overall reduction (from 8.5 to 7.5 m^2/g) in the specific surface area.

Table 4 4 shows that for all powders, the measured values are greater than the calculated values of the specific surface area. The reasons for this difference may include porosity (in the aggregates, for the Si_3N_4 powders, and in the coating, for the composite powders), errors in particle size and surface area measurements, errors in assumed density values, surface roughness, and non-spherical geometry. It is evident form Table 4.4 that for the Si_3N_4 powders, lesser difference between the measured and calculated values is observed for the fractionated powder compared to the as-received powder (differences of ~43% vs ~55%, respectively, for the two powders). This may be attributed to the fact that the fractionated powder contains a relatively lower amount of aggregates. Due to the presence of aggregates, the measured particle size is larger than the primary particle size. Since the measured surface area is mostly determined by the primary particle size, it would be higher than the calculated value which was determined using the measured particle size. Therefore the presence of a higher amount of aggregates results in a greater difference between the measured and calculated surface areas. As shown later in Section 4.3.1, the presence of porosity in the coatings results in significantly higher surface areas (>20 m^2/g) compared to those reported in Table 4 4. This suggests that the coatings on the composite particles described in this section were dense (i.e., there was no significant amount of surface porosity). As discussed earlier, the differences in densities between individual microcomposite particles result in errors in the particle size data and consequently in the calculated surface area values. The non-spherical shape of the particles is also a major factor leading to the differences between measured and calculated specific surface areas. As described later (see Section 4.3.1), it has been shown that microcomposite particles with thicker coatings were usually more spheroidal (and hence they would have lower specific

surface areas) than the corresponding core particles. The data in Table 4.4 is consistent with this observation since the difference in the measured and calculated surface areas is significantly lower for the 80/20 composite powders compared to the Si_3N_4 powders.

4.1.2. Effect of Spatial Distribution of Phases

In order to study the effect of spatial distribution of phases on densification behavior, ~60 vol% SiO_2/ ~40 vol% Si_3N_4 powder compacts prepared with the SiO_2/Si_3N_4 microcomposite particles and the mixture of SiO_2 particles and Si_3N_4 particles were used. An effort was made to avoid significant differences in particle sizes and particle packing densities of the two types of compacts since these factors also affect sintering kinetics. The microcomposite particles were slightly larger (median Stokes' diameter[86] and specific surface area of ~0.35 μm and ~15 m^2/g, respectively, vs. values of ~0.25 μm and ~19 m^2/g, respectively, for the particle mixture) as shown by the particle size distribution plots (Figure 4.11). While this would tend to retard densification slightly, the effect may have been compensated for (at least partially) by the slightly higher measured packing density (as determined by the Archimedes method) for compacts prepared with the microcomposite particles (~61% vs. ~57%, as shown in Tables 4.5 and 4.6).

Densification was directly compared for the ~60 vol% SiO_2/ ~40 vol% Si_3N_4 composite powder compacts and mixed powder compacts by heating to different

---

[86] For the mixed powder, an average density of 2.51 g/cm^3 was calculated by assuming the powder densities of SiO_2 (fd°Cl and Si_3N_4 to be 2.05 and 3.19 g/cm^3, respectively. That value was then used for particle size analysis. Since Stokes' law predicts that the measured diameter is inversely proportional to the powder density, higher sizes will be estimated for the Si_3N_4 particles. This may have been (at least partially) compensated for by the fact that lower sizes will be predicted for the SiO_2 particles.

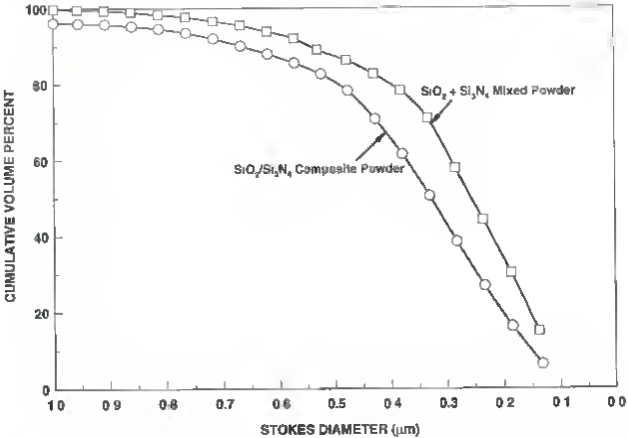

Figure 4.11 Particle size distribution plots for ~60 vol% SiO_2 + ~40 vol% Si_3N_4 mixed powder and 60/40 SiO_2/Si_3N_4 composite powder respectively

temperatures. The results from Archimedes density measurements for these two types of compacts are shown in Tables 4.5 and 4.6, respectively. Figure 4.12 shows plots of bulk density and open porosity vs. sintering temperature for the two types of powder compacts. Figure 4.13 shows plots of relative density vs. temperature for the two compacts. The compact prepared with the microcomposite particles starts to show an increase in bulk density and a decrease in open porosity by 1000°C, while the compact prepared with the particle mixture shows essentially no change until the temperature exceeds 1200°C. The former sample reached a maximum bulk density of ~2.51 g/cm^3 (~97% relative density) by 1275°C and the open porosity approached zero at this temperature. In contrast, the bulk density of the particle mixture compact was only ~1.90 g/cm^3 (~73% relative density) and the open porosity was ~26% at 1275°C. Figure 4.13 also indicates that the composite powder compact reached a maximum relative density of ~97% at 1275°C but the density reduced to ~94% when the same compact was heated further to 1400°C. This may be attributed to the presence of entrapped nitrogen in the closed porosity (~2 %, obtained by subtracting the open porosity from the total porosity) present after the 1275°C heat treatment. Since the sample was sequentially heated further to 1300 and 1400°C, respectively, the expansion of the entrapped gases resulted in "blooming" or increases in the closed pore volume (to ~4% and ~6%, respectively after the two heat treatments) thus leading to reductions in relative density[87]. Despite these reductions in densities, the composite powder compact still had higher densities after the 1400°C heat treatment,

[87] It is noted that when separate samples are used for each heat-treatment (such as described in Section 4.2), the "blooming" phenomenon is obviated.

Table 4.5 Densification Data for 60 vol% SiO_2 + 40 vol% Si_3N_4 Particle Mixture Samples

Temperature (°C)	Bulk Density (g/cm^3)	Open Porosity (%)	Apparent Density (g/cm^3)	Relative Density (%)
600	1.472	43.2	2.592	56.5
	1.466	43.4	2.592	
1000	1.501	41.5	2.568	57.7
	1.489	42.1	2.574	
1100	1.487	42.7	2.595	56.9
	1.475	42.9	2.583	
1200	1.512	41.5	2.583	58.1
	1.507	41.7	2.586	
1250	1.732	32.8	2.579	66.5
	1.729	33.2	2.587	
1275	1.908	25.8	2.572	73.1
	1.903	25.8	2.566	
1300	2.044	19.8	2.549	78.8
	2.057	19.4	2.551	
1400	2.318	0.3	2.324	89.2
	2.324	0.1	2.326	

Table 4 6. Densification data for 60/40 SiO_2/Si_3N_4 Composite Powder Samples

Temperature (°C)	Bulk Density (g/cm^3)	Open Porosity (%)	Apparent Density (g/cm^3)	Relative Density (%)
600	1 574	38 9	2 576	60 4
	1 567	39 4	2 584	
1000	1 652	36 4	2.596	63 5
	1 646	36 7	2.599	
1100	1 724	33 1	2 579	66.2
	1 724	33 3	2 586	
1200	1 932	25 5	2 591	74.2
	1 929	25 5	2.589	
1250	2 314	10 7	2.590	88 8
	2.310	10 9	2.593	
1275	2 519	1 7	2.562	96 5
	2 507	1.6	2 546	
1300	2 461	1 5	2 499	94 6
	2 468	1 8	2 513	
1400	2 432	0.2	2 436	93 5
	2 423	0 4	2.433	

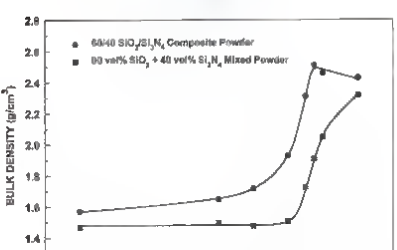

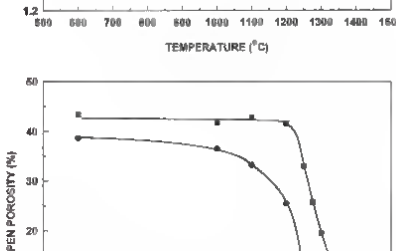

Figure 4.12 Plots of (a) bulk density vs temperature and (b) open porosity vs. temperature for 60/40 SiO_2/Si_3N_4 samples prepared from (i) a mixture of SiO_2 particles and Si_3N_4 particles and (ii) SiO_2-coated Si_3N_4 micro-composite particles

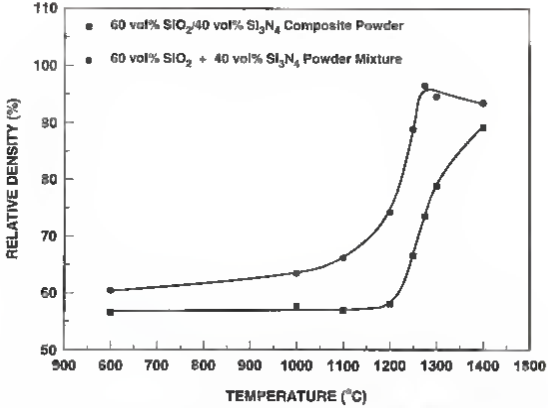

Figure 4.13 Plots of relative density vs. sintering temperature for 60/40 SiO_2/Si_3N_4 powder compacts prepared from (i) a mixture of SiO_2 particles and Si_3N_4 particles and (ii) SiO_2-coated Si_3N_4 microcomposite particles

compared to the mixed powder compact (~94% vs ~89%, respectively, for the two compacts)

Densification behavior was also studied by sintering the samples under isothermal conditions at 1300°C. Tables 4.7 and 4.8 list the results from Archimedes density measurements on these samples. Figure 4.14 shows plots of bulk density and open porosity vs. sintering time for the samples. Figure 4.15 shows the corresponding plots of relative density vs. sintering time. The compacts prepared with the microcomposite particles reached ~100% relative density after sintering for 2 h at 1300°C. In contrast, the compact prepared with the particle mixture had a relative density of only ~73% after the same heat treatment. In addition, the latter sample reached a maximum relative density of only ~90% after long sintering times. Similar densification behavior has been reported [Ram93] for ~60 vol% borosilicate glass + ~40 vol% Si_3N_4 particle mixture composites. It was found that these composites also reached a limiting relative density of ~90% after long sintering times at 650°C. Figure 4.14 also shows that for the particle mixture compact, the amount of open porosity increased when the sample was sintered for 48h. This may be attributed to the presence of trapped nitrogen in the closed pores (~9%) formed during sintering for 24 h at 1300°C. The expansion of the trapped gas ("blooting") during the subsequent heat treatment presumably resulted in some connectivity of the pores to each other and to the pores on the surface, thus resulting in some open porosity. The increase in porosity resulting from this expansion seems to have been mostly compensated for by the densification process. This is indicated by the minimal (~1.6%) reduction in relative density (or ~1.6% increase in total porosity)

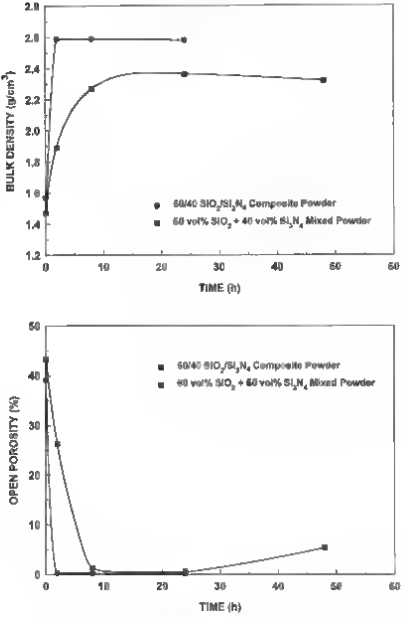

Figure 4.14 Plots of (a) bulk density vs time and (b) open porosity vs time, at 1300°C, for 60/40 SiO_2/Si_3N_4 samples prepared from (1) a mixture of SiO_2 particles and Si_3N_4 particles and (2) SiO_2-coated Si_3N_4 micro-composite particles.

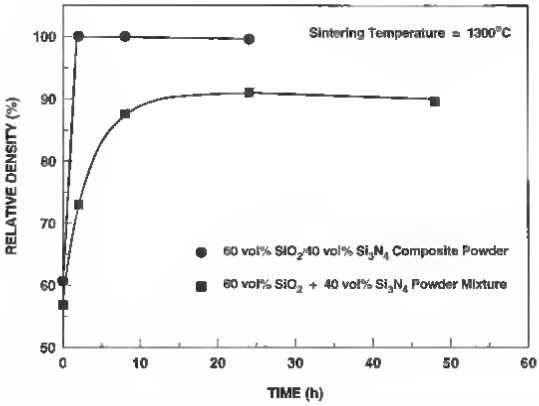

Figure 4.15 Plots of relative density vs. sintering time at 1300°C for 60/40 SiO_2/Si_3N_4 powder compacts prepared from (i) a mixture of SiO_2 particles and Si_3N_4 particles and (ii) SiO_2-coated Si_3N_4 nanocomposite particles

Table 4 7 Isothermal Densification Data at 1300°C for 60 vol% SiO_2 + 40 vol% Si_3N_4 Particle Mixture Samples

Time (h)	Bulk Density (g/cm^3)	Open Porosity (%)	Apparent Density (g/cm^3)	Relative Density (%)
0	1 472	43.2	2 592	56.5
	1 466	43.4	2 592	
2	1 892	26.1	2 560	72.7
	1 860	26 3	2 564	
8	2 276	1·0	2 300	87 3
	2.273	1 2	2.301	
24	2.358	0 9	2.379	90 8
	2 362	0 6	2.376	
48	2 323	5 4	2 456	89.2
	2 319	5 6	2 457	

The sintering results clearly show that significant enhancement in powder compact densification rate can be achieved by using microcomposite particles with controlled microstructure Densification of the mixed powder compacts was retarded due to the formation of rigid networks of non-sinterable Si_3N_4 particles Si_3N_4 particle-particle contacts were evident in the polished and etched microstructure of the sample sintered for 2h at 1300°C under isothermal conditions (Figure 4 16A). In contrast, the corresponding sample prepared with the microcomposite particles showed a relatively uniform dispersion of isolated Si_3N_4 particles in the SiO_2 matrix (Figure 4 16B).

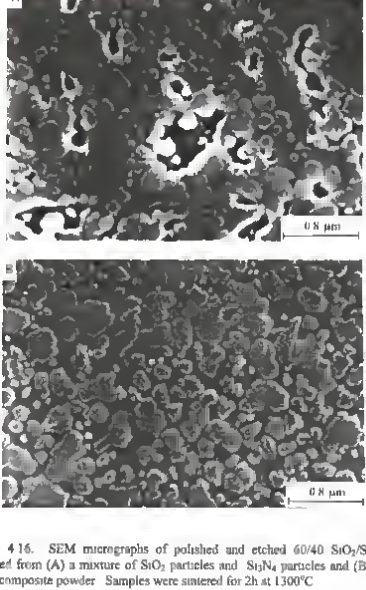

Figure 4.16. SEM micrographs of polished and etched 60/40 SiO_2/Si_3N_4 samples prepared from (A) a mixture of SiO_2 particles and Si_3N_4 particles and (B) Si_3O_2-coated Si_3N_4 composite powder. Samples were sintered for 2h at 1300°C

Table 4 8 Isothermal Densification data at 1300°C for 60/40 SiO_2/Si_3N_4 Composite Powder Samples

Temperature (°C)	Bulk Density (g/cm^3)	Open Porosity (%)	Apparent Density (g/cm^3)	Relative Density (%)
0	1 574	38 9	2 576	60 4
	1.567	39 4	2 584	
2	2.590	0 3	2 598	99 6
	2.590	0.3	2 598	
8	2 592	0.3	2.600	99 6
	2 591	0.2	2.596	
24	2.576	0.2	2.581	99.2
	2 581	0 1	2.584	

4.2. Processing and Properties of Bulk Composites with Low Dielectric Constant

The results pertaining to the experiments conducted using the Series II composite powders will be presented in this section. The results from the characterization of fractionated Series II 60/40 composite powders and FS particles will be discussed in Section 4 2 1 In Section 4.2 2, the results from the suspension and green compact characterization will be described. This will be followed, in Section 4 2.3, by a discussion of the results pertaining to the sintering and microstructural characterization of bulk compacts Finally, the dielectric and mechanical properties of selected samples will be listed and discussed in Sections 4 2.4 and 4 2.5, respectively

4.2.1. Characterization of Particles

The BET specific surface area of the Series II 60/40 composite powder was measured to be 14.3 m^2/g. This value is slightly lower than the surface area of 15.3 m^2/g determined for the Series I 60/40 composite powder (see Table 4.4). The difference may be attributed to the fact that the core particles in the Series II composite powders (i.e., Lot2 Si_3N_4 powder) were slightly larger in size compared to those in the Series 1 composite powders (i.e., Lot1 Si_3N_4 powder). (The median Stokes diameters of the two core powders were ~0.33 and ~0.27 μm, respectively (see Figure 3.1).) As discussed in Section 4.1.1, the relatively low surface area of the composite powder presumably indicates that the coating is dense (i.e., there is no significant amount of open porosity in the SiO_2 phase). Table 4.9 lists the measured electrophoretic mobilities and the calculated zeta potentials for the PS (~1.90 μm dia.) particles. Figure 4.17 shows the plots of zeta potential vs. pH of PS particles and 60/40 microcomposite particles (from Table 4.3), respectively. Both particles are expected to disperse well in water at pH values in the range 9-10 due to the development of high negative surface charges.

Table 4.9 Electrophoretic Mobility* (μ) and Zeta Potential (ζ) Data for PS Particles

	μ μmecm/Vsec					average ζ
pH	T1	B1	T2	B2	average	(mV)
2.0	0.41	0.23	-0.01	-0.20	0.11±0.23	1.4
3.9	-1.76	-1.98	-1.80	-1.53	-1.77±0.16	-23.0
5.5	-5.48	-5.29	-5.53	-5.59	-5.47±0.11	-70.9
8.1	-7.31	-7.43	-6.54	-6.93	-7.05±0.35	-91.4
9.9	-9.79	-9.35	-8.15	-8.69	-9.00±0.62	-116.7

*T: top stationary level, B: bottom stationary level, 1: sample #1, and 2: sample #2

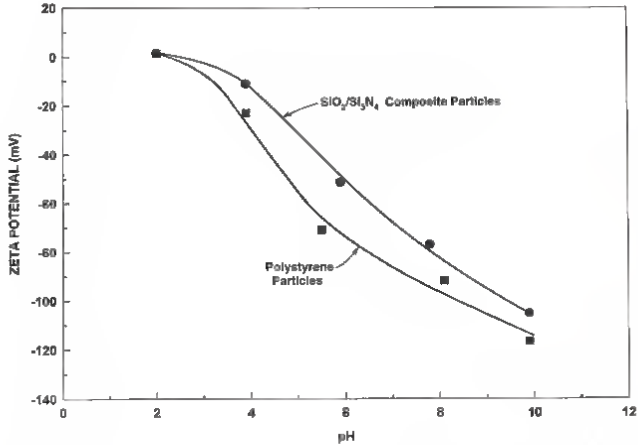

Figure 4.17 Comparison plots of zeta potential vs. pH for polystyrene (PS) and SiO_2/Si_3N_4 microcomposite particles.

Figures 4.18 (a) and 4.18 (b) show the TGA and DTA plots, respectively, for PS particles heated at 3°C/min from 25-1000°C in flowing (~60 cm^3/min) nitrogen. Figures 4.19 (a) and 4.19 (b) show the corresponding plots for PS particles heated under the same conditions in flowing (~60 cm^3/min) air. The rapid weight loss shown in the TGA plots (Figures 4.18 (a) and 4.19 (a)) and the endothermic peak centered at ~397°C observed in the DTA plots (Figures 4.18 (b) and 4.19 (b)) are characteristic of the volatilization of products (such as styrene, toluene, etc.) resulting from the thermodegradation reaction [Car91 Dar90]. The DTG peak temperature (i.e., the temperature corresponding to the maximum in the slope of the TGA curve) and the DTA endothermic peak temperature were nearly identical for each atmosphere (396 vs. 398°C, respectively, for nitrogen, and 398 vs. 396°C, respectively for air). Pyrolysis in nitrogen did not result in any weight loss above ~450°C and a significant amount (~2.5 wt%) of residual weight was observed (Figure 4.18 (a)). This result was consistent with the fact that a brownish-black residue was observed in the crucible after the heat treatment in nitrogen. Darivakis et al. [Dar90] studied the volatilization reactions of PS particles heated in helium at ~1000°C/s to 700°C. It was established that complete burnout occurred (i.e., no residual weight was observed) under these conditions. This is in apparent contradiction to the results from the current investigation which showed that significant amount of carbonaceous residue remained after pyrolysis in an inert (nitrogen) atmosphere at much lower heating rates (3°C/min). One of the possible reasons for this difference is the incomplete removal of additives (e.g. AIBN, hydroquinone) during the washing step (see Appendix C) in the synthesis of the PS particles used in the current investigation. In contrast to the current study Darivakis et al. [Dar90]

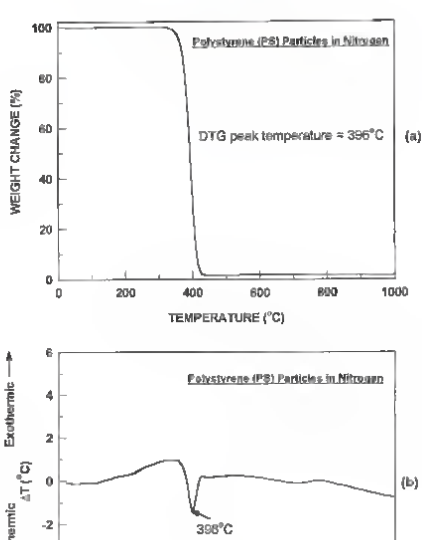

Figure 4.18 Plots showing (a) TGA and (b) DTA curves for PS particles heated at 3°C/min in nitrogen

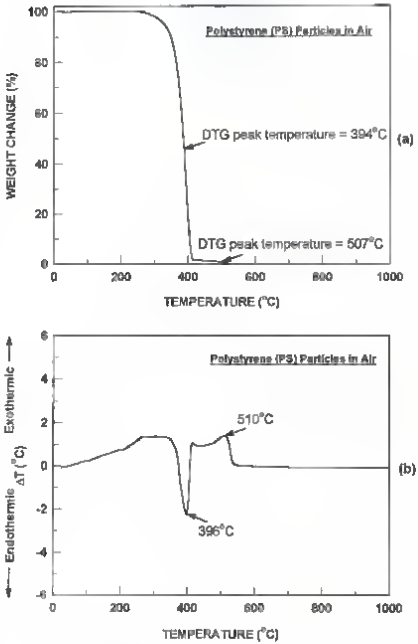

Figure 4.19 Plots showing (a) TGA and (b) DTA curves for PS particles heated at 3°C/min in air

used PS particles that were prepared by a photo-polymerization method (exact details were not specified). Since photo-polymerization generally does not involve additives [Fer89], the resulting polymer is relatively pure. Therefore, the burnout of such a polymer is complete and no residual weight is observed after pyrolysis.

A secondary weight loss with a DTG peak temperature of 507°C (Figure 4.18 (a)) and a corresponding exothermic peak centered at 510°C (Figure 4.19 (b)) was observed for the sample heated in air. This reaction corresponds to the oxidative combustion of the carbonaceous residue resulting from the endothermic reaction that occurred in the temperature range of 300-425°C. The residual weight after the secondary (exothermic) reaction is almost zero (<0.1 wt%) indicating that almost complete volatilization of the PS particles can be achieved by heat treatment in air. This is consistent with the observation that no residue was evident in the crucible after the heat treatment in air. This is important for the development of high-performance low-dielectric constant materials since it has been shown [Cha86] that the presence of carbon can lead to detrimental effects, such as increases in dielectric constants and loss tangents.

4.2.2. Suspension and Green Compact Characterization

Figure 4.20 shows the plots of viscosity as a function of shear rate in the range 0 - 1000 s^{-1} at pH ~9 for ~21 vol% PS and ~36 vol% 60/40 SiO_2/Si_3N_4 suspensions, respectively (see Appendix F for detailed results). Figure 4.20 shows that the viscosity was independent of shear rate for the PS suspension. The Newtonian behavior of the PS suspension can be attributed to having a well-dispersed suspension (due to high repulsive forces between the particles) of moderate solids loading in a Newtonian fluid (water). In

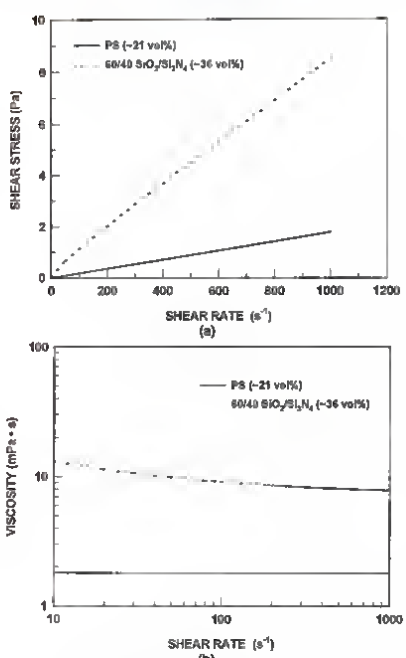

Figure 4.20 Plots of (a) shear stress vs shear rate and (b) viscosity vs shear rate for PS suspension (~21 vol% solids) and 60/40 SiO_2/Si_3N_4 (~36 vol% solids) suspensions, at pH ~ 9.2

contrast to the PS suspension, the SiO_2/Si_3N_4 suspension was slightly shear thinning, i.e., the viscosity decreased slightly as the shear rate increased. Particle/liquid suspensions can show shear thinning flow behavior for a variety of reasons: (1) The liquid may be non-Newtonian. This is not true for the current study as water is a Newtonian fluid. (2) The suspension may contain flocs or agglomerates which break down at high shear rates. This is a minor factor in the current study. The use of fractionated powders resulted in a low concentration of hard agglomerates. The preparation of suspensions at pH ≈ 9 resulted in high interparticle repulsive forces and, thereby, minimized the possibility of floc formation. (3) The particles may have an anisotropic geometry. This is a minor factor for the composite particles since they were mostly equiaxed (Figures 4.1B and 4.2B-4.2D). (4) Electroviscous effects may be operative [Kru72, Yeh88]. This is expected to be important in the current study because electroviscous effects are significant when the thickness of the electrical double layer becomes a substantial fraction of the particle diameter. In this study, the particles were fine (i.e., ~20% were less than ~0.3μm) and the electrical double layer was relatively thick due to the combination of high zeta potential and moderate ionic strength. (5) Brownian motion may be operative [Kru72, Yeh88]. This is expected to be a significant factor for the composite powder suspensions used in this investigation because of the fine particle sizes.

Figure 4.21 shows the rheological behavior for (1) a SiO_2/Si_3N_4 suspension with a solids concentration of ~30 vol%, and (2) a co-dispersed suspension with a ~88/12 volume ratio of SiO_2/Si_3N_4 particles and PS particles and with an overall solids concentration of ~30 vol% (see Appendix F for detailed results). Both suspensions were slightly shear thinning. However, the co-dispersed suspension had a slightly lower viscosity (~3.8 mPa•s

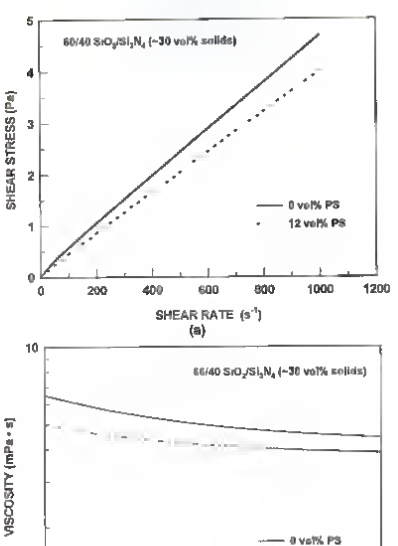

Figure 4.21 Plots of (a) shear stress vs shear rate and (b) viscosity vs shear rate for 60/40 SiO_2/Si_3N_4 (~30 vol% solids) suspensions with and without PS at pH ~ 9.2

at 1000 s^{-1}) compared to that for the SiO_2/Si_3N_4 suspension (~4.7 mPa•s at 1000 s^{-1}). This difference can be attributed to two factors. First, the co-dispersed powder and a bimodal (polydisperse) particle size distribution (PS particles had diameters of ~1.9 μm compared to the median Stokes diameter of ~ 0.45 μm for the 60/40 composite powder). Since polydisperse suspensions have lower viscosities than monodisperse suspensions [Ree88, Ver90], the PS/composite powder mixed particle suspension had a lower viscosity. Second, for a given solids concentration, suspensions made with ultrafine particles (typically with sizes below ~0.5 μm) tend to exhibit higher viscosities due to increased significance of Brownian motion and electroviscous phenomena [Kri72, Yeh88]. Since the composite powder suspension had a greater fraction of finer particles (e.g., less than 0.5 μm) compared to the co-dispersed suspension, it had a greater viscosity.

Fracture surfaces of green compacts were observed under the SEM to determine if any obvious segregation occurred during slip-casting. In particular, regions near the top and the bottom of the samples were studied to determine if there were differences in particle size. The SiO_2/Si_3N_4 powder contains particles in the size range ~0.05 - 0.8 μm. If segregation occurred, the concentration of larger particles would increase near the bottom of the sample and the concentration of smaller particles would be higher near the top of the sample. In the case of compacts made using the co-dispersed suspension, segregation could occur between the PS particles and the SiO_2/Si_3N_4 particles due to the significant difference in their powder densities (the true densities of PS and SiO_2/Si_3N_4 powders are ~1.05 g/cm^3 and ~2.51 g/cm^3, respectively) and the difference in their particle sizes. Several fields of view from the top, middle, and bottom portions of the samples were observed by SEM and no significant differences were observed, i.e., no obvious segregation of particles was

detected in either type of sample. The lack of segregation may be attributed to the low sample height (~2-3 mm after casting), the use of relatively concentrated suspensions, and the relatively high casting rates (typically, casting occurred in only ~15 min). Figures 4.22(A) and 4.22(B) show representative micrographs of the cross-sections for SiO_2/Si_3N_4 compacts prepared with and without PS particles, respectively. Figure 4.22(B) shows a homogeneous distribution of isolated PS particles. This is expected since the particles were dispersed well in the suspension used for slip-casting. In addition, the volume fraction of PS is sufficiently below the threshold concentration required to form a contiguous network (for a random mixture of equal sized spheres of two phases, percolation occurs at only ~16 vol% [Zal83]).

The pyrolysis of PS results in the formation of large (~1.9 μm diameter) spherical voids in addition to the relatively fine interparticle porosity (associated with packing of the composite powder) that exists in the as-cast state. Since the interparticle pore channels provide the pathway for the elimination of volatiles resulting from the burnout of PS, extremely low heating rates (~0.2°C/min) were used to minimize the stresses generated during pyrolysis. Figure 4.23 shows the weight loss (in percent) versus temperature for SiO_2/Si_3N_4 compacts prepared with 0 and ~12 vol% PS particles, respectively, that were heated in flowing (~60 cm^3/min) air. The initial weight loss (at temperatures <150°C) in both samples is presumably associated with the removal of physisorbed water. For the PS-containing sample, the relatively rapid weight loss that began at ~240°C may be attributed primarily to the pyrolysis of the PS particles. These temperatures are lower compared to those observed in Figure 4.19 due to the significantly lower heating rates (~0.2°C/min vs. ~3°C/min) used. The weight loss data in Figure 4.23 was used to estimate the concentration

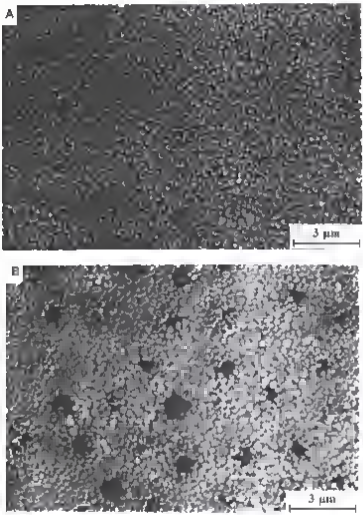

Figure 4.22 SEM micrographs of green compacts prepared by slip-casting (A) 60/40 SiO_2/Si_3N_4 composite powder and (B) a mixture of 60/40 SiO_2/Si_3N_4 microcomposite particles and FS particles

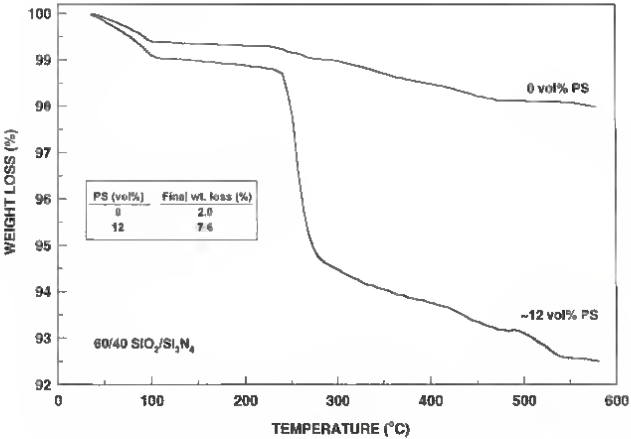

Figure 4.23 TGA plots for 100°C vacuum dried 60/40 SiO_2/Si_3N_4 compacts prepared with and without PS particles.

of PS particles in the green compact. The contribution to the weight loss from the SiO_2/Si_3N_4 composite particles was assumed to be 2.0 wt%, as determined by the TGA of compacts prepared without PS particles. The true densities of the PS and SiO_2/Si_3N_4 particles were assumed to be ~1.05 g/cm^3 and ~2.60 g/cm^3, respectively. Further, it was assumed that PS particles were completely pyrolyzed at 575°C, i.e., the total weight loss (7.6 wt%) at 575°C is the sum of the weight of the PS particles and the weight loss associated with the SiO_2/Si_3N_4 particles. Based on these assumptions, the volume ratio of SiO_2/Si_3N_4 to PS particles was calculated to be ~87/13 which is in good agreement with the expected value of ~88/12.

Figure 4.24 shows the plots of cumulative specific pore volume vs. pore channel diameter determined by Hg penetration porosimetry for pre-sintered (800°C) samples[88] with and without the PS particle-derived pores. Table 4.10 gives the total intruded pore volume, median pore channel radius, and calculated percentage porosity for each sample. The PS particle-derived pores are connected by pore channels formed by the packing of the microcomposite particles. Due to this "ink bottle" structure of the porosity in the compacts it is expected that the bi-modal nature of porosity in these samples would not be reflected in the pore channel distribution data. Previous studies [Lee90, Zhe92] on bi-modal pore structures in powder compacts have shown that larger pores will be detected only at a pressure sufficient to intrude the finer inter-particle pore channels. At relatively low pressures, some of the mercury that penetrates through the largest interparticle pore channels fills the PS particle-derived pores and thus would result in a higher apparent

[88] Reliable pore size measurements could not be carried out on as-cast samples containing PS particles. The PS particles deform under the high pressures used for the porosimetry measurements and thus deformation results in erroneous pore size data (see Appendix G for details).

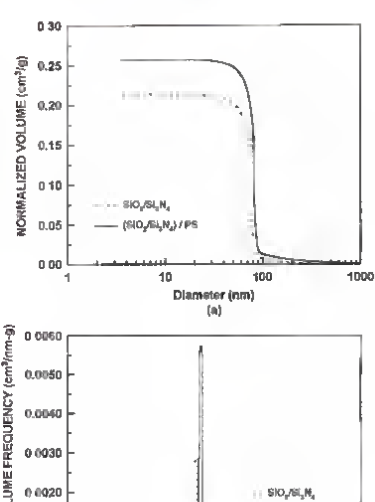

Figure 4.24 Plots of (a) pore volume and (b) specific volume frequency versus pore diameter obtained by mercury porosimetry for 800°C pre-sintered 60/40 SiO_2/Si_3N_4 samples cast with and without PS particles

intruded volume corresponding to these channels This would explain the observation that the median pore radius for the sample with the PS particle-derived pores is higher compared to that for the sample not containing the PS particle-derived pores (Table 4 10) The increased median pore radius for the PS containing samples can also be partly attributed to the increased average particle size (~1 90 μm for PS powder vs. ~0 30 μm for SiO_2/Si_3N_4 powder) which results in increased interparticle pore sizes.

Table 4 10 Results from Hg Penetration Porosimetry on Pre-Sintered Compacts.

Sample Description	Total intruded pore volume (cm^3/g)	Median pore channel radius (nm)	Calculated porosity (%)
SiO_2/Si_3N_4	0.2174	37.3	36 1
SiO_2/Si_3N_4 + PS	0.2542	41 3	39.8

It is interesting to compare the pore size data to those obtained by Randall [Ran93] Randall [Ran93] used PS particles (~4.6 μm diameter) to incorporate controlled, closed porosity in borosilicate glass (BSG average particle size ~1 8 μm) powder matrices. The median pore channel radius for green BSG compacts prepared without PS particles was measured by mercury penetration porosimetry to be ~80 nm. In contrast, the compacts prepared with ~10 vol% PS particles (in total solid volume) had a median pore channel radius of ~110 nm after the pyrolysis of PS particles (and prior to densification) In addition, the measured pore size distribution was uni-modal although the compact had a bi-modal pore size distribution (i.e., a combination of the relatively fine inter-particle pores

and the relatively coarse PS-derived pores) [Ran93]. These observations are consistent with the pore size data reported in the current investigation.

The total amount of porosity (39.8%) in the pre-sintered compact containing the PS particle-derived pores was used to estimate the packing density of the as-cast compact. Assuming that all the pores are detected by the porosimetry measurements, the pre-sintered compact had a relative density of 100-39.8 = 60.2%. Assuming that the volume ratio of SiO_2/Si_3N_4 particles to PS particles in the as-cast compact was ~88/12, and assuming that the PS was completely pyrolyzed during pre-sintering, the relative density of the as-cast compact can be calculated as 60.2/0.88 = 68.4% and the corresponding total porosity will be 100-68.4 = 31.6%. This is significantly lower than the porosity (36.1%), determined from porosimetry, for the samples prepared without the PS particles. The increased packing efficiency (or decreased interparticle porosity) of the samples with PS particles may be attributed to the fact that the compacts prepared with the PS particles had a broader overall size distribution. The ideal packing density of a binary mixture was derived by Furnas [Fur28]. The calculation was based on the assumption that the primary phase particles are very much smaller than the second phase particles. It was shown that the composite relative density, ρ_c, is given by

$$\rho_c = 100 \bullet \rho_1 / [100 - (100 - \rho_1) f_2] \qquad (4.2)$$

where ρ_1 is the relative density of the primary phase particles in the absence of the second phase particles and f_1 is the volume fraction of the primary phase particles in the mixture. In the current study, the composite powder (primary phase) has much smaller particles compared to the PS particles (second phase). For ρ_1 = 63.9% (from Table 4.10, assuming that porosimetry determines the total porosity) and f_1 = 0.12 (corresponding to PS

concentration of ~12 vol% in solids) we obtain from eq (4.2) that ρ_c = 66 8%. In other words, the relative density increased from 63 9% to 66 8% when PS particles were included in the composite powder packing This is slightly lower than the value (68 4%) determined earlier Therefore the bi-modal nature of the particle size distribution may only partly account for the increase in density when PS particles are incorporated in the composite powder compact. Other possible reasons for the increase include errors in the pore volumes determined by porosimetry (discussed later in this section), errors in the assumption of the PS concentration (e.g if PS concentration in solids is assumed to be 11 vol%, the packing densities from porosimetry and the Furnas model would be 67 8% and 66.5% respectively), etc.

Table 4 11 shows the results from Archimedes density measurements for pre-sintered samples with and without the PS-particle derived pores. Table 4 11 shows that the volume percent open porosity determined by the Archimedes method using water as the medium is significantly higher than the total volume percent porosity obtained from porosimetry (Table 4 10). This seems to indicate that the mercury failed to completely penetrate all the open pores. One possible explanation given consideration is the presence of fine porosity in the compact. Since the the lower detection limit of pore channel diameter by mercury penetration is ~40 Å (4 nm) [Gre82], the presence of pores or pore channels finer than this size would prevent complete intrusion of mercury in order to detect the presence of any such fine porosity pore size measurements were carried out using nitrogen gas adsorption on the sample containing the PS-derived pores. Figure 4.25 shows the adsorption and desorption isotherms for the same The isotherms exhibit apparent characteristics of Type IV according to the Brunauer-Emmett-Teller (BET) classification

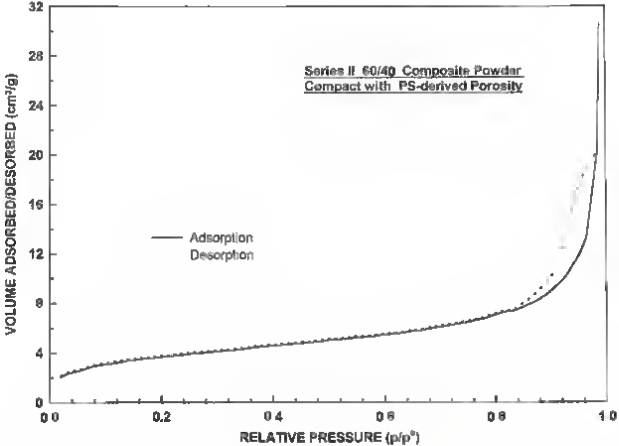

Figure 4.25 Adsorption and desorption isotherm plots for 800°C pre-sintered 60/40 SiO_2/Si_3N_4 powder compacts with PS-derived pores

[Gre82] The hysteresis loop is characteristic of the presence of porosity in the compact [Gre82]

Table 4 11 Density and Porosity Values Determined by the Archimedes Displacement Method Using Different Media.

	0% PS			12% PS		
Medium (saturation time)	Pbulk (g/cm^3)	O P * (%)	Ppycnom (g/cm^3)	Pbulk (g/cm^3)	O P * (%)	Ppycnom (g/cm^3)
water (2h)	1 482 1 478	42 7 42.9	2 584 2 588	1 421 1 420	44 5 44.3	2 562 2.566
ethanol (30 min)	1.497 1 497	32.2 32.2	2.207 2.207	1 435 1.433	36 1 36.3	2.246 2.250
ethanol (3h)	1 495	32.6	2.218	1 433	36.2	2.248
methanol (30 min)	1 486	32.5	2.203	1 437	35 8	2.239

* open porosity

Figure 4.26A shows plots of cumulative pore volume and specific volume frequency, as functions of pore diameter, for the sample containing the PS-derived pores The tri-modal nature of the pore size distribution may be explained as follows The largest pores (i.e., the pores with diameters greater than ~60 nm, which is the second minimum in Figure 4 26A) is presumably due to the porosity associated with the particle packing. The total volume of these pores was calculated to be ~0 0119 cm^3/g. This is significantly lower than the value (0 2542 cm^3/g) determined using mercury porosimetry Thus may be explained by the fact that the upper limit of pore diameters measured by gas adsorption is typically in the range of 300 - 400Å (30 –40 nm) [Gre82] Therefore, most of the inter-

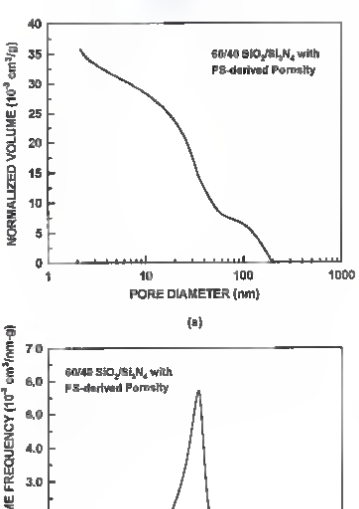

Figure 4 26A. Plots of (a) pore volume and (b) specific volume frequency vs. pore diameter obtained by nitrogen adsorption for a pre-sintered (800°C) 60/40 SiO_2/Si_3N_4 sample with FS particle-derived pores

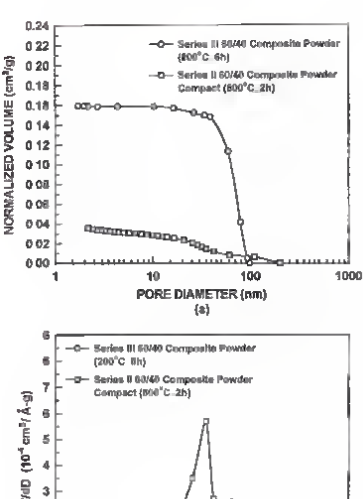
Series II 60/40 Composite Powder (800°C, 6h)
Series II 60/40 Composite Powder Compact (800°C, 2h)
NORMALIZED VOLUME (cm³/g)
PORE DIAMETER (nm)
(a)
Series III 60/40 Composite Powder (200°C, 8h)
Series II 60/40 Composite Powder Compact (800°C, 2h)
dV/dD (10⁻⁴ cm³/Å-g)
PORE DIAMETER (nm)
(b)

Figure 4.25B Plots of (a) pore volume and (b) specific volume frequency (dV/dD) versus pore diameter obtained by nitrogen gas adsorption for 60/40 SiO_2/Si_3N_4 composite powder and powder compact.

particle porosity was not detected using the gas adsorption method. The intermediate pores (corresponding to the peak, centered at a pore diameter of ~35 nm, shown in Figure 4.26A) might be due to the pores present within coated agglomerates. (If an agglomerate of core particles was completely coated by the SiO_2 phase, then the pores within it would not be detected. However, if the same cluster was partially coated, then it would comprise pores with sizes smaller than those observed for typical interparticle pores.) The total volume of these pores was calculated to be ~0.0202 cm^3/g. The finest pores (i.e., those with diameters less than ~4 nm, which is the first minumum in Figure 4.26A) may be attributed predominantly to the porosity within the coated powders in the compact. The total volume of such pores was calculated to be ~0.0035 cm^3/g. The evidence for the presence of porosity in the composite powders is described in Section 4.3.1. If the finest porosity (< 4nm diameter) was not accessible to infiltration by mercury, porosities obtained from mercury penetration porosimetry would be lower than that obtained from the Archimedes measurements. The addition of these pores to the total pore volume results in <1% increase in the porosity and therefore it could not explain the higher (5-7%) discrepancies in the pore volumes as observed earlier. However, it is still possible that the finest porosity comprise pore channels providing access to some of the larger pores (i.e., those within coated agglomerates as those associated with particle packing). This could explain the inability of mercury to intrude some of the porosity.

It is interesting to compare the gas adsorption data for the presintered 60/40 (Series II) composite powder compact (see Figure 4.26A in Section 4.3.1) with the corresponding results for a Series III 60/40 composite powder batch (see Figure 4.6d). Figure 4.26B shows plots of cumulative pore volume and specific volume frequency as functions of pore

diameter for the two cases, respectively. The total specific pore volume of the powder was ~4.5 times that for the powder compact (~0.160 vs ~0.035 cm^3/g, respectively). Furthermore, it is evident from Table 4.18 (see Section 4.3.1) that the total specific pore volumes of the other Series III composite powders were ~3 - 5 times that for the powder compact. Since the powder packing efficiency for the compact is higher than that for the loose powder, the total specific pore volume of the former is expected to be lower. However, the relatively low packing efficiency results in considerably larger pores and some of these larger pores may not be detected by nitrogen gas measurements. (The exact pore sizes associated with the particle packing for the powder and the compact could not be calculated from the dV/dD plots in Figure 4.26B since the corresponding peaks occurred at sizes greater than the upper detectable limit for the technique.) Therefore, it is intriguing that significantly greater pore volumes were detected for the powders compared to the powder compact. (It is noted that the total specific pore volume for the Series II 85/15 powder was ~0.052 cm^3/g (see Table 4.18) which is in reasonable agreement with the value of 0.035 cm^3/g measured for the Series II 60/40 composite powder compact. This may be attributed to the fact that the 85/15 composite particles, and hence the pores associated with the loose packing of these particles, are larger (compared to the other composite powders listed in Table 4.18) due to the relatively thick coatings. Therefore, a significant fraction of these pores would not be detected and a relatively low pore volume would be obtained.) The dV/dD plots in Figure 4.26B show that the powder exhibited a bi-modal pore size distribution whereas the compact exhibited a tri-modal distribution. The intermediate pores, which is presumably associated with the presence of agglomerates (see discussion in

previous paragraph), are seemingly absent in the powder sample. The differences in the specific pore volumes and dV/dD between the loose powder and the powder compact have not been clearly understood yet. However, the comparison shown in Figure 4.26B may not be rigorously valid due to the following two reasons. First, the compacts were prepared using Series II composite powder while Series III powder was used for the loose powder sample. The specific surface area of the powders used in the two samples were different (~14 and ~27 m^2/g, respectively). Therefore, it may not be reasonable to compare the samples prepared from the two powders. Second, the compact used in this study contained PS-derived pores, in addition to the inter-particle porosity. Furthermore, as discussed earlier, the composite particle packing in the PS-containing compacts is presumably different from the packing in the absence of the PS particles. Therefore, it may be necessary to carry out gas adsorption pore size measurements on compacts prepared using Series III composite powders and without the presence of PS particles, in order to make reliable comparisons between the pore size distribution for loose powders and powder compacts.

Table 4.11 shows that the bulk densities determined using ethanol and methanol as the media were nearly identical to those determined using water medium (Table 4.11) but the open porosities were significantly lower (by ~7-9%). This indicates that ethanol and methanol failed to infiltrate all the pores during the saturation step. In addition, the density results were identical for measurements made in ethanol using saturation times of 30 min and 3 h. This seems to indicate that further infiltration was not possible by using long saturation times. One of the possible explanations for the differences in porosities determined using the different media is the difference in their molecular sizes. The length of the O-H bond is 0.94Å, while the lengths of the C-C, C-H, and C-O bonds are 1.52, 1.11,

and 1 43Å, respectively Therefore the H-O-H chain length in the water molecule is 1.88Å, the H-C-O-H chain length in methanol is 3 48Å, and the H-C-C-O-H chain length in ethanol is 5Å[39] If these values were treated as the "molecular" sizes for the different media, ethanol and methanol had slightly higher "molecular" sizes compared to that for water However, it is difficult to conceive that there exists a significant number of pore channels in the narrow size range of 1.88-3 48Å (which is accessible to water but not methanol or ethanol) in order to account for the differences in the measured porosities using water and methanol as the media. Another possible explanation for the density differences observed between the measurements in water and alcohol media is poorer wettability of the alcohols (relative to water) on the composite particles. However further experiments, such as contact angle measurements, are necessary to confirm this hypothesis.

Pore size and Archimedes density measurements were also carried out on SiO_2 and Al_2O_3 samples used in studies conducted by Wang [K. Wang and M.D Sacks, personal communication, 1996] The SiO_2 samples were prepared by slip-casting a well-dispersed (pH ~ 8) suspension of ~0.18 μm dia. SiO_2 particles. The samples were pre-sintered for 6 h at 700°C in air prior to the density measurements. The Al_2O_3 samples were formed by slip-casting a pH ~ 4 suspension and the samples were pre-sintered for 1h at 900°C in air Table 4.12 shows the results from the Hg porosimetry and Archimedes displacement measurements on these samples [K. Wang and M.D Sacks, personal communication, 1996]

[39] This assumption for chain lengths is not rigorously correct since the bond angles were not taken into consideration. For example, the H-O-H bond angle in water is 105° and not 180° as it is implicitly assumed in the current analysis. However this approach is useful in comparing the relative sizes of the different molecules.

Table 4 12 Density and Porosity Values for SiO_2 and Al_2O_3 Determined by Hg Porosimetry and Archimedes Displacement Method.

Sample	Archimedes Method				Hg Porosimetry
	Medium (saturation time)	ρ_{bulk} (g/cm^3)	O P * (%)	$\rho_{apparent}$ (g/cm^3)	Porosity (%)
Al_2O_3	water	2 648	32 4	3 921	
	(2h)	2 641	32 8	3 930	30 8
	ethanol	2 672	32 3	3 948	
	(1h)	2 672	32 4	3 952	
SiO_2	water (2h)	1.307	40 1	2.182	34 0

* open porosity

The open porosity values determined by the Archimedes method for the Al_2O_3 samples were in reasonable agreement with the value determined by porosimetry (~32.5% vs. ~31 0%, respectively). In contrast, there was ~6% difference in the corresponding values determined for the SiO_2 sample This is in apparent contradiction with the observations of Vora [Vor90] that the porosity of 750°C pre-sintered SiO_2 compacts (prepared using the same method as that used in the current study) determined by mercury porosimetry and by the Archimedes method using water as the medium were similar (e.g., ~34 9% and ~35 3%, respectively, for the two methods[Vor90]) However, the SiO_2 particles used in Vora s work [Vor90] were significantly larger than those used in the compacts prepared by Wang [K Wang and M.D Sacks, personal communication, 1996] (~0 60 μm vs. ~0 18 μm dia. respectively) Therefore, it is possible that much finer pore channels were present in the latter compacts which may have lead to incomplete intrusion of mercury in these samples

4.2.3. Sintering and Microstructure Evolution

The pre-sintered samples were heated to temperatures in the range 1000-1400°C. Figures 4.27 and 4.28 show plots of bulk density and open porosity, respectively, versus sintering temperature for compacts prepared with and without PS particles. Figure 4.29 shows plots of relative density versus temperature for the same compacts. Samples prepared without PS particles reached a maximum density of ~2.61 g/cm^3. In contrast, compacts containing the PS particle-derived pores attained a transient maximum density of ~2.40 g/cm^3 (~92% relative density) at ~1250°C but underwent further densification when heated at temperatures greater than 1300°C. The sintering behavior of the latter samples may be explained as follows. At relatively low sintering temperatures (≤ 1250°C), the porosity associated with the composite powder packing reduces as the compacts undergo densification. The reduction in bulk volume associated with this densification results in a corresponding shrinkage of the PS particle-derived pores. If the total porosity in the pre-sintered compact is assumed to be equal to the open porosity determined by Archimedes measurements (in deionized water), the presintered sample with the PS particle-derived pores contained ~55.3 vol% solids. Assuming the volume ratio of SiO_2/Si_3N_4 and PS particles (or the voids created by the pyrolysis of these particles) to be ~88/12, the relative density of the as-cast compact was 55.3/0.88 = 62.8%. The corresponding inter-particle porosity in the sample is 100 - 62.8 = 37.2%. The elimination of this porosity would lead to a corresponding (i.e., 37.2%) shrinkage of the PS particle-derived pores. Based upon this shrinkage, the final concentration of the PS particle-derived pores can be calculated as 0.628×12 = 7.5 vol%. This is in excellent agreement with the amount of closed porosity

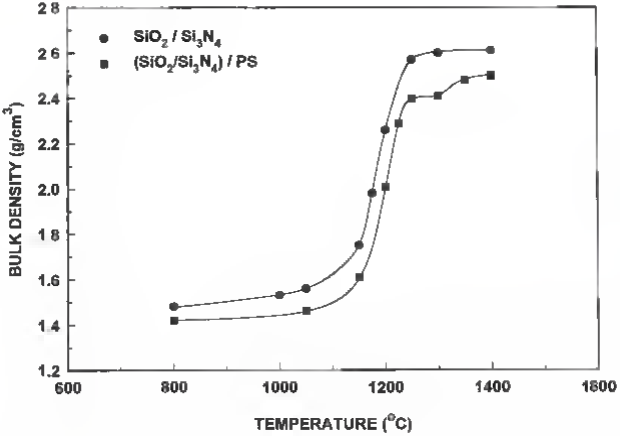

Figure 4.27 Plots of bulk density vs temperature for 60/40 SiO_2/Si_3N_4 samples prepared with and without PS particles

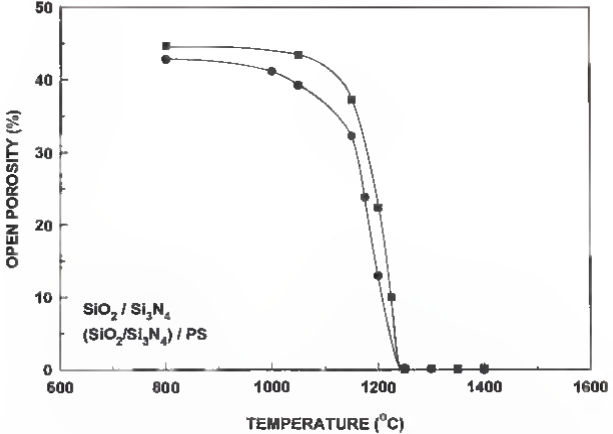

Figure 4.28 Plots of open porosity vs. temperature for 60/40 SiO_2/Si_3N_4 samples prepared with and without PS particles.

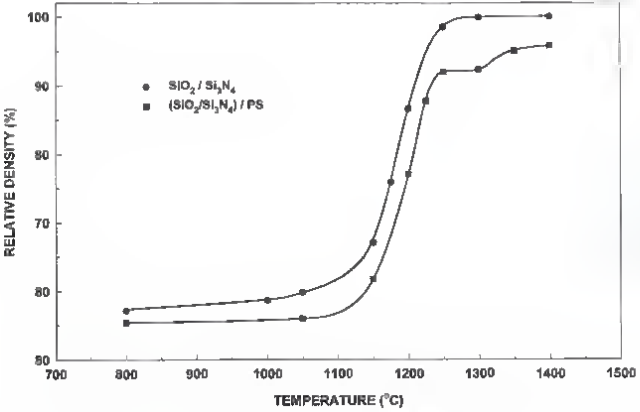

Figure 4.29 Plots of relative density vs temperature for 60/40 SiO_2/Si_3N_4 samples prepared with and without PS particles.

(~7 6 vol%, see Appendix E) in the compact sintered to 1250°C As densification of the powder matrix occurs, the PS particle-derived pores are gradually "pinched-off" or become isolated from each other The open porosity is almost completely eliminated at 1250°C for both compacts (Figure 4.28) which indicates that the kinetics of interparticle pore shrinkage is apparently not significantly affected by the presence of the PS particle-derived pores At this stage the PS particle-derived pores exist as almost isolated, closed pores. When the sample is heated to temperatures ≥ 1250°C, the PS particle-derived pores begin to shrink significantly, thus leading to a further increase in the bulk density

Some investigators [Kat92, Ran93] have studied the effect of PS concentration on the nature of the porosity in sintered glass-ceramic matrices. Kata and Shimada [Kat92] prepared green tapes by tape-casting a suspension containing a mixture of ~15 wt% quartz glass / 20 wt% cordierite / 65 wt% borosilicate glass powder (the average particle sizes of the ceramic and glass constituents were ~3.2 μm and ~3 0 μm, respectively) and PS particles with an average diameter of ~18 μm. Mixtures containing 0-49 vol% PS particles (in solids) were prepared Substrates were fabricated using a conventional green sheet lamination technique. The maximum amount of isolated, closed porosity (without the presence of any open porosity) achieved in these samples was ~13 vol% using a PS concentration of ~23 vol% (in the solid volume) in the green sample Higher loadings of PS resulted in the formation of residual open porosity since the volume fraction was above the percolation threshold, i e, the critical concentration required to form a contiguous network [Zal83] Randall [Ran93] used PS particles (~4 6 μm diameter) to incorporate controlled, closed porosity in borosilicate glass (BSG, average particle size ~1 8 μm)/Si_3N_4 (average particle size ~1.2 μm) mixed powder matrices Samples with an overall BSG/Si_3N_4 volume

ratio of ~80/20 were prepared with PS contents in the range of 0-20 vol% (in solids). The maximum amount of closed porosity (without the presence of any open porosity) achieved was ~11 vol% corresponding to a PS content of 20 vol% in the green sample. Based on these results, it is speculated that higher amounts (presumably up to ~13 vol%) of isolated, closed porosity can be incorporated in SiO_2/Si_3N_4 matrices by using greater amounts of PS (20-25 vol% vs. 12-16 vol% which was used in the current study) in the powder mixture.

Figure 4.30 shows the SEM micrograph of a typical cross-section of the fracture surface of a sample that was sintered at 1300°C. It is evident that the pores are nearly spherical and relatively well-distributed in the dense composite matrix. The typical micrograph of a polished and etched surface of the same sample is shown in Figure 4.31. The microstructure of the SiO_2/Si_3N_4 "matrix" is identical to that observed for samples that were processed without the PS particles (Figure 4.16 (B)), i.e., the SiO_2/Si_3N_4 matrix is almost fully dense and the Si_3N_4 particles are uniformly dispersed in the amorphous SiO_2 matrix. It is noted that the shape of the PS-particle derived porosity depends on the green forming method. Materials for high speed LSI packaging applications are generally fabricated using green sheet lamination techniques [Tum91]. As described earlier, Kata and Shimada [Kat92] used PS particles to introduce controlled, closed porosity in glass/ceramic matrices. It was found that the spherical PS particles tended to deform under the stresses associated with the green sheet lamination process and that the deformation resulted in "egg-shaped" pore geometry in the heat-treated samples. In the current investigation, the porosity was nearly spherical (Figure 4.30) since the processing steps (i.e., slip-casting and pressureless sintering) do not involve any significant stresses.

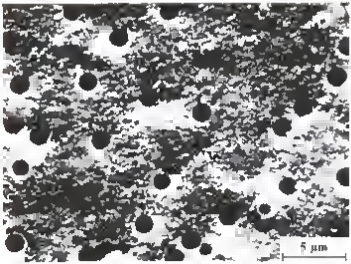

Figure 4.30 SEM micrograph of a fracture surface of a 60/40 composite powder sample (sintered at 1300°C,2h) showing PS-derived pores.

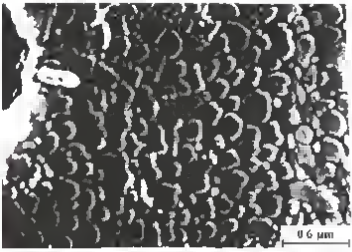

Figure 4.31 SEM micrograph of a polished and etched surface of a 60/40 composite powder sample (sintered at 1300°C,2h) processed with PS particles

4.2.4 Dielectric Properties

Samples for dielectric constant measurements were prepared using a ~46/14 volume ratio of 60/40 SiO_2/Si_3N_4 powder and PS particles. Dielectric properties were measured on compacts sintered for 2 h at 1300°C. While the sample processed without PS was almost fully dense (i.e., no residual porosity), the sample containing the PS particle-derived pores had ~10% total porosity (~0.5% open porosity) as determined by the Archimedes displacement method (Table 3.8). The dielectric properties of these composites were compared with those corresponding to fully dense and porous SiO_2 (~9% total porosity and ~0.3% open porosity) compacts (Table 3.8). Figure 4.32 shows the plots of dielectric constant vs. log frequency for these samples. The dielectric constant values for all the samples are independent of the frequency indicating that there was no polarization mechanisms existing in the frequency range 1.1 kHz - 10 MHz. The dielectric constant of SiO_2 (~3.8) was in excellent agreement with reported values for fused silica (~3.78 for Corning 915°C fused silica [Hip54]) and dense sol-gel derived silica (~3.8 [San89, Gup96]). The dielectric constant of the 60/40 SiO_2/Si_3N_4 sample ($\varepsilon_r \sim 4.9$) was higher than that of SiO_2 ($\varepsilon_r \sim 3.8$) due to the presence of the relatively high dielectric constant particulates in the matrix[90]. (The dielectric constant has been reported to be in the ranges of ~5.8 - 7.5 for high-purity CVD Si_3N_4 films [Hol95, Lem92] and ~6.0 - 6.5 for hot-pressed Si_3N_4 with 1-3 wt% Y_2O_3 additives [Sch84, Coo83]). As expected, the incorporation of closed porosity (PS particle-derived pores) resulted in lower dielectric constants for both SiO_2 ($\varepsilon_r \sim 3.4$) and the 60/40 SiO_2/Si_3N_4 ($\varepsilon_r \sim 4.4$) samples. The dielectric properties of the

[90] Composite models cannot be used to reliably predict the dielectric constant of the composite due to the wide range of dielectric constant values reported for Si_3N_4.

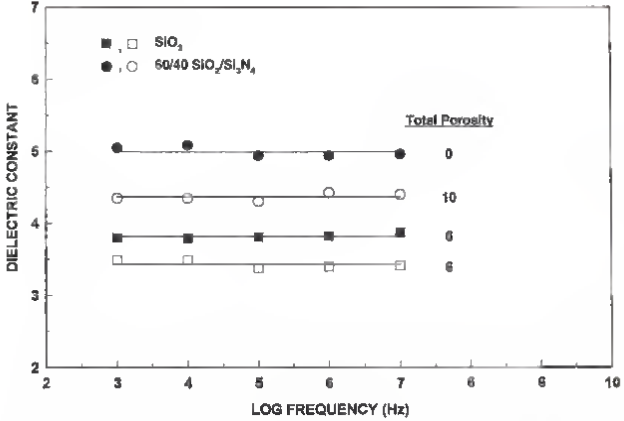

Figure 4.32 Plots of dielectric constant vs frequency for fully dense and porous SiO_2 and 60/40 SiO_2/Si_3N_4 samples

SiO_2/Si_3N_4 composites are comparable to or better than values reported for various glasses and silicate glass/crystalline ceramic composites used for microelectronic packaging applications (Table 2.1)

Dielectric properties were also measured for partially sintered composite samples (with total pore contents of ~24% and ~33%, respectively) prepared without PS particles. (The samples were sintered for 2h at 1175 and 1150°C, respectively, as shown in Table E-III in Appendix E.) Figure 4.33 shows the plot of dielectric constant vs log frequency for these samples compared to the composite powder samples from Figure 4.32 (i.e., with ~0% and ~10% porosity). The dielectric constant of multi phase materials can be predicted from the properties of the constituent phases using various mixing rules. The dielectric constant (ε^*) of a suspension containing a small volume fraction (V_1) of spherical particles (dielectric constant ε_1) in a continuous matrix (dielectric constant ε_2) can be described using the Rayleigh mixture formula [Hal76].

$$\varepsilon^* = \varepsilon_2 \frac{[2\varepsilon_2 + \varepsilon_1 + 2V_1(\varepsilon_1 - \varepsilon_2)]}{[2\varepsilon_2 + \varepsilon_1 - V_1(\varepsilon_1 - \varepsilon_2)]} \qquad (4.3)$$

Hashin and Shtrikman [Has62] established bounds for isotropic composites with arbitrary geometry of the second phase. The upper bound, $\varepsilon^*_{(+)}$, is mathematically equivalent to ε^* in eq. (4.3). The lower bound, $\varepsilon^*_{(-)}$, can be expressed in the usual notation as,

$$\varepsilon^*_{(-)} = \varepsilon_1 + \frac{(1 - V_1)}{[1/(\varepsilon_2 - \varepsilon_1) + (V_1/3\varepsilon_1)]} \qquad (4.4)$$

In the current treatment, the SiO_2/Si_3N_4 composite material was considered as the matrix phase with $\varepsilon_r = 4.94$ (average value at 1 MHz). The porosity ($\varepsilon_r = 1$) was treated to be the second phase. The data from Figure 4.33 was used to plot the dielectric constant (at 1

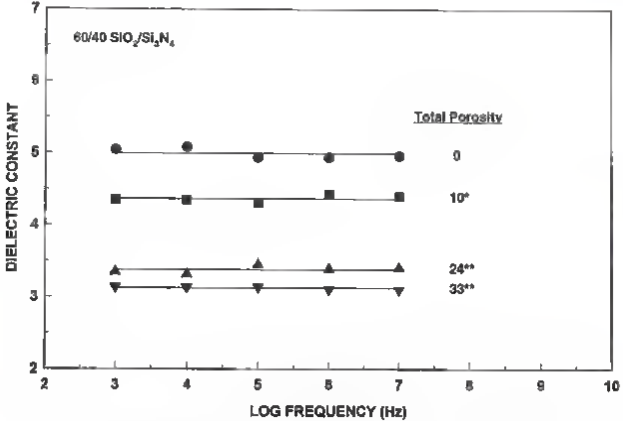

Figure 4.33 Plots of dielectric constant vs. frequency for 60/40 SiO_2/Si_3N_4 samples with varying amounts of total porosity (*) PS particle-derived, closed porosity (~0 5% open porosity). (**) open porosity

MHz) as a function of the total porosity (Figure 4.34). Figure 4.34 also shows the plots from the theoretical predictions corresponding to eqs. (4.3) and (4.4). The sample with ~10% porosity consisted of a dilute dispersion of closed, nearly spherical voids. Therefore, the dielectric constant of this sample can be predicted by the Rayleigh mixture formula (eq. 4.3), as indicated by the solid line in Figure 4.34. In contrast, the samples with ~24% and ~33% total porosity did not follow eq. (4.4) because they contained interconnected (i.e., non-isolated) pores with non-spherical geometry. However, the measured values of dielectric constant lie within the Hashin-Shtrikman bounds (indicated by the solid and dashed lines in Figure 4.34).

Table 4.13. Loss Tangent (tan δ) Values for SiO_2 and 60/40 SiO_2/Si_3N_4 Samples

Sample Description	tan δ at 1MHz
SiO_2 (~0% porosity)*	0.0001
SiO_2 (~9% porosity)*	0.0001
60/40 SiO_2/Si_3N_4 (~0% porosity)*	0.0002
60/40 SiO_2/Si_3N_4 (~10% porosity)*	0.0002
60/40 SiO_2/Si_3N_4 (~24% porosity)	0.0042
60/40 SiO_2/Si_3N_4 (~33% porosity)	0.0058

* These samples contained almost no open porosity, i.e., the samples were hermetically sealed.

Table 4.13 lists the loss tangent (tan δ) values for fully dense and porous SiO_2 and SiO_2/Si_3N_4 samples. The samples that are fully dense (i.e., almost no porosity) and the samples that contain only closed porosity (i.e., the PS particle-derived pores) are hermetically sealed. In contrast, the samples with open porosity are susceptible to infiltration of atmospheric contaminants (e.g., moisture) from the surface, which would tend

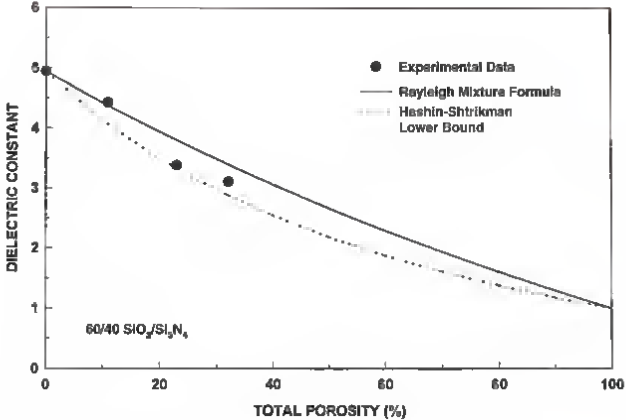

Figure 4 34 Plots of dielectric constant vs porosity for 60/40 SiO_2/Si_3N_4 samples showing comparisons with theoretical predictions of eqs (4.3) and (4 4)

to increase dielectric losses. As expected, low loss factors (0.0001 - 0.0002) were observed for hermetic samples whereas the samples with open porosity exhibited much higher loss factors (0.0040 - 0.0060).

4.2.5. Mechanical Properties

Table 4.14 lists mechanical properties for SiO_2 and the 60/40 SiO_2/Si_3N_4 composite powder compacts. The SiO_2 samples had an average strength of 61 MPa, average Vicker's hardness of 6.9 GPa, and average fracture toughness of 1.1 $MPa \cdot m^{1/2}$. These values are comparable to reported values for sol-gel derived (Vicker's hardness ~ 7 GPa [Kan95]) and fused silicas (average strength ~50 MPa [Lyo94]). SEM observations of typical fracture surfaces of SiO_2 indicate that surface defects (e.g., machining defects) are the controlling flaws for fracture (Figure 4.35). The fully dense SiO_2/Si_3N_4 composite sample had an average flexural strength of 183 MPa, average Vicker's hardness of 8.7 GPa and average fracture toughness[91] of ~1.7 $MPa \cdot m^{1/2}$. These properties are significantly better than the values determined for SiO_2 (Table 4.14) and are comparable to values reported for various silicate glass/crystalline ceramic composites and crystallized glass-ceramics (e.g., cordierite) with low dielectric constant (Table 2.1).

The increase in toughness (1.7 vs. 1.1 $MPa \cdot m^{1/2}$) due to the inclusion of Si_3N_4 in the SiO_2 matrix may be partly attributed to crack deflection mechanisms as illustrated by a typical crack path shown in Figure 4.36A. (Some isolated residual pores, presumably due to incomplete densification, are also observed in the microstructure.) However, a higher

[91] See Appendix D for the detailed measurement and calculation procedures.

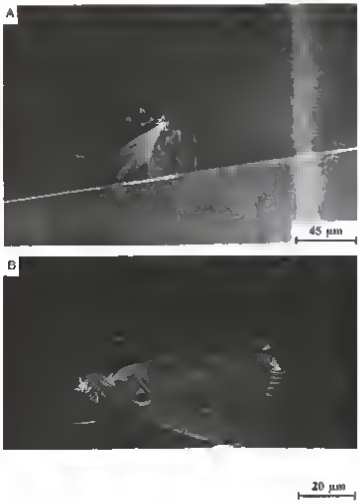

Figure 4 35 SEM micrographs of fracture surfaces showing controlling flaws in flexure-tested SiO_2 samples (A) Sample #3, and (B) Sample #8

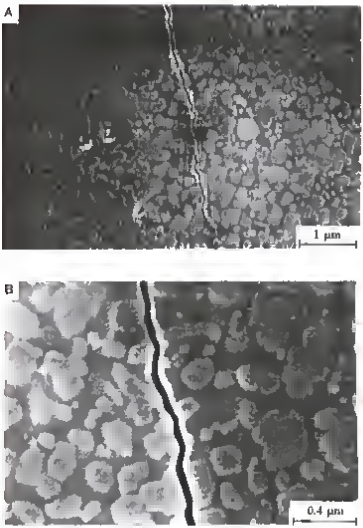

Figure 4 36 SEM micrographs of a polished surface of a 60/40 sample showing a typical crack path at (A) a low magnification and (B) a high magnification. The crack was produced by Vicker's indentation and the surface was etched with HF solution.

magnification micrograph (Figure 4.36B) of the same crack path shows that in some regions, the crack propagates in an intragranular mode (i.e. through the Si_3N_4 inclusions). The increase in toughness may also be attributed to the increases in the elastic modulus and the fracture strength.

Table 4.14 Mechanical Properties of SiO_2 and 60/40 SiO_2/Si_3N_4 Samples

Property	SiO_2 (~0% Porosity)	60/40 SiO_2/Si_3N_4 (~0% Porosity)	60/40 SiO_2/Si_3N_4 (~9% Porosity)[a]
Flexural Strength (MPa)	61 (± 7)	183 (± 33)	183 (± 43)
Vicker's Hardness (GPa)	6.9 (± 0.3)	8.7 (± 0.2)	6.5 (± 0.1)
Fracture Toughness ($MPa{\cdot}m^{1/2}$)	1.1 (± 0.1)	1.7 (± 0.1)	-

[a] Determined by quantitative microscopy measurements.

The incorporation of ~9% closed porosity (i.e., the PS particle-derived pores) resulted in a lower average hardness (6.5 GPa) but the average flexural strength remained the same (183 MPa).[92] The latter result indicates that the closed, spheroidal pores are not the strength-limiting flaws in the 60/40 SiO_2/Si_3N_4 composites. Preliminary observations of the fracture surfaces suggests that the strength may be limited by uncontrolled processing defects, e.g., powder agglomerates which were not broken down during processing. Figures 4.37 and 4.38 show examples of selected fracture surfaces of a fully dense sample and a porous sample, respectively. The mirror-mist-hackle patterns on the fracture surfaces are characteristic of brittle fracture typically observed in glasses and glass-matrix

[92] The fracture toughness could not be determined on the porous sample because the cracks generated during indentation were not well-defined.

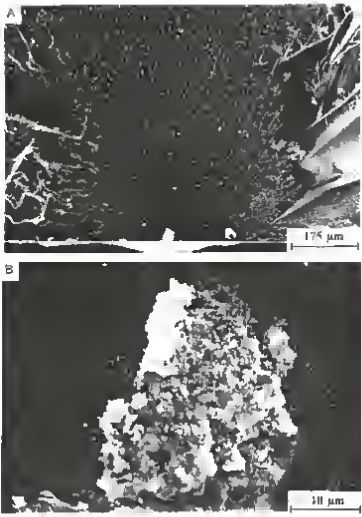

Figure 4.37 SEM micrographs of a fracture surface of a 60/40 sample (sintered at 1300°C 2h) (A) Low magnification micrograph shows the mirror mist-hackle pattern (B) Higher magnification micrograph shows the fracture origin which is a large processing defect (powder agglomerate)

Figure 4.38 SEM micrographs of a fracture surface of a 60/40 sample (sintered at 1300°C 2h) with PS-derived pores (A) Low magnification micrograph shows the mirror-mist-hackle pattern (B) Higher magnification micrograph shows the flaw (powder agglomerate) causing failure

composites[Mec84] Sintered powder agglomerates (Figures 4.37 and 4.38) apparently initiated fracture in both the SiO_2/Si_3N_4 samples. It is expected that the strength of these composites will be significantly increased by eliminating the relatively large powder agglomerates (e.g. by filtration of the suspension, etc.) during processing. The measured values of strength and fracture toughness were used to predict the critical flaw size that led to fracture. The fracture toughness, K_{Ic}, for a sample with a surface crack of depth, c, may be expressed as [Her96]

$$K_{Ic} = Y \sigma_f c^{1/2} \qquad (4.5)$$

where σ_f is the fracture stress (or flexural strength), and Y is a geometric parameter dependent on the flaw and specimen geometries, and the loading configuration. For crack sizes much smaller than the specimen thickness (typically for crack size to specimen size ratio of <5%), the value of Y for four-point bending has been determined to be ~1.9 [Her96]. (In the current study, the sample thicknesses were typically ~2 mm and therefore the value of Y is valid for crack sizes less than ~100 μm.) If a fracture stress value of 183 MPa and a fracture toughness value of 1.7 $MPa \cdot m^{1/2}$ (for the dense 60/40 composite samples, as shown in Table 4.14) are substituted in eq. (4.5), the predicted value of c is ~27 μm. This is in good agreement with the depth of the flaws evident in Figures 4.37 and 4.38, which are in the range of ~25 - 35 μm. It is important to note, however, that the flaw geometry is complex and more rigorous expressions of Y may be necessary for better accuracy in the calculations.

4.3 Effect of Composition on Densification and Creep Behavior

The results pertaining to the compacts prepared using Series III composite powders and Series II 85/15 composite powder will be described in this section. The characterization of the composite powders will be discussed in Section 4.3.1. This will be followed by a discussion (Section 4.3.2) of the methods used for the determination of true densities of composite powders. The analysis of results from densification and creep studies will be presented in Sections 4.3.3 through 4.3.5. The concept of "rigidity threshold" in composite powder compacts will then be introduced in Section 4.3.6. Section 4.3.7 will include the comparison of experimental data with existing theoretical models. Finally, an empirical model for the densification of composite powder compacts will be formulated in Section 4.3.8.

4.3.1 Characterization of Particles

Quantitative microscopy

Figures 4.39 - 4.41 show bright field TEM images of particles from Series III 50/50 and 60/40, and Series II 85/15 composite powder batches, respectively. Each figure shows particles with two different Si_3N_4 core particle sizes. It is evident that for a given powder batch, the coating thickness is qualitatively similar for the two particles.

For each composite powder batch, coating thickness measurements were made on 15-25 particles with a variety of core particle sizes. Figures 4.42 - 4.46 show plots of the area-based coating thickness (eq. (3.18)) vs. the area-based Si_3N_4 core particle diameter

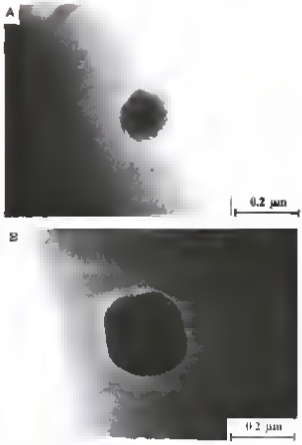

Figure 4.39 Bright-field TEM images of 50/50 microcomposite particles with (A) relatively smaller and (B) relatively larger core particles. The coating thickness is ~28nm for both particles

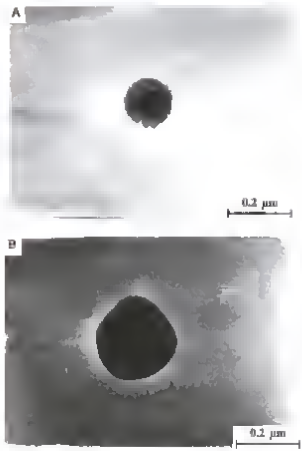

Figure 4 40 Bright field TEM images of 60/40 microcomposite particles with (A) relatively smaller and (B) relatively larger core particles The coating thickness is ~38nm for both particles

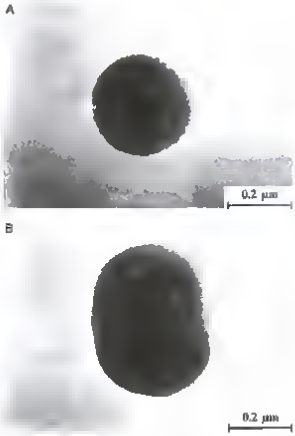

Figure 4.41 Bright-field TEM images of 85/15 microcomposite particles with (A) relatively smaller and (B) relatively larger core particles. The coating thickness is ~110nm for both particles.

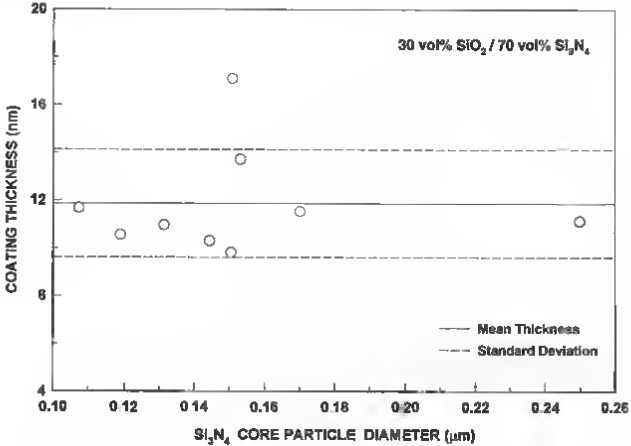

Figure 4 42 Plot of the area-based coating thickness vs Si_3N_4 core particle diameter determined on composite powder with an overall composition of 30/70 SiO_2/Si_3N_4

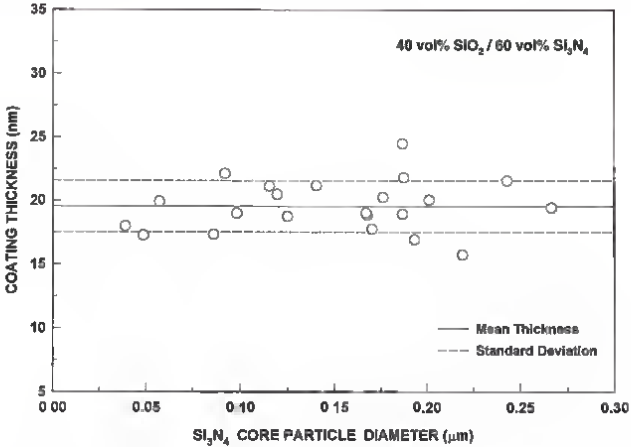

Figure 4.43 Plot of the area-based coating thickness vs Si_3N_4 core particle diameter determined on composite powder with an overall composition of 40/60 SiO_2/Si_3N_4

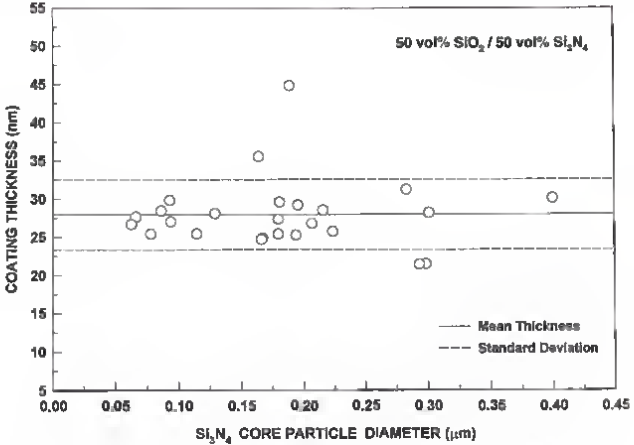

Figure 4 44 Plot of the area-based coating thickness vs Si_3N_4 core particle diameter determined on composite powder with an overall composition of 50/50 SiO_2/Si_3N_4

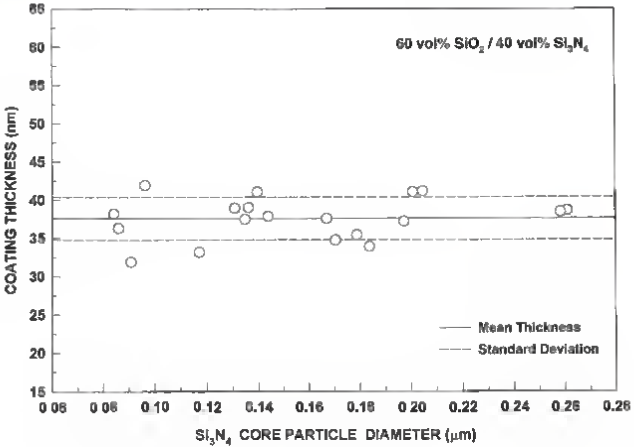

Figure 4.45 Plot of the area-based coating thickness vs Si_3N_4 core particle diameter determined on composite powder with an overall composition of 60/40 SiO_2/Si_3N_4

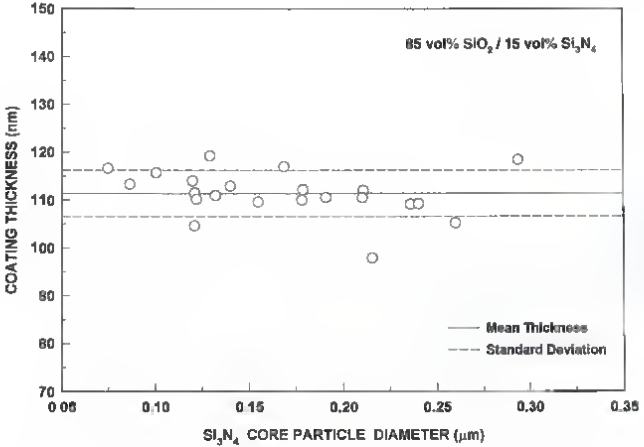

Figure 4.46 Plot of the area-based coating thickness vs Si_3N_4 core particle diameter determined on composite powder with an overall composition of 85/15 SiO_2/Si_3N_4

(eq (3 15)), for 30/70, 40/60, 50/50, 60/40, and 85/15 composite powders, respectively It is evident from these plots that for a given composite powder batch, the coating thickness is nearly independent of the core particle size Figure 4 47 shows a plot of average coating thickness as a function of the overall (or nominal) concentration[93] of SiO_2 in the composite powder As expected, the coating thickness increased for increasing concentrations of the SiO_2 coating phase If D is the diameter of a spherical core particle coated with a material of uniform thickness t, the volume fraction of the core particle in the composite, v_{core}, is given by,

$$v_{core} = (D / D+2t)^3 \qquad (4\ 6)$$

Figures 4 48 4 52 shows plots of the area-based volume fraction of Si_3N_4 in the microcomposite particle vs the area-based Si_3N_4 particle diameter, for 30/70, 40/60, 50/50 60/40, and 85/15 composite powders, respectively The solid lines in the plots represent the values obtained by substituting the average thickness values in Figure 4 47 into eq (4 6). The experimental data fitted very well to the values predicted by eq (4 6) as a consequence of the fact that for a given powder batch, the thickness was nearly constant over a wide range of core particle sizes.

It would be desirable to compare the average compositions predicted based on the QM measurements to the target (nominal) compositions. The weighted average composition for each batch was calculated using the expression

[93] This is the target value calculated from the amount of components in the coating suspension assuming that the precipitation of SiO_2 occurred with a 100% yield. Such values will be referred to as "nominal" values in all the following sections.

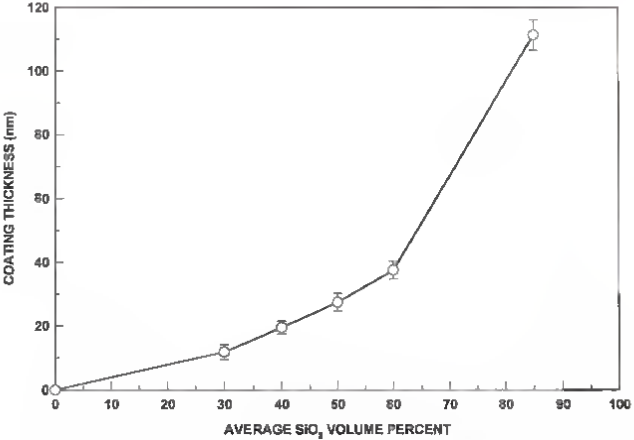

Figure 4 47 Plot of average coating thickness vs average volume percent SiO_2 for SiO_2/Si_3N_4 microcomposite particles

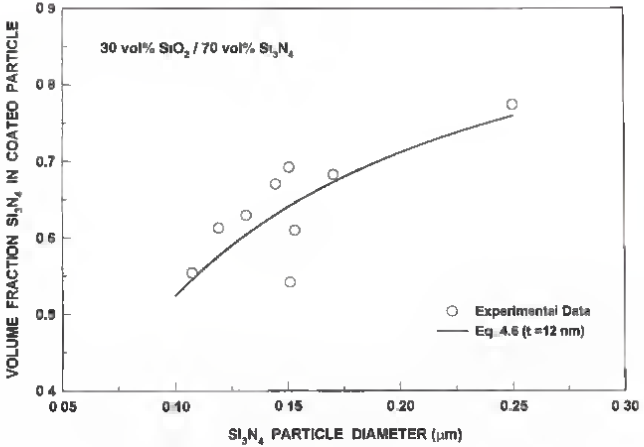

Figure 4.48 Plot of volume fraction Si_3N_4 in coated particle vs Si_3N_4 particle diameter determined on composite powder with an overall composition of 30/70 SiO_2/Si_3N_4

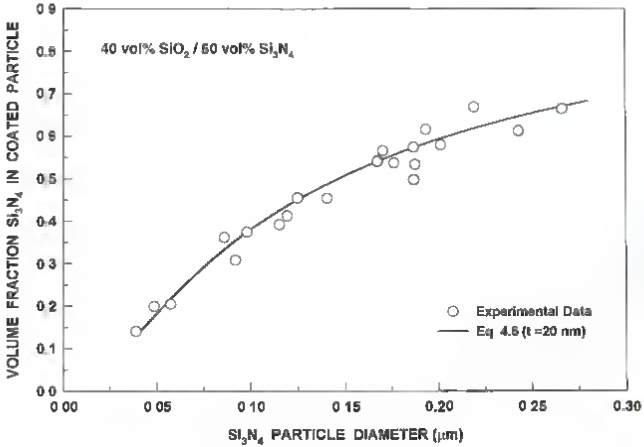

Figure 4.49 Plot of volume fraction Si_3N_4 in coated particle vs Si_3N_4 particle diameter determined on composite powder with an overall composition of 40/60 SiO_2/Si_3N_4

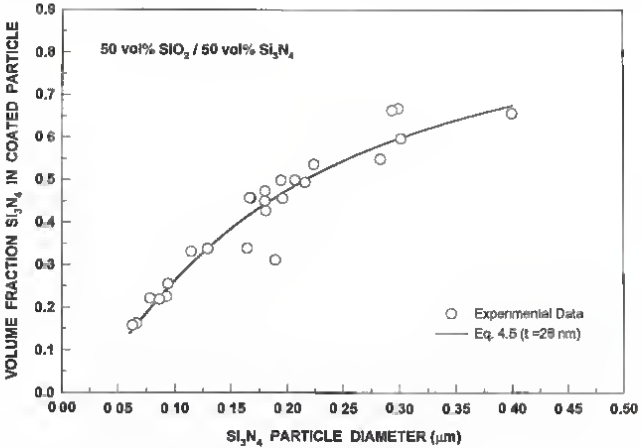

Figure 4.50 Plot of volume fraction Si_3N_4 in coated particle vs Si_3N_4 particle diameter determined on composite powder with an overall composition of 50/50 SiO_2/Si_3N_4.

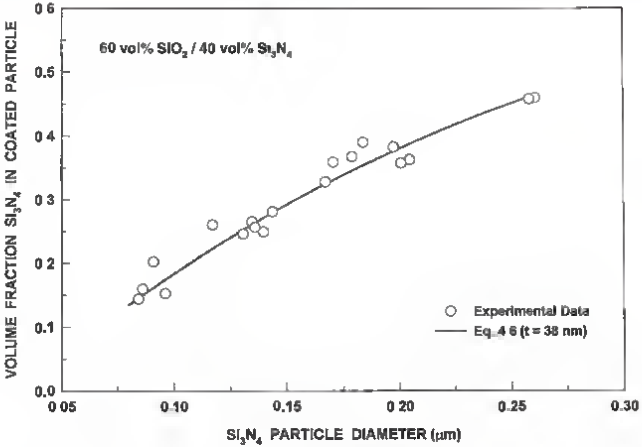

Figure 4 51 Plot of volume fraction Si_3N_4 in coated particle vs Si_3N_4 particle diameter determined on composite powder with an overall composition of 60/40 SiO_2/Si_3N_4

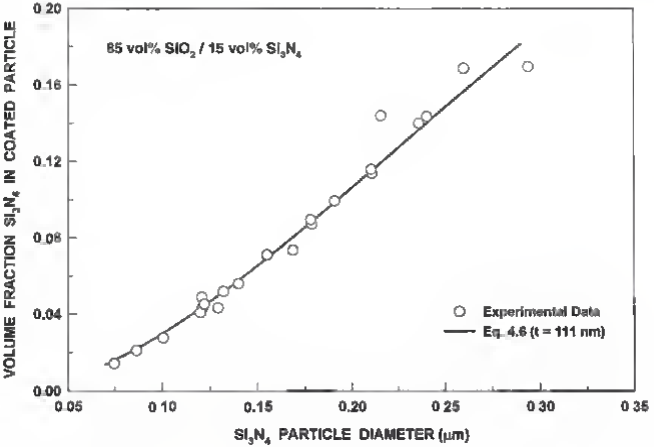

Figure 4.52. Plot of volume fraction Si_3N_4 in coated particle vs. Si_3N_4 particle diameter determined on composite powder with an overall composition of 85/15 SiO_2/Si_3N_4.

$$\bar{v}_{core} = \frac{\sum V^i_{comp} \bullet v^i_{core}}{\sum V^i_{comp}} \qquad (4.7)$$

where $\bar{v}_{core}$ is the average volume fraction of the cores (Si_3N_4 particles, in the current study), V^i_{comp} is the volume of the composite particle i (=$\pi d_c^3/6$, where d_c is the equivalent composite particle diameter for particle i, obtained from eq. (3.16)), v^i_{core} is the volume fraction of the core in the composite particle i, and $\sum_i$ is the summation over all the particles. Table 4.15 lists the calculated values of $\bar{v}_{core}$ compared to the expected (nominal) values. It is evident from Table 4.15 that there is significant deviation of the calculated values from the expected values. This is attributed to the statistical error associated with the low sample size (only 15 - 25 particles) used for the analysis.

Table 4.15 Comparison of Calculated and Expected values of $\bar{v}_{core}$ for Composite Powders.

Powder	$\bar{v}_{core}$ (calculated)	$\bar{v}_{core}$ (expected)
85/15	0.102	0.150
60/40	0.357	0.400
50/50	0.541	0.500
40/60	0.564	0.600
30/70	0.680	0.700

The shape factors of the core particles and the corresponding composite particles were also determined (i.e., using eqs. (3.23) and (3.24) respectively). The shape factors of the core and composite particles were generally greater than unity. The shape factors

of the composite particles were lower (and closer to unity) than the corresponding core particles. Figures 4.53 - 4.57 show plots of the percent reduction in shape factor vs. the shape factor of the core particle for 30/70, 40/60, 50/50, 60/40, and 85/15 powders, respectively. It is evident that the core particles with higher shape factors (i.e., the more irregular-shaped particles) undergo a greater reduction in shape factor (i.e., the particles become more spherical in geometry). In other words, the coating process tends to smooth off any irregular facets that may be present in the core particle[94]. This effect was less pronounced for powders with overall SiO_2 contents of ≤50 vol% (i.e., 30/70, 40/60 and 50/50 powders). This is clearly demonstrated by the combined plots for (1) 30/70, 40/60 and 50/50 powders (Figure 4.58), and (2) 60/40 and 85/15 powders (Figure 4.59), respectively. (For example, for a core particle with a shape factor of ~1.5, the reductions in the shape factor after coating are ~13% for the former set of powders vs. ~23% for the latter set.) The difference in shape factors between the core and the corresponding composite particle indicates that the coating thickness was not uniform within each composite particle. As mentioned earlier, the coating presumably "rounds off" any irregularities on the core particle surface which implies that the concave regions on the core particle surface have thicker coatings than the convex regions.

The results from the quantitative microscopic analysis provides some insight to the coating process. Since there are no concentration gradients present in the coating solution, no long range diffusion processes exist in this process. Since the environment around each core particle in the coating solution is isotropic, the growth of the coating is

[94] Some of the core particles with shape factors near unity (typically less than ~1.06) showed slight (<5%) negative reductions (i.e., positive increases) in shape factor after deposition of the coating. In other words, some composite particles were slightly more irregular in shape compared to the corresponding core particles.

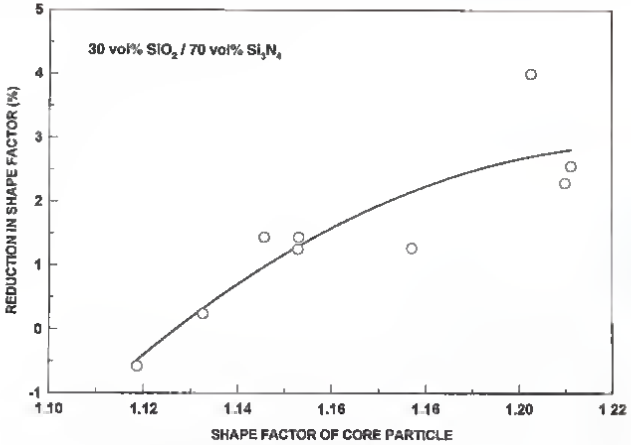

Figure 4 53 Plot of percent reduction in shape factor after coating vs. shape factor of core particle for composite powder with an overall composition of 30/70 SiO_2/Si_3N_4

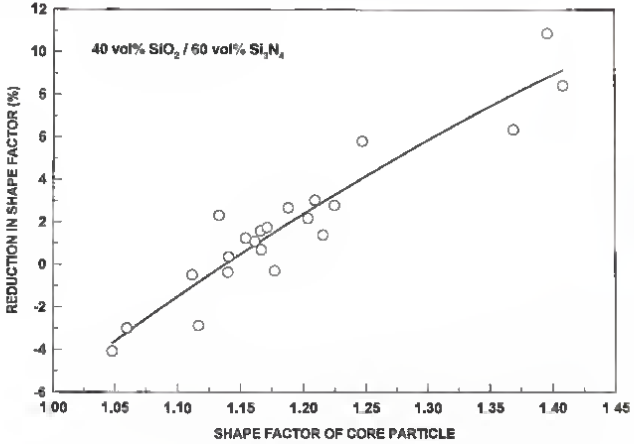

Figure 4.54 Plot of percent reduction in shape factor after coating vs. shape factor of core particle for composite powder with an overall composition of 40/60 SiO_2/Si_3N_4

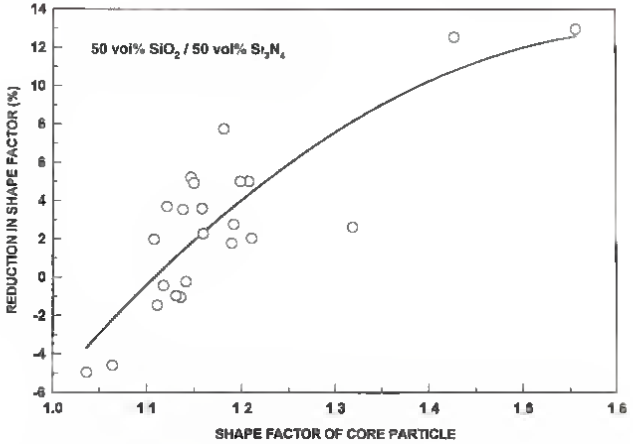

Figure 4 55 Plot of percent reduction in shape factor after coating vs shape factor of core particle for composite powder with an overall composition of 50/50 SiO_2/Si_3N_4

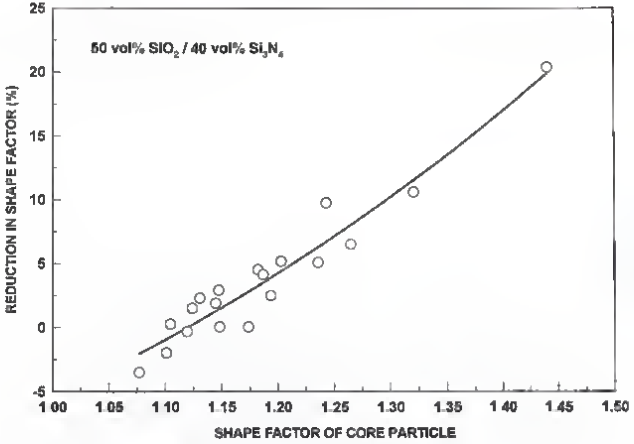

Figure 4.56 Plot of percent reduction in shape factor after coating vs shape factor of core particle for composite powder with an overall composition of 60/40 SiO_2/Si_3N_4

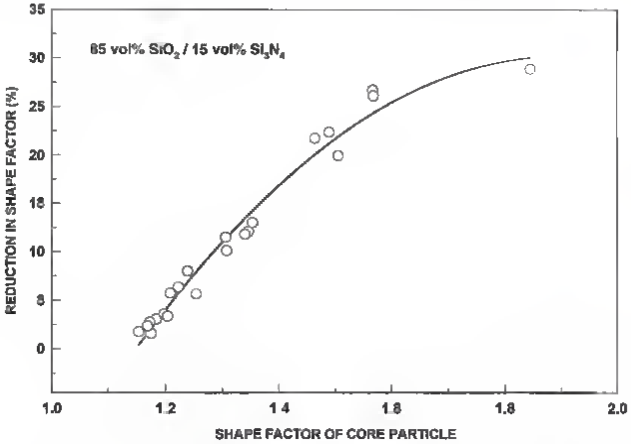

Figure 4 57 Plot of percent reduction in shape factor after coating vs shape factor of core particle for composite powder with an overall composition of 85/15 SiO_2/Si_3N_4

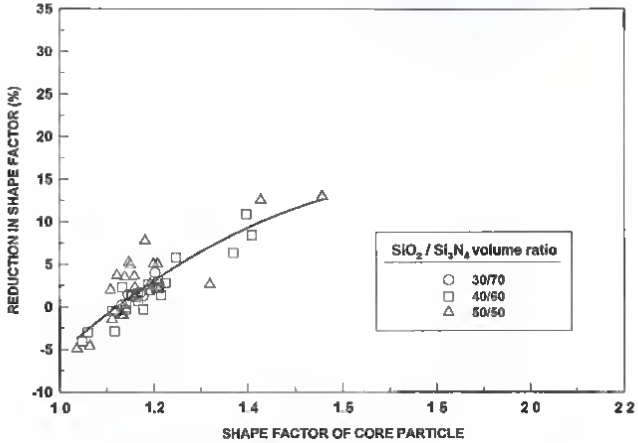

Figure 4.58 Plot of percent reduction in shape factor after coating vs. shape factor of core particle for composite powder with overall compositions of 30/70, 40/60, and 50/50

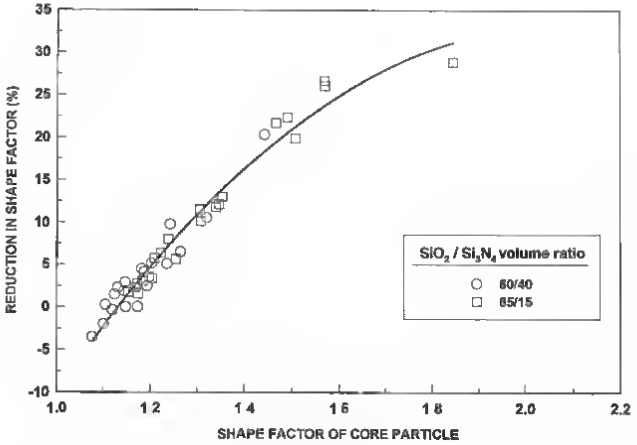

Figure 4.59 Plot of percent reduction in shape factor after coating vs shape factor of core particle for composite powder with overall compositions of 60/40 and 85/15

also isotropic in nature. Recently, DeHoff [R.T. DeHoff, personal communication, 1996] performed a simple simulation experiment to study geometric changes occurring during isotropic growth. The analysis is briefly discussed below. The boundary of any initial shape in two dimensions may be described in polar coordinates by a radius function $r(\theta)$. If this radius increases isotropically with a growth rate $G(\tau)$ (which may be a function of time τ, and not θ), then this adds to the initial radius $r(\theta)_{\tau=0}$. The total radius after time t may be expressed as

$$r(\theta)_{\tau=t} = r(\theta)_{\tau=0} + \int_0 G(\tau)\, d\tau \qquad (4.8)$$

For sufficiently long time t, the integral becomes large in comparison to $r(\theta)$. Since the integral is isotropic, the shape approaches a circle. Simulations [R.T. DeHoff, personal communication, 1996] showed that when $r(\theta)$ corresponds a square, the geometry evolves into a circle after substantial growth had occurred. An analogous argument will demonstrate this result in three dimensions, i.e., any initial shape will gradually evolve to a sphere if the growth is isotropic. In the current investigation, the reduction in shape factor from the core particle to the composite particle (i.e., the fact that the composite particle is more "spherical" than the corresponding core particle) may be a direct consequence of the isotropic nature of the growth of the SiO_2 layer during the coating process. Isotropic growth also results in greater reductions in shape factor corresponding to "thicker" coatings (i.e., lower times in eq. (4.8)) for a given core particle size. This could explain the observation that the reduction in shape factor was less pronounced in samples with overall SiO_2 contents of $\leq$50 vol% (Figure 4.58) in comparison to samples with overall SiO_2 contents of 60 and 85 vol% (Figure 4.59).

It is interesting to calculate "average" core particle sizes based on the average coating thickness determined from the quantitative microscopy and the nominal compositions. The nominal core volume fraction was substituted for v_{core}, and the coating thickness values shown in Figure 4.47 were substituted for t, in eq. (4.6). The resulting value of D is defined as the "average" core particle diameter and the value of (D +2t) is termed as the "average" composite particle diameter, D'. Table 4.16 shows the calculated values of D corresponding to various compositions.

Table 4.16. Estimated Values of "Average" Core Diameter, D

Sample	v_{core} (nominal)	t (μm)	D (μm)	D' (μm)
30/70	0.70	0.0119	0.19	0.21
40/60	0.60	0.0196	0.21	0.25
50/50	0.50	0.0275	0.21	0.27
60/40	0.40	0.0376	0.21	0.29
85/15	0.15	0.1114	0.24	0.46

The predicted "average" core diameters for all the powders was 0.21 ±0.03 μm. The low standard deviation is consistent with the fact that the starting core powders for all the composite powders was the same (i.e., lot2 Si_3N_4). The mean core diameter (i.e., the arithematic mean of all individual "average" diameters = 0.21μm) is significantly lower than the median particle size (~0.33 μm from Figure 3.1) measured for the lot2 Si_3N_4 core powder. The large difference in the two values may be explained by the fact that the value derived from the QM measurements, i.e., eq. (4.6), is the primary particle size. In contrast, the results shown in Figure 3.1 were obtained using suspensions which

may have contained some aggregates Another reason for the difference is based on the fact that the 'average" diameter obtained from QM measurements is actually the diameter of the core particle within a composite particle with composition identical to the overall composition. The median size determined from the photosedimentation method need not be representative of such a composite particle and therefore, it is not surprising that the sizes determined using the two methods are dissimilar However, it is important to note that, for a given composite powder batch, a composite particle corresponding to the core particle with a size equal to the "average" diameter obtained from QM measurements is representative of the powder batch, as regards the overall composition.

Particle size distribution

Figure 4 60 shows the particle size distribution plots for composite powders of different compositions These plots were made using averages of two individual measurements on each sample (the detailed results from the individual runs are shown in Appendix K). As discussed earlier (Section 4 1 1) the results from these plots are limited to the insight that the distribution curves generally shift to larger particle sizes as the amount of the SiO_2 (coating) phase is increased

Surface area and pore size analysis

As indicated earlier, two batches of coated powder were prepared for each composition. They are designated as A and B, respectively Table 4 17 shows the results from the BET surface area measurements.

The surface areas of the composite powders were not uniform among the two batches of any given composition. Although aging of the TEOS solution was found to

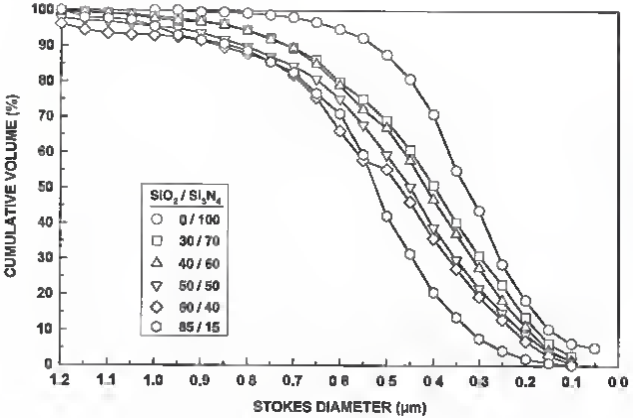

Figure 4 60 Particle size distribution plots for SiO_2/Si_3N_4 composite powders

influence the nature of the coating, the exact reasons for the the lack of reproducibility of the surface area are not clearly understood yet. However, the high surface areas shown in Table 4 17 can be attributed to the presence of porosity in the coating.

Table 4 17 BET Specific Surface Areas of Composite Powder Batches.

Powder Sample	BET Specific Surface Area (m^2/g)
Si_3N_4 Lot2	13
30/70 A	46
30/70 B	71
40/60 A	14
40/60 B	41
50/50 A	32
50/50 B	77
60/40 A	28
60/40 B	27
85/15	9

The batch B powders were used for a more detailed study in which the powders were calcined in static air to different temperatures (heating rate was 10°C/min and dwell time was 6 h) The adsorption and desorption isotherms for these samples are shown in Appendix J The isotherms exhibit apparent characteristics of Type IV according to the Brunauer Emmett-Teller (BET) classification [Gre82] A characteristic feature of the Type IV isotherms is the presence of hysteresis loops which may be explained by the existence of porosity in the powders Within a pore, the adsorbed film acts as a nucleus upon which condensation can take place when the relative pressure reaches the value given by the Kelvin equation (eq. (3 9)) In the converse process of evaporation (during

desorption), nucleation is not a factor, i.e., the liquid phase is already present and evaporation can occur spontaneously from the meniscus (i.e., the adsorbed film) as soon as the pressure is low enough. The differences in the nature of the condensation and evaporation processes result in the hysteresis behavior [Gre82]. Another possible explanation is that the SiO_2 coating contains interlinked pores with an ink-bottle type structure. Along the adsorption branch, condensation occurs in the bottle part when the pressure reaches the value determined by Kelvin's equation. However, an equivalent amount of evaporation does not occur at the same pressure during desorption, since the pore neck is blocked by a meniscus. It is interesting to compare the isotherm data with the nitrogen adsorption studies conducted by Sun et al. [Sun96]. Sun et al. [Sun96] prepared silica-coated α-Fe_2O_3 powders by adding distilled water to a mixture of a TEOS/ethanol solution and an α-Fe_2O_3/ethanol suspension. The powders were degassed at 120°C for 12h prior to surface area measurements by nitrogen gas adsorption. These powders showed hysteresis isotherms (Type IV), similar to those observed in the current study, and this behavior was attributed to pores with an ink-bottle structure present within the silica coating [Sun96].

Figures 4.61-4.65 show the plots of (a) cumulative pore volume and (b) differential pore volume (dV/dD), as functions of pore diameter, for composite powders calcined at different temperatures. It is clear from the dV/dD vs. pore diameter plots that all the powders show bimodal pore size distributions. This may be explained by the presence of relatively fine pores in the coating and relatively coarse interparticle pores (associated with particle packing in the powder sample). Mercury porosimetry experiments on pre-sintered composite powder compacts (e.g., Figure 4.24) had shown

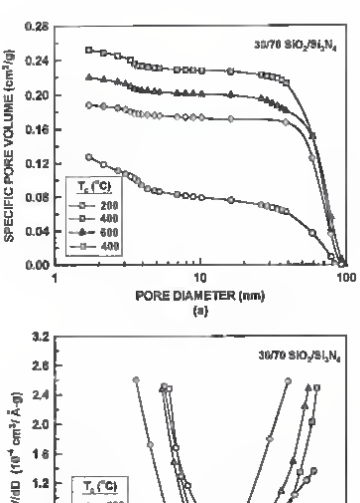

Figure 4.61 Plots of (a) pore volume and (b) specific volume frequency (dV/dD) versus pore diameter obtained by nitrogen gas adsorption for 30/70 SiO_2/Si_3N_4 powders calcined at various temperatures

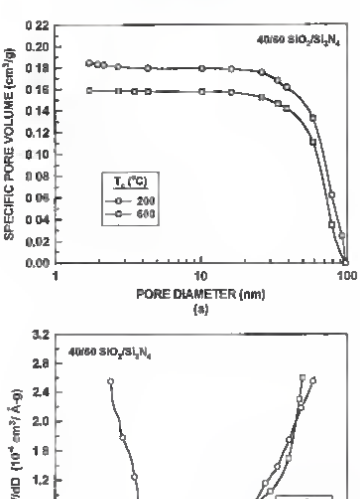

Figure 4.62 Plots of (a) pore volume and (b) specific volume frequency (dV/dD) versus pore diameter obtained by nitrogen gas adsorption for 40/60 SiO_2/Si_3N_4 powders calcined at various temperatures.

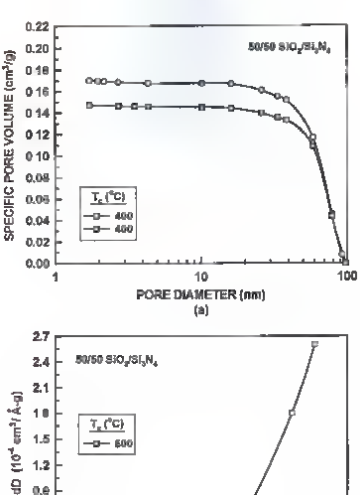

Figure 4.63 Plots of (a) pore volume and (b) specific volume frequency (dV/dD) versus pore diameter obtained by nitrogen gas adsorption for 50/50 SiO_2/Si_3N_4 powders calcined at various temperatures

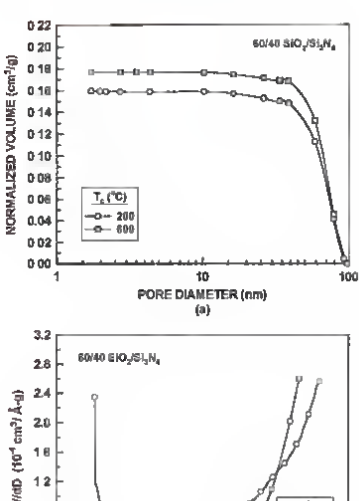

Figure 4.64 Plots of (a) pore volume and (b) specific volume frequency (dV/dD) versus pore diameter obtained by nitrogen gas adsorption for 60/40 SiO_2/Si_3N_4 powders calcined at various temperatures

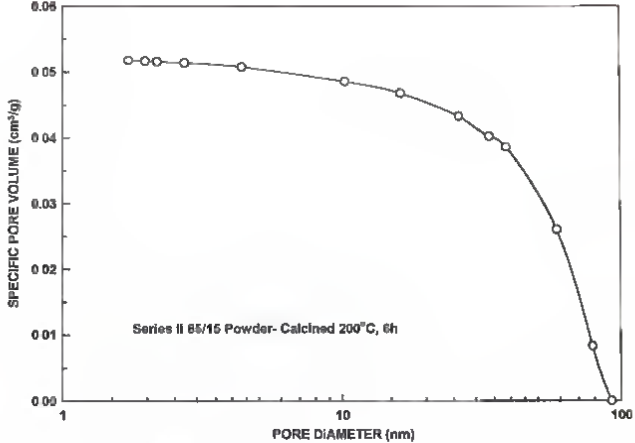

Figure 4 65 Plot of cumulative desorption pore volume vs pore diameter obtained by nitrogen adsorption for 85/15 SiO_2/Si_3N_4 powders calcined for 6h at 200°C

that the pore channel radii were typically in the range of 30-40 nm. Therefore, it is presumed that the smallest interparticle pores (corresponding to the regions of densest packing) in the powder samples used for gas desorption had similar pore channel radii. Since the points of inflection, i.e., the minima (defined as δ, the size demarcating the two types of pores), in the plots of dV/dD vs. pore diameter were typically in the range of 4-20 nm, it may be reasonable to assume that all the pores with diameters less than δ are associated with the coating and that the remaining pores are part of the interparticle porosity. Since the powders were loosely packed in the measuring cell, the packing geometry of each powder sample may be different. Therefore it would be more informative to compare the volume of pores associated with the coating, instead of the total pore volumes, for each sample.

Table 4.18 shows the detailed summary of results obtained from the surface area and pore size measurements on powders calcined to different temperatures. It is evident that the specific pore volume in the coating (i.e., volume of pores less than δ in diameter and micropore volume) and the BET specific surface area decrease as the samples are calcined at higher temperatures. This indicates that the porosity in the coating is gradually "sintered out" or eliminated (presumably due to viscous flow) as the powder is heated to higher temperatures. For the 40/60, 50/50, and the 60/40 samples, negligible porosity (<0.002 cm^3/g) remained in the coating after the 600°C calcination treatment. In contrast, the 30/70 samples retained a much higher amount (~0.015 cm^3/g) of porosity even after calcining at 800°C. This may be partly attributed to the relatively higher initial (200°C calcined) pore sizes in the 30/70 sample (~200Å for the 30/70 sample vs. ~60Å and ~40Å for the 40/60 and 60/40 samples, respectively). The differences in the pore

Table 4.18. Results from Surface Area and Pore Size Measurements on Calcined Series III Composite Powders

Sample	T* (°C)	δ* (Å)	Desorption Pore Volume (cm³/g)			Surface Area (m²/g)		
			Total	Pores < δ Å	Mic...	Total (BET)	External	M...
30/70 B	200	~200	0.127	0.0531	0.0090	71	55	16
	400	~100	0.252	0.0242	0.0050	58	49	9
	600	~100	0.220	0.0195	0.0019	46	42	4
	800	~90	0.188	0.0147	0.0005	36	35	1
40/60 B	200	~60	0.185	0.0052	0.0010	38	36	2
	600	~50	0.159	0.0008	0.0009	15	13	1
50/50 B†	200	--	--	--	0.0058	78	65	13
	400	~60	0.170	0.0028	0.0015	21	18	3
	600	~60	0.147	0.0016	0.0013	15	13	2
60/40 B	200	~40	0.160	0.0008	0.0008	20	18	2
	600	~40	0.177	0.0000	0.0010	13	11	2
85/15†	200	~40	0.052	0.0008	0.0014	10	7	2

* Calculation temperature

¶ minimum in the dV/dD plots (see Figures 4.61 - 4.65)

† Some of the raw data for this powder was lost due to computer hard drive failure.

sizes and pore volumes are directly compared in plots of specific pore volume and differential pore volume, vs pore diameter for the 200°C-calcined samples of different composition (Figure 4 66) It is also evident from Figure 4 66 (and Table 4 18) that lower values of δ (i e. smaller pore sizes in the coating) were observed for samples with lower initial surface area. (δ values of ~200 Å, ~60Å, and ~40Å, corresponding to BET surface areas of 71, 38, and 20 m^2/g, were observed for the 30/70, 40/60, and 60/40 samples, respectively) It is interesting to note that the value of δ for the 30/70 powder is higher than the coating thickness determined from quantitative microscopy experiments (~20 nm vs. ~12 nm, respectively) Therefore it is likely that some of the pore channels provide access to the core Si_3N_4 particle surface (Such channels were not evident from TEM observations presumably due to one or more of the following reasons: (1) The pore channels may be tortuous, i.e., not perfectly parallel to the electron beam. (2) The channel sizes may have been too small to be resolved at the magnifications used to this study (3) Some of the pore channels may have undergone some sintering under the electron beam)

The pore volumes shown in Table 4 18 were used to estimate the volume percent porosity in the volume of the composite as well as in the volume of the coating using the procedure described below The total specific pore volume in the coating was calculated to be the sum of the specific volume of pores in the size range of ~20Å to δ, and the specific micropore volume (i e , less than ~20Å). The true densities of the composite powders were calculated by assuming the nominal composition. The true densities of SiO_2 (coating) corresponding to calcination temperatures of 200 400, 600, and 800°C were assumed to be 2.08, 2 11, 2.16, and 2.20 g/cm^3 respectively [Sac84a] The true

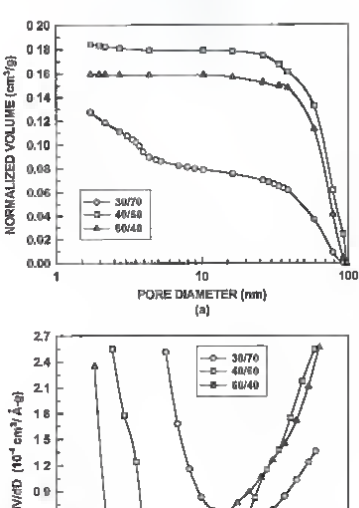

Figure 4.66 Plots of (a) pore volume and (b) specific volume frequency (dV/dD) versus pore diameter obtained by nitrogen gas adsorption for 30/70, 40/60 and 60/40 composite powders (calcined for ~6h at 200°C)

density of Si_3N_4 (core particles) was assumed to be 3.19 g/cm^3 [Bag92]. The reciprocal of the true densities of the composite powders were calculated to obtain the total specific solid volume (in cm^3/g). The specific volume of the coating was then calculated from the nominal composition. The specific solid and pore volumes were then used to calculate the volume fraction of porosity in the coating. Table 4.19 lists the calculated volume percent porosity in the composite powders.

Table 4.19 Calculated Vol% Porosity in the Coating and Composite Powder Volumes.

Sample	T* (°C)	Pore Volume in Coating (cm^3/g)	Total Solid Volume (cm^3/g)	Coating Volume (cm^3/g)	vol% Pores in Composite	vol% Pores in Coating
30/70 B	200	0.0621	0.3500	0.1050	15.1	37.1
	400	0.0292	0.3489	0.1047	7.7	21.8
	600	0.0214	0.3471	0.1041	5.8	17.0
	800	0.0152	0.3457	0.1037	4.2	12.8
40/60 B	200	0.0062	0.3642	0.1457	1.7	4.1
	600	0.0017	0.3600	0.1440	0.5	1.2
50/50 B	200					
	400	0.0043	0.3774	0.1887	1.1	2.2
	600	0.0029	0.3738	0.1869	0.8	1.5
60/40 B	200	0.0016	0.3962	0.2377	0.4	0.7
	600	0.0010	0.3852	0.2311	0.3	0.4
85/15	200	0.0022	0.4451	0.3784	0.5	0.6

* Calcination temperature

Table 4.19 shows that the 30/70 powder had a significant volume of porosity in the coating (~37%) after the 200°C calcination, whereas the other composite powders had much lower (<5%) amounts of porosity. As expected, the volume fraction of pores decreased as the calcination temperature increased. However, the 30/70 powders retained ~13 vol% porosity in the coating, even after calcination at 800°C. As described in the

next section, high pore volume fractions in the 30/70 composite powders play an important role in determining the electrokinetic behavior of the particles

Electrophoretic mobility

Table 4.20 shows the results from electrophoretic mobility measurements on Series III composite powders of different compositions at pH values in the range of ~8.0 to 8.7. Table 4.21 shows the corresponding results, measured at pH values in the range of ~9.0 - 9.3, for 30/70B powder calcined at temperatures in the range of 200 - 800°C.

Table 4.20 shows that the 40/50, 50/50, and 60/40 powders had average zeta potential values in the range of ~72 - 77 mV in the pH range of 8.3 - 8.7. These values are consistent with the reported values (Tables 4.1 and 4.3) for SiO_2 (e.g., -61.7 mV at pH~7.2) and Series I 60/40 composite powders (e.g., -77.0 mV at pH~7.8). In contrast, the 30/70 powders showed lower zeta potential values (~41 - 43 mV at pH in the range of ~7.9 - 8.0). One of the possible reasons for the lower values is the lower pH values used for the 30/70 samples (~8.0 vs. ~8.3-8.7 for the other compositions). However, as shown in Table 4.21, the zeta potential of the 30/70B sample was only ~43.7 mV even at a pH value of ~9.1.

Another possible explanation for the low zeta potentials measured for the 30/70 composite powders is the relatively thin and porous nature of the coatings (which presumably provides access to the core Si_3N_4 particle surface). Si_3N_4 is known [Mal92, Fuh89] to strongly react with the H^+ and OH^- in water leading to surface dissolution. At high pH values (i.e., above the isoelectric point for Si_3N_4), it was proposed that two types of reactions occur: (1) silanol-related surface reactions of the type [Mal92]

$$Si\text{-}OH \Leftrightarrow SiO^- + H^+ \qquad (4.9)$$

Table 4.20 Electrophoretic Mobility* (μ) and Zeta Potential (ζ) Data for Series III Composite Powders at pH Values in the Range of ~8.0 - 8.7

		μ μmecm/ V•s					average ζ
Powder	pH	T1	B1	T2	B2	average	(mV)
30/70 A	7.98	-2.82	2.78	-2.90	-2.54	-2.76±0.13	-42.4
30/70 B	7.93	-2.50	-2.57	-2.64	-2.58	-2.57±0.05	-41.1
40/60 A	8.73	-4.44	-4.47	-4.56	-4.41	-4.47±0.06	-74.5
40/60 B	8.60	-4.50	-4.35	-4.48	-4.37	-4.43±0.07	-74.5
50/50 A	8.68	-4.67	-4.78	-4.62	-4.48	-4.64±0.10	-77.1
50/50 B	8.72	-4.52	-4.66	-4.50	-4.44	-4.53±0.08	-74.5
60/40 A	8.30	-4.35	-4.21	-4.33	-4.13	-4.26±0.09	-71.9
60/40 B	8.40	-4.12	-4.26	-4.23	-4.22	-4.21±0.05	-71.9

*T top stationary level B bottom stationary level, 1 sample #1, and 2 sample #2

Table 4.21 Results from Electrophoretic Mobility Measurements on Calcined 30/70B Composite Powders at pH Values in the Range of ~9.0 - 9.3.

Calcination Temperature		μ μmecm/ Vas					average ζ
(°C)	pH	T1	B1	T2	B2	average	(mV)
60	9.06	-2.98	-2.79	-2.78	-2.86	-2.85±0.08	-43.7
200	9.22	-3.12	-2.92	-3.09	-2.89	-3.01±0.10	-46.2
400	9.04	-3.94	-3.96	-3.99	-3.98	-3.97±0.02	-66.8
800	9.31	-4.32	-3.99	-4.25	-4.31	-4.22±0.13	-71.9

*T top stationary level, B bottom stationary level 1 sample #1, and 2 sample #2

and (2) ammonia and amine-related surface reactions such as [Mal92]

$$Si_2NH \Leftrightarrow Si_2N^- + H^+ \quad (4.10a)$$

$$Si_3N_{4\,(S)} + 12H_2O_{(L)} \Leftrightarrow 3H_4SiO_{4(S)} + 4NH_{3(L)} \quad (4.10b)$$

$$NH_{3(L)} + H_2O_{(L)} \Leftrightarrow NH_4^+{}_{(L)} + OH^-{}_{(L)} \quad (4.10c)$$

Bergstrom and Pugh [Ber89] conducted leaching studies on the same grade of Si_3N_4 powder as that used in the current study. They obtained a high value of $[NH_4^+]$ (0.85 μmol per m^2 of powder) in the solution after leaching with high pH (adjusted to >9.0 by additions of NaOH) water, which clearly demonstrated that the zeta potential was controlled by the formation of amine species as represented by eq. (4.10). In the 30/70 powders used for the current study, the amine species that originate from the dissolution of the Si_3N_4 accessible to the composite powder surface (due to the porosity) may have strongly influenced the zeta potentials. Since the zeta potentials of Si_3N_4 were significantly lower than those for SiO_2 (e.g., -30 vs. -72 mV, respectively, for pH ~10 from Tables 4.1 and 4.2), lower zeta potentials were obtained for the 30/70 samples. Moreover, since (as shown in Table 4.19) calcination at progressively higher temperatures decreased the pore volume in the coating and thereby presumably decreased the amount of "exposed" Si_3N_4 surface, the zeta potentials gradually increased to values approaching that for SiO_2 particles. In contrast to the 30/70 powder, the other powders had thicker coatings and much smaller pore sizes and pore volumes (Table 4.19). Therefore, it is speculated that the amounts of the "exposed" Si_3N_4 surface in these powders were not significant enough to cause deviations of zeta potentials from the expected value (i.e., that of SiO_2).

Another possible explanation for the low zeta potentials of the 30/70 powders at low calcination temperatures is based on a gel model applied to the electrical double layer theory

[Jam87] A particle surface, which has acquired a charge or an electric potential different from the medium it is suspended in, accumulates a counter charge in order to preserve electroneutrality The counter charge consists of a diffuse atmosphere of counter ions and a compact layer of bound charge as well The surface, compact, and diffuse layer charges form the electrical double layer (EDL) [Jam87] The existence of the EDL results in a distribution of potential ranging from the surface potential, φ_o, at the particle surface, to a value of φ at any distance x from the surface For relatively low surface potential values, the potential, φ, is given by [Ree88]

$$\varphi = \varphi_o \exp(-\kappa x) \qquad (4.11)$$

where κ is the Debye-Hückel parameter, as defined by eq (3.12) It may be recalled that the zeta potential (ζ or φ_d) is defined as the potential corresponding to the plane formed by the compact layer (called the "electrokinetic shear plane") which is located at a distance d from the particle surface [Ree88] Therefore it follows from eq (4.11) that

$$\varphi_d = \varphi_o \exp(-\kappa d) \qquad (4.12)$$

In the gel model [Jam87] the particle surface is assumed to have a porous "gel" structure in which counter ions can penetrate thereby extending the diffuse layer into the pore channels In such a case, the outer surface of the "gel" serves as the electrokinetic shear plane. In order to quantitatively determine the resulting change in zeta potential, we assume that the shear plane is shifted by a distance λ away from the particle surface Therefore the corresponding "apparent" zeta potential φ_d' may be written, from eq (4.11), as

$$\varphi_d' = \varphi_o \exp[-\kappa(d+\lambda)] \qquad (4.13)$$

It follows from eqs (4.12) and (4.13) that

$$\varphi_d' / \varphi_d = \exp(-\kappa\lambda) \qquad (4.14)$$

Table 4.22 shows the calculated values of φ_d'/φ_d and the values of φ_d' corresponding to φ_d = 80 mV and 50 mV (zeta potentials for SiO_2 at pH ~8 and ~9, respectively, as shown in Figure 4.9), for $\kappa = 1.04 \times 10^8$ cm^{-1} (see Section 3.2.1 for details) and for values of λ ranging from 0 to 12 nm.

It is clear from Table 4.22 that the presence of pore channels on the particle surface results in significant decreases in the zeta potentials. Since the 30/70 powder had significant amount of relatively large pores, the relatively low zeta potential values can be partly attributed to the extension of the diffuse counter-ion layer into the pore channels. For example, if the pore channels cause an effective shift in the shear plane of ~6 nm, the expected zeta potential is ~49 mV at pH ~9.0. Upon heat-treatment at progressively higher temperatures, the pore channels decrease in size and volume, thereby leading to gradual increases in zeta potentials (Table 4.21). In contrast to the 30/70 powder, the other composite powders contain much lower sizes and volumes of porosity in the coating. Therefore, it is possible that the effective shift in shear plane is negligible for these powders, thereby resulting in zeta potentials similar to that obtained for SiO_2 powder. It is important to note that eq. (4.12) is a relatively simplistic representation of the potential distribution and that it is valid only for low surface potentials (typically $\leq$ 25mV) [Jam87]. It may be necessary to use more exact expressions for the potential decay with distance from the particle surface, and to conduct potentiometric titration experiments to determine the various ionic concentrations, in order to rigorously analyze the effect of porosity on the predicted zeta potential.

Table 4.22. Calculated Values of φ_d' for Different Values of the Shift in Shear Plane (λ).

λ (nm)	φ_d' / φ_d	φ_d' (mV) [for φ_d=80 mV]	φ_d (mV) [for φ_d=90 mV]
0	1 00	80	90
3	0 73	59	65
6	0 54	43	49
9	0 39	31	35
12	0.29	23	26

X Ray photoelectron spectroscopy (XPS) analysis

Figure 4 67 - 4 71 show XPS plots of Lot2 Si_3N_4 30/70, 40/60, 50/50, and 60/40 powders, respectively (see Appendix I for full-scale plots) As seen in Section 4 1 1, no nitrogen peaks were observed for the composite powder samples indicating that the first ~20 Å of the surface contains SiO_2 (As noted earlier the secondary peaks adjacent to the main element peaks are satellite peaks which are characteristic of the XPS technique [Bar93]) Since the analysis depth is less than the smallest coating thickness (~12 nm for 30/70 powders), this method is not sufficient to study the extent of surface coverage by the coating. (For example, the presence of pore channels exposing the surface of the Si_3N_4 core particles cannot be detected. Evidence for the presence of such porosity has been presented in earlier sections)

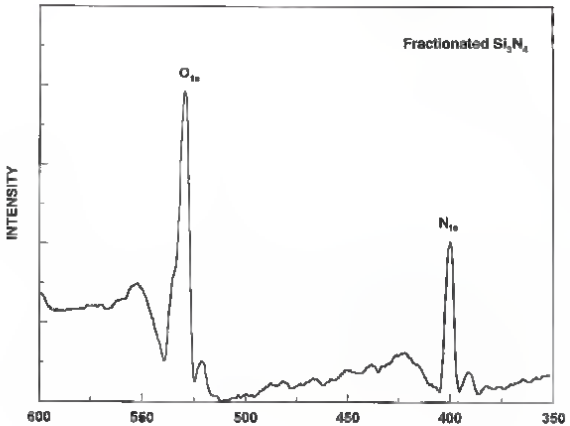

Figure 4.67 XPS plot for Si_3N_4 powder showing the presence of oxygen on the surface.

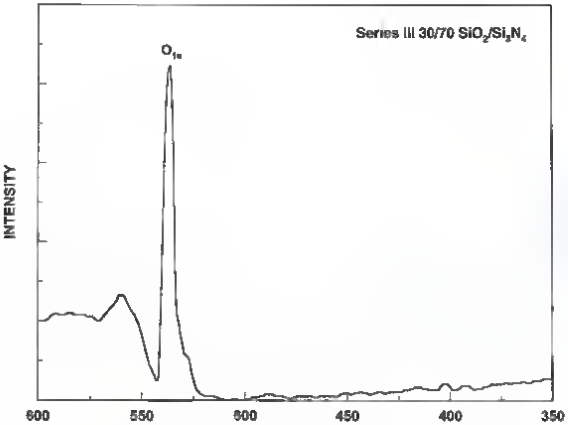

Figure 4 68 XPS plot for 30/70 composite powder showing the absence of any nitrogen peaks

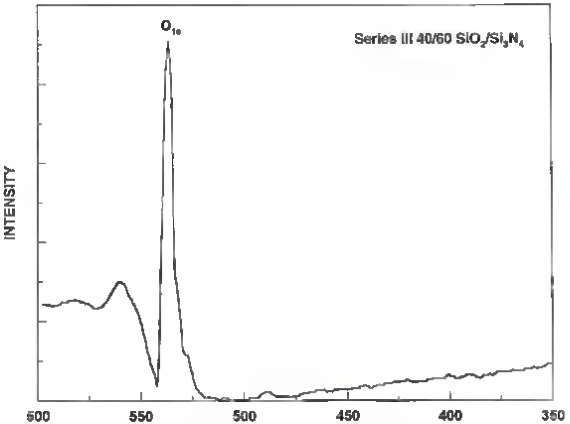

Figure 4.69 XPS plot for 40/60 composite powder showing the absence of any nitrogen peaks

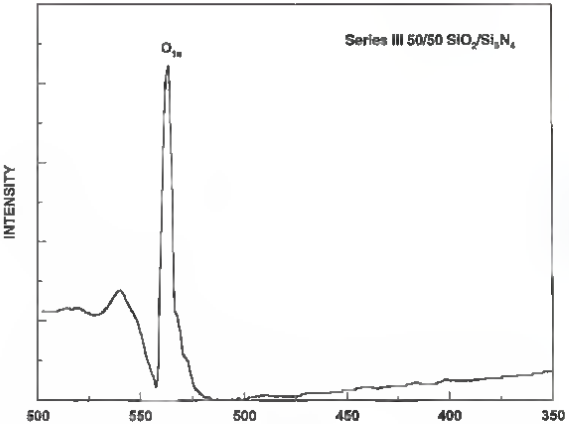

Figure 4.70 XPS plot for 50/50 composite powder showing the absence of any nitrogen peaks.

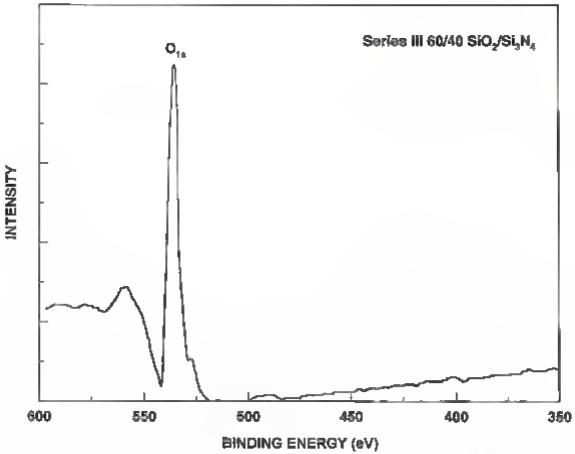

Figure 4 71 XPS plot for 60/40 composite powder showing the absence of any nitrogen peaks

Inductively coupled plasma (ICP) analysis

Table 4 23 shows the calculated values of the weight of leached SiO_2 (W_3) from the ICP measurements

In order to calculate the weights of the different components (see Section 3 2 1) in the composite powder eq (3.25) was used First, the values of $f_{OH} = 0\ 0168$ and $f_S^{SN} = 0\ 0298$ (see Section 3.2.1) were inserted into eq (3 25) to obtain eq (4 15)

$$W_T = 1\ 0298W_{SN} + 1\ 0171\ (W_3 - 0\ 0298W_{SN}) \tag{4 15}$$

Therefore

$$W_T - 1.0171W_3 = 0\ 9995W_{SN} \text{ or,}$$

$$W_{SN} = (W_T - 1\ 0171W_3)/0\ 9995 \tag{4 16}$$

The weight of SiO_2 in the core powder can be written using eq (3.23) as

$$W_S^{SN} = 0\ 0298W_{SN} \tag{4 17}$$

The weight of TEOS-derived SiO_2 may be expressed using eq (3.24) as

$$W_S^S = W_3 - 0\ 0298W_{SN} \tag{4 18}$$

Finally the weight of OH groups in the TEOS-derived SiO_2 (i.e., the coating) is given, using eq (3.23), by

$$W_{OH} = 0\ 0171W_S^S \tag{4 19}$$

Table 4 24 shows the weights of the different components calculated using eqs (4 15)-(4 19) The weight fraction of these components were calculated using eqs (3.26)-(3.29) and the resulting values are listed in Table 4 25

It would be instructive to calculate the volume percent of the different components in order to compare with the nominal values. The nominal (estimated) values were based on the volume percent of the core particles (i.e , including the SiO_2 in

Table 4.23 Summary of Results from ICP Analysis.

Powder	Total Weight W_T (g)	ppm Si in Solution	SiO_2 Weight W_S (g)
30/70	0.25122	29	0.05205
	0.25051	27	0.04889
40/60	0.23059	39	0.07002
	0.19943	33	0.05812
50/50	0.25045	56	0.09688
	0.25049	52	0.09443
60/40	0.24178	64	0.11752
	0.25146	67	0.12073
85/15	0.24980	108	0.19897
	0.25132	103	0.18992

Table 4.24 Calculated Weights of Different Components in the Composite Powders

Sample	W_{SN} (g)	W_S^{SN} (g)	W_S^S (g)	W_{OH} (g)
30/70	0.1984	0.0059	0.0461	0.0008
	0.2009	0.0060	0.0429	0.0007
40/60	0.1595	0.0048	0.0653	0.0011
	0.1404	0.0042	0.0539	0.0009
50/50	0.1520	0.0045	0.0924	0.0016
	0.1545	0.0046	0.0898	0.0015
60/40	0.1223	0.0036	0.1139	0.0019
	0.1287	0.0038	0.1169	0.0020
85/15	0.0475	0.0014	0.1976	0.0034
	0.0582	0.0017	0.1882	0.0032

the Si_3N_4) and the volume percent of TEOS-derived SiO_2 in the OH-free composite powder. The calculated values of volume percent of the core particles and the coating (i.e., the TEOS-derived SiO_2) were determined from the weight percent values (Table 4.25) by assuming their true densities to be 3.19 and 2.20 g/cm^3, respectively. (The true density of the SiO_2 in the powders used for ICP analysis is 2.15 g/cm^3, corresponding to a 450°C heat treatment [Sac84a]. However, since the nominal compositions of the composite powders were determined by assuming the true density of SiO_2 to be 2.20 g/cm^3, which corresponds to heat treatment temperatures ≥800°C [Sac84a], it is reasonable to assume the same value for the calculation of volume fractions from ICP results. Moreover, in order to compare the calculated compositions with those predicted by the sintered compact densities, it would be more appropriate to use the value corresponding to high heat treatment temperatures, i.e., 2.20 g/cm^3.) The volume percent of Si_3N_4 phase was calculated from the weight percent by assuming the true density of the Si_3N_4 to be 3.21 g/cm^3. Table 4.26 lists the volume percent of the core particles and the Si_3N_4 particles, in the dry composite powder, for samples with different nominal compositions.

Table 4.26 shows that the calculated values of vol% core particles were slightly higher than the nominal values. The possible reasons for this deviation include: (1) Incomplete dissolution of SiO_2 in the ICP experiments. (2) Errors in the assumed values of the SiO_2 content in Si_3N_4. (If the assumed values are higher than the actual value, the calculated vol% cores would also be higher than the nominal value.) (3) Errors in the assumed values of OH content in the TEOS-derived SiO_2. (If the assumed values are lower than the actual OH content, higher vol% of cores would be obtained.) (4) Some of

Table 4 25 Calculated Weight Percent* of the Components in the Composite Powders.

Sample	w_{SN} (%)	w_S (%)	w_{core} (%)	w_{coat} (%)
30/70	79.2	20 8	81 6	18 4
	80 4	19 6	82 8	17 2
40/60	69.5	30.5	71 6	28 4
	70 7	29.3	72.8	27 2
50/50	61 1	38.9	62 9	37 1
	62 1	37.9	63 9	36 1
60/40	51 0	49 0	52.5	47 5
	51 6	48 4	53 1	46 9
85/15	19 3	80 7	19 8	80.2
	23 5	76 5	24 1	75.9

*w_{SN}= weight percent Si_3N_4 in the dry (i e , OH-free) composite powder w_S= weight percent SiO_2 in the dry composite powder. w_{core}= weight percent core Si_3N_4 particles in the dry composite powder w_{coat}= weight percent TEOS-derived SiO_2 (i e coating) in the dry composite powder

Table 4.26 Calculated Volume Fractions of Components in the Composite Powders

Sample	vol% Cores (Nominal)	vol% Cores (ICP)	vol% Si_3N_4 (ICP)
30/70	70	75.3	72.3
	70	76 9	73 8
40/60	60	63 4	60 9
	60	64 9	62 3
50/50	50	53 9	51 8
	50	55 0	52.9
60/40	40	43.3	41 6
	40	43.9	42 2
85/15	15	14 6	14 0
	15	18.0	17 4

the TEOS does not precipitate as SiO_2 on core particles. (This may be due to incomplete conversion of TEOS to SiO_2 as well as due to the formation of independent SiO_2 particles.)

4.3.2 Estimation of Composite True Densities

In order to determine the composite relative densities, true densities of the samples are desired. Three different methods were used to estimate the true density values. In the first method (Method I) the average volume ratios of the components (i.e., Si_3N_4 and SiO_2) determined by ICP measurements were used. (The average of the two individual values for each composition given in Table 4.26 were used.) As explained in the previous section densities of SiO_2 and Si_3N_4 were assumed to be 2.20 g/cm^3 and 3.21 g/cm^3, respectively and the composite densities were determined by linear extrapolation.

In method II, the apparent densities of 800°C pre-sintered samples were used[95]. The apparent densities of the pre-sintered samples will be equal to the powder true density values assuming that there is no closed porosity in the samples. In Method III, the maximum apparent density value obtained from sintering experiments (Tables E-VIII – E-XII in Appendix E and Table 4.31) is considered to be the powder true density. Table 4.27 shows the density values estimated from the aforementioned methods.

[95] The individual values measured on both the rod samples (Table E-IV) and the disk samples (Table E-V) were averaged to determine the apparent density.

Table 4.27 Estimated Powder True Densities Determined by Three Different Methods

SiO_2/Si_3N_4	Estimated Powder True Density (g/cm^3)		
	Method I	Method II	Method III
30/70	2.94	2.90	2.93
40/60	2.82	2.76	2.82
50/50	2.73	2.67	2.72
60/40	2.62	2.57	2.61
85/15	2.36	2.33	2.35

The powder density values determined using ICP (Method I) and the maximum apparent densities (Method III) are in reasonable agreement with each other. However the corresponding apparent density values (Method II) determined on the green samples were slightly (~1-2 %) lower. This may be attributed to the presence of hydroxyl groups in the SiO_2 coating. Sacks et al. [Sac84a] have reported powder true density measurements for SiO_2 particles prepared by the method of Stober et al. [Sto68]. The as-prepared powder had a true density of ~2.05 g/cm^3 and the density increased to ~2.20 g/cm^3 (similar values are usually reported for fused SiO_2 [Ile79]) as the powder was calcined for 24 h at 800°C. This increase was attributed to the removal of chemically bonded water (i.e., hydroxyl groups). In the current study, the SiO_2 coatings precipitated on to the Si_3N_4 particles contain hydroxyl groups which may not have been completely eliminated after heating for 2h at 800°C. The dehydroxylation process strongly depends on composition (i.e., the amount of SiO_2 coating) and heat-treatment conditions (e.g. heating rate, isothermal time, etc.) and therefore the calculation of the powder true densities during the early stages of heat-treatment becomes complicated. In this investigation the densities

determined using Method III was used. This would lead to a slight (~1-2%) error in the density values at lower temperatures for the constant heating rate (CHR) sintering experiments, and at lower hold times for the isothermal sintering experiments. However, the error reduces gradually as the densification occurs.

4.2.3. Constant Heating Rate (CHR) Sintering Studies

Densification behavior was directly compared for samples with Si_3N_4 contents in the range of 40-70 vol% (i.e., 60-30 vol% SiO_2) by heating at ~11°C/min to ~1500°C in the dilatometer. Figure 4.72 shows the plots of bulk density vs. temperature for the SiO_2/Si_3N_4 compacts. The final sintered densities were also determined using the Archimedes method with water as the medium. Table 4.28 shows the results from these measurements compared with those obtained using dilatometry.

It is evident from Table 4.28 that the bulk density values determined using dilatometry were slightly (0 - 2%) lower than those obtained using the Archimedes method. These differences may be attributed to the fact that the dilatometry data was collected immediately preceding the cooling step, i.e., thus data did not account for the slight densification that occurred during the cooling step (i.e., when the furnace temperature reduced from ~1500°C to room temperature, which typically occurred in ~1 h). For example, the bulk density of the 30/70 samples increased from ~2.02 to ~2.07 g/cm^3 when heated from ~1350 to ~1500°C (Figure 4.72). This corresponds to a significant (~2.5%) increase in density during the final ~15 min (corresponding to a heating rate of ~11°C/min and temperature range of ~150°C) of the heating. It may be reasonable to conclude that slight increases in density occurred during the cooling. For example, if an additional 2%

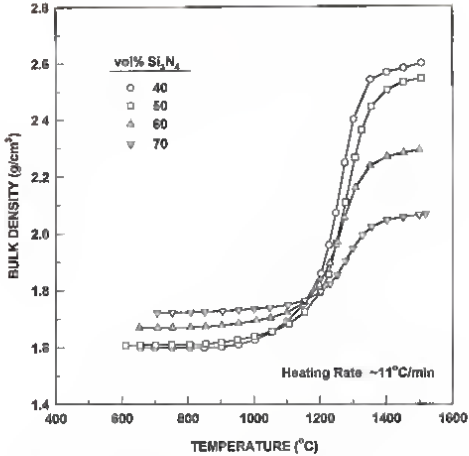

Figure 4.72 Plots of bulk density vs temperature for SiO_2/Si_3N_4 samples heated at ~11°C/min

densification was assumed to occur during cooling, the expected sample density is ~2.12 g/cm^3 which is in good agreement with the measured Archimedes density values.

Table 4.28 Table of Sintered Densities Determined by Dilatometry and by Archimedes Measurements Samples were Heated at ~11°C/min to ~1500°C

	Archimedes Method			Dilatometry
Sample*	ρ_{bulk} (g/cm^3)	% O.P.	$\rho_{apparent}$ (g/cm^3)	ρ_{bulk} (g/cm^3)
30/70a #1	2.116	26.9	2.897	2.084
#2	2.115	27.0	2.892	
30/70b #1	2.103	27.8	2.911	2.074
#2	2.105	27.7	2.908	
40/60a #1	2.312	17.7	2.809	2.295
#2	2.304	17.5	2.793	
40/60b #1	2.307	18.0	2.813	2.288
#2	2.298	17.8	2.795	
50/50a #1	2.560	0.3	2.568	2.534
#2	2.554	0.2	2.558	
50/50b #1	2.586	0.2	2.591	2.544
#2	2.579	0.2	2.583	
60/40a #1	2.602	0.1	2.605	2.593
#2	2.597	0.3	2.604	
60/40b #1	2.600	0.3	2.607	2.604
#2	2.595	0.2	2.600	

* #1 and #2 denote results from two independent measurements on each sample.

Powder true density values listed in Table 4 27 (Method III) were used to calculate relative densities as functions of temperature (Figure 4 73) The corresponding densification rates were also calculated and plotted as functions of temperature (Figure 4 74) The temperatures corresponding to the rate maxima in Figure 4 74 are listed in Table 4.29

Table 4 29 List of Temperatures (T_{max}) Corresponding to the Densification Rate Maxima in the Plots Shown in Figure 4 74

SiO_2/Si_3N_4	T_{max} (°C)
30/70	1275
40/60	1260
50/50	1274
60/40	1258

Figure 4 73 shows that the samples containing 40 vol% Si_3N_4 sintered to nearly full density (i e , no residual porosity) at ~1500°C In contrast, the samples with 50, 60, and 70% Si_3N_4 reached relative densities of ~95% ~82%, and ~72%, respectively, after sintering under the same conditions. Moreover the densification rates for these samples are very low (<0 25 x 10^{-4} s^{-1}) at ~1500°C, indicating that almost no further densification is expected to occur upon heating these samples at higher temperatures. The decrease in maximum density[96] with increasing Si_3N_4 content indicates that Si_3N_4 particles were forming rigid networks at the higher volume fractions The cores of the composite

[96] This maximum sintered density refers to the value obtained after heat treatment at temperatures up to 1500°C in which densification is primarily controlled by viscous flow of SiO_2 (Section 4.34) Preliminary studies (see Appendix N) indicate that additional densification occurs at higher temperatures (>1600°C) due to dissolution of Si_3N_4 in the SiO_2 matrix.

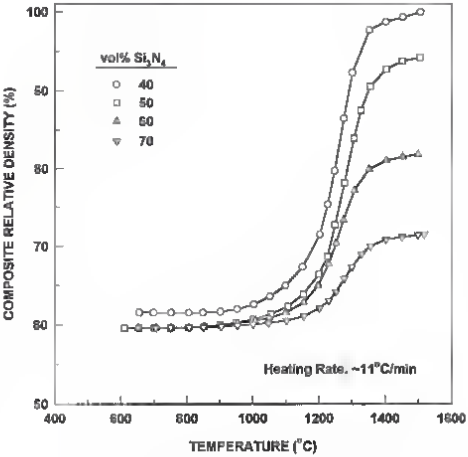

Figure 4 73 Plots of relative density vs. temperature for SiO_2/Si_3N_4 samples heated at ~11°C/min

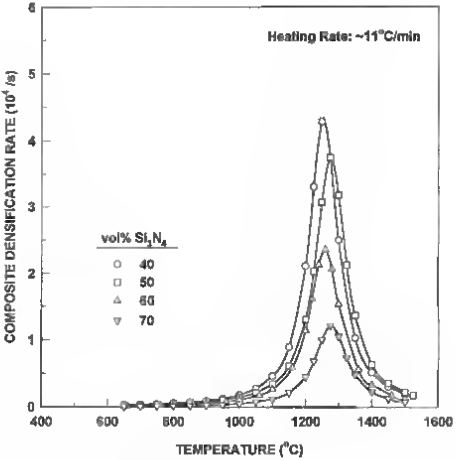

Figure 4.74. Plots of composite densification rate vs. temperature for SiO_2/Si_3N_4 samples heated at ~11°C/mn.

particles will approach each other as the powder compact shrinks and the matrix (coating) phase is redistributed during sintering. A contiguous particle network will form prior to complete densification if the core volume fraction is above a critical threshold value[97].

CHR experiments were also used to measure the activation energy for densification of 60/40 compacts. Figure 4.75 shows plots of relative density vs. temperature for samples heated at three heating rates, viz., ~6°C/min, ~11°C/min, and ~19°C/min. (For clarity, the results corresponding only to the temperature range of 1000-1500°C are shown.) The corresponding plots of densification rate vs. temperature are shown in Figure 4.76. Eq. (3.45) was applied to the data in Figures 4.75 and 4.76 in the following way. Four different values of composite relative density, viz., 70%, 75%, 82%, and 87% were arbitrarily chosen for activation energy calculations. For each density level, three values of densification rate and the corresponding temperatures were obtained at the three heating rates. These three values were fitted to eq. (3.45) and the resulting Arrhenius plots are shown in Figure 4.77. The calculated values of activation energy at the four density levels are listed in Table 4.30.

Table 4.30. Activation Energy Estimates for Densification of 60/40 SiO_2/Si_3N_4 Samples

Relative Density	Activation Energy (kJ/mol)
70	616
75	595
82	550
87	572
Average	*583 ± 29*

[97] For ideal powder compacts, the threshold value is numerically equal to the compact packing density. However, as elucidated in Section 4.3.6, experimental non-uniformities (e.g., in particle packing, interparticle particle phase distribution, etc.) will result in lower threshold values.

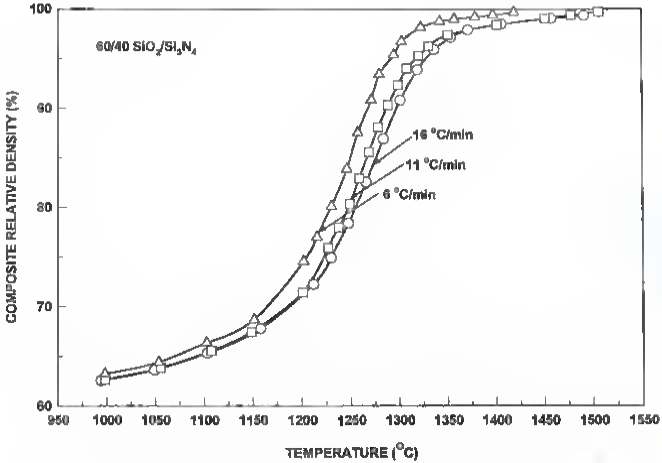

Figure 4 75 Plots of relative density vs temperature for 60/40 SiO_2/Si_3N_4 samples heated at three different heating rates (a) ~6°C/min, (b) ~11°C/min, and (c) ~19°C/min.

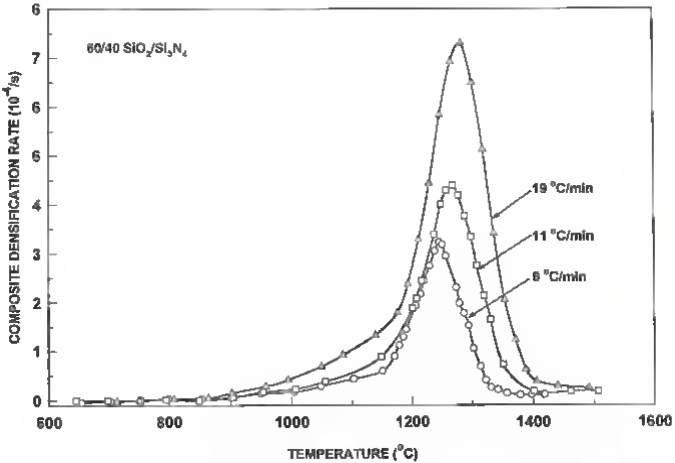

Figure 4 76 Plots of densification rate vs. temperature for 60/40 SiO_2/Si_3N_4 samples heated at three different heating rates (a) ~6°C/min, (b) ~11°C/min, and (c) ~19°C/min

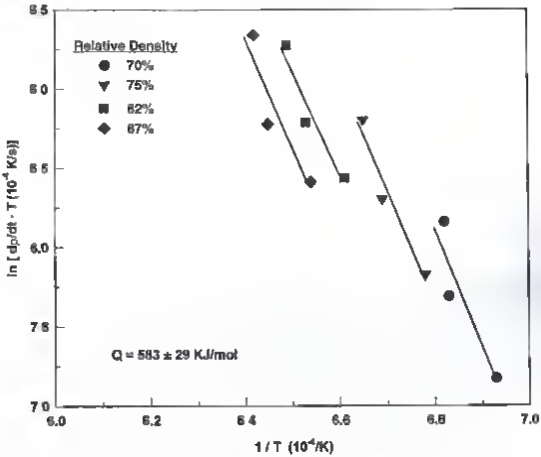

Figure 4 77 Arrhenius plots for 60/40 SrO_2/Si_3N_4 samples at four different values of composite relative density (a) 75%, (b) 75%, (c) 82%, and (d) 87%

The average activation energy of 583 ± 29 kJ/mol is comparable but slightly higher than reported values (510 kJ/mol) for viscous flow of fused SiO_2 with high hydroxyl concentration [Het64]. It is also slightly higher than values (506 - 543 kJ/mol) reported for amorphous SiO_2 samples prepared using powders formed by hydrolysis/condensation of TEOS [Sac84b, Vor90]. Since the SiO_2 in the 60/40 composite powders were also derived from TEOS, it may be reasonable to expect that the activation energies would be similar to those measured on the samples mentioned above. The difference in the activation energies may be explained as follows. The samples used for dilatometry were pre-sintered at 800°C (2 h) which is a higher temperature than those used by Sacks and Tseng [Sac84b] (500°C, 1 h) and Vora [Vor90] (700°C, 6 h). Furthermore, the former samples were heat treated in nitrogen while the latter two types of compacts were heated in ambient air atmosphere, which contained relatively larger concentrations of moisture. Finally, the sintering temperatures used in this study were significantly higher (1500°C vs. 950-1150°C respectively). Therefore it is reasonable to expect that the compacts used for dilatometry contained relatively smaller amounts of hydroxyl groups. Since it has been shown [Het64] that the activation energy for viscous flow of SiO_2 increases with reducing hydroxyl concentration, a higher value of activation energy was obtained in the current investigation. (The effect of hydroxyl content on activation energy of fused SiO_2 was investigated by Hetherington et al. [Het64]. For example, they showed that the activation energy for viscous flow of fused SiO_2 increased from ~509 to ~711 kJ/mol as the hydroxyl content decreased from 0.12 to 0.0003 wt%.)

It is apparent from the activation energy results that the densification of the composite powder compacts is controlled by the viscous flow of the SiO_2 matrix.

4.3.4 Isothermal Sintering Studies

The effect of composition on densification was investigated using Series III SiO_2/Si_3N_4 composite powder compacts with Si_3N_4 contents in the range of 15-70 vol% (i.e., 85-30 vol% SiO_2). The compacts were densified in nitrogen under isothermal conditions at 1225°C. Figures 4.78 and 4.79 show plots of bulk density vs. time and percentage open porosity vs. time, respectively, for compacts with Si_3N_4 contents in the range of 40-70 vol%. Figures 4.80 and 4.81 show the corresponding plots for batch 3 SiO_2 compacts. Series II SiO_2/Si_3N_4 composite powder compacts with 15 vol% Si_3N_4, and SiO_2+Si_3N_4 mixed powder compacts with 15 vol% Si_3N_4 (Samples were heated isothermally at 1225°C). Table 4.31 summarizes the particle sizes, pre-sintering conditions, and green compact densities of these compacts. Figures 4.82 and 4.83 show the plots of relative density vs. time for composite powder compacts for sintering times in the ranges of 0-1440 min and 0-600 min, respectively. Figure 4.84 shows the plots of relative density vs. sintering time for the SiO_2 compacts, 85/15 compacts, and SiO_2+Si_3N_4 mixed powder compacts with 15 vol% Si_3N_4. Composite powder samples containing 15 and 40 vol% Si_3N_4 could be sintered to ~100% relative density after heat treatment at 1225°C for ~150 min and ~600 min, respectively. In contrast, samples with 50, 60, and 70 vol% Si_3N_4 reached relative densities of only ~93%, ~81%, and ~71% after sintering for ~1440 min at the same temperature.

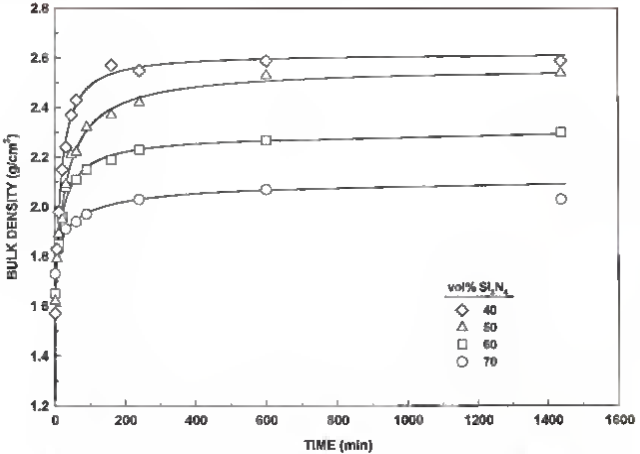

Figure 4.78 Plots of bulk density vs. temperature for microcomposite powder compacts with Si_3N_4 contents in the range of 40-70 vol%

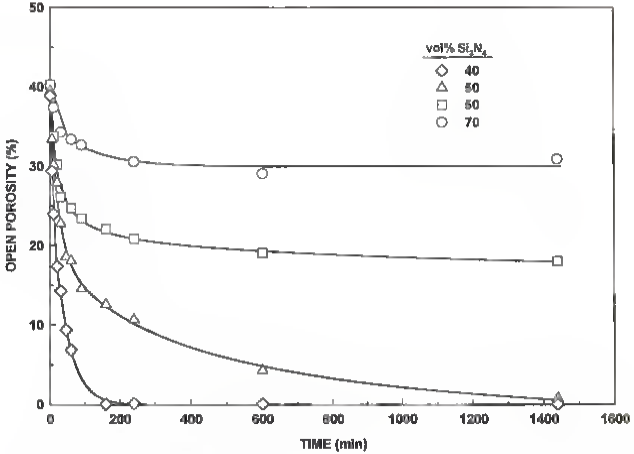

Figure 4.79 Plots of % open porosity vs temperature for microcomposite powder compacts with Si_3N_4 contents in the range of 40-70 vol%

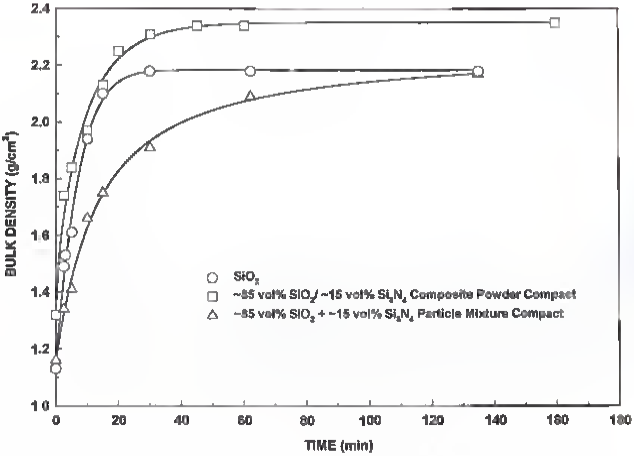
BULK DENSITY (g/cm³)
TIME (min)
SiO2
~85 vol% SiO2/ ~15 vol% Si3N4 Composite Powder Compact
~85 vol% SiO2 + ~15 vol% Si3N4 Particle Mixture Compact

Figure 4.80 Plots of bulk density vs. temperature for SiO_2 and SiO_2/Si_3N_4 composite samples

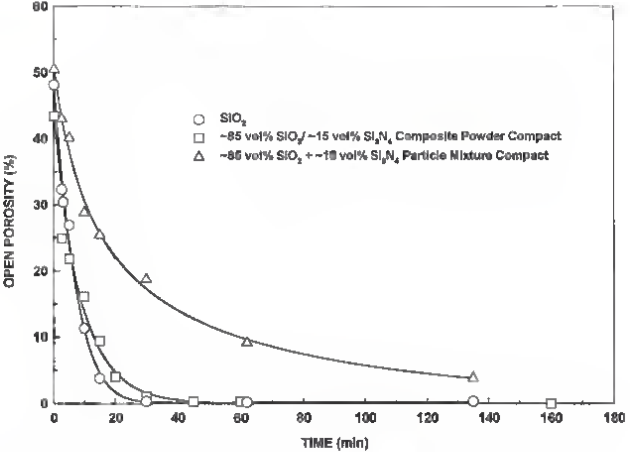

Figure 4 81 Plots of % open porosity vs temperature for SiO_2 and SiO_2/Si_3N_4 composite samples

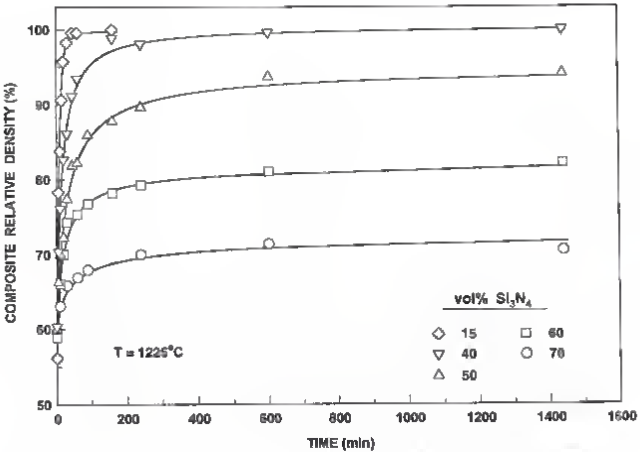

Figure 4.82 Plots of composite relative density vs. sintering time for composite powder compacts with Si_3N_4 contents in the range of 15-70 vol%. The compacts were sintered isothermally in nitrogen at 1225°C.

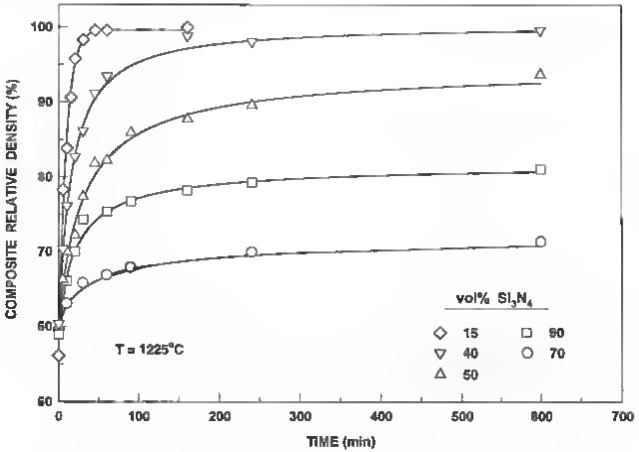

Figure 4 83 Plot showing the data from Figure 4 82 at sintering times in the range of 0-600 min

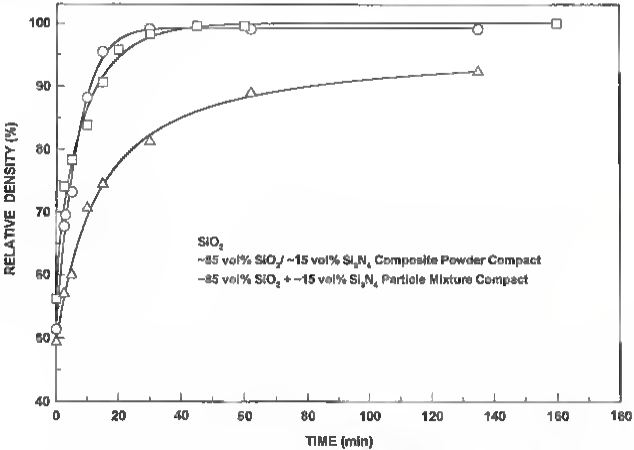

Figure 4.64 Plots of relative density vs sintering time for SiO_2 and SiO_2/Si_3N_4 compacts sintered isothermally in nitrogen at 1225°C

Table 4.31 Summary of Particle Sizes, Pre-sintering Conditions, and Pre-sintered Densities for SiO_2 compacts, 85/15 SiO_2/Si_3N_4 composite powder compacts and SiO_2+Si_3N_4 mixed powder compacts with 15 vol% Si_3N_4

Sample	Median Stokes Diameter (μm)	Pre-sintering Conditions	Pre-sintered Density (%)
batch 3 SiO_2	0.52	700°C, 6 h (air)	52
Series II 85/15 SiO_2/Si_3N_4 Composite Powder Compact	0.52	800°C, 2 h (nitrogen)	57
~85 vol% SiO_2 + ~15 vol% Si_3N_4 Mixed Powder Compact	0.52 (SiO_2) 0.33 (Si_3N_4)	800°C, 2 h (nitrogen)	50

Table 4.32. Density Results for Samples Heated at 1500°C for 2 h.

Sample	ρ_{bulk} (g/cm^3)	% O.P	$\rho_{apparent}$ (g/cm^3)	Relative Density (%)
30/70 #1	2.097	28.3	2.923	~72
#2	2.088	28.9	2.923	
40/60 #1	2.293	19.0	2.820	~81
#2	2.280	19.2	2.823	
50/50 #1	2.620	0.0	2.622	~97
#2	2.617	0.0	2.617	
60/40 #1	2.601	0.0	2.601	~100
#2	2.602	0.0	2.602	

Some pre-sintered (800°C, 2 h) samples were heated to 1500°C (at 5°C/min) in nitrogen in a tube furnace[98] in an attempt to achieve higher densities. Table 4.32 shows the density results from samples that were heated at 1500°C for 2 h. It is evident that the densities were similar or slightly higher (~97%, ~81%, and ~72%, respectively, for samples with 50, 60 and 70 vol% Si_3N_4) compared to the corresponding values (i.e., ~93%, ~81%, and ~71%, respectively) for samples sintered at 1225°C for 1440 min (24 h). Therefore the densities listed in Table 4.32 can be regarded as the maximum sintered densities. Figure 4.85 shows a plot of maximum relative density after sintering as a function of the Si_3N_4 volume percent. The decrease in maximum density with increasing Si_3N_4 content is consistent with the results from the CHR experiments (Figure 4.73). It indicates that the Si_3N_4 particles were forming rigid networks at higher volume fractions. As noted earlier, the cores of the microcomposite particles will approach each other as the powder compact shrinks and the matrix phase is redistributed during sintering. A contiguous particle network will form prior to complete densification if the core particle fraction exceeds a critical threshold value. The network is established at decreasing composite relative densities (i.e. higher residual porosities) as the matrix/core volume ratio decreases. The rigidity of the network is indicated by the observation that there is little change in the relative densities upon increasing the sintering temperature from 1225°C to 1500°C.

Figure 4.86 shows the XRD plots in the 2θ range of 18° - 24° for composite powder samples sintered at 1500°C for 2 h. The crystalline peaks in Figure 4.86

[98] Model 64259. Lindberg Co., St. Watterton, WI

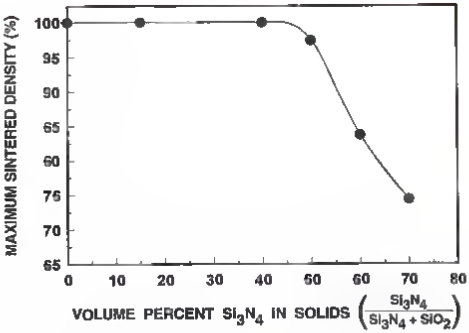

Figure 4 85 Plot of maximum relative density vs. amount of Si_3N_4 for composite powder compacts.

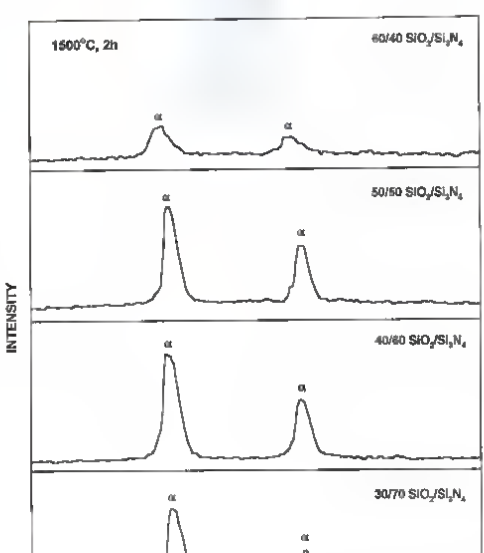

Figure 4.86 XRD plots for SiO_2/Si_3N_4 composite powder compacts heated at 5°C/min to 1500°C and soaked for 2h. The crystalline peaks (marked α) for all the samples correspond to α-Si_3N_4

correspond to α-Si_3N_4. The absence of any cristobalite peak (corresponding to $2\theta \sim 22^\circ$) indicates that the SiO_2 phase was amorphous. Previous studies [Sac84a, Vor90] have shown that amorphous SiO_2 devitrifies to form cristobalite at relatively low ($\leq$1200°C) temperatures. Therefore it is interesting that the SiO_2 present in the composite powders does not undergo any crystallization even at temperatures as high as 1500°C. It is also interesting to compare the result with the study conducted by Zeng et al. [Zen92] on SiO_2+Si_3N_4 (with ~14-38 vol% SiO_2) mixed powder compacts. They reported (based on XRD observations which were not illustrated in the publication) that the SiO_2 phase remained amorphous even after the compacts were hot-isostatically pressed at temperatures in the range of 1800 - 2000°C. However, these temperatures are higher than the melting point of SiO_2 and therefore it may not be appropriate to compare the crystallization behavior with that reported in the current study. Wusirika [Wus90] introduced 0-24 wt% nitrogen into vitreous SiO_2 by reacting fumed silica and ammonia at 600 - 1200°C. The nitrided powders were hot pressed in nitrogen at temperatures in the range of 1550 - 1650°C. It was found that while samples with 0-1 wt% nitrogen crystallized to cristobalite, samples with 2-10wt% nitrogen were stable against devitrification, even at 1650°C. It is possible that the small amounts of nitrogen dissolved into the SiO_2 phase in the composite powder and acted as a devitrification inhibitor. Detailed elemental analysis (such as EDS coupled with a high-resolution TEM) on sintered compacts may be necessary to confirm this hypothesis. Another possible explanation for the absence of crystallization is that the "rigid" Si_3N_4 phase constrains the volumetric shrinkage in the SiO_2 phase associated with the crystallization reaction. (The

true density increases from 2 20 g/cm^3 for amorphous SiO_2 to 2 32 g/cm^3 for cristobalite [Be79]) It is also interesting to compare the results with the studies conducted by Wang [K. Wang and M.D Sacks, personal communication, 1996] using amorphous SiO_2/α-Al_2O_3 composite powder compacts. Significant amounts of cristobalite formed at temperatures in the range of 1300 - 1350°C (2 h) It was also observed that some of the Al_2O_3 dissolved in the SiO_2 phase at relatively low temperatures (< 1375°C) [K. Wang and M D Sacks personal communication, 1996] Since the presence of Al^{+3} ions in the SiO_2 can enhance crystallization [Bro59], it was speculated that the devitrification was partly a consequence of the dissolution process It is noted, however that the crystallization temperatures in these compacts were still higher than those reported for pure SiO_2 [Vor90] the reasons for which have not yet been established

The relative density vs time data for selected samples (SiO_2 compacts and composite powder compacts with 15 40 and 50 vol% Si_3N_4) was fitted to smooth curves using a non-linear regression algorithm[99] Analytical differentiation was performed using the algorithm to obtain densification rates corresponding to each sample. Plots of densification rate vs matrix relative density for these samples are shown in Figure 4 87 The densification rates fall off rapidly with increasing densities It can also be seen from Figure 4 87 that samples containing higher volume fractions of Si_3N_4 show lower densification rates This indicates that the inclusion interactions, which lead to reduction in densification rates, are more pronounced in samples with higher volume fractions of inclusions.

[99] TableCurve 2D Jandel Scientific, Rafael CA

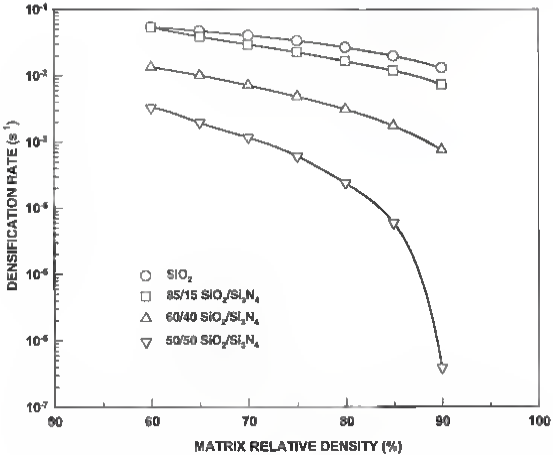

Figure 4.87 Plots of compact densification rate vs matrix relative density for SiO_2 compacts and composite powder compacts with Si_3N_4 contents in the range 15-50 vol%.

The effect of inclusions can also be analyzed by estimating the stresses caused by the inclusions in the sintering matrix. The sintering stress, Σ, in place of the free strain rate, ε_{fm}, can be used to to describe the densification behavior. The hydrostatic tensile stress in the matrix, σ_m is related to the strain rates by the equation[Sch87]

$$\frac{\dot{\rho}_m}{\rho_m} = -3\,\varepsilon_{fm} - \frac{\sigma_m}{K_m} \qquad (4.20)$$

where $\frac{\dot{\rho}_m}{\rho_m}$ (= 3 times the matrix strain rate, ε_m) is the ratio of the matrix densification rate to the matrix density, ε_{fm} is the matrix free strain rate (i.e., strain rate of the matrix with no inclusions), and K_m is the bulk modulus of the matrix. K_m is related to ε_{fm}, by

$$\Sigma = 3K_m\,\varepsilon_{fm} \qquad (4.21)$$

Combining this expression with eq. (4.20) we obtain

$$\frac{\dot{\rho}_m}{\rho_m} = -3\,\varepsilon_{fm}\left(1 - \frac{\sigma_m}{\Sigma}\right) \qquad (4.22)$$

This can be further reduced to

$$\frac{\dot{\rho}_m}{\rho_m} = -\frac{\dot{\rho}_{fm}}{\rho_{fm}}\left(1 - \frac{\sigma_m}{\Sigma}\right) \qquad (4.23)$$

where $\frac{\dot{\rho}_{fm}}{\rho_{fm}}$ is the ratio of the matrix densification rate to the matrix density for samples with no inclusions (i.e., the matrix free strain rate).

The terms in eq. (4.23) were calculated from the experimental data as follows. The composite densification rates ($\dot{\rho}_c$) in Figure 4.87 and the corresponding composite relative densities (ρ_c) were substituted in eq. (3.36) to obtain the matrix strain rates (left

side of eq (4 23)) for the composites. The matrix free strain rates were obtained as the strain rate of the SiO_2 compacts (i.e., compacts without any Si_3N_4 inclusions). The two strain rates were then substituted into eq (4 23) to calculate the value of the normalized hydrostatic stress in the matrix (σ_m/Σ). These calculations were performed for four samples, the SiO_2/Si_3N_4 composite powder compacts with 15, 40, and 50 vol% Si_3N_4, respectively, and the SiO_2+Si_3N_4 mixed powder compacts with 15 vol% Si_3N_4. (Composite densification rates for the mixed powder compact was obtained by the same procedure as that used for the composite powder compacts.) Figure 4 88 shows the plots of normalized hydrostatic stress in the matrix (σ_m/Σ) vs. matrix relative density (ρ_m) for the composite powder compacts. σ_m/Σ increases as ρ_m increases since inclusion particle interactions increase as the particles approach each other during densification. For the same reason, higher values of σ_m/Σ are observed for samples containing higher volume fractions of inclusions. (For example, at a matrix density of ~70%, σ_m/Σ was calculated to be ~0.22, ~0 77, and ~0 96 for samples with 15, 40 and 50 vol% Si_3N_4, respectively.)

The effect of spatial distribution of the phases on the inclusion interactions was studied by comparing the plots of σ_m/Σ vs. ρ_m for composite powder compacts with 15 and 40 vol% Si_3N_4, respectively, and mixed powder compacts with 15 vol% Si_3N_4 (Figure 4 89). For samples containing 15 vol% Si_3N_4, the hydrostatic stresses in the matrix were higher for the mixed powder compact compared to those estimated for the composite powder compact. This is consistent with the results described in Section 4 1.2 which demonstrated that densification was retarded for 60/40 SiO_2/Si_3N_4 mixed powder compacts (compared to 60/40 SiO_2/Si_3N_4 composite powder compacts) due to the formation of rigid networks of the non-sinterable Si_3N_4 particles. Similar retardation in

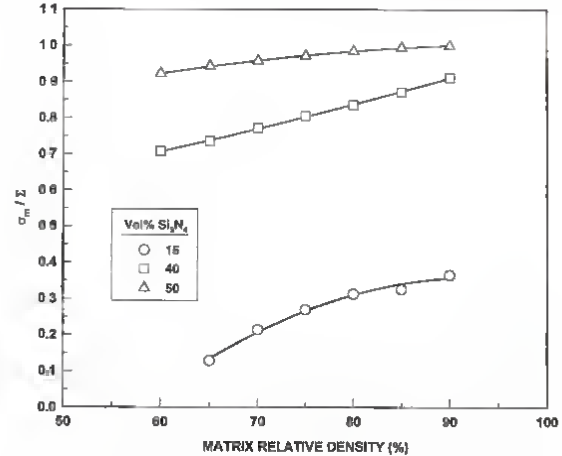

Figure 4.88 Hydrostatic stress in the matrix normalized by the sintering pressure, σ_m/Σ, vs matrix relative density, ρ_m, for composite powder compacts with the indicated volume fractions of Si_3N_4

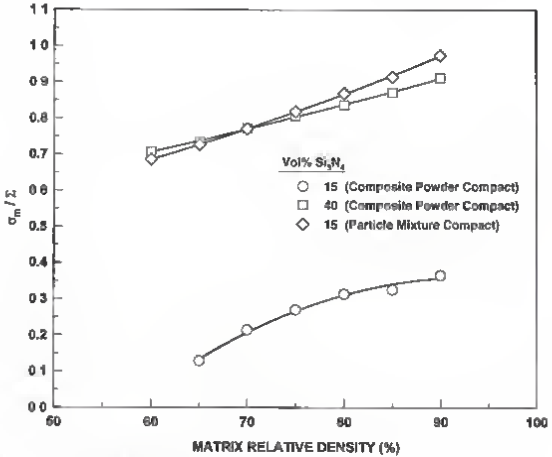

Figure 4.19 Hydrostatic stress in the matrix normalized by the sintering pressure, σ_m/Σ, vs matrix relative density, ρ_m, for composite powder compacts and particle mixture compacts.

densification was observed for the mixed compacts (vs composite powder compacts) prepared with 15 vol% Si_3N_4 (Figure 4 80) The high stresses associated with the formation of these networks results in increased σ_m/Σ values for the mixed powder compacts. It is interesting to note that σ_m/Σ values for mixed powder compacts with only 15 vol% Si_3N_4 was almost comparable to the corresponding values for composite powder compacts with 40 vol% Si_3N_4 This clearly demonstrates the advantage of using the composite powder approach in order to reduce inclusion interactions and to enhance the densification behavior

Microcomposite powder compacts which sinter to full density develop microstructures with minimal Si_3N_4 particle-particle contacts. This is illustrated in Figures 4 90 (A) and 4 90 (B) for samples containing 15 and 40 vol% Si_3N_4 respectively Particle-particle contacts are more common in the sample with 50 vol% Si_3N_4 (Figure 4 90 (C)) but the microstructure still shows mostly isolated Si_3N_4 particles This is consistent with the high relative density (~93%) obtained for this sample In contrast, the sample containing 60 vol% Si_3N_4 shows more extensive particle-particle contacts (Figure 4 90 (D)) which is consistent with the lower relative density (~81%) High-resolution microscopy (HRTEM) was performed to examine the nature of these contacts A 40/60 sample sintered at 1400°C for 2 h was used for the analysis. Figure 4 91 shows a thin layer (~5 nm) of amorphous SiO_2 situated between adjacent Si_3N_4 particles This type of amorphous layer was typical throughout the microstructure In addition, pure Si_3N_4 particle-particle contacts or grain boundaries were not evident in the microstructure[109]

[109] Approximately 15 fields each containing 2-4 inclusion particles were observed.

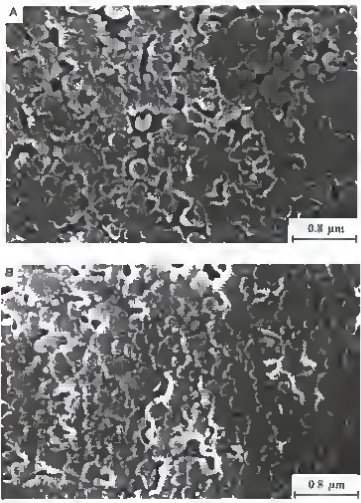

Figure 4 90 SEM micrographs of polished and etched samples prepared from composite powders with different SiO_2/Si_3N_4 volume ratios (A) 85/15 (B) 60/40, (C) 50/50 and (D) 40/60 Samples were sintered at 1225°C for 24h

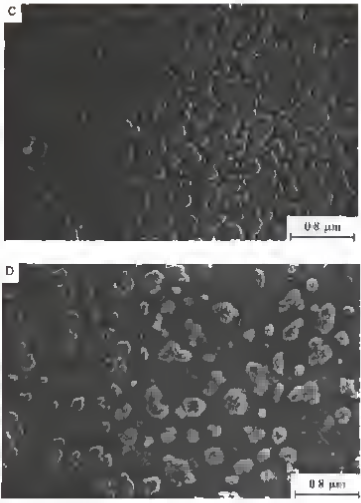

Figure 4.90 (continued).

Figure 4 91 High resolution trasmission electron micrograph of a 40/60 sample sintered at 1400°C for 2 h. The lattice fringes depict adjacent Si_3N_4 particles while the thin (~5 nm) layer separating the two particles is amorphous SiO_2

Since the corresponding SEM microstructure (Figure 4 90 (D)) showed apparent Si_3N_4 particle-particle contacts, it follows from the HRTEM analysis that the thin amorphous SiO_2 layers could not be resolved by observing etched samples under the SEM. The presence of such amorphous layers is consistent with a theoretical analysis by Lange [Lan82] This analysis applied a theory, developed for plates that sandwich a liquid layer, to spherical particles which undergo liquid phase sintering. The study showed that although the thickness of the liquid layer reduces with time, a finite thickness will always remain if the liquid perfectly wets the solid

Quantitative microscopy was used to estimate volume fractions of phases (i.e, porosity, SiO_2, and Si_3N_4) and average Si_3N_4 intercept sizes on samples sintered at 1225°C for 1440 min (i.e., sintered to nearly the maximum relative density) Table 4 33 shows the results from these measurements.

Table 4 33 Results from Quantitative Microscopy on Sintered (1225°C-24h) Samples.

	SiO_2/Si_3N_4			
	40/60	50/50	60/40	85/15
Si_3N_4 Intercept Size (μm)	0.213±0 138	0 185±0.128	0 150±0.089	0 143±0.090
Inclusion Volume%	53 9	50 3	42 0	15 4
Matrix Volume%	28 4	44 1	58 0	84 6
Pore Volume%	17 7	5 6	~0	~0
Volume% Si_3N_4 in Solids	65	53	42	15

For samples with 15 and 40 vol% Si_3N_4 the microstructures reveal minimal particle-particle contacts Therefore the intercept sizes measured for the two samples are almost identical (0 14 μm and 0 15 μm, respectively) and the measured volume fractions

of SiO_2 and Si_3N_4 are close to the nominal values. In contrast, the intercept sizes for samples with 50 and 60% Si_3N_4 were higher (0.19 μm and 0.21 μm, respectively). As indicated earlier, for samples with ≥ 50 vol% Si_3N_4 (in the solid volume), there exist regions of the microstructure containing thin layers of SiO_2 between adjacent Si_3N_4 particles which cannot be resolved by the SEM. Consequently, some clusters of such Si_3N_4 particles appear as larger particles which result in the higher values of the "apparent" intercept size. Furthermore, it also results in erroneously higher values of the measured volume fractions of Si_3N_4 (53 and 65 vol% Si_3N_4 for samples with 50 and 60 vol% Si_3N_4, respectively). It is interesting to note that for samples with minimal Si_3N_4 particle-particle contacts (i.e., 60/40 and 85/15 sintered compacts), the Si_3N_4 concentrations shown in Table 4.33 are in excellent agreement with the values determined from ICP measurements (Table 4.26). (The Si_3N_4 concentrations corresponding to the 60/40 and 85/15 samples were determined to be 42.0 and 15.4 vol%, respectively, by quantitative microscopy and ~41.9 and ~15.7 vol%, respectively, by ICP analysis.)

4.3.5. Compression Creep Studies

Figures 4.92 - 4.95 show plots of strain rate vs. stress and Table 4.34 lists the corresponding stress exponent (n) values for SiO_2, 85/15, 60/40, and 50/50 samples, respectively. The average n values (arithmetic average of values obtained at various temperatures) for the samples were determined to be 1.02 ± 0.06, 1.11 ± 0.02, 1.03 ± 0.10, and 1.32 ± 0.12, respectively. These results indicate that the n value for the SiO_2, 85/15, and 60/40 were nearly unity which is characteristic of Newtonian flow behavior. In

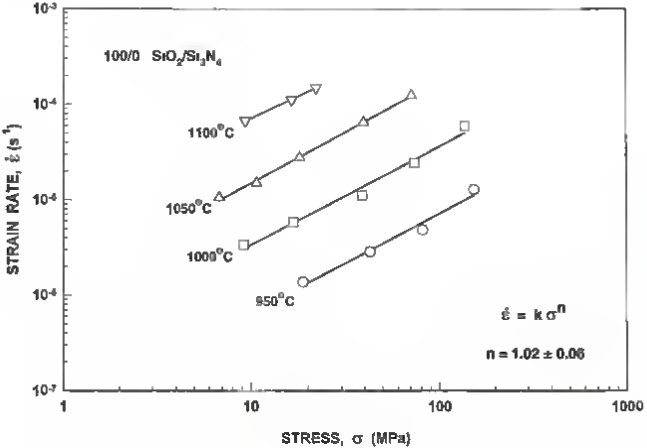

Figure 4.92 Plots of strain rate vs stress for the compression creep of SiO_2 samples at temperatures in the range 900 - 1100°C

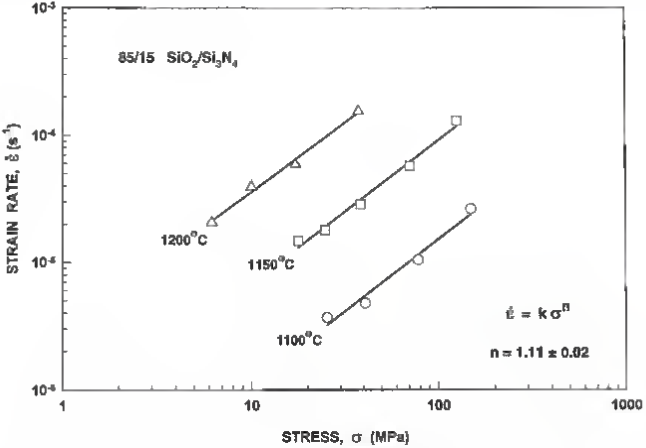

Figure 4.93 Plots of strain rate vs stress for the compression creep of 85/15 SiO_2/Si_3N_4 samples at temperatures in the range 1100 - 1200°C.

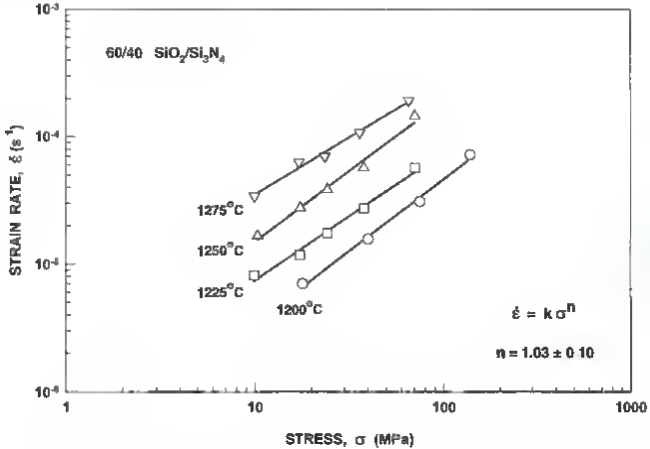

Figure 4 94 Plots of strain rate vs stress for the compression creep of 60/40 SiO_2/Si_3N_4 samples at temperatures in the range 1200 – 1275°C

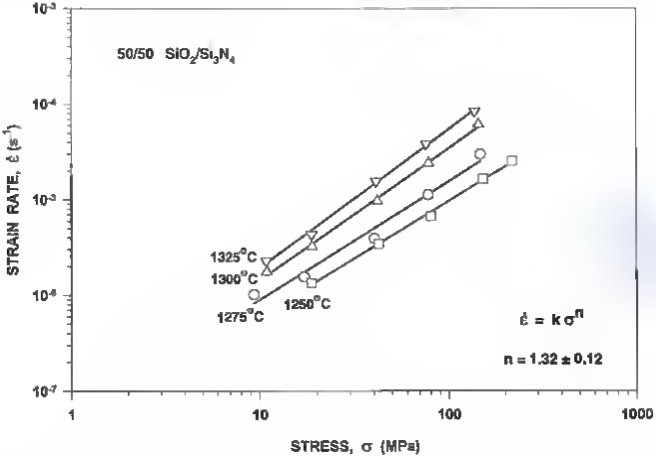

Figure 4.95 Plots of strain rate vs stress for the compression creep of 50/50 SiO_2/Si_3N_4 samples at temperatures in the range 1250 - 1325°C.

Table 4.34 List of n Values as a Function of Test Temperature for SiO_2 and Composite Samples

SiO_2		85/15		60/40		50/50	
T (°C)	n	T (°C)	n	T (°C)	n	T (°C)	n
950	1 03	1100	1 13	1200	1 13	1250	1.20
1000	1 03	1150	1 12	1225	1 00	1275	1.24
1050	1 07	1200	1 09	1250	1 10	1300	1.38
1100	0 93			1275	0.90	1325	1 45

Table 4.35 List of Activation Energies(E) at Various Compressive Stresses (σ), for SiO_2 and Composite Samples.

SiO_2		85/15		60/40	
σ (MPa)	E (kJ/mol)	σ (MPa)	E (kJ/mol)	σ (MPa)	E (kJ/mol)
5	429 1	5	586.5	10	551 1
10	434 5	10	576 9	20	584 9
20	416.6	20	581 7	50	472.2
50	422 0	50	570 4	100	506.1

contrast, the 50/50 sample exhibits much higher n values and hence a non Newtonian (or shear thinning) type of creep deformation.

Figures 4.96 - 4.99 show plots of the steady state creep rate as a function of inverse temperature for SiO_2, 85/15, 60/40, and 50/50 samples, respectively. Table 4.35 lists the activation energies calculated from these plots. It is clear that the activation energy for compression creep was almost independent of stress for samples with 0 -15, and ~40 vol% Si_3N_4 respectively. The average activation energies for these samples were calculated to be 426 ± 8, 579 ± 7, and 529 ± 49 kJ/mol respectively.

The calculated activation energy for the creep deformation of SiO_2 was considerably lower than the reported values for the viscous flow of amorphous silica [Vor90, Sac84b, Het64]. Sacks and Tseng [Sac84b] used calcined (200°C, 24 h) SiO_2 powder to slip-cast bulk compacts. The compacts were pre-sintered at 500°C for 1 h in air and subsequently sintered in the range of 900°C to 1050°C in static air. Viscosities were determined by fitting the experimental sintering data to available theoretical models. Based on these viscosities, the activation energy for viscous flow was determined to be ~506 kJ/mol which was in good agreement with 510 kJ/mol measured on fused SiO_2 with high hydroxyl concentration [Het64]. Vora [Vor90] also prepared similar compacts using SiO_2 powder calcined at 700°C for 6 h. Pre-sintering was carried out at 700°C for 6 h in air and the samples were sintered at 1150°C to full density (i.e., zero residual porosity). The activation energy for viscous flow was determined by high-temperature bend tests to be ~545 kJ/mol. Vora [Vor90] argued that since the powder compacts were extensively pre-sintered, considerable amounts of hydroxyl groups were removed which led to an activation energy value higher than that obtained by Sacks and Tseng [Sac84b]. This was consistent

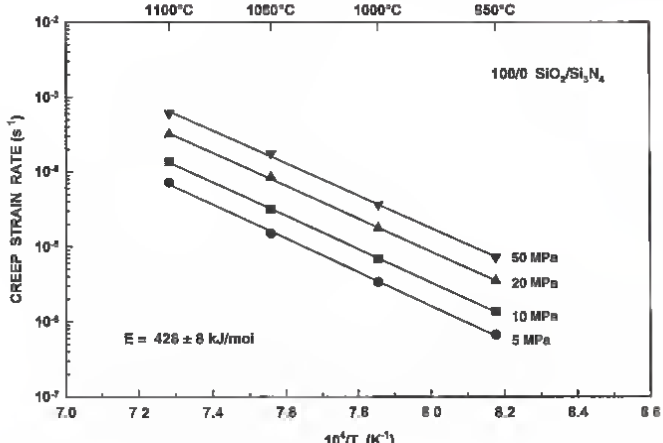

Figure 4 96 Plots of creep strain rate at indicated stresses, as a function of inverse temperature for SiO_2 samples

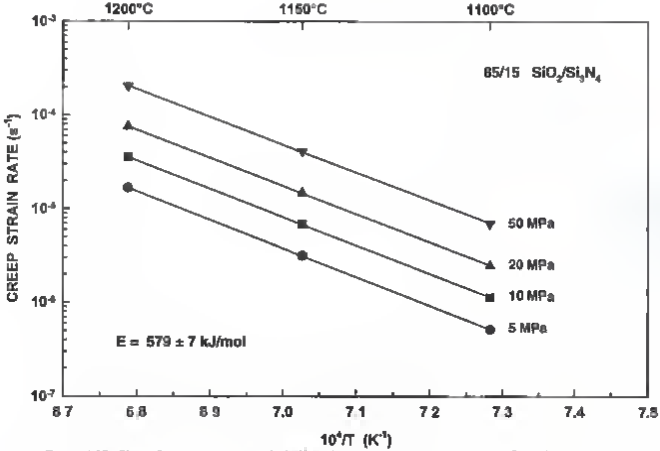

Figure 4 97.. Plots of creep strain rate at the indicated stresses, vs inverse temperature for 85/15 SiO_2/Si_3N_4 samples

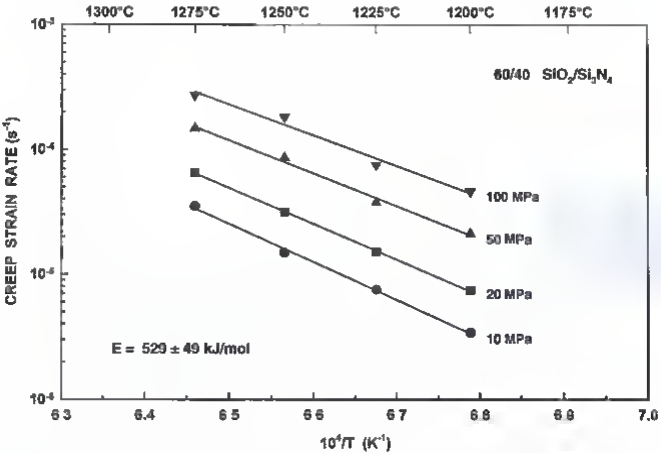

Figure 4.98 Plots of creep strain rate at the indicated stresses, vs inverse temperature for 60/40 SiO_2/Si_3N_4 samples

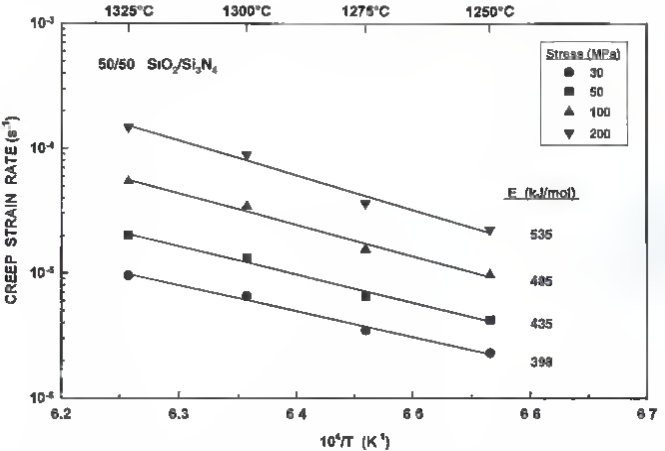

Figure 4 99 Plots of creep strain rate at the indicated stresses, vs inverse temperature for 50/50 SiO_2/Si_3N_4 samples

with the observation by Hetherington et al [Het64] that the activation energy increases with decreasing hydroxyl concentration. (They showed that the activation energy of fused silica increased from ~509 to ~711 kJ/mol when the hydroxyl content in the sample decreased from 0.12 to 0.0003 wt% [Het64].) Although the SiO_2 compacts used in this study were pre-sintered at 700°C, the starting powder (batch 2) was calcined at only ~200°C prior to consolidation. Therefore, it is possible that higher amounts of hydroxyl groups were present in these compacts compared to those used by Vora [Vor90]. The powders used in the current study were calcined at the same temperature (i.e., 200°C, 24 h) but the compacts were pre-sintered at higher temperatures (700 vs. 500°C) compared to that used by Sacks and Tseng [Sac84b]. Consequently, there is presumably smaller amounts of hydroxyl groups in the former samples compared to the latter samples. However, this is in contrast with the fact that the activation energy for viscous flow determined in the current study is lower than that reported by Sacks and Tseng [Sac84b]. Hence, further work (such as measurement of the OH content) is needed to understand the reasons for the low activation energy obtained in the current study.

The viscosity values reported in the studies of Sacks and Tseng [Sac84b] and Vora [Vor90] were compared with those obtained in the current investigation. The viscosities were determined by taking the ratio of the true stress and the true strain rate. Table 4.36 shows the comparison of viscosity values at 1100°C and 1150°C (the data at 1150°C was obtained by extrapolating the curves in Figure 4.96). Table 4.36 shows that the measured viscosities were significantly (1-2 orders of magnitude) lower than those reported by Vora [Vor90] which seem to suggest that significantly greater amounts of hydroxyl groups were present in the samples used in the current investigation. The study of Sacks

and Tseng [Sac84a] reported much lower viscosities compared to those obtained in the current investigation. However, in that study viscosities were obtained by an indirect method, i.e., by fitting the densification data to Scherer's model [Sch77] for viscous sintering. Vora [Vor90] compared the viscosities determined from direct measurements (high-temperature flexure tests) to those predicted by the method used by Sacks and Tseng [Sac84a]. It was found that the predicted values were 1-2 orders of magnitude lower than the measured values. This difference was attributed to errors in the assumption of the pore geometry in Scherer's model. (The pore size was assumed to be equal to the particle diameter. It was argued that since the pore size continuously changes during densification, the assumption is not accurate [Vor90].) Therefore it may not be reasonable to compare the viscosities obtained by Sacks and Tseng [Sac84a] to those measured in the current study.

Table 4.36. Comparison of Viscosities Measured by Creep Experiments with Values Determined by Vora [Vor90] and Sacks and Tseng [Sac84b].

	η (Poise)		η (Poise) *(this study)*			
T (°C)	*Vora* [Vor90]	*Sacks et al.* [Sac84a]	5 MPa	10 MPa	20 MPa	50 MPa
1100	$\sim 2 \times 10^{13}$	$\sim 2 \times 10^{10}$	6.9×10^{11}	7.3×10^{11}	6.3×10^{11}	8.2×10^{11}
1150	$\sim 4 \times 10^{12}$	$\sim 5 \times 10^{9}$	2.6×10^{11}	2.1×10^{11}	2.3×10^{11}	3.0×10^{11}

Compared to the SiO_2 compacts, the 85/15 and the 60/40 powder compacts were sintered at much higher temperatures (1300°C vs. 1150°C for SiO_2) and hence considerable amounts of hydroxyl groups were removed. Therefore, it is not surprising that the average activation energies for the deformation for the 85/15 and 60/40 samples were higher than the value determined for SiO_2 (579 and 529 kJ/mol, respectively vs. 426 kJ/mol). The

differences in the activation energies between the 85/15 and 60/40 samples can also be attributed to the differences in hydroxyl contents. As explained in Section 3.8, the pre-sintered (800°C 2 h) 85/15 samples were heated to 1150°C for 2 h in order to provide strength for machining purposes. However, the 60/40 samples were only pre-sintered at 800°C for 2 h. Therefore 85/15 samples contained lower concentrations of hydroxyl groups which would explain the higher measured value of the activation energy for deformation.

The effect of sintering temperature on deformation behavior was demonstrated by performing the following experiment. A 60/40 sample was sintered at 1400°C for 2 h in nitrogen and creep-tested at 1200°C in the stress range of 20 – 200 MPa. Figure 4.100 shows a comparison of the strain rate vs. stress behavior for 60/40 samples which were sintered at 1300 and 1400°C and tested at 1200°C. (The data for the former sample is same as shown in Figure 4.94.) Although the stress exponents for both samples were ~1 (i.e. the flow was Newtonian in both cases), the sample sintered at the higher temperature (i.e., 1400°C) exhibited significantly lower strain rates. This is consistent with the argument that higher heat-treatment temperatures lead to higher activation energies and higher viscosities due to the reduction in hydroxyl concentration in the compacts.

Deformation behavior was directly compared for 30/70, 40/60, 50/50, and 60/40 compacts by performing creep tests at 1275°C. Figure 4.101 shows the plots of strain rate vs. stress for these samples. The n values were calculated to be ~1.11, ~0.94, ~1.24, and ~0.94, for the 30/70, 40/60, 50/50, and 60/40 samples, respectively. It is evident from Figure 4.101 that the creep behavior of the 30/70, 40/60, and 50/50 compacts were essentially identical and the average stress exponent corresponding to a combination of dom

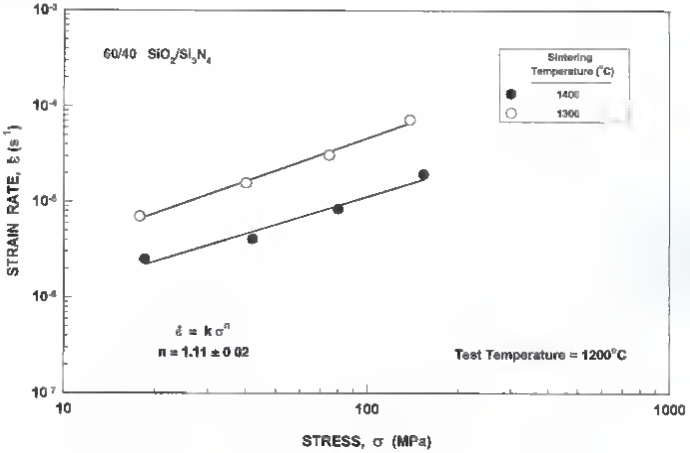

Figure 4.100 Plots of strain rate vs stress for 60/40 SiO_2/Si_3N_4 samples showing the effect of sintering temperature on the creep behavior

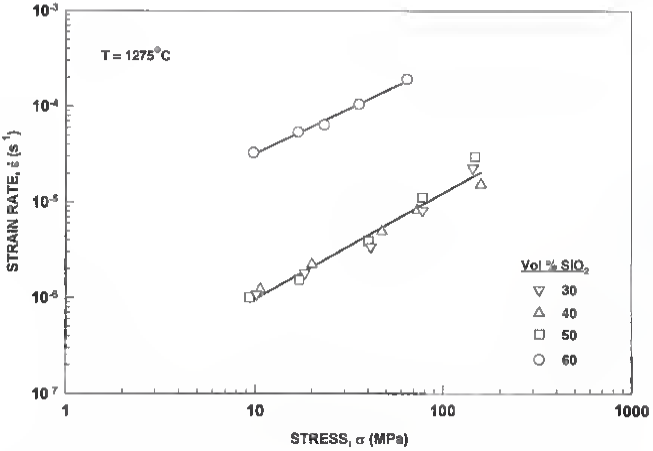

Figure 4.101 Plots of strain rate vs stress for the compression creep of composite samples with SiO_2/Si_3N_4 ratios of 30/70 40/60, 50/50, and 60/40, at 1275°C

from the three samples was determined to be ~1 10 In contrast, the 60/40 sample showed much higher creep rates and the corresponding stress exponent was ~0 94.

As indicated in Section 4.3 4, the 30/70 40/60, and 50/50 compacts reached limiting maximum densities due to the formation of contiguous networks of Si_3N_4 particles Although these networks are "rigid" under the sintering stresses, particle rearrangement is possible under high external stresses (i.e , higher than the sintering stresses) In order to estimate the rigidity of Si_3N_4 particle-particle contacts, creep experiments were carried out on a Si_3N_4 powder compact. The powder compact was formed by slip-casting a well-dispersed (pH ~ 9.6) ~30 vol% aqueous suspension using a procedure similar to that described in Sections 3 4 and 3 5 The compact was dried at 80°C for 24 h, pre-sintered in flowing (~60 cm^3/min) nitrogen at 800°C for 2 h, and subsequently sintered in the same atmosphere at 1500°C for 2 h. The bulk density and the open porosity of the sintered compact were measured by the Archimedes displacement method using deionized water as the medium. The values were 1 84 g/cm^3 and 42%, respectively This sample was compression tested at 1275°C in the stress range of 20 200 MPa. It was found that the sample did not undergo any deformation over the entire stress range studied confirming that the Si_3N_4 particle particle contacts are indeed "rigid" under the creep conditions. This is in contrast with the results obtained for 30/70, 40/80 and 50/50 samples (Figure 4 101) which underwent significant deformation even at relatively low stresses. The latter result is attributed to a thin "lubricating" layer of SiO_2 separating the Si_3N_4 particles which would then allow for particle rearrangement to occur (by viscous flow of the amorphous SiO_2) under an external applied stress. Such a layer is consistent with the HRTEM observations discussed in regard to Figure 4 91

The concentration of Si_3N_4 in the bulk volume (ratio of Si_3N_4 volume to the sum of Si_3N_4 SiO_2 and pore volumes) was determined for 30/70 40/60 and 50/50 samples (after creep testing). The values were obtained by multiplying the relative density (obtained by dividing the bulk densities in Table 4 37 by the corresponding true density) by the nominal Si_3N_4 core particle volume fraction[10] in the solids Table 4 37 shows the results from these calculations

Table 4 37 Calculated Values of Vol% Si_3N_4 in Bulk Volume of Creep Tested Samples

Sample	ρ_{bulk} (g/cm^3)	Relative Density (%)	Nominal Si_3N_4 Fraction in Solids	Vol% Si_3N_4 in Bulk Volume
30/70	2 16	73 7	0 70	51 6
40/60	2 36	83 4	0 60	50 0
50/50	2 62	96 3	0.50	48.2

Table 4.37 shows that the vol% Si_3N_4 cores in bulk volume increased slightly with increase in the Si_3N_4 content in solids. However, the standard deviation in the three values was small (~1 4% corresponding to the average value of ~49 9%) Based on this observation, it may be reasonable to expect that the number of Si_3N_4 particle-particle contacts were similar for these compacts Consequently under an applied external stress, the local stresses on the Si_3N_4 particles would be identical which would explain the similarity in the creep behavior of these samples

[10] As noted in Section 3 2 1 the volume fraction of Si_3N_4 is slightly lower than that of the core particles due to the presence of SiO_2 in the latter particles. For example, if the core volume fraction is 0 50, and the core particles contained 2vol% SiO_2 the Si_3N_4 volume would be 0 98x0 50 = 0.49

In contrast to the SiO_2, 85/15 and 60/40 composite compacts, the 50/50 compacts showed a non-Newtonian flow behavior (n>1, as shown in Figure 4.95) and the activation energy is a strong function of the applied compressive stress (Figure 4.99). One of the factors considered to explain this was the possible densification of the 50/50 samples during creep experiments. Table 4.38 shows the results from Archimedes density measurements (with water as the medium) for sintered samples used for compression creep experiments. Table 4.39 shows similar data for samples after creep tests were performed at 1275°C. It is evident that the 30/70 , 40/60, and 50/50 samples underwent some densification during the creep treatment (the bulk densities increased from 2.07, 2.27, and 2.60 g/cm^3, respectively, to 2.16, 2.36, and 2.62 g/cm^3, respectively). However the strains associated with this densification were much lower than those observed during the creep experiments (≤1.5% vs. ~20%, respectively). For example, the volumetric strain associated with the densification of 30/70 sample during the creep experiments can be calculated as { (1/2.07 - 1/2.16) / (1/2.07) } ~ 0.04. This translates into an axial strain of 0.04/3 = 0.013 or 1.3%, assuming isotropic shrinkage. Since the 40/40 and 50/50 samples underwent even lesser shrinkages (compared to the 30/70 sample), the axial strains are even lower (1.2 and 0.3%, respectively).

Stress exponent values greater than 1 have been observed for Si_3N_4 samples containing amorphous second phases [Wha90, Koe91, Lue95]. Whalen et al. [Wha90] carried out compression creep measurements on pressureless sintered Si_3N_4 (>99% density) containing ~6.4 vol% of a yttria-based amorphous phase. The stress exponents ranged from 1.9-2.6 for samples tested in the temperature range of 1275 to 1325°C and in the stress range of 207-345 MPa. The creep deformation in these samples were controlled by

Table 4 38 Density Data for Sintered Samples Used for Creep Testing

Sample	Sintering Temperature (°C)	Bulk Density (g/cm^3)	Open Porosity (%)	Apparent Density (g/cm^3)
30/70	1400	2 068	29 2	2.921
		2 065	29 6	2.918
40/60	1400	2 267	18 9	2.814
		2 270	18 5	2.816
50/50	1400	2 595	0 1	2.597
		2 598	0 3	2.594
60/40	1300	2.602	0 0	2 602
		2.594	0,2	2 598
60/40	1400	2.595	0,2	2 601
		2.599	0 1	2 601

Table 4 39 Density Data for Samples Creep Tested at 1275°C.

Sample	Bulk Density (g/cm^3)	Open Porosity (%)	Apparent Density (g/cm^3)
30/70	2 162	24 9	2 879
	2.164	24 8	2 879
40/60	2.355	15.3	2.779
	2 355	15.5	2.788
50/50	2 621	0.3	2 628
	2 623	0 1	2 626
60/40	2 602	0 3	2 611
	2 601	0 3	2.608

cavitation in the amorphous grain boundary phase. This was demonstrated by the high stress exponents (values >2 are typically associated with cavitation [Koe91, Lue95]) and TEM observations of the grain boundary amorphous phase which showed the presence of cavities. Koester et al. [Koe91] conducted constant stress compressive creep studies on hot-pressed Si_3N_4 containing 30vol% SiC whiskers and an initial vitreous phase composed of SiO_2, Y_2O_3, and Al_2O_3 (the sintered sample contained 2.82wt% SiO_2, 4.25wt% Y_2O_3, and 1.05wt% Al_2O_3). The creep experiments were carried out in the temperature range of ~1200-1400°C, and in the stress range of 50-350 MPa. An integrated analysis of all the data indicated that the composite crept via the mechanisms of grain boundary sliding, initially accommodated by viscous flow and subsequently by diffusional processes. At low stresses and temperatures, the former mechanism was dominant leading to relatively low values of stress exponent and activation energies. At higher stresses and temperatures, the latter mechanism (lattice ion diffusion) led to higher stress exponents and activation energies. (For example, the average stress exponents were ~1.01 and ~2.52 for temperatures of 1198 and 1498°C, respectively, and the average activation energies were 497 and 734 kJ/mol for stresses of 100 and 300 MPa, respectively)

The sintered composite samples used in the current study did not show any decrease in density after the creep testing (Tables 4.38 and 4.39). Therefore, it is not likely that any cavitation occurred in the compacts due to the deformation stresses. Since the kinetics of transport of Si_3N_4 through the SiO_2 phase is known to be sluggish [Lar91] at the temperatures used in the creep experiments diffusion through the amorphous phase is not expected to play a significant role in determining the deformation behavior. The viscous flow in the composite samples may be divided into two modes: (1) the deformation of the

matrix SiO_2 under the compression stress, and (2) sliding of Si_3N_4 particulates, accommodated by the viscous flow of the lubricating layer separating the particles. Although both the deformation modes are controlled by viscous flow the corresponding deformation rates may be different. The second mode is presumably associated with higher deformation rates since the contact area between adjacent Si_3N_4 grains is relatively small and the local stresses are relatively large compared to the external stress. Figures 4.90 (A)-(D) showed that while the sintered 60/40 sample had a microstructure with mostly isolated Si_3N_4 particles, the sintered 30/70 and 40/60 samples showed extensive "apparent" Si_3N_4 particle-particle contacts (and relatively few isolated Si_3N_4 particles). Therefore, the dominant creep mode for the 60/40 sample is presumably the matrix deformation (i.e., the first mode) while that for the 30/70 and 40/60 samples is the sliding of Si_3N_4 particles (i.e., the second mode), over the entire range of stresses and temperatures investigated. Since both modes are presumably controlled by Newtonian viscous flow, these samples showed stress exponents of nearly 1. (The 30/70 and 40/60 samples were tested only at 1275°C. It is not known if these samples would exhibit any dependence of stress exponent with temperature and/or any dependence of activation energy with stress.) In contrast to the 60/40, 40/60, and 30/70 sintered samples, the sintered 50/50 compact showed significant numbers of both "apparent" Si_3N_4 particle-particle contacts as well as isolated Si_3N_4 particles (Figure 4.90(C)). Therefore, the 50/50 compact represents a transition case where both the deformation modes may be significant during the creep experiments. It is possible that for this sample, the first mode controls deformation at lower stresses and lower temperatures, while the latter mode dominates at higher stresses and higher temperatures.

In such a case relatively smaller deformation rates would be measured at lower stresses and lower temperatures, and relatively larger creep rates would be observed at higher stresses and higher temperatures. This would explain the high stress exponent values, and the increasing values of activation energies with stress, observed for these samples. Further creep experiments (e.g. compression testing of creep-tested samples) and microscopy analyses (e.g. quantitative analysis of the change in the distribution of the phases, or particle spacing, after creep experiments) may be necessary to confirm this interpretation.

Figure 4.102 shows XRD plots in the 2θ range of 18 - 24° for 50/50 and 60/40 composite powder samples that were creep tested at 1275°C and 1300°C, respectively. The crystalline peaks in both the plots correspond to α-Si_3N_4 while the broad peak centered at $2\theta \sim 22°$ is characteristic of amorphous SiO_2. This clearly indicates that cristobalite did not form under the stresses and temperatures used.

4.3.6. Rigidity Threshold in Composite Powder Compacts

During the sintering of a composite powder compact, the cores (inclusions) of the microcomposite particles will approach each other as the compact shrinks and the coating (matrix) phase is redistributed during sintering. A contiguous particulate network will form prior to complete densification if the core particle volume fraction exceeds a critical threshold value. If the core particles are "rigid" (i.e., non-sinterable), this network imposes a constraint on densification. The rigidity threshold, Φ, is defined as the critical volume

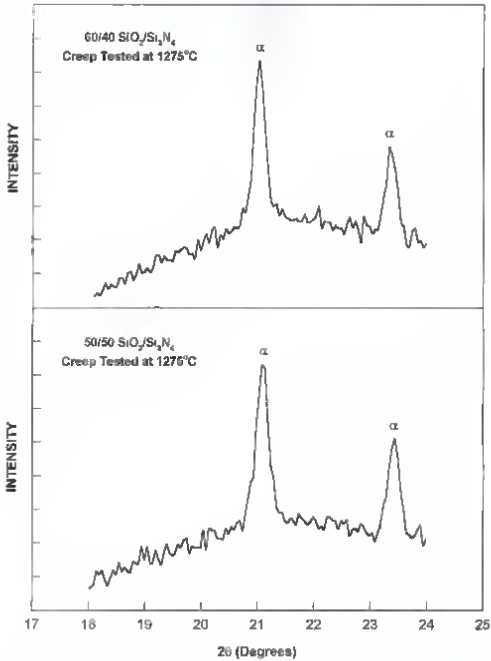

Figure 4 102 XRD plots for SiO_2/Si_3N_4 samples compression creep tested at 1275°C The crystalline peaks (α) for both samples correspond to α-Si_3N_4

fraction of inclusions (in the solid volume) below which the composite can be sintered to full density (i.e., no residual porosity) [10]

Consider a green compact consisting of a randomly packed array of N uniformly coated spherical inclusion particles (Figure 4.103, left side). If R is the radius of the inclusion particle and t is the thickness of the coating, the volume fraction of the inclusion (in the matrix + inclusion volumes), v_i, can be expressed as,

$$v_i = R^3 / (R+t)^3 \tag{4.24}$$

The particle packing is assumed to be homogeneous and the initial packing fraction (i.e., green density) is denoted by ρ_0. Further, it is assumed that the compact undergoes isotropic shrinkage, i.e., the inclusion packing geometry remains unaltered, during the sintering process. In the limiting case (corresponding to the rigidity threshold), when the inclusions come in contact, the void space is completely occupied by the matrix phase (Figure 4.103, right side) and therefore,

$$v_i = \theta \tag{4.25}$$

The total volume of the matrix phase in the green compact, V_{mg}, is given by,

$$V_{mg} = N \bullet 4\pi/3 \bullet [\,(R+t)^3 \;\; R^3\,] \tag{4.26}$$

The volume of the matrix phase in the sintered (fully dense) compact (Figure 4.103, right hand side) V_{mf} can be expressed as,

$$V_{mf} = N \bullet [(1 - \rho_0)/\rho_0] \bullet 4\pi/3\, R^3 \tag{4.27}$$

[10] In general a percolating cluster of particles is treated as a "rigid" network only when all the contacts between the particles are bonded [Kim95]. In this study, the sintered compacts with high concentrations of Si_3N_4 consisted of a network of particles separated by thin layers of amorphous SiO_2. Creep studies on these compacts (Section 4.3.5) confirmed that the "contacts" were not bonded, i.e., the compacts could be deformed under applied external stresses. However, in the context of densification, sintering stresses are not sufficient to affect this network, and therefore, it may be treated as a "rigid" network.

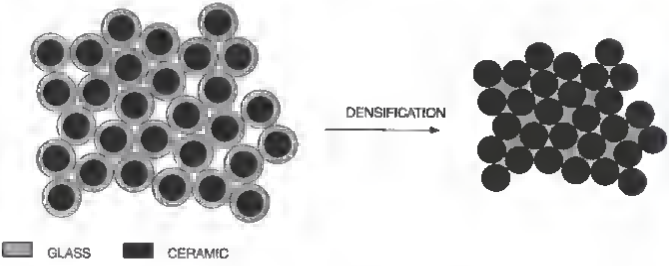

Figure 4 103 Schematic showing the formation of a rigid network of Si_3N_4 particles at the threshold concentration of Si_3N_4 particles (rigidity threshold)

Since the mass is conserved during the sintering process, $V_{no} - V_{nf}$. Equating the terms in eq s (4.26) and (4 27), we obtain,

$$N \bullet 4\pi/3 \bullet [\,(R+t)^3 - R^3\,] = N \bullet [(1 - \rho_0)/\rho_0] \bullet 4\pi/3\, R^3$$

$$(R+t)^3 / R^3 = [(1 - \rho_0)/\rho_0] \bullet R^3$$

$$[(R+t)^3 / R^3] - 1 = 1/\rho_0 - 1 \qquad (4\ 28)$$

Substituting eq.s (4.26) and (4.27) into eq (4.28), we obtain,

$$1/\theta = 1/\rho_0 \qquad \text{or,}$$

$$\theta = \rho_0 \qquad (4\ 29)$$

Therefore the rigidity threshold is numerically equal to the green compact density if the inclusion packing geometry does not change during sintering.

The rigidity threshold can also be defined as the limiting volume fraction of the inclusion particles in the bulk volume of the sintered compact. This is particularly useful for comparison of theoretical predictions with experimental results. Figure 4.104 shows a plot of maximum volume fraction of Si_3N_4 in the bulk volume [63] (including the porosity) as a function of Si_3N_4 in solids (corresponding to the data in Table 4.32, and calculated using the same procedure as described in the previous section). The maximum volume fraction reached a limiting value of ~49 vol% for samples with ≥50 vol% Si_3N_4 in solids. (It is noted that the maximum volume fraction increased slightly with Si_3N_4 content (values were ~48.2, ~48.7, and ~50.2 vol% for 50/50, 40/60, and 30/70 samples, respectively). However the standard deviation for the values was only 0.8 vol%. Thus is considerably lower than the green densities (~60 vol%). The deviation of the rigidity threshold from the theoretical

[63] The value calculated was actually the volume fraction of the Si_3N_4 core particles. As noted earlier the volume fraction of Si_3N_4 would be slightly lower than this value due to the presence of SiO_2 in the core powder. However this does not alter the arguments presented in this paragraph.

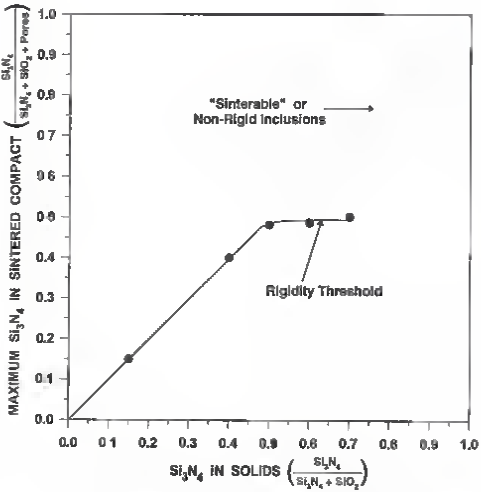

Figure 4 104 Plot of Si_3N_4 in the bulk volume at the maximum sintered density vs Si_3N_4 content in solids. The rigidity threshold value is ~49 vol%

predictions may be attributed to experimental non-uniformities, e g , in particle packing, microcomposite particle phase distribution etc It was shown in Section 4 3 1 that for a given powder batch, the composite powders exhibit a distribution in composition as a consequence of the thickness being uniform for all core sizes This means that there are local SiO_2/Si_3N_4 composition variations, in which some composite particle-particle contacts have relatively thin SiO_2 layers Therefore, during the sintering of composite powder compacts, local networks of Si_3N_4 can form between particles containing relatively low volume fractions of SiO_2

The dependence of composition distribution on sintering was investigated by preparing samples with the same overall composition (i.e., SiO_2/Si_3N_4 ratio) but varying local distribution of the phases Samples with the overall composition of 50 vol% SiO_2 / 50 vol% Si_3N_4 were prepared by consolidating three different powder suspensions - a 50/50 composite powder suspension (30 vol%, pH ~9 2), a 1 1 (by volume) mixture of 40/60 and 60/40 composite powder suspensions (each ~30 vol%, pH ~9.2), and), a 5 1 (by volume) mixture of Si_3N_4 (fines) and 60/40 composite powder suspensions (each ~30 vol% solids and at pH ~9.2) The samples were designated 50/50 40/60+60/40 and SN+60/40, respectively The samples were first pre-sintered to 800 °C (2 °C/min, 2 h hold, in N_2) The samples were then sintered to 1450°C and 1500°C (2 h hold) in an alumina tube furnace[104] in a nitrogen atmosphere Densities were measured after each heat-treatment using the Archimedes displacement method with water as the medium. Tables 4 40 and 4 41 show the results from the density measurements

[104]Model 64259 Lindberg Co., Watertown, WI

Table 4 40 Pre-sintered Densities for Mixed Powder Compacts.

Sample		ρ_{Bulk} (g/cm^3)	% O.P	$\rho_{Apparent}$ (g/cm^3)
50/50	#1	1 616	39 7	2 679
	#2	1 615	39 4	2 665
40/60+60/40	#1	1 613	39 9	2.682
	#2	1 608	40 1	2.686
SN+60/40	#1	1 601	40 1	2 673
	#2	1 594	40 4	2.675

Table 4 41 Sintered Densities for Mixed Powder Compacts.

Sample		ρ_{Bulk} (g/cm^3)	% O P	$\rho_{Apparent}$ (g/cm^3)	Relative Density (%)
1450°C - 2h					
50/50	#1	2 620	0 0	2.621	
	#2	2.618	0 1	2.621	96 7
40/60+60/40	#1	2.551	0 0	2 552	
	#2	2.551	0 0	2.552	94 1
SN+60/40	#1	2.486	0 0	2 486	
	#2	2 496	0 1	2.500	91 9
1500°C - 2h					
50/50	#1	2 629	0 0	2 629	
	#2	2 618	0 1	2 621	96 7
40/60+60/40	#1	2 566	0 0	2 566	
	#2	2 551	0 0	2 552	94 1
SN+60/40	#1	2 512	0 0	2 512	
	#2	2 496	0 1	2 500	92 3

It is evident from Table 4.40 that the green densities of the samples prepared by the three different routes have very similar values. This would eliminate differences in green density as a factor affecting the sintering kinetics. It is clear from Table 4.41 that despite the fact that the green densities of all the samples were similar, the sintered densities increased as the uniformity of the spatial distribution of phases throughout the compact increased. Since all the samples underwent marginal densification between 1450°C and 1500°C, it may be assumed that all the samples reached limiting densities. The density data clearly demonstrates that non-uniformities in composition of powders and in the spatial distribution of phases in the compact lead to retardation in densification kinetics and a decrease in the value of the rigidity threshold. It is noted that these results are consistent with the results from the experiments comparing the composite powder and mixed powder compacts (Sections 4.1.3 and 4.3.4) which also demonstrated that the densification is retarded if the spatial distribution of the phases is non-uniform.

4.3.7. Comparison of Experimental Data with Theoretical Models

As indicated earlier, Figure 4.84 shows the plots of relative density vs. sintering time, at 1225°C, for SiO_2 compacts, 85/15 compacts, and SiO_2+Si_3N_4 mixed powder compacts with 15 vol% Si_3N_4. The solid lines in the plots were obtained by fitting smooth curves using the same procedure as described earlier. The procedures described in Sections 2.5.1 and 2.5.2 were used to evaluate the theoretical and experimental values of the ratio of the strain rate of the composite and that predicted by the rule-of-mixtures,

$\frac{\dot{\varepsilon}_c}{\dot{\varepsilon}_c^m}$ (the normalized strain rate)

In Figure 4.105, the experimental results for $\frac{\varepsilon_L}{\varepsilon_L^m}$ are compared with the predictions of Scherer's model. It is evident that the experimental data shows poor agreement with theoretical estimates. The potential reasons for the deviation from theory are discussed below. Scherer's model [Sch87] assumes that the inclusions must be much larger than the sintering (matrix) particles so that the matrix can be regarded as a continuum. Moreover, the model does not allow for the fact that the inclusions will mutually interfere and later will come into contact and stop densification at some critical volume fraction which generally corresponds to the percolation threshold. Rahaman and DeJonghe [Rah87a] tested the validity of Scherer's model using powder compacts prepared from mixtures of soda-lime silicate glass powder (~4 μm average diameter) and SiC powder (average diameter ~35 μm). It was shown that the experimental results were in excellent agreement with theoretical predictions if the inclusion concentration was ≤ 12 vol%. Above this value, the interactions between the inclusions caused significant deviations from theory. Boccaccini [Boc94] conducted similar studies using compacts prepared from a mixture of aluminosilicate glass particles (~8 μm mean diameter) and alumina platelets (5 - 25 μm major axes). It was demonstrated that the sintering results showed good agreement with model predictions provided the platelet content was ≤ 15 vol%. It is noted that both these studies utilized inclusion particles much larger than the matrix particles. However, particle mixtures with matrix particles larger than the inclusion particles exhibited a different behavior. Dutton et al. [Dut92] have shown that in such particle mixtures, there is a relatively higher degree of continuity between a larger

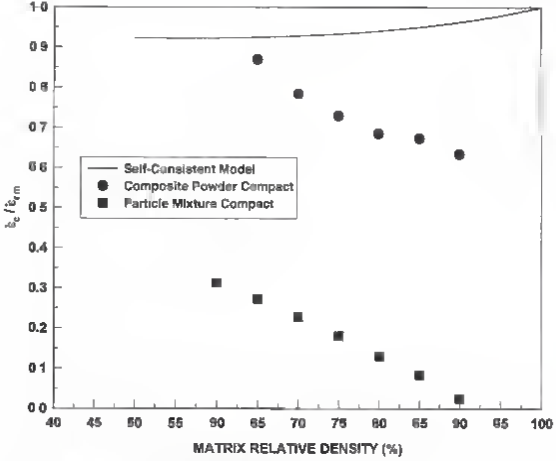

Figure 4.105 Comparison plots of the normalized linear strain rate of the composite vs the relative density of the matrix, for SiO_2/Si_3N_4 composites containing 85 vol% SiO_2

number of inclusion particles This was demonstrated by electrical conductivity measurements carried out on compacts formed from a mixture of ~90 vol% soda-lime glass powder (10 - 15 μm diameter) matrices and ~10 vol% nickel inclusions (6 - 10 μm diameter). These results are also consistent with theoretical analyses conducted by Kusy [Kus77] and simulations carried out by Bouvard and Lange [Bou91]. Kusy [Kus77] showed, using a probabilistic approach, that lower conductivity percolation thresholds were predicted for mixtures with a greater matrix particle to inclusion particle size ratio β. For example, the threshold values decreased from ~22 vol% to ~8 vol% as β increased from ~2 to ~7. Bouvard and Lange [Bou91] carried out simulations of inclusion matrix particle (with spherical geometry) mixtures at various size ratios and phase proportions. The relative packing density ranged from 57% to 61% depending on size ratio and composition. Percolation threshold were determined for different values of the matrix to inclusion particle size ratio β. It was shown that the percolation threshold decreased as β increased (threshold values were ~22, ~18, and ~11 vol% for β values of 0.5, 1, and 2, respectively). In the current investigation the inclusion (i.e., Si_3N_4) particles used in the SiO_2+Si_3N_4 mixed powder compacts were smaller in diameter than the matrix (i.e., SiO_2) particles (median Stokes' diameters of ~0.3 μm and ~0.5 μm, respectively). The deviation of experimental results from theory for SiO_2+Si_3N_4 mixed powder compacts can therefore be explained in part by the increased inclusion interactions arising from the size differences between the constituent phases.

The spatial distribution of the phases in a composite powder compact is such that the inclusion particles are completely isolated from each other in the green state. Consequently, for the 85/15 composite powder compact, the inclusion interactions are

minimal and the matrix (SiO_2) phase can be regarded as a continuum. Therefore the experimental values of $\frac{\varepsilon_c}{\varepsilon_c^m}$ are closer to theoretical predictions for the composite powder compact compared to those for the mixed powder compact (Figure 4.105). However, significant deviations from theory still exist. In order to explain the deviations, it is important to consider the differences between the SiO_2 compacts and the 85/15 composite powder compacts. If there are significant differences (*e.g.*, in particle size, packing, hydroxyl contents, etc.) between the compacts, it may not be reasonable to normalize ε_c (determined from the composite powder compacts) with respect to ε_c^m (determined using the SiO_2 compacts). Possible factors given consideration were the differences in the particle size distributions and the particle packing characteristics between the SiO_2 compact and the 85/15 compact. Although the median Stokes diameters for the two particles were similar (~0.50 μm), the 85/15 powder had a broader particle size distribution (Figures 3.2 and 4.60). It has been shown (e.g. for Al_2O_3 [Yeh88] and SiO_2 [Vor90] compacts) that for the same median particle size, broader size distributions result in enhanced densification rates. Furthermore, the green densities of the SiO_2 and the 85/15 compacts were ~52%[105] and ~57%, respectively (see Table 4.31). Therefore, the 85/15 compact would densify faster than it would if it had size distribution and packing characteristics similar to those for the SiO_2 compact. However, this would lead to the prediction of higher $\frac{\varepsilon_c}{\varepsilon_c^m}$ values and thereby result in smaller deviations from the

[105] It is noted that the green densities (see Table 4.31) of the SiO_2 and 85 vol% SiO_2+15 vol% Si_3N_4 particle mixture compacts were very low (~52 and ~57%, respectively). This was possibly due to the presence of some agglomerates in the suspension used for casting. Further analysis (e.g., rheology of suspensions used for casting, SEM of green compacts etc.) may be necessary to confirm this interpretation.

theoretical predictions. Another explanation considered was based on the difference in hydroxyl contents in the SiO_2 and the 85/15 composite samples. The composite samples were pre-sintered at higher temperatures compared to the SiO_2 samples (800 vs. 700°C, respectively). In addition, while the 85/15 samples were heated in a flowing nitrogen atmosphere, the SiO_2 samples had been pre-sintered in static air which has higher concentrations of moisture. Therefore it is likely that the SiO_2 compacts had relatively higher amounts of hydroxyl groups. Since an increase in hydroxyl content leads to a reduction in viscosity [Het64], the densification rates are enhanced. This results in a higher estimated value of the strain rate predicted by the rule-of-mixtures (and, therefore, lower predicted $\frac{\varepsilon_z}{\varepsilon_r}$), and hence, contributes to the deviation of the experimental data from model predictions.

The densification data was also compared with the results from two-particle simulations [Jag94] of the sintering of coated particles. The density data obtained from the simulations were expressed as functions of normalized time τ' which is defined as $(3/4\ \pi)^{1/3}\ \tau\gamma\ /\ \eta R'$ where τ is the sintering time, γ is the surface energy (~ 0.28 J/m^2 [Bru82] for SiO_2), η is the bulk viscosity of SiO_2 phase, and R' is the radius of the composite particles. As explained earlier, the composite particle sizes determined by sedimentation measurements (Figure 4.60) may not be accurate due to the distribution of compositions for particles comprising a given powder batch (with a given overall composition). Therefore, the "average" diameters determined from quantitative microscopy (Table 4.16) were used to calculate the average particle radius for each powder batch. The viscosity of SiO_2 was determined from creep experiments as the ratio

of the compressive stress to the compressive strain rate at a stress of 10 MPa. The viscosity at 1100°C (1373K) was calculated to be ~ 7×10^{11} Pa·s. This was extrapolated to 1225°C (1498K) using the activation energy value of 429 kJ/mol (Figure 4.96) in the Arrhenius equation and the corresponding viscosity was determined to be ~ 1.7×10^{9} Pa·s. It is noted that the SiO_2 samples used for creep testing (i.e., viscosity measurements) probably contained different amounts of hydroxyl groups compared to the composite powder compacts. This is because they were heated to different temperatures and in different environments. (The SiO_2 samples were pre-sintered at 700°C for 6 h and sintered for at 1150°C 24 h in static air prior to creep measurements whereas the composite powder compacts were pre-sintered at 800°C for 2 h and sintered at 1225°C in flowing nitrogen.) As a consequence, the actual viscosities of the matrix (SiO_2) phase in the composite samples may be different. (Due to the complex nature of the differences in thermal histories of the two types of composite, it is difficult to predict if the actual viscosities are lower or higher than the assumed value.)

Figure 4.106 shows plots of relative density vs. normalized time for the composite powder compacts in this study compared to the theoretical data from Jagota's simulations [Jag94]. It is clear from Figure 4.106 that the experimental data does not follow the predictions of Jagota [Jag94]. This deviation may be due to the non-ideal nature of the composite powder compacts. It has been shown from quantitative microscope techniques that for a given composite powder batch, the composition of the particles is not uniform. This results in non-uniformities of the spatial distribution of phases throughout the compact. It has been demonstrated (Table 4.40) that the sintering kinetics is strongly dependent on the spatial distribution of phases in the powder compact.

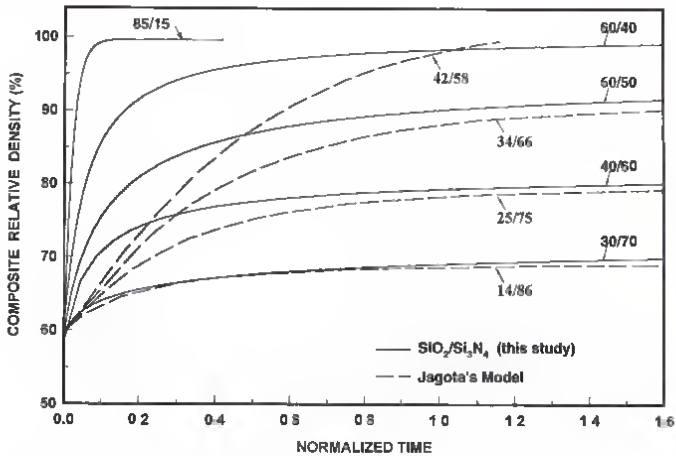

Figure 4.106 Comparison plots of relative density vs normalized time, $\tau' = (3/4\pi)^{1/3}\tau\gamma/\eta R$ for composite powder compacts in this study and simulations of Jagota [Jag94]

As shown earlier, the non-ideal nature of the composite powder compacts resulted in a rigidity threshold value of ~49% which is lower than the theoretical value of ~60% (i.e., the green compact density). Since Jagota's simulation assumes ideal particles and ideal packing, the rigidity threshold used in the the simulations was equal to the green compact density of ~60%. Therefore, the deviations of experimental data from Jagota's predictions may also be attributed to the difference in the rigidity threshold used for the simulation and that obtained for the current study. It is important to note that the theoretical treatment of Jagota [Jag94] involved only a two-particle simulation and therefore, it is not strictly applicable to multi particle systems.

4.3.8. An Empirical Model for Densification of Composite Powder Compacts

Frenkel [Fre45] laid the foundation for all the analyses of viscous sintering. He pointed out that energy is dissipated as heat during viscous flow, and suggested that the reduction in surface area (associated with the neck growth and pore elimination) provides the source of this energy during viscous sintering. Mackenzie and Shuttleworth [Mac49] developed a model in which densification results from the shrinkage of uniform spherical pores in a viscous matrix. The simplicity of the geometry enabled them to write exact expressions of the energy dissipation and the change in surface area during sintering. This approach gives an equation of the form,

$$d\rho'/dt = 2/3\ (4\pi/3)^{1/3}\ n^{1/3}\ (\gamma/\eta)\ (1-\rho')^{2/3}\ \rho'^{1/3} \qquad (4.30)$$

where ρ' is the relative density, n is the number of pores per unit volume, γ is is surface energy, and η is the bulk viscosity of the amorphous phase. Kingery [Kin76] simplified this

expression using the following approach The number of pores depends on pore size (radius r, assuming a spherical geometry) and the relative density and is given by

$$n\,(4\pi/3)\,r^3 = (\text{pore volume} / \text{solid volume}) = (1-\rho')/\rho' \qquad (4.31)$$

Kingery [Kin76] assumed that the pore radius, r, was numerically equal to the initial radius of the particles, r_o. Combining this ($r = r_o$) and eq (4 31) in eq. (4 30), it was shown that

$$dp/dt = (3\gamma / 2\, r_o \eta)\,(1-\rho') \qquad (4\ 32)$$

The sintering data in this study was fitted to eq (4.32) to obtain values of viscosity η as functions of the relative density For the SiO_2 samples, the initial particle radius was assumed to be half the median Stokes diameter determined from particle size measurements However, as explained in Section 4 1 1 particle size measurements on composite powders do not yield accurate results due to the presence of a composition distribution among particles of any given composite powder batch Therefore the average radius of the microcomposite particles obtained from quantitative microscopy (Table 4 16) was used The viscosity for the composite powder samples is an "effective viscosity" or an "equivalent homogeneous viscosity"

Figure 4 107 shows the plots of calculated viscosity vs relative density for the SiO_2 and composite powder compacts. The viscosity of SiO_2 was nearly constant ($\sim 8 \times 10^8$ Pa•s) over the entire density range (which is an indirect evidence to the fact that the experimental data fits the Mackenzie and Shuttleworth model for sintering) This is slightly lower than the value of $\sim 1\ 7 \times 10^9$ Pa•s determined by using the results from creep deformation experiments The equivalent viscosity of the 85/15 composite sample increased slightly with increasing density ($\sim 7 \times 10^8$ Pa•s to $\sim 1 \times 10^9$ Pa•s for relative densities of ~65% and ~95%, respectively). Composite samples containing higher amounts

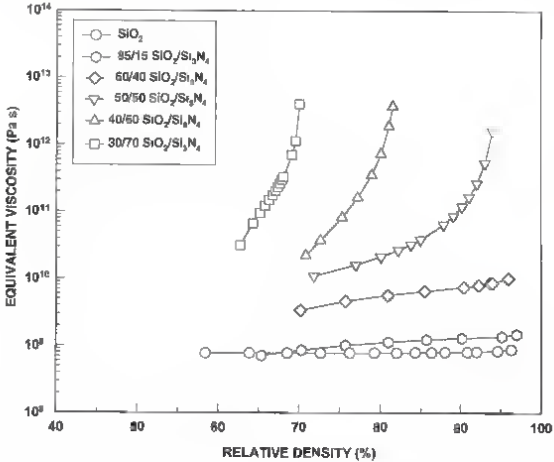

Figure 4 107 Plots of equivalent viscosity (from eq 4 32) vs relative density for SiO_2 and composite powder compacts

of Si_3N_4 showed much higher increases (1-3 orders of magnitude) in viscosity as the samples densified from the green density to the maximum sintered density. This phenomenon may be attributed to the increasing inclusion interactions resulting from the decreasing separation distance between the Si_3N_4 particles (i.e., increasing concentration of Si_3N_4 particles in the bulk volume) during densification. During viscous flow in amorphous systems containing rigid crystalline phases, there is a velocity distribution in the viscous fluid separating adjacent rigid particles. Jagota's study [Jag94] provided evidence for the existence of deformation contours (i.e. velocity distribution in the viscous matrix phase) between a pair of coated particles undergoing sintering. The effective deformation rate D, was defined as

$$D = \sqrt{2\, d_{ij} d_{ij} / 3} \tag{4.33}$$

where d_{ij} is the rate deformation tensor defined in terms of the velocity field v_i as

$$d_{ij} = (v_{i,j} + v_{j,i})/2 \tag{4.34}$$

where i and j are the components of the tensor. The effective deformation rate was normalized as

$$\overline{D} = D\, \frac{\eta(R + t_c)}{\gamma} \tag{4.35}$$

where η and γ are the viscosity and surface tension respectively, of the matrix (coating) phase, R is the radius of the core particles, and t_c is the coating thickness. Simulations were performed to obtain the distribution of $\overline{D}$ in the coating phase as the particles approached each other during sintering. It was determined that the maximum value of $\overline{D}$ decreased

from 1096 to 55 as the neck radius[106] increased from 0 17 (R+t) to 0 34 (R+t), i e., as the core particle separation distance decreased. Since viscosity is inversely proportional to the deformation rate (i e., strain rate), the "effective viscosity" of the matrix phase increased as the particles approached each other The results shown in Figure 4 107 are consistent with this observation

Dryden et al [Dry89] performed a theoretical analysis for a spherical grain, embedded in a linear viscous matrix of a constant thickness, subjected to deformation stresses. The radial and tangential displacement rates increase from zero, at the surface of the grain (assuming that no decohesion occurs), to maximum values at the outer surface of the viscous coating and they are functions (expressed as Legendre polynomials) of the distance from the solid surface The maximum values reduced as the coating thickness reduced. Since viscosity is inversely proportional to the displacement rate (which is directly proportional to the strain rate) the 'effective viscosity' of the coating phase increased as the coating thickness reduced As explained earlier, the core particles approach each other as the composite powder compact undergoes densification Since the core particle separation distance reduces, the "effective" coating thickness reduces and the viscosity increases as observed in Figure 4 107

These studies provide convincing evidence that for composite materials, the displacement rate of the matrix phase in the gap between adjacent inclusions plays an important role in determining the overall flow (or densification) behavior of the bulk material The mean separation distance between the Si_3N_4 particles in the composite

[106] The neck radius is defined as the contact radius between the coated particles. During densification, the neck grows by the viscous flow of the coating under the influence of surface tension.

powder compacts used in this study was calculated as follows The bulk volumetric shrinkage of the composite is given by,

$$\frac{\Delta V}{V_o} = \frac{1/\rho_o - 1/\rho}{1/\rho_o} = 1 - \frac{\rho_o}{\rho} \qquad (4.36)$$

where, ΔV = change in bulk volume
V_o = initial bulk volume (i e the green compact volume),
ρ_o = green packing density and
ρ = instantaneous sintered bulk density

The bulk volume of the green compact may be expressed as

$$V_o = N \cdot 4/3\ \pi\ (R+t_o)^3 / \rho_o \qquad (4.37)$$

where, R = radius of the core particles,
$2t_o$ = initial mean distance of separation between Si_3N_4 particles
= 2 x (initial coating thickness, t_o), and
N = total number of composite particles in the compact.

Assuming that the packing geometry is invariant during the sintering process, the instantaneous bulk volume of the compact may be expressed as

$$V = N \cdot 4/3\ \pi\ (R+t)^3 / \rho \qquad (4.38)$$

where, $2t$ = instantaneous mean distance of separation between Si_3N_4 particles
= 2 x (instantaneous "effective" coating thickness, t)

Recognizing that $\Delta V = V_o - V$, and substituting eq.s (4.37) and (4.38) in eq (4.36), we obtain

$$\frac{\Delta V}{V_o} = 1 - \frac{\rho_o}{\rho} = \frac{4/3\ \pi\ [(R+t_o)^3 - (R+t)^3]}{4/3\ \pi\ (R+t_o)^3} \qquad (4.39)$$

The instantaneous mean distance of separation was calculated from the instantaneous sintered densities using eq (4.39) Figure 4.108 shows the plots of normalized viscosity (η/η_o, where $\eta_o = 8 \times 10^5$ Pa•s, the viscosity of SiO_2) vs the

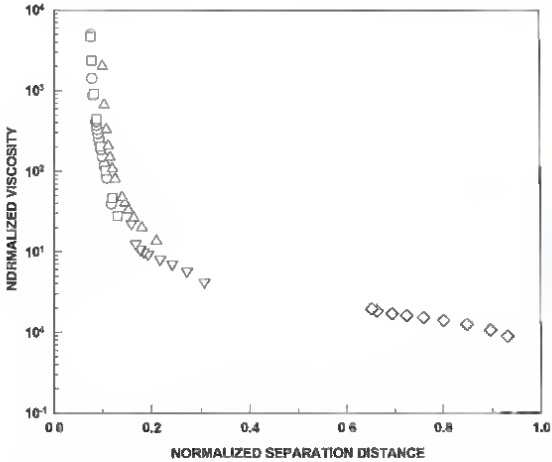

Figure 4.108 Plots of normalized viscosity vs normalized separation distance for the composite samples.

normalized separation distance (2t/R) for the composite powder compacts It is evident that the viscosity increases as the separation distance decreases The plot also shows that the data for all the compositions seem to follow the same trend, i.e., the dependence of viscosity on the separation distance is almost independent of the overall composition of the bulk compact

To better interpret the implication of this analysis, the normalized viscosity was calculated as a function of the instantaneous Si_3N_4 volume fraction in the bulk compact (determined as the product of the relative density and the nominal Si_3N_4 volume fraction in the composite powder) As indicated earlier, the Si_3N_4 particles approach each other during sintering and this would result in an increase in their volume fraction. Figure 4 109 shows the plot of the normalized viscosity vs the instantaneous Si_3N_4 volume fraction for the composite powder compacts The data was then fitted to the Dougherty-Krieger [Kri67] equation for the rheology of concentrated suspensions which is given by,

$$\eta/\eta_o = (1 - \phi/\phi_p)^{-A\phi_p} \qquad (4.40)$$

where, η/η_o is the relative viscosity,
ϕ is the volume fraction of the solids,
ϕ_p is a limiting value of ϕ – a constant, and
A is a constant.

The predicted data (shown by the solid curve in Figure 4 109) was obtained by using a curve-fitting software[107] and the values of ϕ_p and A were determined to be 0 497 and 3 984[108], respectively It is evident from Figure 4 109 that the experimental data fits the predicted values very well It is also interesting to note that ϕ_p is numerically equal to the rigidity threshold. This is not surprising since densification is arrested completely when the

[107] SigmaPlot Ver 2 0 Jandel Scientific, Rafael, CA

[108] Studies {Woo70, Pap70} conducted on polystyrene suspensions with varying solids concentration showed that A ranged from ~2.7 (for aqueous suspensions) to ~7 5 (for suspensions in non-polar solvents such as benzene and CCl_4).

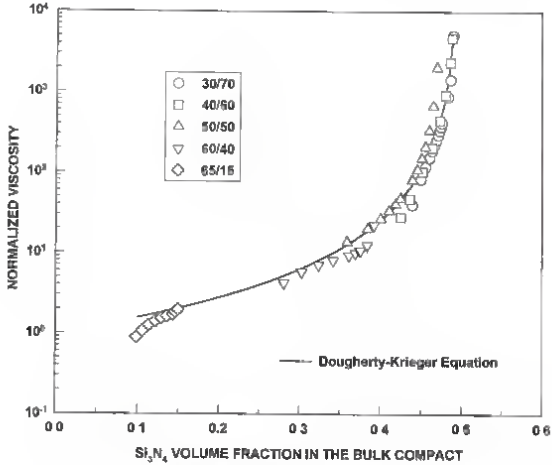

Figure 4 109 Plots of normalized viscosity vs Si_3N_4 volume fraction for the composite samples. The symbols represent the experimental data whereas the solid line depicts Dougherty-Krieger equation

volume fraction of the inclusions approaches the threshold value and this would cause the viscosity values to diverge. The most important implication of this analysis is that the densification behavior of the composite powder compacts with a given composition can be predicted if the values for the matrix viscosity, the rigidity threshold, and the constant A are known. While the first two terms could presumably be determined by conducting a single experiment (creep and densification, respectively) for each, several samples may be required to accurately estimate the value of A.

CHAPTER 5
SUMMARY

5.1 Preliminary Investigations

Microcomposite particles consisting of inner cores of Si_3N_4 and outer coatings of amorphous SiO_2 were synthesized. The steps involved in the synthesis method were (1) mixing TEOS/ethanol solutions with Si_3N_4/ethanol suspensions and (2) inducing the precipitation of the SiO_2 coating by the addition of concentrated (~30 wt%) NH_4OH solution. Composite powders containing overall SiO_2 contents in the range of 40-85 vol% were prepared by varying the TEOS/Si_3N_4 ratio in the coating suspension. TEM observations showed that composite powders with different amounts of the SiO_2 coatings could be synthesized. The absence of any crystal planes in the SiO_2 phase as determined by HRTEM, and the absence of any crystalline SiO_2 peaks in the XRD patterns demonstrated the amorphous nature of the SiO_2 coatings in the microcomposite particles. XPS measurements showed that no nitrogen was present on the microcomposite particle surface indicating that there was complete coverage of the core particle surface by the SiO_2 coating. This was also consistent with electrokinetic data which showed similar zeta potential-pH behavior for both microcomposite and SiO_2 particles. Particle size distribution results were used to qualitatively illustrate the shift to larger particle sizes that occurred due to the precipitation of the coating on the core particles. Surface area measurements showed that that the coatings were relatively dense, i.e., there was no significant amount of porosity present in the SiO_2 phase.

Powder compacts prepared with the microcomposite particles showed enhanced densification. This was demonstrated by directly comparing the sintering behavior of

compacts prepared with SiO_2-coated Si_3N_4 microcomposite particles vs. a mixture of SiO_2+Si_3N_4 particles. A composite powder compact with 60/40 volume ratio of SiO_2/Si_3N_4 reached almost full density within 2 h at 1300°C, while a mixed powder compact of similar composition had only ~73% relative density under the same sintering conditions. Furthermore, a limiting relative density of ~90% was observed for the latter compacts. Electron microscopy observations indicated that the densification was constrained in the mixed powder compacts due to the development of rigid networks of Si_3N_4 particles. In contrast, Si_3N_4 particle-particle contacts were not observed in the samples prepared from the microcomposite particles.

5.2. Processing and Properties of Bulk Composites with Low-Dielectric Constant

The feasibility of using polystyrene (PS) particles to develop isolated, closed pores in a SiO_2/Si_3N_4 matrix was demonstrated. Samples with 60/40 volume ratio of SiO_2/Si_3N_4 and ~9-10 vol% closed, isolated, spheroidal pores (~2 μm dia.) were prepared by using a mixture of microcomposite particles and PS particles. The incorporation of microporosity resulted in a lower dielectric constant (~4.4 at 1 MHz) compared to a fully dense sample (~4.9 at 1 MHz) with 60/40 SiO_2/Si_3N_4 ratio. Both samples had low loss tangent values (~2 x 10^{-4}). The average flexural strength was also the same (183 MPa) but the porous sample had lower Vicker's hardness (8.7 vs. 6.5 GPa). The mechanical and dielectric properties for these composites are similar to or better than reported values for many other glass+ceramic and glass-ceramic systems of interest for microelectronics packaging applications. It may be possible to incorporate a larger amount of closed pores into the samples (and thereby lower the dielectric constant even further) by optimization of the powder characteristics and processing conditions (e.g., the size distributions of the microcomposite particles and the PS particles, sintering conditions, etc.). It may also be

possible to obtain higher strength levels in these samples by reducing the concentration of large processing-related flaws (e g , powder agglomerates and machining flaws).

5.3. Effect of Composition on Densification and Creep Behavior

Composite powders were characterized by performing quantitative microscopy using bright field TEM images It was found that for any given powder batch, the average thickness of the coating on each composite particle was independent of the core particle size Since the core particles had a size distribution, the smaller composite particles had relatively higher concentrations of SiO_2 and larger composite particles had relatively lower concentrations of SiO_2 Shape factor measurements on samples with high amounts of SiO_2 (60-85 vol%) revealed that the microcomposite particles were more spheroidal than the corresponding core particles In other words within any microcomposite particle, the coating thickness was not uniform.

The surface properties of the composite powders were investigated The surface area varied between powder batches of samples with the same composition due to the presence of varying amounts of nano-sized porosity in the coating These pores were generally eliminated upon calcination at ~600°C However, samples with extremely thin (~12nm) coatings retained significant amounts of porosity after heating under the same conditions The zeta potentials for such samples were relatively low possibly due to the leaching of amine species through the pores, and due to the extension of the diffuse layer into the pore channels and toward the SiO_2/Si_3N_4 interface. (For example, it was shown that the shift in the diffuse layer of 6nm, toward the SiO_2/Si_3N_4 interface, could result in a ~46% reduction in the zeta potential) The zeta potentials increased as the surface porosity was reduced by calcining at progressively higher temperatures

Constant-heating-rate (CHR) experiments on bulk compacts showed that densification occurred by the viscous flow mechanism (with an activation energy of ~580

kJ/mol). The effect of composition on densification was investigated by performing isothermal sintering experiments on SiO_2 compacts, SiO_2+Si_3N_4 powder mixture compacts with ~15 vol% Si_3N_4, and SiO_2/Si_3N_4 composite powder compacts with Si_3N_4 contents in the range of 15-70 vol%. Samples with 15 and 40 vol% Si_3N_4 could be sintered to ~100% relative density after heat treatment at 1225°C for ~150 min and ~600 min, respectively. In contrast, samples with 50, 60, and 70 vol% Si_3N_4 reached maximum relative densities of ~97%, ~81% and ~72% respectively after sintering for 2h at 1500°C. The decrease in maximum density with increasing Si_3N_4 content was due to the development of rigid networks of Si_3N_4 particles at higher volume fractions. Composite powder compacts which sintered to full densities developed microstructures with minimal Si_3N_4 particle-particle contacts. Samples with higher inclusion contents (50/50 and 40/60 compacts) showed more extensive particle-particle contacts which was consistent with the lower relative densities.

During the sintering of a composite powder compact, the cores (inclusions) of the microcomposite particles will approach each other as the compact shrinks and the coating (matrix) phase is redistributed during sintering. A contiguous particulate network will form prior to complete densification if the core particle volume fraction exceeds a critical threshold value. If the core particles are "rigid" (i.e., non-sinterable), this network imposes a constraint on densification. The rigidity threshold Φ is defined as the critical volume fraction of inclusions (in the solid volume) below which the composite can be sintered to full density (i.e., no residual porosity). It was shown by a geometrical analysis that the rigidity threshold is numerically equal to the green compact density if the inclusion packing geometry does not change during sintering.

The rigidity threshold in the SiO_2/Si_3N_4 composite powder compacts used in this study was ~50 vol% which is significantly lower than the theoretical value (i.e. the green packing density) of ~60 vol%. The deviation in theory was partly due to the experimental non-uniformities resulting from the phase composition distribution in the composite

powders. This was demonstrated by preparing 50 vol% SiO_2 / 50 vol% Si_3N_4 compacts by consolidating three different powder suspensions - a 50 vol% SiO_2 /50 vol% Si_3N_4 composite powder suspension, a mixture of 40 vol% SiO_2 /60 vol% Si_3N_4 and 60 vol% SiO_2 /40 vol% Si_3N_4 composite powder suspensions, and a mixture of Si_3N_4 and 60 vol% SiO_2 /40 vol% Si_3N_4 composite powder suspensions. After sintering for 2 h at 1500°C, the limiting relative densities obtained on the three samples were ~97%, ~94%, and ~92%, respectively. Therefore, the sintered densities decreased as the "non-uniformity" of the composition of the coated particles increased. This experiment clearly demonstrated that non-uniformities in composition led to retardation in densification kinetics and the decrease in the value of the rigidity threshold.

Compression creep measurements were carried out on samples sintered to the maximum relative density. The values of the creep exponent (~1) and the activation energies (529 - 579 kJ/mol) for the 60/40 and 85/15 samples indicated that deformation was controlled by viscous flow of the SiO_2 matrix. Significant deformation was also observed in samples with Si_3N_4 contents greater than or equal to the rigidity threshold (i.e., in 30/70, 40/60 and 50/50 samples) due to the presence of thin (~5nm) lubricating layers of SiO_2 between adjacent Si_3N_4 particles.

An empirical model for densification was proposed. It was hypothesized that the there exists an "effective viscosity" of the solid material and that its value decreased as the Si_3N_4 particle approached each other during sintering. The viscosity data was extracted by fitting to the Mackenzie-Shuttleworth model for viscous sintering. The viscosity was a function of the instantaneous Si_3N_4 content in the bulk volume and the relationship followed the Dougherty-Krieger model for concentrated suspensions.

CHAPTER 6
SUGGESTIONS FOR FUTURE WORK

Suggestions for future work are given below:

(1) The process used for the coating of SiO_2 on Si_3N_4 could be investigated in detail. The solution phase and the microcomposite particles could be withdrawn at different times during the coating and analyzed to understand the coating mechanism and to establish the growth kinetics. (The solution phase may be analyzed by measuring the changes in TEOS and water contents, measuring the concentrations of Si-containing species that develop due to hydrolysis condensation, etc. The powder phase may be characterized by TEM, XPS, surface area analysis, etc.) Controlled experiments could be performed with variables such as drying conditions for the core powder, aging of the TEOS, reaction environment (e.g., ambient, dry nitrogen, and water vapor+nitrogen), etc., in order to understand the variables affecting the reproducibility of powder surface area and the development of porosity in the coatings.

(2) The origin of the processing defects (powder agglomerates) in the composite powder samples could be investigated. For the SiO_2 compacts, filtration of the powder suspension through a coarse (~10 μm) filter paper had been carried out in an attempt to eliminate agglomerates prior to slip-casting. It was shown that the flexural strength for these samples were controlled by machining flaws, and that no agglomerates were evident.

in the fracture surface. Similar filtration could be performed for the composite powder samples and the fracture behavior of the resulting samples could be evaluated.

(3) Detailed CHR studies on different composite powder compositions could be performed to further confirm that the densification occurs by a viscous flow mechanism. Load-sintering experiments could be carried out using a loading-dilatometry in order to experimentally determine the value of G_c (composite shear viscosity) and test the validity of Scherer's self-consistent (SC) model [Sch87].

(4) The apparent absence of cristobalite in high-temperature (>1400°C) sintered samples needs to be investigated. Detailed characterization techniques such as HRTEM and energy dispersive x-ray spectroscopy (EDS)/TEM could be used to study the structure and composition (e.g., the presence of any dissolved nitrogen, etc.) of SiO_2 corresponding to different sintering temperatures.

(5) The microstructure evolution in composite powder samples could be studied further. Quantitative microscopy (SEM and TEM) could be carried out on polished and etched samples in order to study the formation of local Si_3N_4 particulate networks.

(6) Jagota's finite-element model [Jag95] for the sintering of coated powder packings can be tested more accurately by using a "model" composite powder compact. This compact would consist of spherical, monosized core particles coated with a matrix phase of uniform thickness (both within each particle, and between different particles of the same powder batch). For example, spherical monosized particles of TiO_2 or ZrO_2 could be synthesized using controlled hydrolysis of alkoxides. These particles could then be used as core particles to deposit uniform coatings of SiO_2 using the synthesis method

described in this investigation. The compacts derived from these powders could be sintered isothermally and the neck growth at particle pairs could be compared with predicted values. Such a "model" system could also be used to confirm that the rigidity threshold is ideally equal to the green density. (It is noted that this would be a 'model" system only if the compact derived from the 'model" particles contains no packing heterogeneities.)

APPENDIX A
FRACTIONATION OF Si_3N_4 POWDER

The fractionation of the as-received Si_3N_4 powder[1] was based on sedimentation rates calculated from Stokes' Law. The details of the Stokes' settling calculations have been described by Bagwell [Bag92]. Two different procedures were used to collect fine particle fractions from the as received powder. The two batches of powders prepared were designated as Lot1 and Lot2, respectively. The first method involved using a combination of centrifugal and gravitational sedimentation steps whereas the second utilized only gravitational sedimentation for fractionation. The detailed procedure for the latter method has been described by Bagwell [Bag92]. The following are the step-by-step procedures for the two methods of fractionation of the as-received Si_3N_4.

Preparation of Lot1 Powder

I. Suspension Preparation

A. Preparation of 25 vol% suspension

1. Weigh out 73.78 g of deionized water into a 125 ml plastic bottle.
2. Add 1.5 ml of concentrated (~29 wt%) NH_4OH (to allow electrostatic stabilization of Si_3N_4 at high pH).
3. Add 60.75 g Si_3N_4, mix on a paint shaker[2] for 10 minutes.
4. Add 24.87 g Si_3N_4, mix on a paint shaker for 10 minutes.
5. Check pH. The pH value should be in the range 9.8 – 10.0.

[1] SN E-10, Ube Industries (America), Inc., New York, NY.
[2] Model 5400, Red Devil Co., Brooklyn Park, MN.

6 Sonicate 90 minutes with cooling breaks of 5 minutes after each 30 minutes of sonication[1]

7 Check pH Adjust pH to 9 6 using < 0 10 ml of concentrated NH_4OH (This is done since the pH typically reduces slightly with time as the suspension ages)

B Dilution to a 0 75 vol% suspension

1 Weigh 3561 g of deionized water into a 4 l plastic bottle

2. Add 1 0 ml of concentrated NH_4OH to adjust pH to 9.6

3. Add the 25 vol% sonicated suspension from Part A while mixing the suspension with a magnetic stirrer

4 Close container tightly and age the suspension 4 hr on a roller mill

5 Check pH and if needed, adjust to 9 6 with concentrated NH_4OH

6 Age the suspension for an additional 45 min before fractionation.

II Centrifugal fractionation of as-received suspension

A First fractionation of as-received suspension

1 Let suspension stand for 15 minutes prior to fractionation This is done to settle out the coarsest fraction of powder

2 Pass suspension through a centrifuge[2] at 4650 rpm, by using a pump[3] with a flow rate setting of 2 0 cm^3/s. (The smaller particles flow over to the top of the rotor through an exit tube and into a container The larger particles collect at the bottom of the rotor). Pass the overflow material through the centrifuge again Between the first and second passes, allow the overflow suspension to return into the first pass container for 1 minute before directing the suspension into the second pass container

[1] The ultrasonication in the current appendix was carried out using a titanium-horn sonicator (Model W-375 Heat Systems-Ultrasonics, Inc Farmingdale NY) using a power setting of 9

[2] IEC Centrifuge, International Equipment Co., Needham Heights, MA

[3] Peristaltic Pump, Cole-Parmer Instrument Co. Vernon Hills, IL

3 Carry out particle size analysis on the final overflow material This is done to ensure that less than 7% of the particles are greater than 0 49 μm in diameter

4 Collect the residual material in the rotor into a pre-weighed 500 ml bottle

B Fractionation of re-dispersed rotor material

1 Mix the collected residue for 15 minutes on a paint shaker

2 Sonicate 1 hour with 5 minute cooling breaks every 15 minutes.

3 Add 2500 g of deionized water into a 4 l plastic bottle and adjust pH to 9 6 Add a 3" magnetic stirrer and start stirring Dilute the sonicated residue by adding it to the deionized water

4 Age 1 hour on a roller mill

5 Fractionate again using the steps in II A above

6 Carry out particle size analysis on the overflow suspension

III. Gravitational sedimentation of rotor residue

1 Mix the rotor residue collected after step II B for 15 minutes on a paint shaker

2 Sonicate 2 hours with 5 minute cooling breaks every 15 minutes

3 Dilute to 0 75 vol% by measuring the solids loading and adding an appropriate amount of deionized water Adjust the pH to 9 6 using concentrated NH_4OH

4 Age 1 hour on a roller mill

5 Pour suspension carefully into a 4l plastic settling column. (The settling height, i e , the difference between the initial height of the suspension and the height at which the suspension is withdrawn from the column, was 37 7cm) Remove air bubbles using a long glass rod Cover column with parafilm and aluminum foil

6 Allow suspension to settle undisturbed for 10 days Remove suspension down to 500 cm^3 mark using a peristaltic pump Suspension should be removed at the top level of the column only at a low flow rate (~2 cm^3/s)

7 Perform particle size analysis on this suspension to ensure that less than 7% of the particles are greater than 0 49 μm in diameter

IV Filtration and Mixing

1. Filter all the fractionated suspensions (i.e , from steps II A II B and III) through a pressure filtration apparatus[8] (under 50-60 psi nitrogen pressure) with 0.22 μm cellulose filter paper

2. Dry the filtered powders in a convection oven at 80°C for 24 hours.

3 Mix the dry powders by grinding with an alumina pestle and mortar Transfer the final powder into a plastic bottle and store in a vacuum desiccator

Preparation of Lot2 Powder [Bag92]

I Suspension Preparation

The suspension preparation procedure was identical to that described for the preparation of Lot1 powder

II Sedimentation and Fractionation

1 Pour the suspension carefully into a clean 4 l settling column. (The settling height, i.e., the difference between the initial height of the suspension and the height at which the suspension is withdrawn from the column, was 37 7cm)

2 Remove air bubbles from column using a long glass rod

3 Cover the column with plastic film and aluminum foil.

4 Allow suspension to remain undisturbed for 10 days + then remove suspension down to 2000 cm^3 mark using a peristaltic pump Suspension should be removed at the top level of the column only at a low flow rate (~2 cm^3/sec)

5 Wait 2-3 more days and remove 500 cm^3 more of suspension - repeat until 500cm^3 of suspension is left in column.

[8] Millipore Corp– Bedford, MA

6. Carry out particle size distribution measurement on samples from each portion of suspension removed.

7 Filter suspensions which contain particles with diameters <1μm using a pressure filtration apparatus with 0.22 μm cellulose filter paper

8 Collect the remaining 500 cm^3 of suspension in the column for re-dispersion Repeat the entire settling for this powder in order to increase the yield of submicrometer particles fractionated from the as-received material

III Mixing and Drying

1 Dry the filtered powders in a convection oven at 90°C for 24 hours.

2 Mix the dry powders by grinding with an alumina pestle and mortar Transfer the final powder into a plastic bottle and store in a vacuum dessicator

APPENDIX B
COATING OF Si_3N_4 POWDER WITH SiO_2

B.1. Dispersion of Si_3N_4 Powder

Preliminary investigations [G.W. Scheiffele, personal communication, 1989] showed that a styrene maleic anhydride copolymer[1] could be used as a dispersant for Si_3N_4 in ethanol medium. This copolymer was used to disperse Si_3N_4 in ethanol prior to the preparation of Series I and Series II composite powders. However, initial experiments for the preparation of Series III composite powders revealed that the copolymer-stabilized Si_3N_4 suspensions flocculated (indicated by the formation of a sediment) upon standing for ~5 min. The reasons for this behavior is not clearly understood yet. In an attempt to improve the stability of these suspensions, small quantities (~20 µl in 100ml) of a ~2 vol% suspension) of 3N NH_4OH solutions were added. It was found that the stability of the suspensions improved significantly. This was evident from the fact that no sediment formed even after standing for ~1 h.

The improvement in stability was quantified by performing particle size measurements using an X-ray sedimentation apparatus[2]. 100ml each of three separate ~2 vol% suspensions were prepared for the analysis. In the first case, the dispersion medium was deionized water and the suspension pH was adjusted to ~9.6 using 3N NH_4OH solutions. In the second suspension was prepared in ethanol containing ~1 wt% (of the powder volume) of the dispersant. The third suspension was similar to the second except that ~20µl of ~3N NH_4OH was also included in the suspension. The suspensions were

[1] SMA 1440A, Arco Chemical Co., Hinsdale, IL.
[2] Model 5100, Micromeritics Corp., Norcross, GA.

separately mixed by shaking for ~5 min each and ultrasonicated for ~2 h. Figure B.1 shows the plots of cumulative mass percent vs Stokes diameter for the particles in the three suspensions. (For particle size measurements in ethanol, the density and viscosity of ethanol were assumed to be 0.81 g/ml and 1.10 mPa•s, respectively. The conditions used for the measurements in water were the same as those shown in Table 3.3.) The aqueous suspension was expected to be well-dispersed due to electrostatic stabilization (see Section 4.1.2). The size distribution from the ethanol suspension with NH_4OH was identical to that obtained for the aqueous suspension. In contrast, the ethanol suspension prepared without any NH_4OH was flocculated, i.e., the distribution plot was shifted to higher particle sizes. Based on this experiment NH_4OH was used in the suspensions prepared for the synthesis of Ill composite powders.

B.2 Coating Procedure

1. Filtration of Ethanol

   1. Rinse a 4l glass column with ethanol[3] from a freshly opened container (< 10 days after breaking the seal). Fill the column with ~4l of ethanol.

   2. Place a coarse filtration paper[4] over a plastic colander funnel and wet the paper with ~50 ml of ethanol.

   3. Filter the 4l of ethanol through the funnel into a 4l plastic bottle. Perform steps 1-3 twice to collect ~8l of filtered ethanol. The ethanol referred to in all the following steps is the filtered ethanol.

[3] Denatured, Fisher Scientific, Fair Lawn, NJ
[4] No. 541 Ashless, Whatman, UK

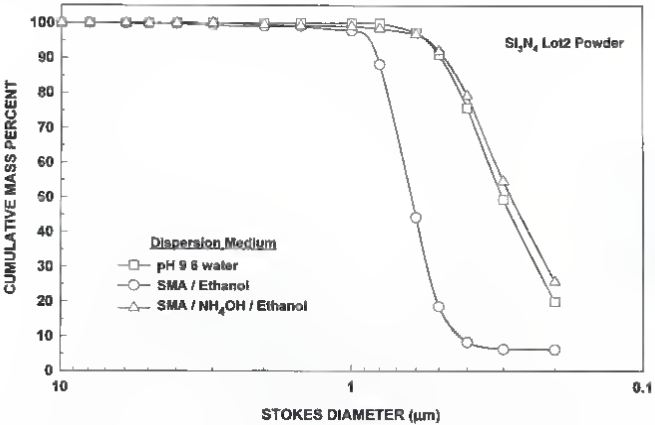

Figure B 1. Plots of cumulative mass percent vs. Stokes diameter for Lot2 Si_3N_4 powder in different media.

II Preparation of Si_3N_4 Suspension

1 Rinse a 250 ml plastic bottle with ethanol and weigh out 162 g (200 ml assuming a density of 0 81 g/ml) of ethanol into it.

2. Add a 1" magnetic stirrer and start stirring

3 Weigh out A g (see Table B-1) of SMA 1440A[3] and add it to the ethanol while stirring

4 Weigh out B g (see Table B-1) of fractionated Si_3N_4 powder and add it gradually to the solution. (Lot1 powder was used for Series I composite powders while Lot2 powder was utilized for Series II and Series III powders)

5 Add 10 µl of a 3N NH_4OH solution to the suspension (for Series III powders only)

6 Remove the stirrer and mix 15 minutes on a paint shaker[4]

7 Sonicate for 2 hours and shake suspension after each 30 min of sonication

III. Preparation of TEOS Solution

1 Rinse a 6 l Erlenmeyer flask with ethanol and add C ml (see Table B-1) of ethanol into it. Add a 3" magnetic stirrer and start stirring

2. Rinse a 1l Erlenmeyer flask with ethanol Measure out 400 ml ethanol in a 500 ml graduated cylinder and transfer it into the flask. Add a 1" magnetic stirrer and start stirring

3 Weigh out D g (see Table B-1) of TEOS and add it to the 1 l flask while stirring. (A commercial grade TEOS[5] was used for the preparation of Series I and Series II powders For the synthesis of Series II powders, high-purity TEOS[6] from a freshly opened bottle was utilized)

4 Wait for 5 min to ensure that the TEOS is mixed thoroughly

---

[3] Arco Chemical Co., Hinsdale, IL
[4] Model 5400 Red Devil Equipment Co., Brooklyn Park, MN
[5] Reagent Grade Fisher Scientific, Fair Lawn, NJ
[6] 99 9999% Alfa Chemical Co., Ward Hill, MA

IV Coating Procedure

1 Add the sonicated Si_3N_4 / ethanol suspension to the 6l flask while stirring at maximum speed

2 Add the TEOS / ethanol solution to the 6 l flask.

3 Measure out E ml (see Table B-1) of concentrated (~29 wt%) NH_4OH from a freshly opened bottle into a 1 l graduated cylinder

4 Add the NH_4OH rapidly (within ~5 s) into the 6l flask.

5. Cover the 6l flask with Parafilm and keep the mixture stirred at maximum speed for 1 hour

V Filtration and Washing

1 Filter the suspension through a filter paper[9] using a teflon coated pressure filtration apparatus[10]. The filtration is carried out at ~50 - 60 psi pressure

2 Keep the suspension in the 6 l flask stirring until all of it is transferred into the filtration chamber. Collect all of the ethanol/NH_4OH/TEOS waste in one container

3 Measure out 8 l of deionized water. Wash the filtered powder by running the deionized water through the filtration chamber

4 Collect the washed powder in a 250 ml plastic bottle and disperse in 200 ml of deionized water

VI Redispersion and Washing

1 Sonicate suspension for 1 hour with a 5 minute cooling break after 30 minutes

2 Pour 3700 ml of deionized water into a 4 l plastic bottle. Add the sonicated suspension into this bottle

[9] 0.22μm nylon, Fisher Scientific, Fair Lawn, NJ
[10] ~6" dia., Mill pore Corp. Bedford, MA

3. Age 8 hours on a roller mill

4 Filter the aged suspension using a pressure filtration apparatus with filter paper[11]

5 Dry the filtered powders in a convection oven at 80°C for 24 hours.

6 Grind the dry powders with an alumina pestle and mortar Transfer the ground powder into a plastic bottle and store in a vacuum desiccator

VI Table of Amounts of Constituents

Table B-1 Amounts of Constituents Used for the Coating Process

Constituent	30/70	40/60	50/50	60/40	85/15
A (g)	0.1949	0.1721	0.1495	0.1239	0.0309
B (g)	19.49	17.21	14.95	12.39	3.09
C (ml)	1525	2305	3202	4106	3853
D (g)	19.76	25.76	35.36	43.74	41.42
E (ml)	425	554	760	940	891
Total Coated Powder (g)	25	25	25	20	15

[11] 0.22μm cellulose ester-free, Fisher Scientific, Fair Lawn, NJ

APPENDIX C
SYNTHESIS OF POLYSTYRENE (PS) PARTICLES

I Solution Preparation

1 Prepare a mixture of 180g styrene monomer[1] and 513ml of a 10% NaOH[2] solution in deionized water in a 1l Erlenmeyer flask (covered loosely with parafilm to prevent contamination) Add a 2" magnetic stirrer and stir for 30 minutes. This dissolves the polymerization inhibitor present in the styrene

2. Separate the styrene from the aqueous solution using a separating funnel Filter this styrene through activated Al_2O_3[3]

3 Transfer 25g of the treated styrene into a 16 oz. glass bottle previously filled with 192ml of ethanol (200 proof)[4], 0.25g of AIBN[5], 3 5g of PVP-K30[6] and 1.0g of AOT-100[7]

4 Purge the solution with nitrogen. Seal the bottle tightly with a rubber cap and parafilm

5 Repeat steps 1-4 to prepare several batches

II. Polymerization

1 Place the bottles in a shaker bath[8] maintained at a constant temperature of 70°C and a shaker speed setting of 4.

2 After 24 hours, remove the bottles from the shaker bath and cool to room temperature

3 Add 0 25g of hydroquinone[9] to each bottle to inhibit further polymerization

[1] Fisher Scientific, Fair Lawn, NJ
[2] Fisher Scientific Fair Lawn NJ
[3] Alfa Aesar Johnson Matthey Ward Hill, MA
[4] Florida Distillers Co Lake Alfred, FL
[5] Fluka Chemie AG, CH-9470 Bucks, Switzerland
[6] ISP Technologies, Wayne, NJ
[7] American Cyanamid Co Wayne, NJ
[8] Model 129 Fisher Scientific Fair Lawn, NJ
[9] Fisher Scientific Fair Lawn, NJ

4 Place the flask in a refrigerator at 4°C and allow suspension to settle undisturbed for 30 days.

5 Withdraw most of the solvent using a peristaltic pump[10] with a flow rate setting of 2.0 mm^3/s and replace with ~400ml of ethanol (200 proof)

6. Shake the bottles vigorously to mix the contents and transfer the suspensions into centrifuge cells.

III Preparation of Aqueous Suspension

1 Centrifuge the suspension at 5000 rpm for 20 minutes using an industrial grade centrifuge Remove the supernatant carefully using a pipette and replace with an equal volume of deionized water

2. Sonicate the suspension for 5 minutes.

3 Repeat Steps 1-2 three more times so that all the unreacted styrene is removed and the ethanol is completely replaced with deionized water

4 Adjust the pH of the final suspension to ~9 and sonicate the suspension for 1 hour Concentrate the suspension to the desired level by evaporating excess solvent from a vigorously stirring suspension placed on a tabletop heater at ~70°C

[9] Model 7520-25 Cole-Parmer Instrument Co. Chicago, IL
[11] Model J2-21 Beckman Instruments, Inc. Schaumburg, IL

APPENDIX D
PHYSICAL PROPERTY MEASUREMENTS

I Flexural Strength

Figures D-1(a) - D-1(d) and D-2(a) - D-2(g) show the plots of load vs. load-span displacement for fully dense (i.e. almost zero porosity) and porous 60/40 SiO_2/Si_3N_4 samples, respectively. Figures D-3(a) - D3(h) show similar plots for SiO_2 samples. Table D-I shows the density data for the porous samples as determined by the Archimedes displacement method using deionized water as the medium. Tables D-II through D-IV list the fracture loads, specimen dimensions and flexure strengths of the SiO_2 samples and the fully dense and porous 60/40 SiO_2/Si_3N_4 specimens, respectively.

II Hardness and Fracture Toughness Measurements.

The tensile surfaces of the following bend tested samples were used for indentation measurements: (a) dense SiO_2- #3 (Table D-II), (b) dense SiO_2/Si_3N_4- #8 (Table D-III), and (c) porous SiO_2/Si_3N_4- #D (Table D-IV). The Vicker's hardness values for the samples were measured to be 6.9±0.3 GPa, 8.7±0.2 GPa, and 6.5±0.1 GPa, respectively (from 20-25 indents). Based on Knoop indentation experiments (15 indents), the average b'/a' (see schematic in Figure 3.12) for the dense SiO_2/Si_3N_4 sample was determined to be 0.125±0.006. Using this value in eq. (3.47), the E/H value was calculated to be 29.2 which resulted in an elastic modulus of 254 GPa. The physical properties of two-phase composites can be predicted from the properties of the individual phases using various theoretical models [Hal76]. One of the most widely used models to calculate elastic moduli of composites was developed by Hashin and Shtrikman [Has63].

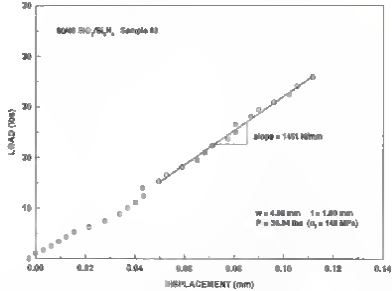

Figure D-1 (a) Plot of load vs. displacement for 60/40 SiO_2/Si_3N_4 sample #3

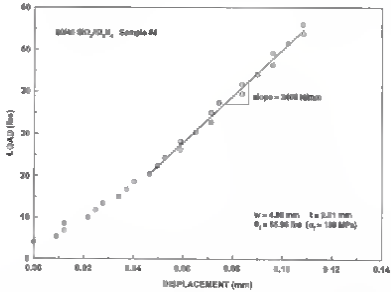

Figure D-1 (b) Plot of load vs. displacement for 60/40 SiO_2/Si_3N_4 sample #4

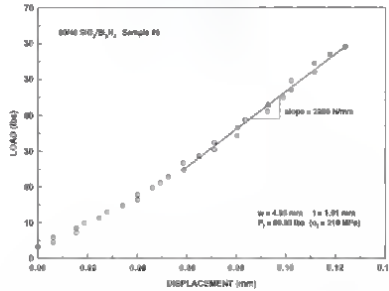

Figure D 1 (c) Plot of load vs displacement for 60/40 SiO_2/Si_3N_4 sample #5

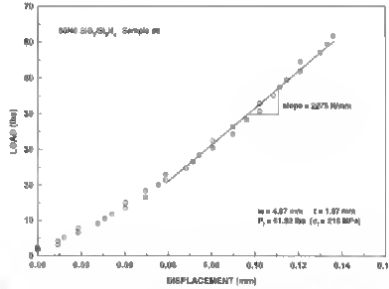

Figure D-1 (d) Plot of load vs. displacement for 60/40 SiO_2/Si_3N_4 sample #6

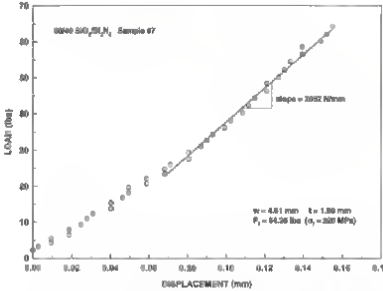

Figure D-1 (e). Plot of load vs displacement for 60/40 SiO_2/Si_3N_4 sample #7

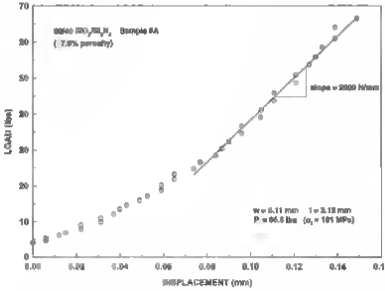

Figure D-2 (a) Plot of load vs. displacement for porous 60/40 SiO_2/Si_3N_4 sample #A.

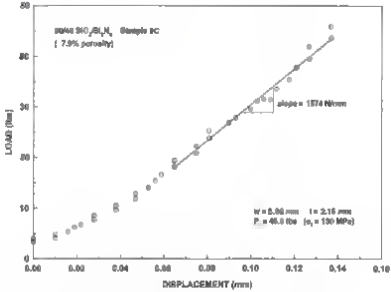

Figure D-2 (b) Plot of load vs displacement for porous 60/40 SiO_2/Si_3N_4 sample #C

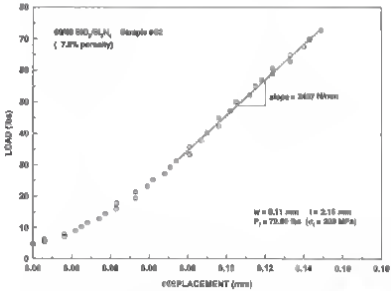

Figure D-2 (c) Plot of load vs displacement for porous 60/40 SiO_2/Si_3N_4 sample #C2.

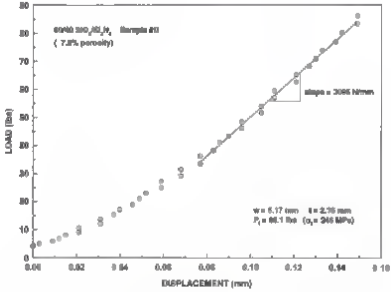

Figure D-2 (d) Plot of load vs. displacement for porous 60/40 SiO_2/Si_3N_4 sample #D

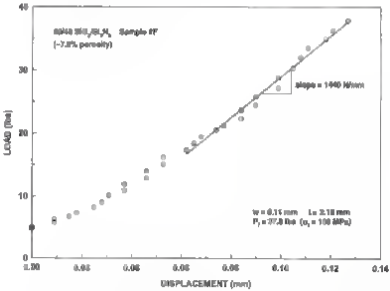

Figure D-2 (e) Plot of load vs. displacement for porous 60/40 SiO_2/Si_3N_4 sample #F

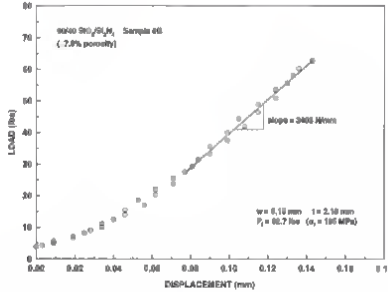

Figure D-2 (f) Plot of load vs displacement for porous 60/40 SrO_2/Si_3N_4 sample #G

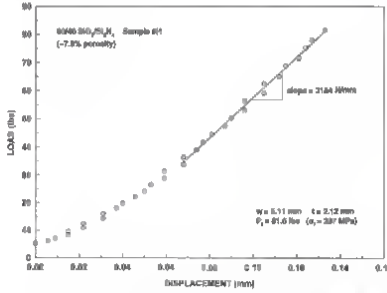

Figure D-2 (g) Plot of load vs displacement for porous 60/40 SrO_2/Si_3N_4 sample #H

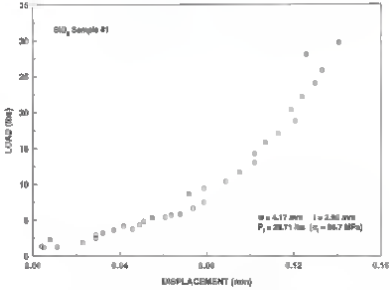

Figure D-3 (a) Plot of load vs. displacement for SrO_2 sample #1

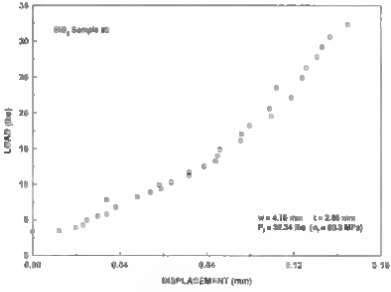

Figure D-3 (b) Plot of load vs. displacement for SrO_2 sample #2

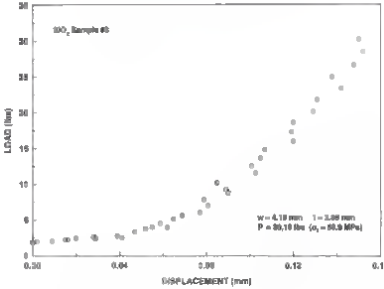

Figure D-3 (c) Plot of load vs displacement for SiO_2 sample #3

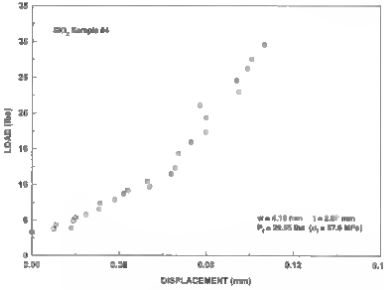

Figure D-3 (d) Plot of load vs. displacement for SiO_2 sample #4

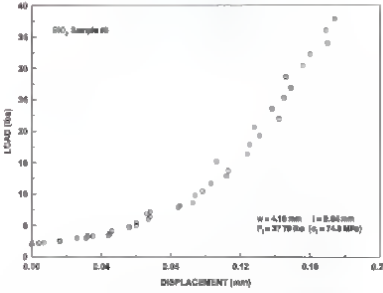

Figure D-3 (e) Plot of load vs. displacement for SiO_2 sample #5

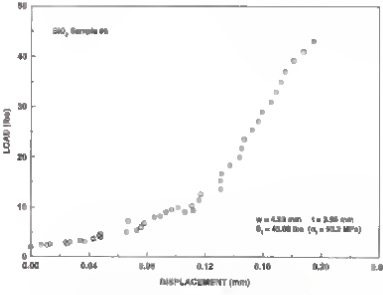

Figure D-3 (f) Plot of load vs displacement for SiO_2 sample #6

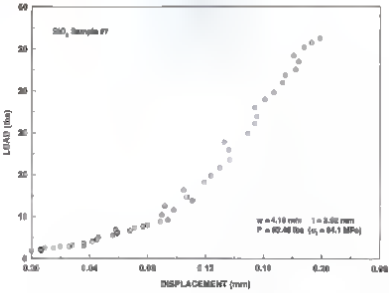

Figure D-3 (g). Plot of load vs displacement for SiO_2 sample #5

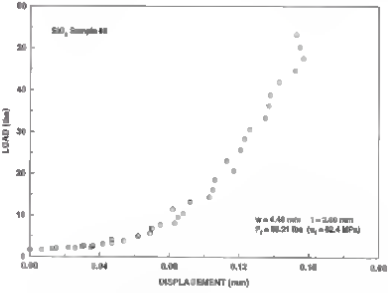

Figure D-3 (h) Plot of load vs displacement for SiO_2 sample #6

Table D-I. Archimedes density results for 60/40 SiO_2/Si_3N_4 samples containing controlled voids created by pyrolysis of PS

Sample No	Bulk Density (g/cm^3)	Open Porosity (%)	Apparent Density (g/cm^3)	Closed Porosity (%)
A	2.38	0.4	2.39	8 1
C	2 38	0.3	2 38	8.5
C2	2.39	0 2	2.39	8 0
D	2 40	0 3	2 41	7 4
F	2.38	0 4	2 39	8 1
G	2 40	0 3	2.40	7 6
H	2 39	0 5	2 40	7 8
I	2.40	0 2	2 41	7 5
Average	*2.39*	*0.4*	*2 40*	*7 9 ± 0.3*

Table D-II. Four-point bend test results for dense SiO_2 samples

Sample No	P_f (lbs)	w (mm)	t (mm)	σ_f (MPa)
1	29 71	4 17	2.9	56 7
2	32.34	4 18	2 86	63.3
3	30 16	4 19	2.86	58 9
4	29 55	4 15	2 87	57 8
5	37 79	4 16	2 85	74 8
6	43 08	4.23	3 58	53.2
7	52.48	4 18	3 62	64 1
8	53.21	4 40	3 60	62 4
			Average	*61 ± 7*

Table D-III. Four-point bend test results for fully dense 60/40 SiO_2/Si_3N_4 samples

Sample No	P_f (lbs)	w (mm)	t (mm)	σ_f (MPa)
1	33.20	4.85	1.82	138
2	41.11	4.88	1.85	164
3	35.84	4.89	1.83	146
4	55.96	4.88	2.01	189
5	59.03	4.95	1.91	218
6	61.52	4.87	1.97	216
7	64.26	4.91	1.99	220
8	58.79	4.73	1.94	220
9	41.02	4.91	1.98	142
10	50.49	4.85	2.00	174
			Average	*183 ± 33*

Table D-IV. Four-point bend test results for 60/40 SiO_2/Si_3N_4 samples containing controlled voids created by pyrolysis of PS

Sample No	P_f (lbs)	w (mm)	t (mm)	σ_f (MPa)
A	66.5	5.11	2.13	191
C	46.0	5.09	2.15	130
C2	72.6	5.11	2.10	203
D	86.1	5.17	2.13	245
F	37.8	5.11	2.13	109
G	62.7	5.12	2.10	185
H	81.6	5.11	2.12	237
I	58.3	5.07	2.17	163
			Average	*183 ± 45*

This model determines upper and lower bounds (H-S bounds) of the modulus without making any special assumptions regarding the phase geometry In order to calculate the theoretical elastic modulus for the SiO_2/Si_3N_4 composites, the moduli of the individual components are necessary The elastic moduli of dense slip-cast fused silica (with a bulk density of ~2 20 g/cm^3) and dense monolithic Si_3N_4 have been determined (using nitrasonic techniques) to be ~70 GPa [Sha88a, Lyo94] and ~310 GPa [Fis92, Pez84], respectively Using these values, the H-S bounds for a 60/40 SiO_2/Si_3N_4 samples were calculated to be 120 GPa and 142 GPa, respectively These values are significantly lower than that (254 GPa) determined by Knoop indentation measurements Although the H-S bounds are merely estimates, they were calculated using elastic moduli of the individual components that were determined by direct measurements. In contrast, Knoop indentation method is an indirect measuring technique [Mar82] and hence it is relatively less accurate. Therefore the H-S bounds of the elastic modulus were used for fracture toughness calculations

Tables D-V and D-VI show the fracture toughness values for SiO_2 and 60/40 SiO_2/Si_3N_4 samples determined from Vicker's indentations made using 500gf (4 905 N) load For the 60/40 SiO_2/Si_3N_4 samples, the H-S bounds were used in eq (3 46) to determine the range of fracture toughness (K_{ic}) values. It is evident from Table D-1V that K_{ic} was in the narrow range of 1 6 - 1 7 MPa • m$^{1/2}$ The fracture toughness could not be determined on the porous sample because the cracks generated during indentation were not well-defined.

[1] Pezzotti et al [Pez84] have determined the elastic modulus (E) for HIPed Si_3N_4 without any additives to be 312±5 GPa. However the incorporation of additives such as sintering aids in Si_3N_4 typically result in <5% variation in the modulus value. For example, Fisher etal [Fis92] measured E for a dense (>99%) sample prepared using ~3% MgO as the sintering aid to be ~316 5 GPa, while Yeheskel et al [Yeh84] determined that a sample with ~10% Y_2O_3 had an E value of ~318 GPa.

Table D-V. Results from fracture toughness measurements on dense SiO_2 samples. The value of elastic modulus (E) used was 70 GPa.

Indent No	c_0 (μm)	K_{Ic} (MPa•m$^{1/2}$)
1	33.9	1.3
2	37.2	1.1
3	34.8	1.2
4	36.1	1.2
5	38.3	1.1
6	39.6	1.0
7	35.9	1.2
8	41.4	0.9
9	33.7	1.3
10	33.7	1.3
Average		1.1 ± 0.1

Table D-VI. Results from fracture toughness measurements on fully dense 60/40 SiO_2/Si_3N_4 samples.

Indent No	c_0 (μm)	K_{Ic} (MPa•m$^{1/2}$)	
		E=120 GPa	E=142 GPa
1	29.5	2.0	1.8
2	29.8	1.9	1.8
3	32.9	1.7	1.5
4	32.6	1.7	1.6
5	32.8	1.7	1.6
6	32.8	1.7	1.6
7	34.1	1.6	1.5
8	33.2	1.7	1.5
9	31.3	1.8	1.7
10	32.1	1.7	1.6
11	33.1	1.7	1.5
12	33.9	1.6	1.5
13	32.7	1.7	1.6
14	32.9	1.7	1.5
15	31.8	1.8	1.6
Average		1.7 ± 0.1	1.6 ± 0.1

III. Dielectric Properties

Relative dielectric constant (ε_r) values were determined at five frequencies- 1 1 kHz, 10kHz, 100kHz, 1MHz, and 10 MHz. Loss tangents (tan δ) values were collected at 1 MHz. Table D-VII shows the detailed results from these measurements The dielectric measurments were less accurate at lower frequencies since the capacitance values were obtained with fewer significant figures

Table D-VII Relative Dielectric Constants (ε_r) and Loss Tangents ($\tan \delta$) for Selected SiO_2 and 60/40 SiO_2/Si_3N_4 Samples

Sample Description	ε_r					$\tan \delta$
	1 1 kHz	10 kHz	100 kHz	1 MHz	10 MHz	(1 MHz)
SiO_2 (~0% porosity)	3 80 ± 0 00	3 80 ± 0.00	3.810 ± 0 013	3 821 ± 0.036	3 872 ± 0 021	0 0001
SiO_2 (~9% porosity)	3 49 ± 0.06	3 49 ± 0 06	3.376 ± 0 005	3 403 ± 0 008	3 412 ± 0 012	0 0001
60/40 SiO_2/Si_3N_4 (~0% porosity)	5 05 ± 0.06	5 08 ± 0 00	4 941 ± 0 007	4 943 ± 0 013	4 965 ± 0 015	0 0002
60/40 SiO_2/Si_3N_4 (~10% porosity)	4.35 ± 0 04	4 35 ± 0 04	4 306 ± 0 003	4 426 ± 0 027	4 402 ± 0.041	0 0002
60/40 SiO_2/Si_3N_4 (~23% porosity)	3 35	3.31	3 449	3.383	3 404	0 0042
60/40 SiO_2/Si_3N_4 (~32% porosity)	3 14	3 14	3 142	3 109	3 101	0 0058

APPENDIX E
ARCHIMEDES DENSITY RESULTS

Table E-I Densification data for Series II 60/40 SiO_2/Si_3N_4 samples without the controlled pores

Temperature (°C)	Bulk Density (g/cm³)	Open Porosity (%)	Apparent Density (g/cm³)	Closed Porosity* (%)
800	1.482	42.7	2.584	0.0
	1.478	42.8	2.588	
1000	1.529	41.3	2.594	0.0
	1.524	41.1	2.597	
1050	1.557	39.6	2.579	0.7
	1.563	39.0	2.561	
1150	1.753	32.3	2.589	0.4
	1.749	32.3	2.582	
1175	1.981	23.7	2.596	0.1
	1.976	23.8	2.593	
1200	2.254	12.9	2.588	0.1
	2.257	13.0	2.593	
1250	2.565	0.1	2.568	0.9
	2.575	0.2	2.579	
1300	2.604	0.1	2.607	0.0
	2.600	0.1	2.603	

*Powder true density was assumed to be 2.61 g/cm³

Table E-II Densification data for Series II 60/40 SiO_2/Si_3N_4 samples with the controlled pores

Temperature (°C)	Bulk Density (g/cm^3)	Open Porosity (%)	Apparent Density (g/cm^3)	Closed Porosity[a] (%)
800	1.421	44.5	2.562	0.0
	1.416	44.9	2.571	
1000	1.458	43.1	2.562	0.7
	1.455	43.1	2.558	
1050	1.451	43.8	2.581	0.3
	1.464	43.2	2.577	
1150	1.614	37.3	2.574	0.6
	1.612	37.4	2.575	
1175	1.981	23.7	2.596	0.0
	1.976	23.8	2.593	
1200	1.984	23.9	2.607	0.0
	1.983	24.0	2.610	
1225	2.294	9.9	2.547	1.9
	2.289	10.0	2.543	
1250	2.395	0.1	2.398	7.6
	2.395	0.1	2.397	
1300	2.405	0.2	2.409	7.1
	2.406	0.2	2.410	
1350	2.477	0.0	2.477	4.5
	2.477	0.1	2.479	
1400	2.495	0.1	2.495	3.6
	2.498	0.2	2.493	

[a] Powder true density was assumed to be 2.61 g/cm^3

Table E-III Green Density Data for Presintered (800°C, 2h) Series III Rod Shaped Samples used for Dilatometer Experiments

SiO_2 /Si_3N_4*	Bulk Density (g/cm^3)	Open Porosity (%)	Apparent Density (g/cm^3)
30/70 A	1 729	40 4	2 900
	1 722	40 7	2.903
30/70 B	1 730	40.2	2 891
	1 720	40 7	2 898
40/60 A	1 676	39 0	2 746
	1 670	39 2	2.747
40/60 B	1 673	39 1	2 748
	1.665	39 7	2 762
50/50 A	1 611	39.3	2 654
	1 605	39 8	2.665
50/50 B	1.610	39 4	2 658
	1 605	39 9	2 672
60/40 A	1 593	38.2	2 577
	1 586	38.2	2.567
60/40 B	1 601	37.8	2.574
	1 601	37.7	2 569

* Measurements were carried out on two independent samples designated as "A" and "B" respectively

Table E-IV Green Density Data for Presintered (800°C, 2h) Series III Disk Shaped Samples used for Isothermal Sintering Experiments at 1225°C

SiO_2 /Si_3N_4*	Bulk Density (g/cm^3)	Open Porosity (%)	Apparent Density (g/cm^3)
30/70 A	1 734	40 1	2 895
	1 723	40 0	2 873
30/70 B	1 731	40.3	2 898
	1 721	40.6	2 895
40/60 A	1.654	40 4	2 776
	1 645	40 7	2 774
40/60 B	1 661	40 1	2 774
	1 656	40 1	2 767
50/50 A	1 616	39 7	2 682
	1.615	39 4	2.664
50/50 B	1 621	39 6	2.664
	1 619	39 4	2 671
60/40 A	1.574	39 0	2.578
	1 574	38 7	2 567
60/40 B	1.573	39 1	2.582
	1 575	38 7	2 568
85/15 A	1.320	43 4	2 331
	1 314	43 8	2.338

* Measurements were carried out on two independent samples designated as "A" and "B", respectively

Table E V Densification Data for Batch 3 SrO_2 Disk-Shaped Samples Sintered at 1225°C in Flowing N_2

Isothermal Time (min)	Bulk Density (g/cm^3)	Open Porosity (%)	Apparent Density (g/cm^3)
2 5	1 492	32 2	2.201
	1 482	32 3	2.190
3	1.526	30 3	2 191
	1.528	30 5	2.198
5	1 614	26.8	2.205
	1 599	26.9	2 186
10	1 941	11 3	2 188
	1 945	11.3	2 192
15	2.101	4 0	2 188
	2 095	3 6	2 173
30*	2.201	0 1	2.203
	2.181	0.3	2 188
62*	2 174	0.3	2.180
	2 188	0.0	2 188
135*	2 176	8.5	2 186
	2 182	0.2	2 187

* Translucent samples

Table E-VI Densification Data for Series II #5/15 SiO_2/Si_3N_4 Disk-Shaped Samples Sintered at 1225°C in Flowing N_2

Isothermal Time (min)	Bulk Density (g/cm^3)	Open Porosity (%)	Apparent Density (g/cm^3)
2.5	1.743	24.9	2.322
	1.746	24.9	2.325
5	1.840	21.8	2.353
	1.839	21.7	2.349
10	1.972	16.3	2.355
	1.977	15.9	2.350
15	2.131	9.4	2.352
	2.130	9.1	2.342
20	2.246	3.9	2.338
	2.247	4.0	2.341
30	2.302	1.1	2.328
	2.309	0.8	2.327
45	2.339	0.2	2.344
	2.337	0.3	2.344
60	2.340	0.3	2.347
	2.346	0.2	2.349
160	2.354	0.0	2.354
	2.354	0.0	2.354

Table E-VII Densification Data for Series III 60/40 SiO_2/Si_3N_4 Disk-Shaped Samples Sintered at 1225°C in Flowing N_2

Isothermal Time (min)	Bulk Density (g/cm^3)	Open Porosity (%)	Apparent Density (g/cm^3)
5	1.834	29.4	2.599
	1.829	29.4	2.592
10	1.985	23.8	2.603
	1.970	24.1	2.606
20	2.159	17.3	2.610
	2.150	17.5	2.604
30	2.236	14.3	2.610
	2.239	14.2	2.611
45	2.368	9.4	2.612
	2.365	9.3	2.609
60	2.427	6.9	2.606
	2.425	6.8	2.603
160	2.565	0.2	2.569
	2.570	0.0	2.571
240	2.551	0.2	2.556
	2.550	0.1	2.553
600	2.586	0.1	2.589
	2.591	0.0	2.592
1440	2.594	0.1	2.596
	2.594	0.1	2.595

Table E-VIII Densification Data for Series III 50/50 SiO_2/Si_3N_4 Disk-Shaped Samples Sintered at 1225°C in Flowing N_2

Isothermal Time (min)	Bulk Density (g/cm^3)	Open Porosity (%)	Apparent Density (g/cm^3)
5	1 789	33 3	2 683
	1 781	33 5	2 680
10	1 891	30 0	2 701
	1 886	30.3	2.704
20	1 952	27 8	2 705
	1 946	27 9	2 699
30	2 088	22 8	2.704
	2 092	22 7	2 707
45	2 206	18 7	2 713
	2.209	18 4	2 707
60	2.220	18 1	2 711
	2.219	18 1	2.710
90	2.320	14.5	2 713
	2.320	14 6	2 716
160	2 374	12 6	2.716
	2.374	12.5	2 714
240	2.426	10 6	2 713
	2 422	10 7	2 712
600	2 524	4.4	2 641
	2.529	4 1	2 638
1440	2.546	0 7	2 564
	2.541	0 9	2 565

Table E-IX. Densification Data for Series III 40/60 SiO_2/Si_3N_4 Disk-Shaped Samples Sintered at 1225°C in Flowing N_2

Isothermal Time (min)	Bulk Density (g/cm^3)	Open Porosity (%)	Apparent Density (g/cm^3)
10	1.855	33.6	2.793
	1.850	33.9	2.798
20	1.957	30.1	2.799
	1.954	30.3	2.801
30	2.074	26.0	2.804
	2.076	26.2	2.813
60	2.121	24.5	2.809
	2.108	24.9	2.807
90	2.154	23.4	2.813
	2.153	23.4	2.810
160	2.191	22.1	2.813
	2.189	22.8	2.808
240	2.229	20.7	2.811
	2.223	21.0	2.813
600	2.271	19.0	2.803
	2.270	19.1	2.806
1440	2.299	17.9	2.801
	2.291	18.0	2.796

Table E-X Densification Data for Series III 30/70 SiO_2/Si_3N_4 Disk-Shaped Samples Sintered at 1225°C in Flowing N_2

Isothermal Time (min)	Bulk Density (g/cm^3)	Open Porosity (%)	Apparent Density (g/cm^3)
10	1.827	37.3	2.914
	1.824	37.5	2.920
30	1.912	34.2	2.907
	1.915	34.3	2.914
60	1.947	33.2	2.915
	1.938	33.5	2.913
90	1.970	32.5	2.920
	1.963	32.8	2.921
240	2.032	30.4	2.918
	2.026	30.7	2.922
600	2.069	29.0	2.915
	2.069	29.1	2.914
1440	2.031	30.7	2.931
	2.015	31.2	2.930

Table E-XI Densification Data for Disk-Shaped 85vol% SrO_2 + 15vol% Si_3N_4 Particle Mixture Samples Sintered at 1225°C in Flowing N_2

Isothermal Time (min)	Bulk Density (g/cm^3)	Open Porosity (%)	Apparent Density (g/cm^3)
2.5	1.343	43.0	2.357
	1.334	43.0	2.338
5	1.416	40.0	2.359
	1.408	40.1	2.352
10	1.662	28.7	2.331
	1.656	28.8	2.326
15	1.759	25.4	2.357
	1.746	25.4	2.340
30	1.912	18.7	2.352
	1.898	18.6	2.331
62	2.088	9.1	2.298
	2.093	9.2	2.302
135	2.169	3.8	2.255
	2.171	3.8	2.257

APPENDIX F
DATA ANALYSIS FOR RHEOLOGICAL MEASUREMENTS

Suspension rheological flow characteristics (shear stress, τ, versus shear rate, $\dot{\gamma}$ behavior) were determined using a concentric cylinder viscometer[1], in the shear rate ranges of 0 - 100 s^{-1} and 0 - 1000 s^{-1}, respectively. For each measurement, the shear rate was first increased to the maximum value in 2 min (to obtain the "up-curve") and subsequently reduced to zero in 2 min (to obtain the "down-curve"). The data corresponding to the first ~10% of the shear rate range from each of the two measurements were not used for viscosity calculations. The remaining data points (i.e., corresponding to ~10 - 100 s^{-1} and ~100 - 1000 s^{-1}, for the two measurements, respectively) from both measurements were merged and fitted to smooth curves using a curve-fitting algorithm[2]. Rheological measurements were carried out for ~21 vol% PS particle suspension, ~36 vol% Series II 60/40 composite powder suspension and ~30 vol% mixed particle suspensions containing 0 and ~12 vol% PS particles (in a mixture of Series II 60/40 microcomposite particles and PS particles). Figure F-1 and F-2 show the plots of shear stress vs shear rate (corresponding to both "up" and "down" curves) in the shear rate ranges of ~10 - 100s^{-1} and ~100 - 1000s^{-1}, respectively. For both plots, the symbols represent the experimental data, while the solid line represents the fitted values. Viscosity values for these suspensions were calculated from the flow curves using eq. (3.30).

[1] Model RV 100/CV 100 viscometer, Haake Inc., Saddle Brook, NJ
[2] TableCurve 2D, Jandel Scientific, San Rafael, CA

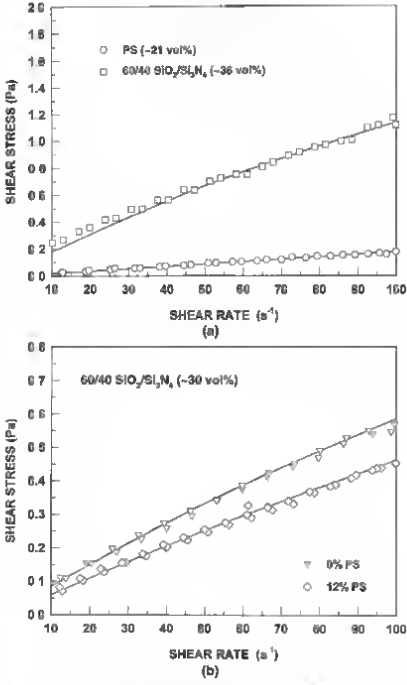

Figure F-1 Plots of shear stress vs shear rate for PS, Series II SiO_2/Si_3N_4, and mixed particle suspensions in the range of 10-100 s^{-1}. The solid lines are the curves fit to the experimental data.

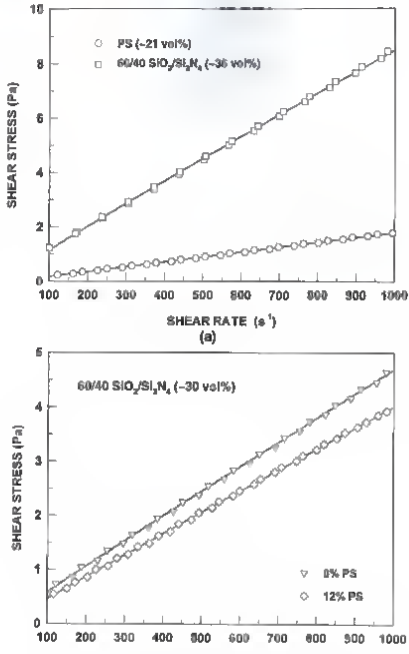

Figure F-2 Plots of shear stress vs shear rate for PS, Series II SiO_2/Si_3N_4, and mixed particle suspensions in the range of 100-1000 s^{-1} The solid lines represent the curves fit to the experimental data.

APPENDIX G
POROSIMETRY ON SiO_2/PS COMPACTS

Some preliminary experiments were carried out to demonstrate the ability to incorporate controlled, closed, spheroidal porosity in SiO_2 matrices by using the approach described in Section 2.4. Separate well-dispersed aqueous suspensions of both PS and batch1 SiO_2 powders were initially prepared. The suspensions were stabilized against flocculation by adjusting the pH to ~9 and ultrasonicating for ~2 hours to break down the agglomerates. Mixed suspensions with an overall concentration of 30 vol% were prepared by combining ~35 vol% SiO_2 suspension, ~15 vol% PS suspension and deionized water in a proportion such that the overall SiO_2/PS powder volume ratio was 95/5. This suspension was used to slip-cast disk-shaped compacts (~2.3 mm thick and ~19 mm diameter). After casting for ~48 hours, the compacts were dried at 100°C for 12 hours in a vacuum oven and subsequently stored in a vacuum desiccator. Some compacts were pre-sintered (to pyrolyze the PS particles and provide green strength) using a heating schedule identical to that shown in Figure 3.6, except that the final temperature was only ~700°C (compared to 800°C in Figure 3.6).

The dried and pre-sintered compacts were characterized by mercury porosimetry[1] to obtain pore-size and pore-volume information. The detailed measurement procedure can be found in Section 3.4. The powder densities of SiO_2 (calcined 200°C) and PS particles were assumed to be 2.10 g/cm^3 [Sac84a] and 1.05 g/cm^3, respectively. These values were used to estimate, by linear interpolation, the average powder density for the dried compact. This value was determined to be 2.05 g/cm^3 for a SiO_2/PS volume ratio

[1] Model Autoscan 60, Quantachrome Corp. Syosset, NY

of 95/5 For the pre-sintered samples, the SiO_2 powder density was assumed to be 2.18 g/cm^3

Figure G-1 shows plots of pore volume vs pore radius for both dried (100°C) and pre-sintered (800°C) samples Based on the maximum intruded volumes, the percent porosities in the two samples were calculated to be 39 6% and 39 7%, respectively (Despite the differences in the total intruded volumes, the pore volume percent for both the samples are similar This is due to the difference in the assumed true densities of 2 05 and 2.18 g/cm^3, respectively, for the two samples.) It is evident from Figure G-1 that for the pre-sintered sample, there was no mercury intrusion corresponding to a pore channel radii below ~30 nm (i.e., as the mercury pressure was increased above ~3530 psi, which corresponds to a pore channel radius of 30 nm) In contrast, mercury intrusion in the dried samples continued to occur at pressures corresponding to much lower pore channel radii. This seems to indicate that at relatively high pressures (greater than ~3530 psi), the PS particles deform (shrink) and the decrease in volume is compensated by a corresponding increase in the intruded volume In order to quantify the effect of this deformation, the intrusion data corresponding to pore channel radii less than ~30 nm was neglected. The corrected intruded volume (i e , total intruded volume corresponding to pore channel radii greater than ~30 nm) for the dried sample was determined to be ~0.301 cm^3/g (0 3006 cm^3/g at a radius of 29 5 nm, as shown in Figure G-1) which corresponds to a relative density of 61 9% Since the composition of the compact was such that 95% of the solid volume was occupied by SiO_2, the concentration of SiO_2 in the bulk volume was 0 95•61 9 = 58 8 vol% If during the pre-sintering, complete burnout of the PS particles occurred and the SiO_2 did not undergo any significant densification, the relative density of the pre-sintered compact is expected to be 58 8% or the porosity for the same compact is expected to be 41 2% Thus is slightly higher than the measured value of 39 6%. The difference may be attributed, at least in part, to the fact that the PS particles may have undergone some deformation at pressures even lower than ~3530 psi In such a

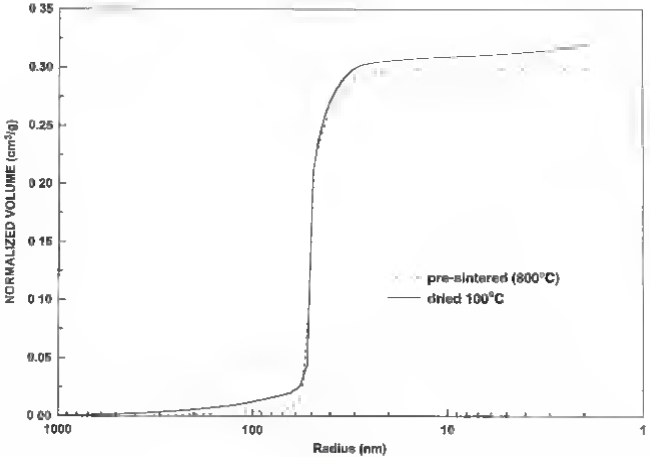

Figure G-1 Plots of pore volume versus pore radius obtained by mercury porosimetry for dried and pre-sintered (800°C) 60/40 SiO_2/Si_3N_4 samples cast with PS particles.

case, some of the intruded volume corresponding to pore channel radii greater than 30 nm would have been a result of the deformation If this intruded volume was subtracted from the total intruded volume assumed earlier, lower pore volumes (compared to 41 2%) would be estimated for the dried and pre-sintered compacts

This analysis demonstrates that reliable pore size measurements cannot be carried out on as-cast samples containing PS particles

APPENDIX H
DILATOMETRY RAW DATA

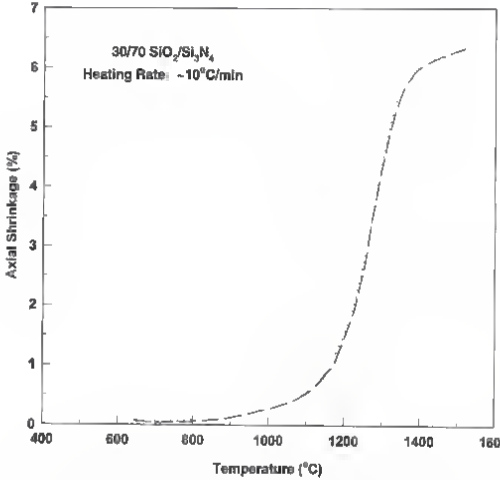

Figure H-1 Plots of corrected axial shrinkage vs temperature for two independent 30/70 SiO_2/Si_3N_4 samples heated at ~11°C/min in the dilatometer

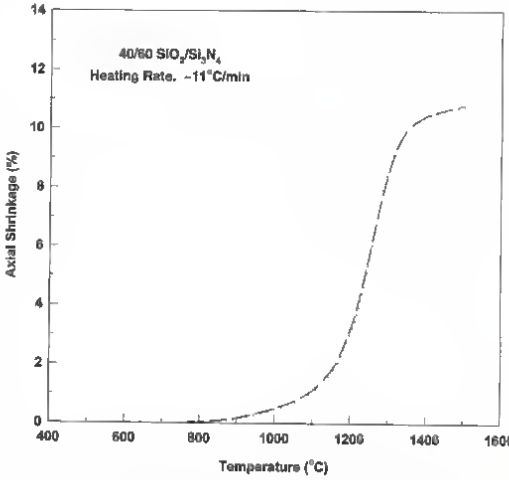

Figure H-2 Plots of corrected axial shrinkage vs temperature for two independent 40/60 SiO_2/Si_3N_4 samples heated at ~11°C/min in the dilatometer

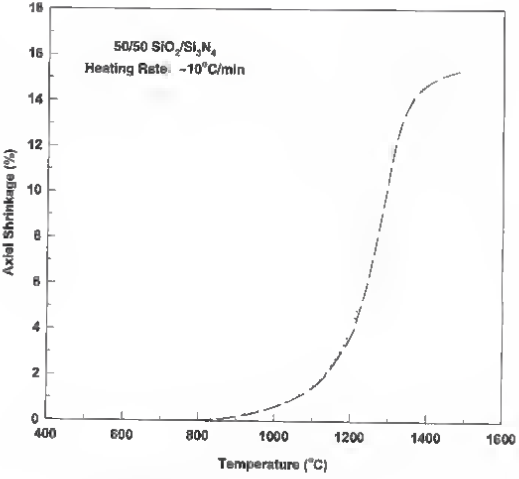

Figure H-3 Plots of corrected axial shrinkage vs temperature for two independent 50/50 SiO_2/Si_3N_4 samples heated at ~11°C/min in the dilatometer

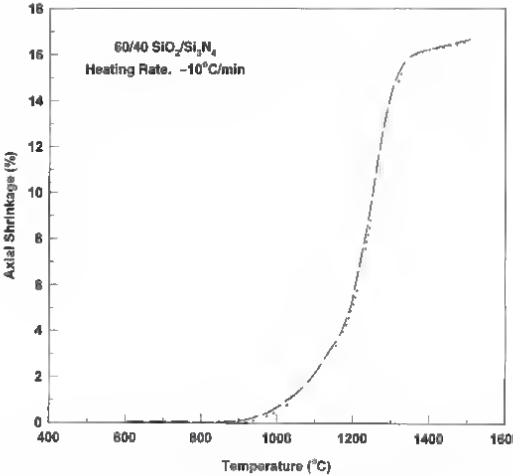

Figure H-4 Plots of corrected axial shrinkage vs temperature for two independent 60/40 SiO_2/Si_3N_4 samples heated at ~11°C/min in the dilatometer

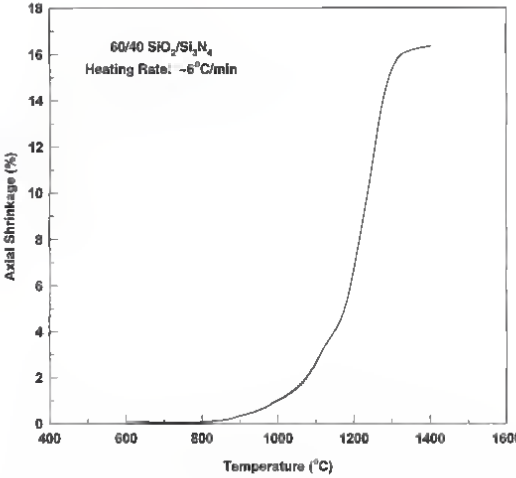

Figure H 5 Plots of corrected axial shrinkage vs. temperature for a 60/40 SiO_2/Si_3N_4 sample heated at ~6°C/min in the dilatometer

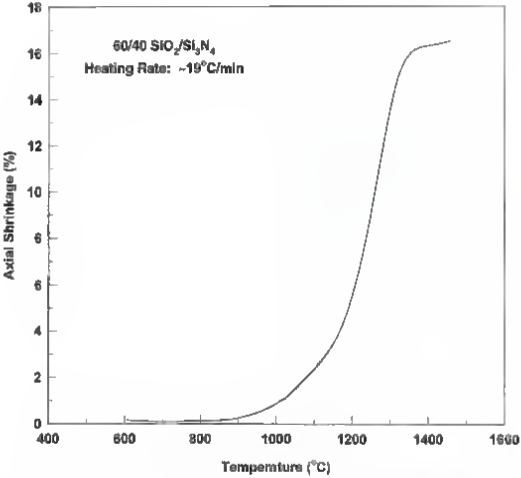

Figure H-6 Plots of corrected axial shrinkage vs. temperature for a 60/40 SiO_2/Si_3N_4 sample heated at ~19°C/min in the dilatometer

APPENDIX I
X-RAY PHOTOELECTRON SPECTROSCOPY (XPS) PLOTS

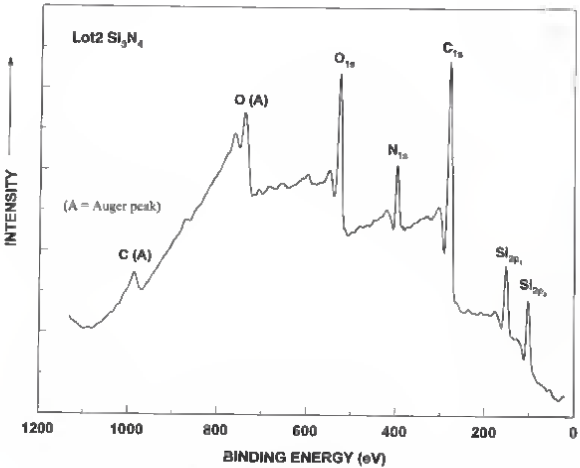

Figure I-1 XPS plot for Si_3N_4 powder showing the presence of oxygen on the surface

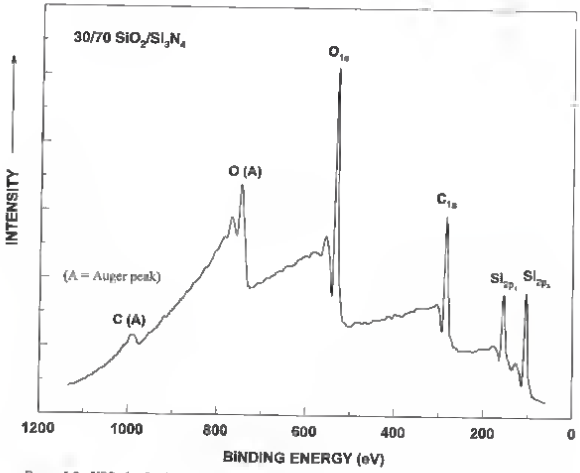

Figure I-2 XPS plot for Series III 30/70 composite powder showing the absence of any nitrogen peaks

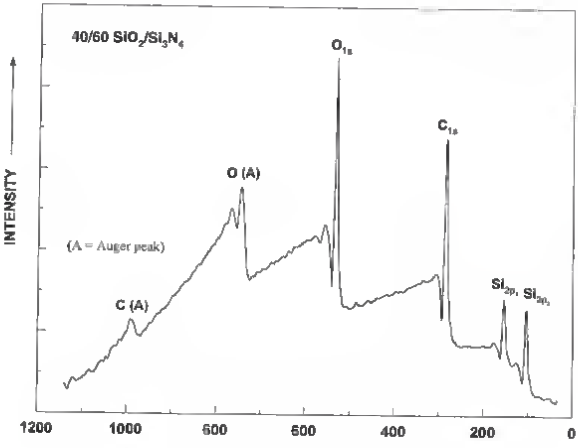

Figure I-3 XPS plot for Series III 40/60 composite powder showing the absence of any nitrogen peaks.

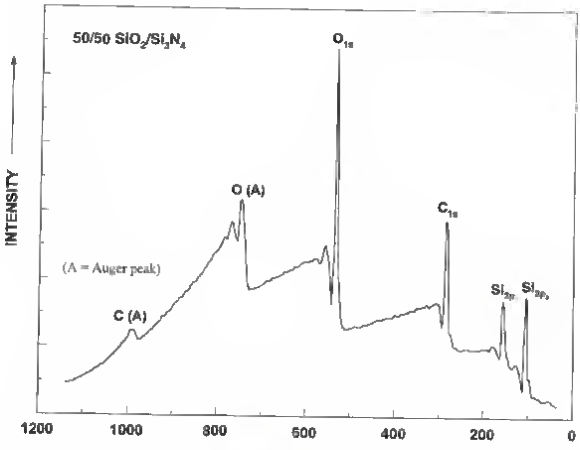

Figure 1-4 XPS plot for Series III 50/50 composite powder showing the absence of any nitrogen peaks.

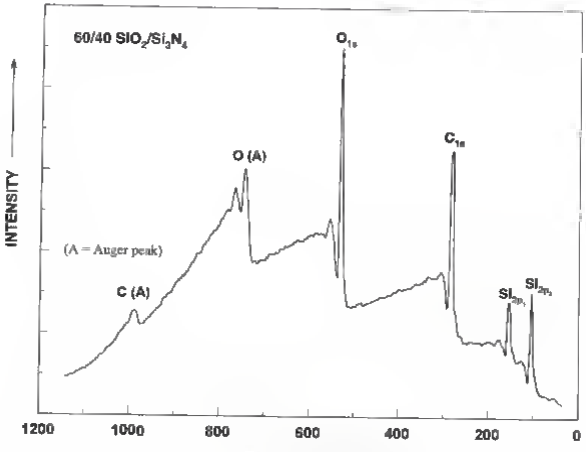

Figure I-5 XPS plot for Series III 60/40 composite powder showing the absence of any nitrogen peaks

APPENDIX J
NITROGEN GAS ADSORPTION AND DESORPTION ISOTHERMS

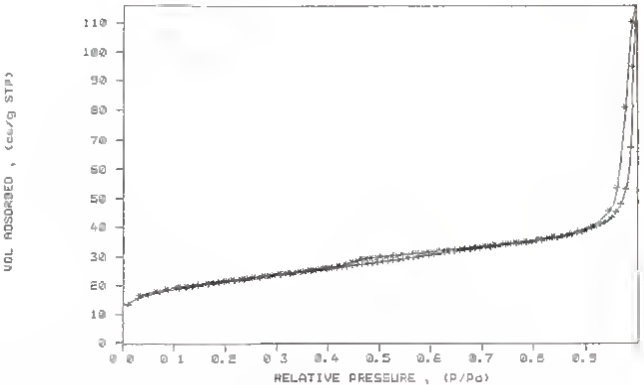

Figure J-1 Plots of adsorption and desorption isotherms for Series III 30/70B powder heated for 2h at 100°C in vacuum (degassed for ~6h at 200°C in nitrogen)

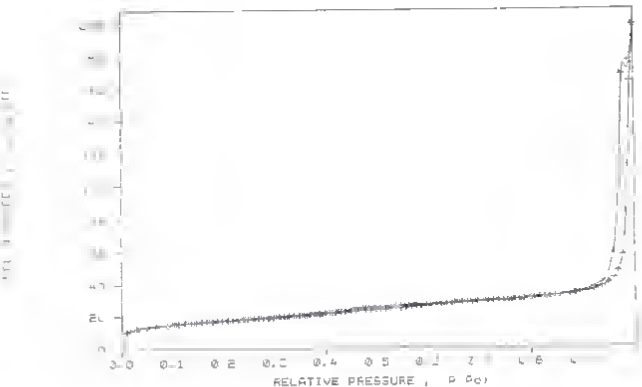

Figure J-2 Plots of adsorption and desorption isotherms for Series III 30/70B powder heated for 6h at 400°C in air (degassed for ~6h at 200°C in nitrogen)

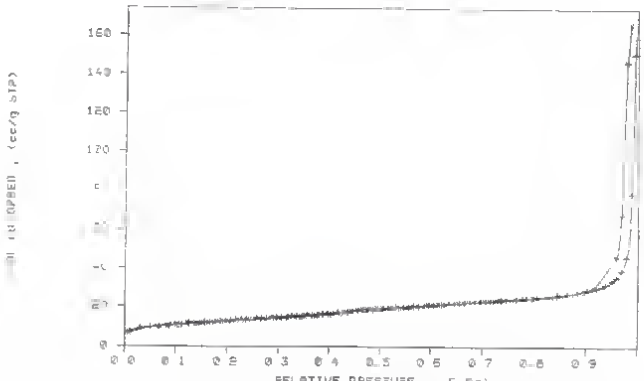

Figure 1-3 Plots of adsorption and desorption isotherms for Series III 30/70B powder heated for 6h at 600°C in air (degassed for ~6h at 200°C in nitrogen)

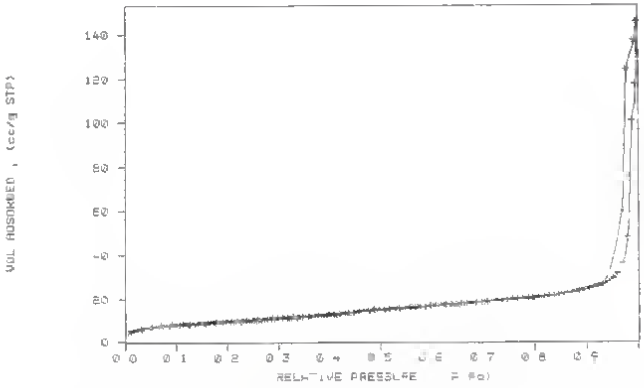

Figure J-4 Plots of adsorption and desorption isotherms for Series III 30/70B powder heated for 6h at 800°C in air (degassed for ~6h at 200°C in nitrogen)

Figure J-5 Plots of adsorption and desorption isotherms for Series III 40/60B powder heated for 2h at 100°C in vacuum (degassed for ~4h at 200°C in nitrogen)

Figure 3-6 Plots of adsorption and desorption isotherms for Series III 40/60B powder heated for 6h at 600°C in air (degassed for 6h at 200°C in nitrogen)

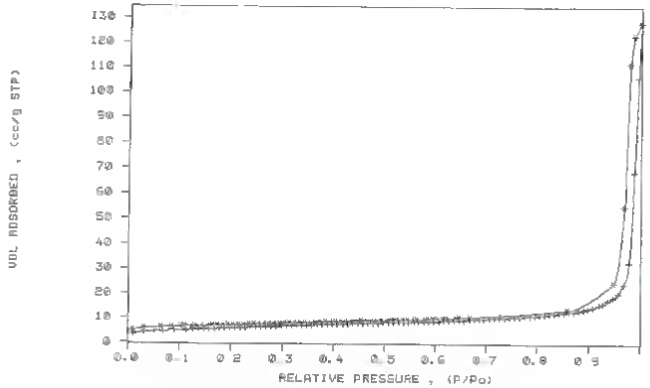

Figure 1 7 Plots of adsorption and desorption isotherms for Series III 50/50B powder heated for 6h at 400°C in air (degassed for ~6h at 200°C in nitrogen)

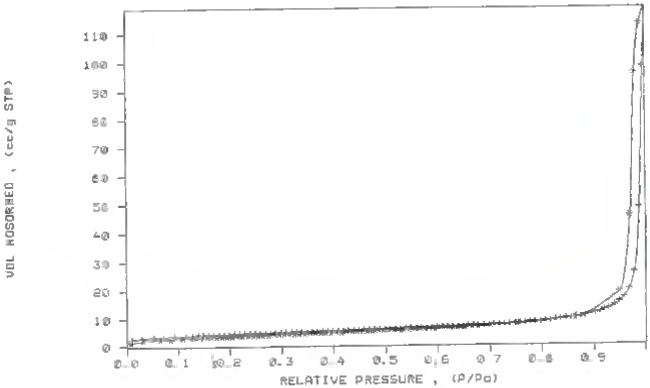

Figure J-8 Plots of adsorption and desorption isotherms for Series III 50/50B powder heated for 6h at 600°C in air (degassed for ~6h at 200°C in nitrogen)

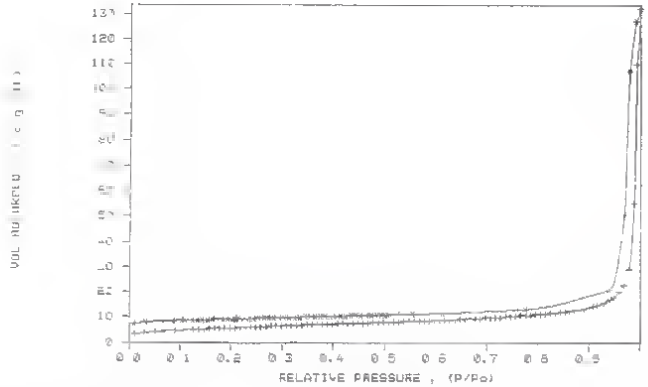

Figure J-9 Plots of adsorption and desorption isotherms for Series III 60/40B powder heated for 2h at 100°C in vacuum (degassed for ~6h at 200°C in nitrogen)

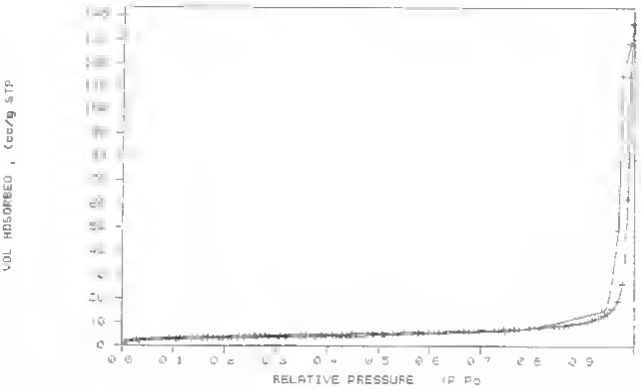

Figure J-10 Plots of adsorption and desorption isotherms for Series III 60/40B powder heated for 6h at 600°C in vacuum (degassed for ~6h at 200°C in nitrogen).

APPENDIX K
PARTICLE SIZE DISTRIBUTION PLOTS

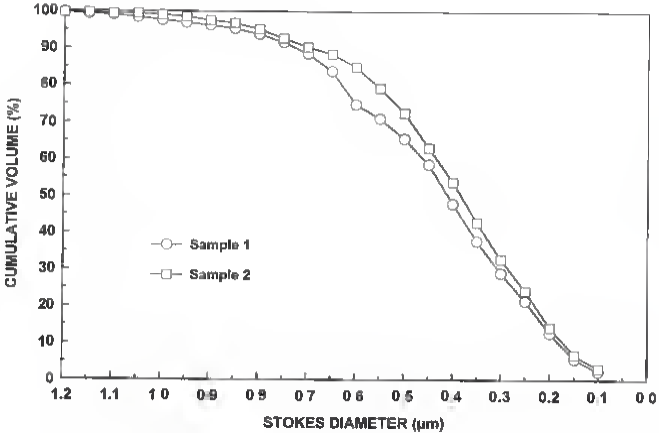

Figure K-1 Particle size distribution plots (two independent samples) for Series III 30/70 composite powder

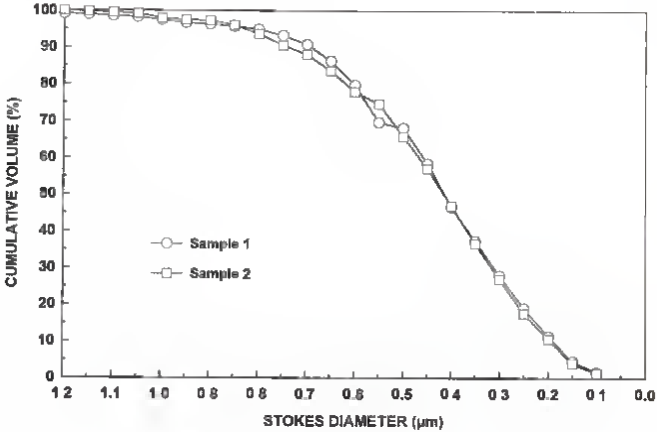

Figure K-2. Particle size distribution plots (two independent samples) for Series III 40/60 composite powder

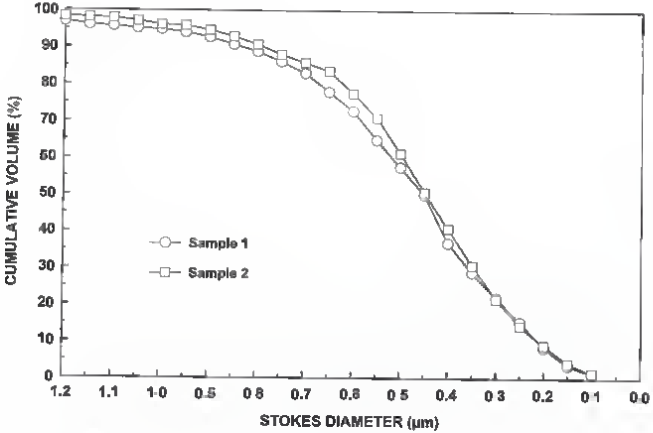

Figure K-3 Particle size distribution plots (two independent samples) for Series III 50/50 composite powder

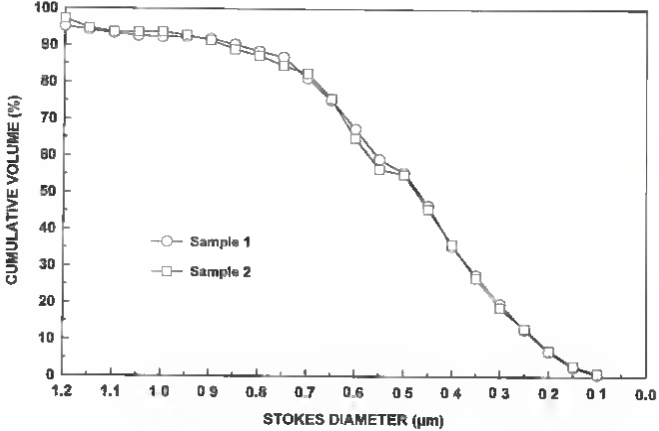

Figure K-4 Particle size distribution plots (two independent samples) for Series III 60/40 composite powder

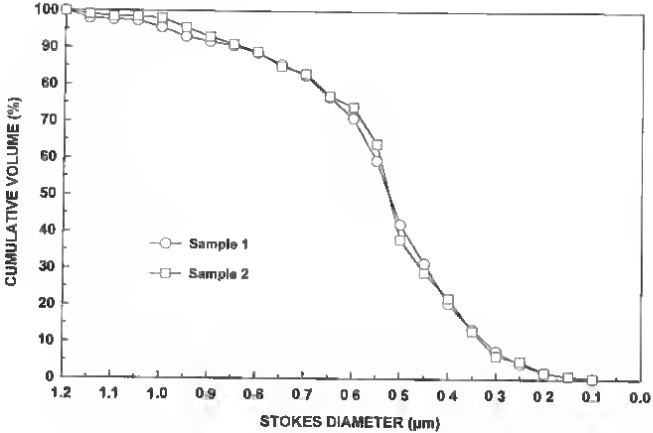

Figure K 5 Particle size distribution plots (two independent samples) for Series II 85/15 composite powder

APPENDIX I.
BOROSILICATE GLASS / ALUMINA COMPOSITES

I.1 Introduction

Sacks et al [Sac91a] prepared composite powders consisting of inner cores of Al_2O_3 and outer coatings of amorphous SiO_2. Slip-cast samples were prepared from particles with ~27/73 volume ratio of SiO_2/Al_2O_3 using the same procedure as that described for the Series III SiO_2/Si_3N_4 compacts used for the isothermal densification studies (see Sections 3.3 and 3.4). The SiO_2/Al_2O_3 compacts were pre-sintered in air at 800°C for 2 h and the bulk density of these samples were determined to be ~2.27 g/cm^3. (If the theoretical densities of SiO_2 and Al_2O_3 are assumed to be 2.20 and 3.98 g/cm^3, respectively, the true density of the composite powder compact is calculated by linear interpolation to be 3.50 g/cm^3. The relative density of the pre-sintered compact is then calculated as 2.27 x 100 / 3.50 = ~65%. Therefore, the Al_2O_3 content in these samples (~73 vol%) is significantly higher than the theoretical value[1] of the rigidity threshold, i.e., the green density value of ~65 vol%.) It was shown that these samples could be sintered to full density (i.e., almost no residual porosity) at 1300°C. In contrast, SiO_2/Si_3N_4 composite powder compacts with only 60 vol% Si_3N_4 (i.e., equal to the theoretical rigidity threshold of ~60 vol%) approached a limiting density of ~82% under the same heating conditions (see Section 4.3.6). One of the possible explanations for this

[1] In Section 4.3.6, rigidity threshold was estimated by assuming monosized particles with spherical geometry, uniform coating thickness, uniform packing, uniform shrinkage at each contact, etc. In this appendix, the value of rigidity threshold will be regarded as the "theoretical" value.

difference in densification behavior is based on the sinterability of Al_2O_3 at these temperatures. Recent experiments conducted by Wang [K. Wang and M.D. Sacks, personal communication, 1996] showed that compacts prepared with the Al_2O_3 core particles (with essentially the same particle size distribution as in the study by Sacks et al. [Sac91a]) could be sintered to nearly full density at ~1300°C. Based on this result, it may be argued that the network of Al_2O_3 particles which formed during the sintering of the SiO_2/Al_2O_3 compacts is not "rigid" (i.e., it is "sinterable") and therefore, densification continued even after the network was established. However, further experiments (such as detailed microstructural evolution studies) are necessary to confirm this hypothesis.

One approach to render the Al_2O_3 particles "rigid" involves reducing the sintering temperature of the composite, such that the Al_2O_3 particles are non-sinterable. It has been shown [Sac93] that the incorporation of boria in the SiO_2 coating (i.e., to produce borosilicate (BS) glass coatings) significantly reduces the viscosity of the amorphous phase and therefore results in significantly lower sintering temperatures. For example, SiO_2/Si_3N_4 and BS (~0.4 B Si)/Si_3N_4 composite powder compacts with ~60/40 volume ratio of the amorphous phase/crystalline phase were sintered at various temperatures. While the former samples reached ~100% relative density at ~1300°C, the latter samples could be sintered to the same density at only ~800°C. Based on these results it may be reasonable to expect that composites with similar coatings (i.e., BS glass) and Al_2O_3 cores would also sinter at relatively low temperatures. Therefore, it would be interesting to study the densification behavior of BS glass/Al_2O_3 composites with a relatively high volume fraction of Al_2O_3 cores and compare that with the densification behavior of

SiO_2/Si_3N_4 composite powder compacts with a similar volume fraction of the core particles. In this appendix, experiments performed using composite powders consisting of inner cores of Al_2O_3 and outer coatings of amorphous borosilicate (BS) are described.

L.2. Coating Procedure

I Filtration of Ethanol

The filtration procedure was the same as that described in Section B.2

II Preparation of Al_2O_3 Suspension

1 Rinse a 125 ml plastic bottle with filtered ethanol and weigh out 76 g (94 ml assuming a density of 0.81 g/ml) of ethanol into it

2 Add a 1" magnetic stirrer and start stirring

3. Weigh out 0.0748 g of Klucel E[2] and add it to the ethanol while stirring.

4 Weigh out 7.475 g of fractionated Al_2O_3 powder[3] and add it gradually to the solution

5 Remove the stirrer and mix 15 minutes on a paint shaker[4]

6 Sonicate for 2 hours and shake suspension after each 30 min of sonication

III Preparation of Alkoxide Mixture

1 Rinse a 2 l Erlenmeyer flask with ethanol and add 656 ml of ethanol into it Add a 2" magnetic stirrer and start stirring

[2] Aqualon Chemical Co Hercules, IL.
[3] The fractionated Al_2O_3 was prepared by Wang JK. Wang and M D Sacks, personal communication, 1996) and it had a median Stokes diameter of ~0.18 μm.
[4] Model 5400 Red Devil Equipment Co. Brooklyn Park, MN

2 Rinse a 250 ml Erlenmeyer flask with ethanol Measure out 180 ml ethanol in a 200 ml graduated cylinder and transfer it into the flask. Add a 1" magnetic stirrer and start stirring

3 Weigh out 6 496 g of TEOS[5] and add it to the 250 ml flask while stirring.

4 Measure out 4 95 ml of tributyl borate (TBB)[6] and add it to the 250 ml flask while stirring.

5 Wait for 5 min to ensure that the TEOS TBB and ethanol are mixed thoroughly

IV Coating Procedure

1 Add the sonicated Al_2O_3 / ethanol suspension to the 2 l flask while stirring at maximum speed

2. Add the TEOS / TBB / ethanol solution to the 2 l flask

3 Measure out 228 ml of concentrated (~29 wt%) NH_4OH from a freshly opened bottle into a 500 ml graduated cylinder

4 Add the NH_4OH rapidly (within ~5 s) into the 2 l flask

5 Cover the 2 l flask with Parafilm and keep the mixture stirred at maximum speed for 1 hour

V Filtration and Washing

1 Filter the suspension through a filter paper[7] using a teflon coated pressure filtration apparatus[8] The filtration is carried out at ~50 psi pressure

[5] Reagent Grade, Fisher Scientific, Fair Lawn, NJ
[6] Reagent Grade Fisher Scientific, Fair Lawn, NJ
[7] 0 22μm nylon Fisher Scientific, Fair Lawn, NJ
[8] ~4" dia. Millipore Corp., Bedford, MA

2 Keep the suspension in the 2 l flask stirring until all of it is transferred into the filtration chamber Collect all of the ethanol / NH_4OH / TEOS waste in one container

3 Measure out 2 l of filtered ethanol Wash the filtered powder by running the ethanol through the filtration chamber

4 Collect the washed powder in a 125 ml plastic bottle and disperse in 100 ml of filtered ethanol.

VI Redispersion and Washing

1 Sonicate suspension for 1 hour with a 5 minute cooling break after 30 minutes

2 Pour 1600 ml of filtered ethanol into a 2 l plastic bottle Add the sonicated suspension into this bottle

3 Age 8 hours on a roller mill

4 Filter the aged suspension using a pressure filtration apparatus with filter paper[9]

5 Dry the filtered powders in a vacuum oven at 80°C for 12 h.

6 Grind the dry powders with an alumina pestle and mortar Transfer the ground powder into a plastic bottle and store in a vacuum desiccator

L.3. Consolidation and Heat Treatment

The BS/Al_2O_3 powder was dispersed in filtered ethanol (at a solids concentration of ~30 vol%) using ultrasonication for ~2 h to break down agglomerates and the addition of 1 wt% (in solids) PVP K-15[10] to achieve stabilization against flocculation. Slip-cast samples were prepared by pouring suspensions into teflon molds (~20 mm in diameter)

[9] 0.22μm nylon, Fisher Scientific, Fair Lawn, NJ
[10] ISP Technologies, Wayne, NJ

set on porous plaster blocks A 0 22 μm nylon filter paper[11] was placed between the molds and the plaster The samples were covered with a plastic cover and allowed to dry under ambient conditions for ~48 h They were subsequently vacuum oven-dried (~80°C, 12 h), pre-sintered in a quartz tube furnace[12] at 500°C (heating rate ~2°C/min) for 2 h in ambient air, and stored in a vacuum desiccator The samples were ~2-3 mm thick and weighed ~1 g, after pre-sintering The pre sintered samples were sintered in static air in a box furnace[13] at temperatures in the range of 800 1250°C The heating rate was 10°C/min and the samples were held at the sintering temperature for 2 h The bulk density apparent density, and open porosity values were determined on the samples using the Archimedes displacement method with filtered ethanol as the liquid medium. Prior to the measurement, the samples were saturated for ~30 min with the ethanol using vacuum impregnation

L 4 Results and Discussion

Table L-I shows the results from density measurements for BS/Al_2O_3 samples sintered at various temperatures. The true density of the composite may be estimated as follows The specific volume, V in cm^3/g, of a borosilicate glass is given by [Zar91]

$$V = 0.453 \cdot X_S + 0.526 \cdot X_B \qquad (L.1)$$

where, X_S and X_B are the weight fractions of B_2O_3 and SiO_2, respectively The weight fractions of B_2O_3 and SiO_2 in the coating was calculated to be 0 258 and 0 742, respectively (This calculation assumed that during coating the conversion of TEOS to SiO_2 and TBB to B_2O_3 occurred with 100% yields. Kisailus [D Kisailus and M D Sacks,

[11] 0.22μm nylon, Fisher Scientific, Fair Lawn, NJ
[12] Model 59344 Lindberg Co., St. Waterton, WI
[13] Model DT 31, Deltech, Inc. Denver CO

Table L-1 Table of Sintered Densities for BSA/Al_2O_3 Samples

Temperature (°C)	ρ_{bulk} (g/cm^3)	Open Porosity (%)	ρ_{app} (g/cm^3)
500	2.108	35.5	3.269
	2.105	35.8	3.276
800	2.177	33.4	3.270
	2.188	33.2	3.275
900	2.259	32.6	3.353
	2.253	32.8	3.351
950	2.308	31.8	3.383
	2.316	31.7	3.391
975	2.399	29.2	3.387
	2.414	28.8	3.392
1000	2.659	21.5	3.386
	2.650	21.7	3.385
1025	2.675	21.2	3.397
	2.683	20.8	3.387
1050	2.794	17.9	3.405
	2.798	17.6	3.395
1100	3.008	10.6	3.365
	3.003	10.6	3.359
1150	3.179	4.5	3.330
	3.186	4.3	3.330
1200	3.385	0.1	3.390
	3.379	0.1	3.384
1250	3.388	0.0	3.388
	3.392	0.0	3.392

personal communication, 1996] prepared BS glass coated Si_3N_4 composite powders using a method similar to that described in Section L.2. He showed from HF leaching experiments that the conversion of TBB to B_2O_3 occurred with yields less than 100%. Therefore, the actual density of the BS glass coating, and hence the actual density of the composite, may be higher than the calculated value. The error in the calculated composite density may have been partially compensated for by the fact that the calculated volume fraction of BS glass is higher than the actual value.) Substituting these values in eq. (L.1), V was calculated to be 0.4718 cm^3/g. Therefore, the true density of the glass phase is 1/V or 2.12 g/cm^3. Assuming that the composite has the nominal volume-based composition of 39/61 BS/Al_2O_3, and that the true density of Al_2O_3 is 3.98 g/cm^3, the true density of the composite was estimated by linear interpolation to be (0.39•2.12 + 0.61•3.98) = 3.25 g/cm^3.

Table L-1 shows that the apparent density value was ~3.27 g/cm^3 for samples heated in the temperature range of 500-800°C. This value is in reasonable agreement with the estimated true density value of ~3.25 g/cm^3. Table L-1 also indicates that the apparent density increased gradually to ~3.39 g/cm^3 as the sintering temperature increased to 950°C. Possible reasons for the increase in apparent density are discussed below.

(1) There may be a decrease in closed porosity between 800 and 950°C. It is possible that fine pores (such as those described in Table 4.18 for Series III SiO_2/Si_3N_4 composite powders) were present in the composite particles. Such pores may not be accessible to ethanol during Archimedes density measurements. (Nitrogen gas adsorption measurements are necessary to assess the contribution of such porosity to the total porosity.) However, it was shown in Section 4.3.1 that for 40/60 SiO_2/Si_3N_4 powders,

such pores were almost completely eliminated (or "sintered out") by heating to 600°C The ~39/61 BS/Al_2O_3 powders used in this appendix presumably had a composition (i e, volume ratio of the amorphous and crystalline phases) similar to the 40/60 SiO_2/Si_3N_4 powders. Moreover, the addition of boron into SiO_2 reduces the viscosity of the amorphous phase Therefore, it may be reasonable to expect that heat treatment at 800°C would be sufficient to eliminate (or "sinter out") any fine porosity which may be present in the composite particles.

(2) During heat-treatment, boron may be removed from the BS coating as boric oxide by leaching and subsequent volatilization The effect of boron removal can be assessed by performing a simple calculation. First, it is assumed that all the boron is removed i.e , the composite is comprised of only SiO_2 and Al_2O_3. This is equivalent to performing the coating (see Section L.2) without the addition of TBB Based on the amounts of TEOS and Al_2O_3 used in the coating the expected volume ratio of SiO_2/Al_2O_3 is ~31/69 (It was assumed that the TEOS completely converted to SiO_2 and that the true densities of SiO_2 and Al_2O_3 were 2 20 and 3 98 g/cm^3, respectively) Therefore, the true density of the composite is calculated to be 0.31x2.2 + 0 69x3 98 = 3.43 g/cm^3 This is only slightly (~1%) higher than the measured apparent density after the 1050°C heat treatment These calculations seem to indicate that most of the boron presumably volatilized as boric oxide upon heating at relatively high temperatures

(3) Crystallization of BS glass at relatively high temperatures could have contributed to the increase in apparent density However, detailed XRD analyses will be necessary to confirm this hypothesis. It is noted that previous studies [Sac93 D Kisailus

and M D Sacks personal communication, 1996] conducted on similar composites did not provide any evidence of such crystallization behavior

Figure L-1 shows plots of bulk density and open porosity vs. temperature for BS/Al_2O_3 samples described in this section and ~39/61 SiO_2/Al_2O_3 composite powder compacts used in the study of Sacks et al [Sac91a] The compacts prepared with the SiO_2/Al_2O_3 composite powder show no significant change in density until the temperature exceeds ~1150°C, while the compacts prepared with the BS/Al_2O_3 composite powder start to show an increase in bulk density and a decrease in open porosity by ~900°C The former samples reach a maximum bulk density of ~3.27 g/cm^3 at 1400°C (The reduction in density at 1500°C was attributed to the volume expansion associated with the reaction between SiO_2 and Al_2O_3 to form mullite [Sac91a]) In contrast, the latter compacts seemed to attain a transient maximum density of ~2 67 g/cm^3 at ~1025°C but underwent further densification when heated at temperatures greater than 1050°C One possible explanation for the sintering behavior of the latter samples is described below The Al_2O_3 core particles approach each other as the compact undergoes densification by viscous flow of the BS coating At ~1025°C, the rigidity threshold is attained and the Al_2O_3 particle-particle network impedes the densification process (The theoretical rigidity threshold can be estimated as follows If it is assumed that the pre-sintered sample comprised only open pores, the green density and hence the theoretical rigidity threshold would be ~64% (from Table L-1) The change in apparent density with temperature complicates the calculation of the experimental value of the rigidity threshold since, as discussed earlier, the relative volume fractions of BS glass and Al_2O_3 also presumably changes with temperature.)

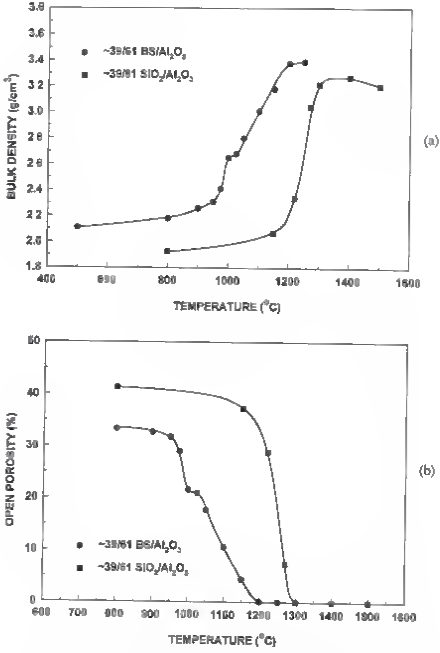

Figure L-1 Plots of (a) bulk density vs temperature and (b) open porosity vs. temperature for ~39/61 BS/Al_2O_3 and ~39/61 SiO_2/Al_2O_3 [Sae91a] compacts prepared from microcomposite particles

However, when the compacts are heated to temperatures >1050°C, further densification occurs due to diffusion and/or dissolution and re-precipitation processes. It is noted that further experiments are necessary to confirm this interpretation. First, chemical analyses are needed to determine if changes in boron content (and hence, changes in the B Si ratio in the glass and changes in the BS glass/Al_2O_3 volume ratio) with temperature. This is because a decrease in boron content increases the silicate glass viscosity and, therefore, decreases the densification rate. If the boron content changes significantly with temperature, it would further complicate the analysis presented above. Second, the sintering experiments should be repeated on another set of samples to check the reproducibility of the densification behavior. The temperature range corresponding to the transient maximum density is only ~25°C. Therefore, errors in temperature measurement and/or inconsistencies in the sample placement in the furnace may result in an "apparent" transient density. Third, SEM of polished and etched cross-sections of the sintered samples may be carried out to study the microstructure evolution. This would provide further insight into the changes in the distribution of phases (such as formation of Al_2O_3 particle-particle contacts) during sintering.

APPENDIX M
OXIDATION OF Si_3N_4 COMPACTS

M.1 Introduction

This appendix will report the results from some preliminary investigations concerning a unique oxidative processing technique to fabricate SiO_2/Si_3N_4 composites

M.2 Calculations

The reaction describing the complete oxidation of Si_3N_4 to SiO_2 may be expressed as:

$$Si_3N_4 + 3O_2\uparrow \rightarrow 3SiO_2 + 2N_2\uparrow \qquad (M.1)$$

In the current study partial oxidation reactions were carried out to prepare composites with SiO_2/Si_3N_4 volume ratios of 38/62, 45/55, and 50/50. The calculations involved in the preparation of 38/62 composite samples are described below. If a sample has an initial volume of the solids of 100 cm^3, it would be comprised of 38 cm^3 of SiO_2 and 62 cm^3 of Si_3N_4. If the true densities of SiO_2 and Si_3N_4 were assumed to be 2.20 and 3.19 g/cm^3, respectively, the weights of the two components would be 38 x 2.20 = 83.6 g and 3.19 x 62 = 197.8 g, respectively. Since the molecular weights of SiO_2 and Si_3N_4 are 60 g and 140 g, respectively, the number of moles of the two components can be calculated as 83.6 / 60 = 1.39 and 197.8 / 140 = 1.41, respectively. If it is assumed that the SiO_2 forms by the partial oxidation of Si_3N_4, the formation of 1.39 moles of SiO_2 would require 1.39 / 3 = 0.46 moles of Si_3N_4 (from eq. (M.1)). Therefore, the total number of moles of Si_3N_4

required prior to oxidation would be 1 41 + 0 46 = 1 87 The partial oxidation reaction for Si_3N_4 corresponding to the 38/62 composition can now be expressed by

$$1\ 87\ Si_3N_4 + 1\ 39\ O_2\uparrow \rightarrow (1\ 41\ Si_3N_4 + 1\ 39\ SiO_2) + 0\ 93\ N_2\uparrow \qquad (M\text{-}2)$$

The weight gain for the condensed phases for eq (M-2) can be calculated as 1 41 x 140 + 1 39 x 60 - 1 87 x 140 = 19g Since the weight of the starting Si_3N_4 is 1 87 x 140 = 261 g g the net weight gain for the condensed phases is 19 x 100 / 261 8 = 7 2% The volume expansion of the condensed phases after oxidation is 1 41 x 140 / 3 19 + 1 39 x 60 / 2 2 - 1 87 x 140 / 3 19 = 17 7 cm^3 Since the volume of the starting Si_3N_4 is 1 87 x 140 / 3 19 = 82.1 cm^3 the net expansion in volume is 17 7 x 100 / 82.1 – 21 6%

Similar calculations were also performed for the 45/55 and 50/50 compositions. The partial oxidation reactions for these samples can be expressed by:

$$1\ 80\ Si_3N_4 + 1\ 65\ O_2\uparrow \rightarrow (1.25\ Si_3N_4 + 1\ 65\ SiO_2) + 0\ 90\ N_2\uparrow \qquad (M\text{-}3)$$

for the 45/55 composition, and

$$1\ 75\ Si_3N_4 + 1\ 83\ O_2\uparrow \rightarrow (1\ 14\ Si_3N_4 + 1\ 83\ SiO_2) + 0\ 88\ N_2\uparrow \qquad (M\text{-}4)$$

for the 50/50 composition The weight gain values (of condensed phases) pertaining to eqs (M-3) and (M-4) are 8 9% and 10 0%, respectively The corresponding volume expansion values are 26 6% and 30 2%, respectively

M.3 Experimental Procedure

The Lot2 Si_3N_4 fractionated powder was used to prepare a concentrated (~30 vol%) aqueous suspension The suspension was subjected to ultrasonication for ~2 h to break down powder agglomerates and pH adjustment (to ~9 6 using 3N NH_4OH solution) to achieve electrostatic stabilization. The consolidation procedure was similar to that

described for the disk-shaped Series III composite samples (see Section 2 4 1) Slip-cast samples were prepared by pouring the suspension into molds set on porous plaster blocks A 0 22 μm cellulose filter paper was placed between the molds and the plaster Teflon molds were used to prepare disk-shaped compacts (~2-3 mm thick and ~19 mm diameter) The compacts were dried at ~80°C for 24 h in air and subsequently at 100°C for 12 h in vacuum One of the dried compacts was pre-sintered in a quartz tube furnace[1] at 800°C (heating rate ~2°C/min) for 2 h in flowing (~50 cm^3/mn) nitrogen and density measurements were carried out using the Archimedes displacement method with water as the medium Table M-I summarizes the results from these measurements

Table M-1 Density Results for 800°C (2 h) Pre-Sintered Si_3N_4 Compact

Measurement No	ρ_{theor} (g/cm^3)	% O P	$\rho_{apparent}$ (g/cm^3)
1	1 843	42 1	3 183
2	1 846	41 9	3 177
average	1 84	42	3 18

One of the dried compacts was heated in a thermal gravimetric analysis (TGA) apparatus[2] (heating rate of ~10°C/mn) to 1200°C in a flowing (~60 cm^3/min) oxygen atmosphere and held at that temperature for ~4 h Figure M-1 shows plots of (a) temperature vs time (i e , the temperature profile) and (b) weight gain vs. time for the Si_3N_4 compact. It was established from Figure M-1 that the total hold times at 1200°C required to prepare the 38/62, 45/55 and 50/50 composite compacts were ~140 mn (for ~7.2% weight gain), ~195 mn (for ~8 9% weight gain) and ~245 mn (for ~10 0% weight gain),

[1] Model 59344 Lindberg Co St. Waterton, WI
[2] Netzsch STA409 Exton PA

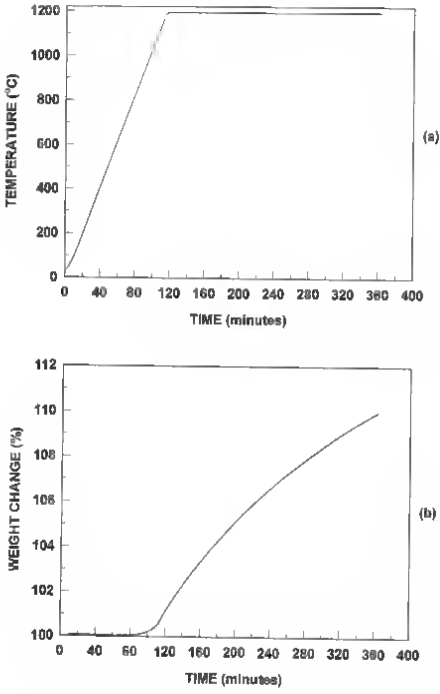

Figure M-1 Plots of (a) temperature vs time (i e. the temperature profile) and (b) weight gain vs. time for the Si_3N_4 compact.

respectively. Three independent samples were then heated under these conditions, respectively. Sample weights measured before and after each oxidation experiment indicated that the desired amount of oxidation occurred (i.e., the target weight gains were achieved). The oxidized samples were then heated to successively higher temperatures in a tube furnace[3] in flowing (~60 cm^3/min) nitrogen. After each heat treatment, density measurement was carried out using the Archimedes displacement method with water as the medium. Polished and/or etched samples for SEM observations were prepared using the procedure described in Section 3.6. X-ray diffraction (XRD) patterns were obtained on selected samples using a diffractometer[4] with Ni-filtered CuKα radiation and a scan rate of 3°/min. Data was collected in the 2θ range of 5° - 85°.

M.4 Results and Discussion

Figures M-2 (A) and M-2 (B) show the XRD patterns for the 45/55 and 50/50 composite samples, respectively, which were prepared by oxidation of the Si_3N_4 compacts. (The weight gain values corresponding to the two samples were ~8.9% and ~10.0%, respectively.) The crystalline peaks in both the plots correspond to α- Si_3N_4 while the broad peaks centered at 2θ ~ 22° are characteristic of amorphous SiO_2. These results clearly demonstrate the amorphous nature of the SiO_2 formed by the oxidation of Si_3N_4. Plucknett and Wilkinson [Plu93] carried out oxidation of dry-pressed α Si_3N_4 powder compacts in a static air atmosphere. The samples were oxidized at various temperatures between 950 and 1200°C for a duration of 200 h. The SiO_2 formed by oxidation was

[3] Model 64259. Lindberg Co., St. Waterton, WI
[4] Model APD 3720. Philips Electronic Instruments Co. Mt. Vernon, NY

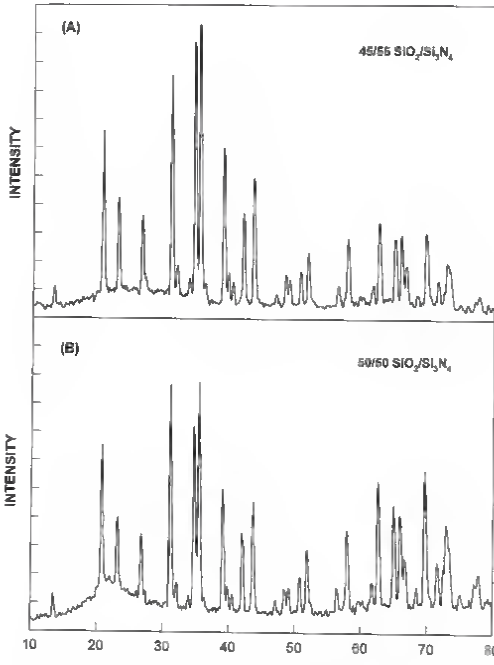

Figure M-2 XRD plots for (A) 45/55 and (B) 50/50 SiO_2/Si_3N_4 samples formed by oxidizing Si_3N_4 compacts at 1200°C in oxygen. The crystalline peaks for both samples correspond to α-Si_3N_4.

amorphous in nature, which is consistent with the results reported for the current investigation.

Table M-II shows the results from the density measurements for the oxidation-derived 45/55 and 50/50 composite samples

Table M-II Density Results for 1200°C Oxidized Si_3N_4 Compacts.

Sample	Time at 1200°C (min)	Weight Gain (%)	ρ_{bulk} (g/cm^3)	%OP	$\rho_{apparent}$ (g/cm^3)
45/55	195	8 9	2 064	24.2	2 711
			2.061	24 1	2 715
50/50	245	10 0	2 110	21 2	2 678
			2 101	21 6	2 680

Assuming the true densities of SiO_2 and Si_3N_4 to be 2.20 and 3 19 g/cm^3, respectively the expected true densities of the 45/55 and 50/50 composite samples was calculated (by linear interpolation) to be 2 74 and 2.70 g/cm^3, respectively Based on these values, the relative densities of the 45/55 and 50/50 samples (after the oxidation heat treatment) were calculated to be 2 06 x 100 / 2.74 = 75.2% and 2.11 x 100 / 2 70 = 78 1%, respectively Therefore, the total porosities in the two samples were 24 8% and 21 9%, respectively The relative density of the starting Si_3N_4 compact (prior to oxidation) was calculated from the bulk density values in Table M-I (using a true density value of 3 19 g/cm^3) to be 57 7%. As explained earlier, there is a volume expansion associated with the oxidation process In the following treatment, it is assumed that this volume expansion is entirely accommodated by the porosity (or "pore-filling" takes place) i e., the increase in solid

volume results in an equal decrease in the pore volume (It is implicitly assumed that the total bulk volume remains unaltered during oxidation.) In such a case, the increase in relative density associated with the oxidation process for the formation of 45/55 and 50/50 samples can be calculated as 1 266 x 57 7 = 73 0% (for 26 6% volume expansion) and 1 302 x 57 7 = 75 1% (for 30.2% volume expansion), respectively These values are in reasonable agreement with the measured relative densities of 75 2 and 78 1%, respectively This seems to indicate that a significant portion of the increase in density is presumably associated with the "pore filling" which occurred as a result of the volume expansion during oxidation The difference in the measured and predicted values of relative density may be attributed to the densification of the composite occurring by viscous flow of the amorphous SiO_2 phase formed during the oxidation step[3] However, it may be necessary to continuously monitor the dimension change in the samples (e g using a dilatometer) during oxidation in order to confirm this interpretation

Table M III shows the density results for the oxidized samples which were successively heated to higher temperatures. The relative densities were obtained by assuming the true densities of the 38/62, 45/55 and 50/50 samples (corresponding to weight gains of 7 8, 8 9, and 10 0%, respectively) to be 2 81, 2.74 and 2.70 g/cm^3 respectively (These values were calculated by linear interpolation assuming the true densities of SiO_2 and Si_3N_4 to be 2.20 and 3 19 g/cm^3, respectively) It is evident from Table M-III that the 45/55 and 50/50 composite samples underwent significant

[3] The densification plot in Figure 4 16 showed that a 60/40 composite powder compact with a green density of ~61% densified to ~74% relative density when heated to 1200°C for 2 h In the current study lower increases in density were observed presumably due to the fact that much lower amounts of SiO_2 are present in the initial stages of oxidation Moreover the final SiO_2 contents for the oxidized samples are lower than that present in the composite powder compact described in Figure 4 16 (45 and 50 vol% vs. 60 vol%, respectively)

Table M-III Density Results for Oxidation-Derived Composite Compacts Sintered at Various Temperatures (O P = open porosity)

Sample	Sintering Temperature (°C)	ρ_{bulk} (g/cm^3)	% O P	$\rho_{apparent}$ (g/cm^3)	Relative Density (%)
38/62	1300 (38 h)	2 334	16.2	2.785	
		2 326	16.6	2 789	82.9
	1400 (2 h)	2.331	15 8	2 768	
		2.332	16 0	2 776	82 9
45/55	1300 (2 h)	2 456	8 9	2 696	
		2 464	8 3	2 687	89 8
	1300 (38 h)	2 508	0.2	2.513	
		2 507	0 1	2.510	91 6
	1350 (2 h)	2 518	0 1	2 521	
		2 521	0 1	2.524	92 0
50/50	1300 (2 h)	2 560	0.2	2.565	
		2.560	0 1	2.563	94 8
	1300 (38 h)	2.579	0 2	2 584	
		2 576	0 1	2 579	95 6
	1350 (2 h)	2 585	0 1	2.588	
		2 586	0 1	2 589	96.0

densification after sintering at 1300°C for 2 h The bulk density of the two samples increased from 2 06 and 2 11 g/cm^3, respectively, to 2 46 and 2 56 g/cm^3, respectively In addition, the open porosity values for the same samples decreased from ~24 and ~21%, respectively, to ~9 and ~0%, respectively (The density of the 3#/62 sample was not measured after the oxidation step and, therefore the extent of densification in this sample was not known However, if it is assumed that the ~21 6% volume expansion associated with the formation of the 3#/62 compact was completely accommodated by "pore filling" the relative density of the sample prior to sintering at 1300°C (3# h) would be 57 7 x 1 216 = 70 2% If this is the case, it can be deduced from Table M-3 that the relative density of the sample increased from ~70% to ~83% after sintering at 1300°C for 3# h.) All the samples showed minimal (only 0 - 1%) increases in relative density values after heat treatment at temperatures higher than 1300°C This seems to indicate that the 3#/62 45/55, and 50/50 samples attained limiting relative densities of ~83, ~92, and ~96%, respectively The concentration of Si_3N_4 in the bulk volume (ratio of Si_3N_4 volume to the sum of Si_3N_4, SiO_2, and pore volumes) was determined for 3#/62, 45/55, and 50/50 samples after the limiting densities were reached The values were obtained by multiplying the relative density by the nominal Si_3N_4 volume fraction in the composite The calculated values of the limiting concentration of Si_3N_4 in the bulk volume were ~51, ~51 and ~48% for the 3#/62 45/55 and 50/50 samples, respectively These values are in good agreement with the rigidity threshold value of ~49% determined for composite powder compacts (see Figure 4 106 and related discussion in Section 4.3 6) This would seem to indicate that the

spatial distribution of phases (i.e., the distribution of SiO_2 and Si_3N_4 in the microstructure) in the two types of compacts were similar

In the current investigation, the oxidized samples were not heated at temperatures >1400°C. Plucknett and Wilkinson [Plu93] pressureless sintered the oxidized Si_3N_4 compacts (with a ~38/62 volume ratio of SiO_2/Si_3N_4) in a high-purity nitrogen atmosphere with the samples situated in a protective "powder-bed" of 50/40/10 (weight fraction) $BN/Si_3N_4/SiO_2$. The XRD plots of compacts sintered at 1800°C showed that the major phase present was Si_2N_2O (silicon oxynitride) while the minor phase was α-Si_3N_4. It is noted that similar high-temperature experiments could be performed on the samples in the current study to study the formation of oxynitride.

Figures M-3 (A)-(C) and M-4 (A)-(B) show low magnification (270x) SEM micrographs for polished cross-sections of the sintered (1350°C, 2 h) oxidation-derived 45/55 and 50/50 samples, respectively. For each sample, (A), (B) and (C) denote fields in the "top", "middle" and "bottom" regions, respectively. (This designation was based on the as-cast configuration. In other words, "top" denotes the region of the cross-section near the top of the cast sample.) The micrographs show the presence of powder agglomerates similar to those reported for the composite samples used for flexure testing (see Figures 4.37 and 4.38). It is also evident that concentration of these defects are seemingly higher in the "middle" and "bottom" regions in comparison to the "top" region". This would seem to indicate that the agglomerates were present in the suspension used for slip-casting, and that they presumably segregated (due to gravitational forces) to the lower regions of the sample. Figures M-5 (A)-(C) and M-6

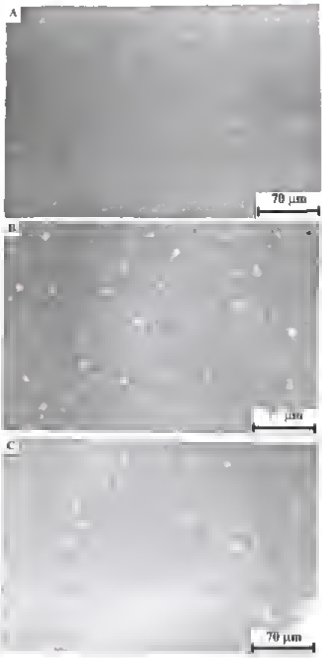

Figure M-3 SEM micrographs (270x magnification) of polished cross-sections of the oxidation-derived 45/55 sample sintered at 1350°C for 2 h. (A) (B) and (C) denote fields in the "top", "middle", and "bottom" regions, respectively. (This notation is based on the as-cast configuration. For example, "top" denotes the region of the cross-section near the top of the cast sample.)

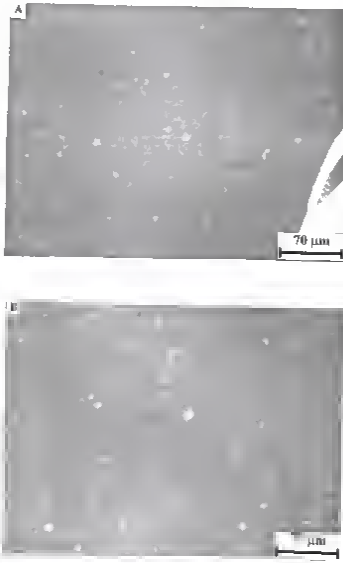

Figure M-4 SEM micrographs (270x magnification) of polished cross-sections of the oxidation-derived 50/50 sample sintered at 1350°C for 2 h. (A) and (B) denote fields in the "top" and "middle regions, respectively

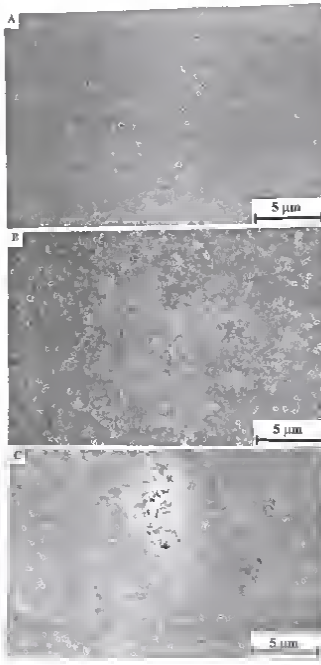

Figure M-5 SEM micrographs (4000x magnification) of polished cross-sections of the oxidation-derived 45/55 sample sintered at 1350°C for 2 h (A) (B) and (C) denote fields in the "top", "middle", and "bottom" regions respectively

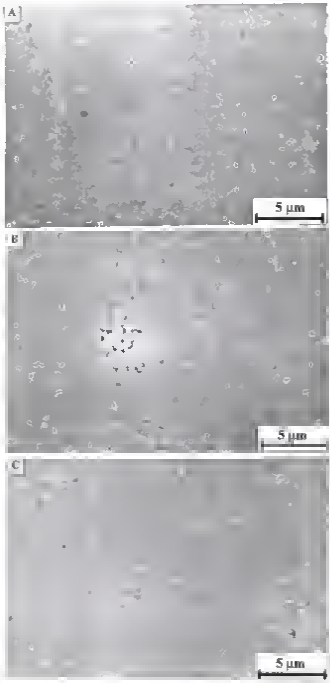

Figure M-6 SEM micrographs (4000x magnification) of polished cross-sections of the oxidation-derived 50/50 sample sintered at 1350°C for 2 h (A) (B) and (C) denote fields in the "top", "middle", and "bottom" regions, respectively

(A)-(C) show higher magnification (4000x) micrographs of the regions corresponding to the microstructures shown in Figures M-3 (A)-(C) and M-4 (A)-(C), respectively. For any given region, the 45/55 sample showed greater amounts of porosity than the 50/50 sample. This observation is consistent with the lower relative density measured for the 45/55 sample (Table M-III). It is also evident from Figures M-5 (A)-(C) and M-6 (A)-(C) that for each sample, there are greater amounts of porosity in the "middle" region relative to the "top" and "bottom" regions. The likely reason for this is that the surface of the sample (i.e., the "top" and "bottom" regions) oxidized to a greater extent relative to the interior (i.e., the "middle" region). In such a case, the concentration of the SiO_2 phase would be larger in the surface relative to the bulk, which would then result in relatively higher densification for the regions near the surface. The non uniform oxidation behavior may be explained as follows. Two concurrent processes are active during oxidation, viz., (1) the diffusive flow of oxygen into the open pore channels and removal of nitrogen through the same channels, and (2) the reaction of oxygen with Si_3N_4. Plucknett and Wilkinson [Plu93] showed that at low oxidation temperatures (~1000°C), the latter process is sluggish and a uniform level of oxidation is observed in the bulk and on the surface. This was consistent with the parabolic nature of the oxidation kinetics. In contrast, at higher temperatures, the reaction of oxygen with Si_3N_4 is considerable faster, and the concentration of SiO_2 was the highest at the surface and reduced gradually into the bulk region. This was reflected by the asymptotic oxidation kinetics exhibited at these temperatures. In the current study, more uniform oxidation may be presumably

achieved by heating to relatively lower temperatures (<1200°C) for relatively longer periods of time

Figures M-7 (A)-(C) and M-8 (A) (C) show high magnification (25,000x) micrographs of the regions corresponding to the microstructures shown in Figures M-4 (A)-(C) and M-4 (A)-(C), respectively The microstructures are similar to those obtained for composite powder compacts (see Figures 4 90 (C) and (D)) Thus indicates that the oxidation process presumably resulted in the formation of SiO_2 coatings on individual Si_3N_4 particles. The uniformity of these coatings may be rigorously assessed by quantitative microscopy measurements such as described in Section 4 3 4

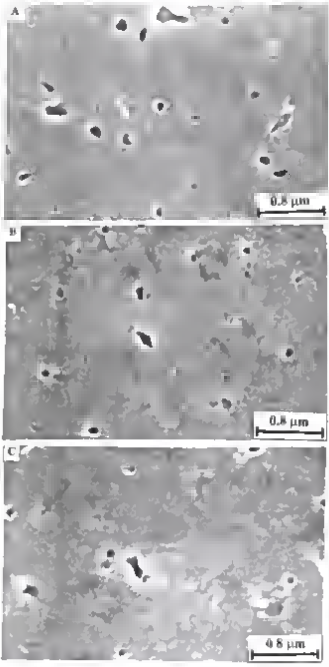

Figure M-7 SEM micrographs (25,000x magnification) of polished cross-sections of the oxidation-derived 45/55 sample sintered at 1350°C for 2 h (A) (B) and (C) denote fields in the "top" "middle", and "bottom" regions respectively

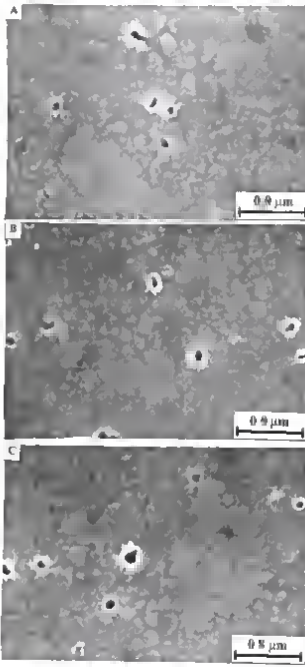

Figure M-8 SEM micrographs (25,000x magnification) of polished cross-sections of the oxidation-derived 50/50 sample sintered at 1350°C for 2 h. (A), (B) and (C) denote fields in the "top" "middle" and 'bottom' regions, respectively

APPENDIX N
HIGH TEMPERATURE HEAT TREATMENT OF SiO_2/Si_3N_4 COMPACTS

N.1 Introduction

Reaction sintering [Eks92] of SiO_2 and Si_3N_4 has been done either by pressureless sintering with additives of magnesia, yttria, and/or alumina, or by hot-pressing with alumina or ceria to obtain dense oxynitride ceramics. The reaction sintering of pure silicon oxynitride (Si_2N_2O) involves a transient melt of silica in which the initial Si_3N_4 grains dissolve and Si_2N_2O grains re-precipitate and grow. The kinetics of this process is known to be sluggish mainly due to the high viscosity of the pure silica melt in comparison to the eutectics formed with additives. Weight loss during sintering is generally suppressed by increased nitrogen pressures (~1 MPa) combined with a protective bed of the oxynitride composition (1:1 mole ratio of SiO_2 Si_3N_4) around the green body. Larker [Lar92] sintered mixtures of SiO_2 and Si_3N_4 by HIPing at temperatures in the range of 1700°C to 1950°C. He demonstrated that oxynitride formed at temperatures ≥ 1700°C and that the amount of this phase increased from ~5% at 1700°C to >80% at 1800°C. The objective of the following experiment is to study the reactions and the densification in composite powder compacts heated to temperatures in the range of 1300 - 1800°C.

N.2 Experimental Procedure

Composite powders with an overall composition of ~36/64 SiO_2/Si_3N_4 were synthesized by the procedure used for Series II composite powders (See Appendix B for detailed procedure The amounts of various components used were A = 0 0720 g, B = 7 2050 g C = 443 ml, D = 9 698 g and E = 209 ml) These powders were consolidated to form compacts using the procedure described in Section 3 4 1 for Series II composite powders The compacts were pre-sintered in a quartz tube furnace[1] at 800°C for 2 h in flowing (~50 cm^3/min) nitrogen One of the samples was then sintered sequentially in the temperature range of 1300 - 1800°C (heating rate was ~10°C/min and dwell time was ~2 h at each temperature) in flowing (~60 cm^3/min) nitrogen The heat treatments in the temperature range of 1300 - 1500°C were carried out in an alumina tube furnace[2] while the treatments at higher temperatures were carried out in a box furnace[3] Prior to each heat treatment, the sample was encapsulated in a loose packing of a $SiO_2 + Si_3N_4$ powder mixture[4] in an alumina crucible. Density measurements were carried out on the sintered sample by the Archimedes displacement method using water as the medium X-ray diffraction (XRD) patterns were obtained using a diffractometer[5] with Ni-filtered CuKα radiation and a scan rate of 3°/min. Data was collected in the 2θ range of 10° - 60°

---

[1] Model 59344 Lindberg Co. St Waterton, WI
[2] Model 54259 Lindberg Co. St Watertoo, WI
[3] Model M-60 Centuer Vacuum Industries, Sun Cook, NH
[4] The powder was a mixture of Si_3N_4 E-03 Ube Industries (America), Inc New York, NY) and batch 2 SiO_2 mixed in a 1 1 mole ratio using an alumina pestle and mortar The powder was heated to 1000°C for 2 h in air before using in the sintering experiments.
[5] Model APD 3720, Philips Electronic Instruments Co. Mt. Vernon NY

N.3 Results and Discussion

Table N-I shows the sample weight and density results obtained on the sample sintered at various temperatures. Table N-I shows that there was very little (<1%) weight change during heat treatments upto 1600°C. However, heating to higher temperatures led to increasingly significant weight losses and to corresponding increases in apparent densities. The weight losses may be attributed to the volatilization of SiO_2 as SiO vapor. Ekstrom and Nygren [Eks92] hot-pressed mixtures of SiO_2 and Si_3N_4 to form oxynitride ceramics. They found that weight loss during sintering (at temperatures ≥1600°C) can be suppressed by increased nitrogen pressures (at least ~1 MPa) combined with the use of a protective bed of SiO_2 + Si_3N_4 (1:1 mole ratio) around the green body. In the current investigation, the weight loss is presumably due to the removal of SiO vapor formed due to the relatively low nitrogen pressures (~0.15 MPa) used in the sintering experiments. The corresponding increase in apparent density values may also be attributed to the decrease in the concentration of the SiO_2 phase in the compact. In order to estimate the effect of SiO_2 loss on the apparent density, it was assumed that the composition was 36/64 at 1300°C. (The true density of this composite was calculated to be 2.834 g/cm^3 assuming the theoretical density of SiO_2 and Si_3N_4 to be 2.20 and 3.19 g/cm^3, respectively. This is in reasonable agreement with the apparent density value of ~2.844 g/cm^3 determined by the Archimedes method.) It is further assumed that the weight loss at higher temperatures is entirely due to the volatilization of SiO_2 as SiO. (This is not rigorously accurate since the removal of some residual OH groups in the SiO_2 phase may also contribute to the weight loss. However, this contribution is presumed to be

Table N-I Sample Weights and Densities for Heat-Treated 36/64 Composite Compacts.

Temperature (°C)	Weight (g)	ρ_{bulk} (g/cm^3)	Open Porosity (%)	ρ_{app} (g/cm^3)
1300	0 9091	2.221	21 9	2 844
		2.215	22 1	2 843
1400	0 9069	2.223	21·9	2 846
		2.226	21 8	2 847
1500	0 9034	2.228	22 0	2 856
		2.234	21 6	2 849
1600	0 8958	2.243	21 3	2 850
		2.246	21 1	2 847
1650	0.8712	2 253	21 4	2.866
		2.248	21 8	2 875
1750	0 8229	2 429	15 7	2.881
		2 439	15.2	2 876
1800	0.6223*	2 078	30 2	2 977
		2.082	29 9	2 970

* The sample cracked into several pieces after sintering at 1800°C This value represents the weight of the largest piece from cracked sample

Table N-II Estimated and Measured Densities for Sintered 36/64 Composite Compacts.

Temperature (°C)	Estimated True Density (g/cm^3)	Measured Apparent Density (g/cm^3)
1300	2 834	2.844
		2 843
1400	2 836	2 846
		2 847
1500	2 839	2.856
		2 849
1600	2 847	2 850
		2 847
1650	2.868	2.866
		2 875
1750	2 920	2 881
		2 876
1800	N/A	2 977
		2.970

negligible). The true density of the composite was then calculated from the corrected composition assuming the theoretical density of SiO_2 and Si_3N_4 to be 2.20 and 3.19 g/cm^3, respectively. Table N-II shows the comparison between the estimated true densities and the measured apparent densities for various sintering temperatures. (The data for the 1800°C heat treatment is not reported since the sample had cracked during heating.) The two values are in reasonable agreement for temperatures in the range of 1300 - 1650°C. The estimated density is slightly higher than the apparent density for the sample heated at 1750°C. One of the possible reasons for this difference may be a small error in sample weight measurement. During the 1750°C heat treatment, the ~6% weight loss was also accompanied by a ~5% reduction in open porosity. Since this temperature is above the melting point of pure SiO_2, it is likely that densification occurred by liquid phase sintering. This hypothesis is also supported by the formation of β-Si_3N_4, as described in the next paragraph. The sharp increase in open porosity at 1800°C is presumably due to the voids resulting from the catastrophic loss of SiO_2.

Figures N-1 - N-6 show the XRD plots for the samples heat treated at 1400, 1500, 1600, 1650, 1750, and 1800°C, respectively. Tables N-III - N-VIII show the list of XRD peak intensities for the same samples and for reference Si_3N_4 samples. The weight fractions of α-Si_3N_4 and β-Si_3N_4 were determined from the XRD patterns using the method of Gazzara and Messier [Gaz77] as described below. The intensities of the {210} peaks for the two phases were designated as $I_{\alpha(210)}$ (at $2\theta \approx 35.3°$) and $I_{\beta(210)}$ (at $2\theta \approx 36.1°$), respectively. The intensity ratio, R, was then calculated as

$$R = I_{\beta(210)} / I_{\alpha(210)} + I_{\beta(210)} \qquad (N.1)$$

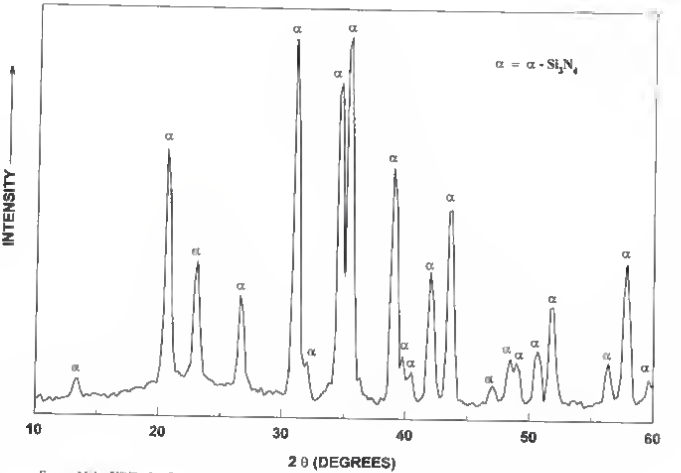

Figure N.1 XRD plot for 36/64 SiO_2/Si_3N_4 composite powder compact sintered at 1400°C for 2 h in nitrogen

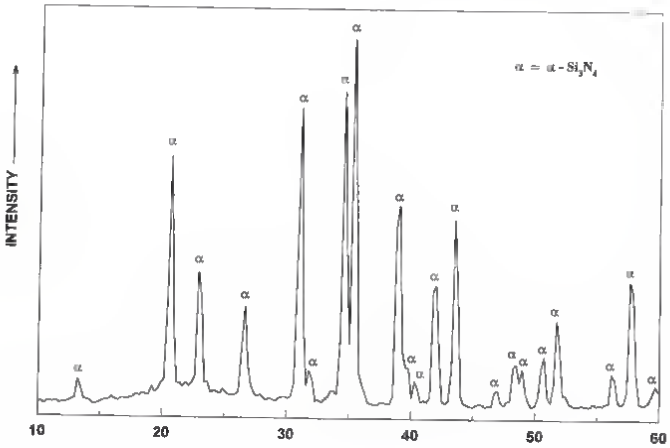

Figure N-2 XRD plot for 36/64 StO_2/Si_3N_4 composite powder compact sintered at 1500°C for 2 h in nitrogen.

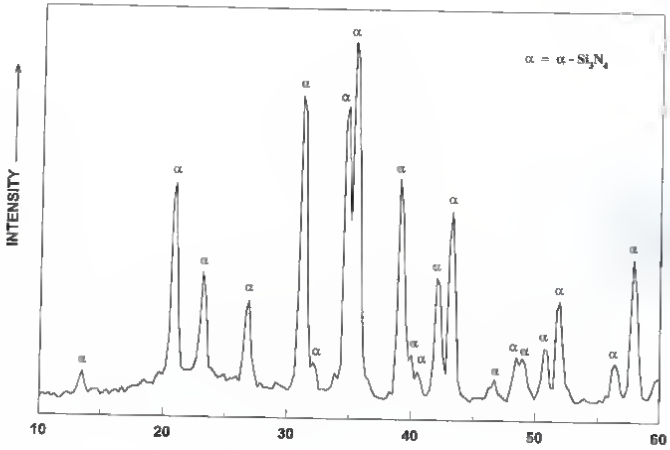

Figure N-3 XRD plot for 36/64 SiO_2/Si_3N_4 composite powder compact sintered at 1600°C for 2 h in nitrogen

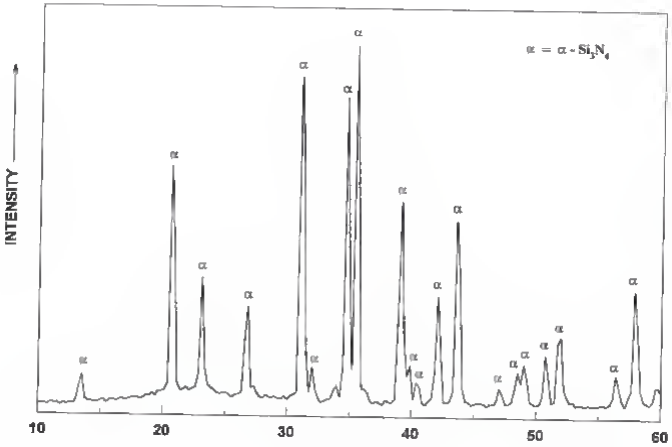

Figure N-4 XRD plot for 36/64 SiO_2/Si_3N_4 composite powder compact sintered at 1650°C for 2 h in nitrogen

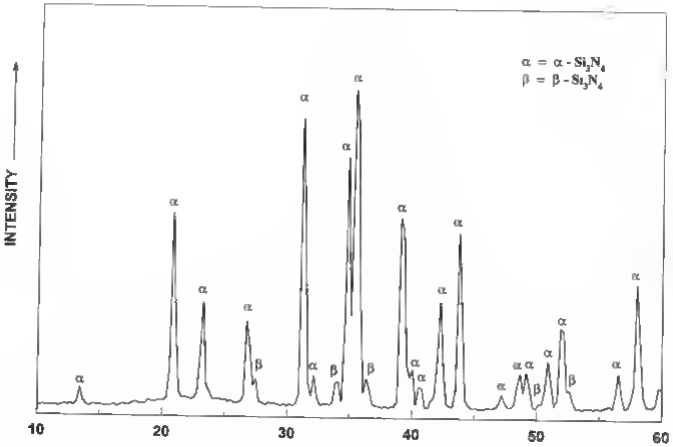

Figure N-5 XRD plot for 36/64 SiO_2/Si_3N_4 composite powder compact sintered at 1750°C for 2 h in nitrogen

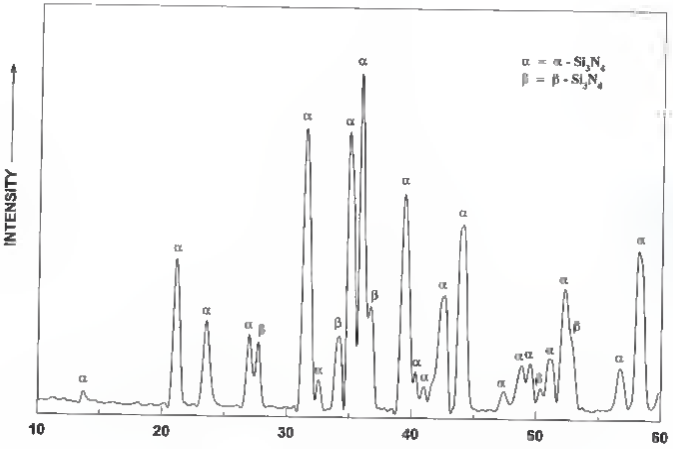

Figure N-6 XRD plot for 36/64 SiO_2/Si_3N_4 composite powder compact sintered at 1800°C for 2 h in nitrogen

Table N-III List of XRD Peaks for 36/64 Composite Sample Heated at 1300°C

Experimental Data			Si_3N_4 Reference Peaks [JCPDS pat]			
d(Å)	2θ (degrees)	I/I_o	d(Å)	2θ (degrees)	I/I_o	Phase
6.602	13.4	6	6.690	13.2	9	α
4.267	20.8	61	4.320	20.5	59	α
3.847	23.1	31	3.880	22.9	30	α
3.336	26.7	24	3.370	26.4	30	α
2.864	31.2	94	2.893	30.9	85	α
2.786	32.1	9	2.823	31.7	5	α
2.579	34.9	84	2.599	34.5	75	α
2.529	35.9	100	2.547	35.2	100	α
2.302	39.1	91	2.320	38.8	90	α
2.263	39.9	12	2.283	39.4	5	α
2.226	40.5	8	2.244	40.2	5	α
2.145	42.1	35	2.159	41.9	30	α
2.070	43.7	52	2.093	43.4	55	α
1.928	47.1	5	1.937	46.9	2	α
1.875	48.5	12	1.884	48.3	9	α
1.854	49.1	12	1.864	48.8	9	α
1.799	50.7	15	1.806	50.5	12	α
1.700	51.9	27	1.771	51.6	25	α
1.630	56.4	11	1.637	56.1	5	α
1.593	58.0	38	1.596	57.7	35	α
1.549	59.7	5	1.552	59.5	2	α

Table N-IV List of XRD Peaks for 36/64 Composite Sample Heated at 1400°C

Experimental Data			Si_3N_4 Reference Peaks (JCPDS pat)			
d(Å)	2θ (degrees)	I/I_o	d(Å)	2θ (degrees)	I/I_o	Phase
6.602	13.4	6	6.590	13.2	8	α
4.267	20.8	64	4.320	20.5	50	α
3.847	23.1	33	3.880	22.9	30	α
3.336	26.7	25	3.370	26.4	30	α
2.864	31.2	48	2.893	30.9	85	α
2.795	32.0	8	2.823	31.7	5	α
2.576	34.8	82	2.599	34.5	75	α
2.527	35.5	100	2.547	35.2	100	α
2.302	39.1	60	2.320	38.8	60	α
2.283	39.8	11	2.283	39.4	5	α
2.226	40.5	6	2.244	40.2	5	α
2.149	42.0	36	2.150	41.8	30	α
2.070	43.7	49	2.083	43.4	55	α
1.932	47.0	5	1.937	46.9	2	α
1.875	48.5	13	1.884	48.3	8	α
1.858	49.0	11	1.864	48.8	6	α
1.799	50.7	15	1.806	50.5	12	α
1.764	51.8	24	1.771	51.6	25	α
1.633	56.3	9	1.637	56.1	5	α
1.591	57.9	35	1.596	57.7	35	α
1.550	59.6	5	1.552	59.5	2	α

Table N-V List of XRD Peaks for 36/64 Composite Sample Heated at 1500°C

Experimental Data			Si_3N_4 Reference Peaks [JCPDS pat]			
d(Å)	2θ (degrees)	I/I_o	d(Å)	2θ (degrees)	I/I_o	Phase
6.554	13.5	8	6.690	13.2	8	α
4.247	20.9	64	4.320	20.5	50	α
3.831	23.2	31	3.880	22.9	30	α
3.312	26.9	25	3.370	26.4	30	α
2.855	31.3	91	2.893	30.9	85	α
2.778	32.2	8	2.823	31.7	5	α
2.569	34.9	84	2.599	34.5	75	α
2.513	35.7	100	2.547	35.2	100	α
2.302	39.1	61	2.320	38.8	60	α
2.258	39.9	12	2.283	39.4	5	α
2.228	40.6	7	2.246	40.2	5	α
2.135	42.3	33	2.158	41.8	30	α
2.065	43.8	55	2.083	43.4	55	α
1.924	47.2	6	1.937	46.9	2	α
1.875	48.5	11	1.884	48.3	6	α
1.850	49.2	11	1.864	48.8	6	α
1.796	50.8	16	1.806	50.5	12	α
1.757	52.0	30	1.771	51.6	25	α
1.625	56.6	11	1.637	56.1	5	α
1.589	58.0	41	1.596	57.7	35	α
1.545	59.8	6	1.552	59.5	2	α

Table N VI. List of XRD Peaks for 36/64 Composite Sample Heated at 1650°C

Experimental Data			Si_3N_4 Reference Peaks [JCP-pat]			
d(Å)	2θ (degrees)	I / I_o	d(Å)	2θ (degrees)	I / I_o	Phase
	13 4	7	6 690	13 2	8	α
	20 6	60	4 320	20.5	50	α
	23.2	32	3 880	22 9	30	α
	26.8	58	3.370	26 4	30	α
	31.2	90	2.893	36.9	85	α
	32 1	7	2.823	31 7	5	α
	33 9	4	2.599	34.5	75	α
	34 8	85	2.547	35.2	100	α
	35 6	100	2.320	38 8	60	α
	39.2	56	2.263	39 4	5	α
	39 8	11	2.244	48.2	5	α
	48 5	6	2 150	41.8	30	α
	42 1	33	2 083	43 4	55	α
	43 7	51	1 937	46 9	2	α
	47 1	5	1 884	48.3	6	α
	48.5	10	1 864	48 8	6	α
	49 1	11	1 806	50.5	12	α
	40.8	13	1 771	51 6	25	α
	51 9	22	1 751	52.2	2	α
	56.4	9	1 637	56 1	5	α
	57 9	33	1 596	57 7	35	α
	59 7	6	1.543	59 9	3	α

Table N-VII List of XRD Peaks for 36/64 Composite Sample Heated at 1750°C

Experimental Data			Si_3N_4 Reference Peaks [JCPDS-pat]			
d(Å)	2θ (degrees)	I/I_o	d(Å)	2θ (degrees)	I/I_o	Phase
	13.5	6	6.690	13.2	8	α
			6.630	13.3	17	β
	20.9	55	4.320	20.5	50	α
	23.2	29	3.880	22.9	30	α
			3.870	23.3	20	β
	26.9	26	3.370	26.4	30	α
	27.4	7	3.310	26.9	85	β
	31.4	89	2.893	30.9	85	α
	32.2	9	2.823	31.7	5	α
	34.0	8	2.668	33.6	100	β
	34.9	83	2.599	34.5	75	α
	35.7	100	2.547	35.2	100	α
	36.4	9	2.492	36.0	100	β
	39.3	62	2.326	38.8	60	α
			2.312	38.9	9	β
	40.0	12	2.283	39.4	5	α
	40.6	7	2.244	40.2	5	α
	42.3	33	2.158	41.8	30	α
			2.160	41.8	35	β
	43.9	53	2.083	43.4	55	α
	47.2	5	1.937	46.9	2	α
	48.6	11	1.884	48.3	6	α
	49.2	12	1.864	48.8	6	α
	50.9	15	1.806	50.5	12	α
	52.0	27	1.771	51.6	25	α
	52.5	7	1.751	52.2	2	α
			1.753	52.1	70	β
	56.5	18	1.637	56.1	5	α
	58.1	38	1.596	57.7	35	α
			1.593	57.8	20	β
	59.8	7	1.552	59.5	2	α

Table N-VIII List of XRD Peaks for 36/64 Composite Sample Heated at 1800°C

Experimental Data			Si_3N_4 Reference Peaks			
d(Å)	2θ (degrees)	I/I_o	d(Å)	2θ (degrees)	I/I_o	Phase
6.359	13 8	3	6.890	13.2	8	α
			6.830	13 3	17	β
4 190	21.2	44	4 320	20.5	50	α
3 770	23 5	26	3 880	22 9	30	α
			3 820	23.3	20	β
3.285	27 1	23	3 370	26.4	30	α
3.210	27 7	19	3.310	26 9	85	β
2.827	31.6	85	2 893	30 9	85	α
2 752	32 5	7	2 823	31 7	5	α
2.615	34 3	23	2 668	33 6	100	β
2 549	35.2	79	2 599	34 5	75	α
2 495	36 0	100	2 547	35.2	100	α
2.446	36 7	28	2.492	36.0	100	β
2.277	39.6	85	2.320	38 8	90	α
			2 312	38 9	9	β
2.239	40 3	12	2 283	39.4	5	α
2.205	40 9	7	2.244	40.2	5	α
2.121	42 8	35	2 158	41 8	30	α
			2 160	41 8	35	β
2 050	44 1	57	2 083	43 4	55	α
1 912	47.5	7	1 937	46 9	2	α
1 862	48.9	13	1 884	48.3	8	α
1 838	49 6	13	1 864	48 8	8	α
1 809	50 4	6	1 827	49 9	20	β
1 783	51 2	10	1 806	50.5	12	α
1 745	52 4	36	1 771	51 6	25	α
1 729	52.9	19	1 751	52.2	2	α
			1 753	52 1	70	β
1 617	56 9	13	1 637	56 1	5	α
1 579	58 4	48	1 596	57 7	35	α

The weight fraction of the β-Si_3N_4 phase was then calculated from the R value using a standard plot reported by Gazzara and Messier [Gaz77]. (It is noted that this approach neglected any grain orientation that may be present in the sample. Since the starting Si_3N_4 core particles were relatively equiaxed and no external load was applied during sintering, it may be reasonable to expect that the Si_3N_4 in the composite samples did not contain any significant preferred orientation.) The relative amounts of the β-Si_3N_4 phase were calculated to be ≤ 4% and 21.9% corresponding to heat treatments at 1750 and 1800°C, respectively. The presence of the β-Si_3N_4 at these temperatures indicates that some of the α-Si_3N_4 seemingly dissolved in the molten SiO_2 phase and re-precipitated as β-Si_3N_4. It also suggests that the slight densification that occurred at 1750°C was presumably due to mass transport through the liquid (SiO_2) phase. Larker [Lar92] and Ekstrom and Nygren [Eks92] also reported the formation of β-Si_3N_4 in SiO_2 + α-Si_3N_4 mixtures pressure sintered at temperatures ≥ 1700°C. Larker [Lar92] carried out reaction sintering of mixtures of SiO_2 and Si_3N_4 by HIPing in the temperature range of 1700°C to 1950°C. It was found that conversion to oxynitride increased steeply from a level of ~5% at 1700°C to >80% at 1800°C and that it increased a few percent further at higher temperatures. The absence of oxynitride in the sample used in the current study may be partly attributed to the depletion of SiO_2 (by the volatilization reaction) occurring at these temperatures.

LIST OF REFERENCES

Acc92 *Accelarated Surface Area and Porosimetry System 2000*, Operator's Manual V2.04, pp. C1-C28, Micromeritics, Norcross, GA (1992)

Agr90 D.C. Agrawal, R. Raj, and C. Cohen, "In-Situ Measurement of Silica-Gel Coating on Particles of Alumina," *J. Am. Ceram. Soc.*, 73 [7] 2163-64 (1990)

Ans81 G.R. Anstis, P. Chantikul, B.R. Lawn, and D.B. Marshall, "A Critical Evaluation of Indentation Techniques for Measuring Fracture Toughness: I, Direct Crack Measurements," *J. Am. Ceram. Soc.*, **64**[9] 533-38 (1981)

Azu91 Y. Azuma, K. Nogami, and N. Ohshima, " Coating of Ferric Oxide Particles with Silica by Hydrolysis of TEOS," *J. Ceram. Soc. Japan*, **100** [5] 646-51 (1991)

Bab88 Y. Baba, K. Higashiyama, and S. Segawa, "Co-Fireable Copper Multilayer Ceramic Substrates," *Proc. Int. Symp. on Microelectronics*, ISHM, Reston, VA, 405-13 (1988)

Bag92 A.E. Bagwell, "Fabrication and Characterization of SiAlONs and SiAlON-Based Composites Prepared by a Novel Processing Technique," M.S. Thesis, University of Florida (1992)

Bar93 T.L. Barr, *Modern ESCA: The Principles and Practice of X-ray Photoelectron Spectroscopy*, CRC Press, Inc., Boca Raton, FL (1993)

Ber89 L. Bergstrom and R.J. Pugh,' Interfacial Characterization of Silicon Nitride Powders,' ," *J. Am. Ceram. Soc.* **72**[1]103- 109(1989)

Bet84 Better Ceramics Through Chemistry, Mat. Res. Soc. Symp. Proc., Vol. 32, edited by C.J. Brinker, D.E. Clark, and D.R. Ulrich, Elsevier Science Pub. Co., New York, NY, 1984

Bet86a Better Ceramics Through Chemistry II, Mat. Res. Soc. Symp. Proc., Vol. 73, edited by C.J. Brinker, D.E. Clark, and D.R. Ulrich, Materials Research Society, Pittsburgh, PA, 1986

Bet86b Better Ceramics Through Chemistry III, Mat. Res. Soc Symp Proc. Vol 121, edited by C.J Brinker, D.E Clark, and D R. Ulrich, Materials Research Society, Pittsburgh, PA, 1986

Bet90 Better Ceramics Through Chemistry IV, Mat. Res. Soc Symp Proc., Vol. 180 edited by B.J.J Zelinski, C J Brinker D E Clark, and D.R. Ulrich, Materials Research Society, Pittsburgh, PA 1990

Boc92 A.R. Boccaccini and G Ondracek, "Viscous Sintering of Non-Spherical Borosilicate-Glass Powder." *Glastech. Ber.*, **65** [3] 73-78 (1992).

Boc94 A.R. Boccaccini, "Sintering of Glass Matrix Composites Containing Al_2O_3 Platelet Inclusions," *J Mater Sci*, **29** 4273-78 (1994)

Bor88 R.K. Bordia, and G W Scherer, "On Constrained Sintering-II Comparison of Constitutive Models", *Acta Metall*, **36** [9] 2399-2409 (1988)

Bou91 D Bouvard and F F Lange, "Relation Between Percolation and Particle Coordination in Binary Powder Mixtures", *Acta Metall Mater*, **39** [12] 3083-90 (1991).

Bro59 S D Brown and S S Kistler "Devitrification of High SiO_2 Glasses of the System Al_2O_3-SiO_2," *J Am Ceram Soc* **42**[6]263-70 (1959)

Car91 F Carniti, P L Beltrame, M Armada, A. Gervasini, and G Audisio, "Polystyrene Thermodegradation. 2 Kinetics of Formation of Volatile Products," *Ind. Eng. Chem. Res.* **30** 1624-29 (1991)

Cer90 Ceramic Powder Science III, Ceramic Transactions, Vol.12, edited by G.L Messing, S-I. Hirano, and H Hausner, American Ceramic Society, Inc., Westerville, OH, 1990

Cha86 G V Chandrashekhar and M.W Shafer, in Better Ceramics Through Chemistry II, eds C.J Brinker, D E. Clark, and D R. Ulrich, *Mater Res Soc. Symp Proc* **73** 705-10 (1986)

Che92 Chemical Processing of Advanced Materials, edited by L L. Hench and J.K. West, John Wiley and Sons, Inc., New York, NY, 1992.

Che94 C- C Chen and F- S- Yen, "Effects of Amorphous Silica Coatings on the Sintering Behaviors of SiC Whisker-Reinforced Al_2O_3 Composites," *J Mater Sci*, **29** 3215-20 (1994).

Coo83 Coors Porcelain Co., Golden CO, Data Sheet for Si_3N_4-CPC-RMO46 (1983)

Dar90 G S Darivakis, J B Howard, and W.A. Peters, "Release Rates of Condensables and Total Volatiles from Rapid Devolatilization of Polyethylene and Polystyrene" *Combust. Sci. and Tech.*, **74** 267-81 (1990)

Deh68 R.T DeHoff and F N Rhines, *Quantitative Microscopy*, McGraw-Hill, Inc., New York, NY (1968)

Dej86 L.C DeJonghe M.N Rahaman, and C H Hsueh, "Transient Stresses in Bimodal Compacts During Sintering," *Acta Metall.* **34**[7] 1467-71 (1986)

Des95 P G Desai Z Xu, and J.A. Lewis, "Synthesis and Properties of $CaAl_2O_4$ Coated Al_2O_3 Microcomposite Powders," *J Am. Ceram. Soc.*, **78** [11] 2881 88 (1995).

Dry89 J.R. Dryden, D Kucerovsky, D S Wilkinson and D F Watt, 'Creep Deformation Due to a Viscous Grain Boundary Phase," *Acta Metall.*, **37**[7] 2007-15 (1989).

Duc89 V C Ducamp and R Raj "Shear and Densification of Glass Powder Compacts," *J Am Ceram Soc.*, **72**[5] 798-804 (1989)

Dut92 R.E. Dutton and M.N. Rahaman, 'Sintering, Creep and Electrical Conductivity of Model Glass Matrix Composites," *J Am Ceram. Soc.*, **75**[8] 2146 54 (1992)

Eks92 T Ekström and M Nygren SiAlON Ceramics, *J Am. Ceram. Soc.*, **75**[2] 259-76 (1992)

Fan92 C-L Fan, and M.N Rahaman, "Factors Controlling the Sintering of Ceramic Particulate Composites: I, Conventional Processing", *J Am. Ceram. Soc* **75** [8] 2056-65 (1992).

Fer89 M R Ferrick, J Murtagh, and J K. Thomas, ' Synthesis and Characterization of Polystyrene Latex Particles," *Macromolecules*, **22**[4] 1515-17 (1989)

Fer92 M K Ferber and M G Jenkins, " Evaluation of Strength and Creep Fatigue Behavior of Hot Isostatically Pressed Silicon Nitride," *J Am. Ceram Soc* **75**[9] 2453-62 (1992)

Fis92 E.S Fisher M H Manghnani, J.-F Wang, and J L Routbort, "Elastic Properties of Al_2O_3 and Si_3N_4 Matrix Composites With SiC Whisker Reinforcement," *J Am Ceram Soc* **75**[4] 908-14 (1992)

Fra92 R.K. Frazer, "Evaluation of Silicon Nitride as an Advanced Radome Material," *Johns Hopkins APL Tech. Dig.* **13**[3] 393-99 (1992)

Fub89 B. Fubini, M. Volante, V. Bolis, and E. Giamello, "Reactivity Towards Water of Silicon Nitride: Energy of Interaction and Hydration Dehydration Mechanism," *J. Mater. Sci.* 549-56 (1989)

Fur28 C.C. Furnas, "The Relations Between Specific Volume, Voids and Size Compositions in Systems of Broken Solids of Mixed Sizes," *Bur. Mines Rep. Invest.* **2894**[7] 1-10 (1928)

Gaz77 C.P. Gazzara and D.R. Messier, "Determination of Phase Content of Si_3N_4 by X-Ray Diffraction Analysis," *Am. Ceram. Soc. Bull.*, **56** [9] 777-81 (1977).

Ghe86 P. Gherardi and E. Matijevic, "Interactions of Precipitated Hematite with Preformed Colloidal Titania Dispersions," *J. Colloid Interface Sci.* **109** [1] 57-68 (1986)

Gie94 H. Giesche and E. Matijevic, "Preparation, Characterization, and Sinterability of Well-Defined Silica/Yttria Powders," *J. Mater. Res.* **9** [2] 436-50 (1994)

Gre82 S.J. Gregg and K.S.W. Sing, *Adsorption, Surface Area, and Porosity*, 2nd Ed., Ch. 2 and 3, Academic Press, London, U.K. (1982)

Gup96 T.K. Gupta and J.-H. Jean, "Principles of the Development of a Silica Dielectric for Microelectronics Packaging," *J. Mater. Res.* **11**[1] 243-63 (1996)

Hal76 D.K. Hale, "Review: The Physical Properties of Composite Materials," *J. Mater. Sci.* **11** 2105-41 (1976)

Has62 Z. Hashin and S. Shtrikman, "Elastic Behavior of Multiphase Materials," *J. App. Phys.* **33** 3125 (1962)

Has63 Z. Hashin and S. Shtrikman, "A Variational Approach to the Theory of the Elastic Behavior of Multiphase Materials," *J. Mech. Phys. Solids*, **11** 127-40 (1963).

Hen31 G. Henry, "Electrophoretic Behavior of Colloids," *Proc. Royal Soc.*, A133, 106 (1931).

Her95 J.L. Martinez-Herrera and J.J. Derby, "Viscous Sintering of Spherical Particles via Finite Element Analysis," *J. Am. Ceram. Soc.*, **78**[3] 645-49 (1995)

Het64 G. Hethrington, K.H. Jack, and J.C. Kennedy, "The Viscosity of Vitreous Silica," *Phys. Chem. Glasses*, **5**[5] 130-37 (1964)

Heu90 A.H. Heuer and V.L.K. Lou, "Volatility Diagrams for Silica, Silicon Nitride, and Silicon Carbide and Their Application to High-Temperature Decomposition and Oxidation," *J. Am. Ceram. Soc.*, **73**[10] 2785-3128 (1990)

Hip54 A.R. von Hippel, *Dielectric Materials and Applications*, Wiley, NY (1954)

Hir91 S.-I. Hirano, T. Togo, and K.-I. Kikuta, "Processing of Functional Ceramics by Metallorganic Route," *J. Ceram. Soc. Japan*, **99** [10] 1026-35 (1991)

Hol95 S. Holland, "Oxide-Nitride-Oxide Capacitor Dielectric Film for Silicon Strip Detectors," *IEEE Trans. Nuclear Science*, **42** [4] 423-27 (1995)

Hpp89 *HP 16451B Dielectric Test Fixture: Operation and Service Manual*, Yokogawa-Hewelett-Packard Ltd., Tokyo, Japan (1989)

Hse86 C.H. Hseuh, A.G. Evans, R.M. Cannon, and R.J. Brook, "Viscoelastic Stresses and Sintering Damage in Heterogeneous Powder Compacts," *Acta Metall.* **34**[5] 927-36 (1986)

Hu92 C.-L. Hu and M.N. Rahaman, "Factors Controlling the Sintering of Ceramic Particulate Composites: II, Coated Inclusion Particles," *J. Am. Ceram. Soc.* **75**[8] 2066-70 (1992)

Hu93 C.-L. Hu and M.N. Rahaman, "SiC-Whisker Reinforced Al_2O_3 Composites by Free Sintering of Coated Powders," *J. Am. Ceram. Soc.*, **76** [10] 2549-54 (1993)

Hu94 C.-L. Hu and M.N. Rahaman, "Dense Al_2O_3/ZrO_2 Composites by Free Sintering of Coated Powders," *J. Am. Ceram. Soc.*, **77**[3] 815-19 (1994)

Hwa93 C.-S. Hwang, C.-Y. Lin, and H.-H. Lu, "Effect of SiO_2 and TiO_2 on the Sinterability and Microstructure of Alumina Ceramics," *J. Ceram. Soc. Japan*, **101**[6] 649-53 (1993)

Ile79 R.K. Iler *The Chemistry of Silica* Wiley & Sons, New York, 1979

Jag94 A. Jagota, "Simulation of Viscous Sintering of Coated Particles," *J Am Ceram. Soc*, **77**[8] 2237-39 (1994)

Jag95 A. Jagota and G W Scherer, "Viscosities and Sintering Rates of Composite Packings of Spheres," *J Am. Ceram. Soc*, **78**[3] 521-28 (1995)

Jam87 R O James, "Characterization of Colloids in Aqueous Systems," pp349-410 in *Advances in Ceramics Vol 21 Ceramic Powder Science*., American Ceramic Society, Westerville, OH (1987).

Jan95 H M Jang, "Surface Precipitation Route for the Development of Cordierite-Zirconia Composites," *J Am. Ceram. Soc*, **78**[3] 723-27 (1995)

JCP-pat JCPDS Card Index File Card Nos 9-250 (α-Si_3N_4) and 9-259 (β-Si_3N_4), JCPDS International Center for Diffraction Data, Newtown Square PA

Kat92 K Kata and Y Shimada, "Low Dielectric Constant Glass-Ceramic Composite with Controlled Isolated Porosity," *J Ceram. Soc Japan*, **100**[4] 570-76 (1992)

Kel87 D.W Kellerman, "The Development and Characterization of a Low Dielectric Constant Thick Film Material" pp 316-27 in IEEE 37th Electronics Components Conference Proceedings IEEE, Washington, DC (1987)

Kin76 W D Kingery, "Grain Growth, Sintering, and Vitrification," in *Introduction to Ceramics*, 2nd ed , Wiley, NY (1976)

Kit76 C Kittel "Dielectrics and Ferroelectrics" Chap 13 in *Introduction to Solid State Physics*, 5th ed , Wiley, NY (1976)

Koe91 D.A Koester, K.L. More, and R F Davis, "Deformation and Microstructural Changes in SiC Whisker-Reinforced Si_3N_4 Composites" *J Mater Res* **6**[12] 2735-46 (1991)

Kou92 J B Kouroupis, "Flight Capabilities of High-Speed Radome Materials," *Johns Hopkins APL Tech. Dig* **13**[3] 386-92 (1992)

Kri67 I M Krieger, *Chap.2* in "Surface Coatings on Paper and Wood," Ed s R. Marchessault and C Skaar Syracuse University Press, Syracuse, New York (1967)

Kri72 I M Krieger, "Rheology of Monodisperse Lattices," *Adv Colloid Interface Sci* , **3** 111-36 (1972)

Kum92 A H. Kumar S Knickerbocker and R.R Tummala, "Sinterable Glass-Ceramics for High Performance Substrates," pp. 678-81 in *Proceedings of the 42nd Electronic Components and Technology Conference*. San Diego, CA Publ IEEE, Piscataway, NJ (1992)

Kuo95 C -H Kuo and P.K. Gupta, "Rigidity and Conductivity Percolation Thresholds in Particulate Composites," *Acta Metall Mater* **43**[1] 397-403 (1995)

Kur90 T Kurihara, M Horiuchi, Y Takeuchi, and S -I Wakabayashi "Mullite Ceramic Substrate for Thin-film Application," Proceedings of the 40th Electronic Components and Technology Conference vol 1 Publ by IEEE, IEEE Service Center, Piscataway, NJ (1990)

Kur95 C R. Kurkjian, "Indentation Behavior of Soda-Lime Silica Glass, Fused Silica, and Single-Crystal Quartz at Liquid Nitrogen Temperature," *J Am Ceram Soc* , **78**[3] 737-44 (1995)

Kus77 R.P Kusy, "Influence of Particle Size Ratio on the Continuity of Aggregates," *J Appl Phys* **48**[12] 5301-5 (1977)

Lan82 F F Lange "Liquid Phase Sintering Are Liquids Squeezed Out from Between Compressed Particles?" *J Am Ceram. Soc* **65**[2] 352 (1982)

Lar92 R. Larker, 'Reaction Sintering and Properties of Silicon Oxynitride Densified by Hot Isostatic Pressing,' *J Am. Ceram. Soc* , **75**[1] 62-66 (1992)

Lee90 H.H Lee, "Validity of Using Mercury Porosimeter to Characterize the Pore Structure of Ceramic Green Compacts," *J Am. Ceram. Soc* , **73**[8] 2261-65 (1990)

Lem92 M Lemitt, S Audisio, J.C Dupuy and B Balland, "Silicon Nitride Films Deposited by Hg-Photosensitization Chemical Vapor Deposition,' *J Non Cryst Solids*, **144**[2-3] 261-68 (1992)

Lu88 Y Y Lu, M S El-Aasser and J W Vanderhoff, 'Dispersion Polymerization of Styrene in Ethanol Monomer Partitioning behavior and Locus of Polymerization, *J Polymer Sci. PartB Polymer Physics*, **26** 1187-1203 (1988)

Lue95 W E Luecke, S.M Wiederhorn, B.J Hockey, R.F Krause, Jr, and G G Long, "Cavitation Contributes Substantially to Tensile Creep in Silicon Nitride," *J Am Ceram Soc* **78**[8] 2085 96 (1995)

Lyo94 J S Lyons and T L Starr "Strength and Toughness of Slip-Cast Fused Silica Composites," *J Am Ceram Soc*, 77[6] 1673-75 (1994)

Mac49 J K Mackenzie and R Shuttleworth, "Phenomenological Theory of Sintering," *Proc Phys Soc (London) Sect B*, **62**[12] 833-52 (1949)

Mal92 S G Malghan, "Dispersion of Si_3N_4 Powders: Surface Chemical Interactions in Aqueous Media," *Colloids and Surfaces*, **62**[1] 87-99 (1992)

Mar82 D B Marshall, T Noma, and A G Evans, "A Simple Method for Determining Elastic Modulus-to-Hardness Ratios using Knoop Indentation Measurements," *J Am Ceram Soc*, **64**[10] C175-C176 (1982)

Mec84 J J Mecholsky, Jr and S W Freiman "Determination of Fracture Mechanics Through Fractographic Analysis of Ceramics," in *Fractography of Ceramic and Metal Failures*, **ASTM STP 827** pp 136-49 (1984)

Mil83 "Flexural Strength of High Performance Ceramics," *Military Standard* MIL-STD-1942 (MR) Department of the Army Washington DC (1983)

Mit95 T D Mitchell Jr, and L. C De Jonghe "Processing and Properties of Particulate Composites form Coated Powders," *J Am Ceram. Soc.*, **78** [1] 199-204 (1995)

Nis85 S Nishigaki, S Yano, J Fukuta, M. Fukuya, and T Fuwa, "A New Multilayered Low-Temperature-Firable Ceramic Substrate," *Proc Int Symp on Microelectronics*, ISHM, Reston, VA, 225-34 (1985)

Pap70 Y S Papir and I M Krieger, "Rheological Studies on Dispersions of Uniform Colloidal Spheres, I Aqueous Dispersions in Steady Shear Flow," *J Colloid Interface Sci* **34**[1] 91-99 (1970)

Par81 G D Parfitt *Dispersion of Powders in Liquids*, 3rd ed. Applied Science Publishers London (1981)

Par93 R. E. Partch, Y Xie S T Oyama, and E Matijevic, "Preparation and Properties of Uniform Coated Colloidal Particles. VIII Titanium Nitride on Silica," *J Mater Res*, **8** [8] 2014-18 (1993)

Pez84 G Pezzotti, I Tanaka, T Okamoto, M Kozzumi and Y Miyamoto, "Processing and Mechanical Properties of Dense Si_3N_4-SiC Whisker Composites Without Sintering Aids," *J Am Ceram Soc*, **72**[8] 1461-64 (1984)

Plu93 K P Plucknett and D.E Wilkinson "Transient Viscous Phase Reaction Sintering (TVPRS) Silicon Oxynitride Ceramics," *Mat Res Soc Symp. Proc*., Vol. **287** pp 381-86 Publ by Materials Research Society, Pittsburgh, PA (1993).

Rah87a M N Rahaman and L C De Jonghe, "Effect of Rigid Inclusions on the Sintering of Glass Powder Compacts," *J Am. Ceram. Soc*., **70**[12] C348-C351 (1987)

Rah87b M N Rahaman, L.C De Jonghe G W Scherer, and R.J Brook, "Creep and Densification During Sintering of Glass Powder Compacts," *J Am Ceram. Soc*., **70**[10] 766-74 (1987)

Rah90 M N Rahaman and L C De Jonghe "Sintering of Spherical Glass Powder under a Uniaxial Stress," *J Am Ceram Soc*., **73**[3] 707-12 (1990)

Raj82 R. Raj "Separation of Cavitation Strain and Creep Strain During Deformation", *J Am. Ceram Soc*., **65** [3] C-46 (1982).

Raj84 R. Raj and R.K Bordia, "Sintering Behavior of Bi-Modal Powder Compacts," *Acta Metall* **32**[7] 1003 19 (1984)

Ran93 M S. Randall "Processing, Characterization and Modelling of Borosilicate Glass Matrix Particulate Silicon Nitride Composites. Containing Controlled Additions of Porosity, for Use in High Speed Electronic Packaging", PhD Dissertation, University of Florida (1993).

Ree88 J S Reed, *Introduction to Principles of Ceramic Processing*, John Wiley and Sons, Inc , New York, NY (1988)

Sac84a M.D Sacks and T -Y Tseng "Preparation of SiO_2 Glass from Model Powder Compacts I, Formation and Characterization of Powders, Suspensions, and Green Compacts," *J Am Ceram Soc*, **67**[8] 526-32 (1984).

Sac84b M D Sacks and T -Y Tseng, "Preparation of SiO_2 Glass from Model Powder Compacts II, Sintering," *J Am Ceram Soc*, 67[8] 532-37 (1984)

Sac91a M D Sacks, N Bozkurt, and G W Scheiffele, "Fabrication of Mullite and Mullite-Matrix Composites by Transient Viscous Sintering of Composite Powders," *J Am Ceram Soc*, **74**[10] 2428-37 (1991)

Sac91b M D Sacks, G W Scheiffele, N Bozkurt, and R. Raghunathan, "Fabrication of Ceramics and Composites by Viscous and Transient Viscous Sintering of Composite Particles," pp 437-55 in Ceramic Transactions, Vol 22, Ceramic Powder Science IV, Edited by G L. Messing, S -I Hirano, and H H Hausner, American Ceramic Society, Westerville, OH, 1991

Sac92 M.D Sacks, G W Scheiffele N Bozkurt, R. Raghunathan, and A. Bagwell, "Fabrication of Ceramics and Composites by Viscous Sintering and Transient Viscous Sintering of Composite Particles," pp 557-75 in *Chemical Processing of Advanced Materials* edited by L.L Hench and J K West, Wiley, NY (1992)

Sac93 M D Sacks, R. Raghunathan, I Y Park, and G W Scheiffele, "Processing and Properties of Glass/Ceramic Composites with Low Dielectric Constant Prepared from Microcomposite Particles," pp 243-59 in *Microelectronic and Optoelectronic Packaging*, Ceramic Transactions, Vol 33, edited by H C Ling, K. Niwa, and V N Shukla, American Ceramic Society, Westerville OH (1993)

San89 L.E Sanchez and D Ngo "Electrical Characterization of Matched Impedence Cofired, High-Speed, Microelectronic Packages Made from Low Dielectric Constant Boron-Doped, Sol-Gel Silica," *Int J Hybrid. Microelectronics* **12**[2] 95-101 (1989)

Sch77 G W Scherer "Sintering of Low Density Glasses: I, Theory," *J Am Ceram. Soc* **60**[5 6] 236-39 (1977)

Sch79 G W Scherer, "Sintering of Inhomogeneous Glasses Application to Optical Waveguides," *J Non Cryst Solids*, **34** 239-56 (1979)

Sch84 B Schwartz, "Review of Multilayer Ceramics for Microelectronic Packaging," *J Phys Chem. Solids* **45**[10] 1051-68 (1984)

Sch87 G W Scherer, "Sintering with Rigid Inclusions," *J Am. Ceram Soc* **70**[10] 719-25 (1987)

Sch91 G W Scherer, "Viscous Sintering of Particle-Filled Composites", *Am. Ceram. Soc Bull* **70** [6] 1059-63 (1991)

Sel61 J Selsing, "Internal Stresses in Ceramics," *J Am. Ceram. Soc*, **44**[8] 419 (1961)

Sha88a J F Shackleford, *Materials Science for Engineers*; p. 391, Macmillan, New York, NY (1988)

Sha88b A Shaikh, D Hankey, D Leandri, and G Roberts, "A Hermetic Low k Dielectric for Alumina Substrates" *Proc Int Symp. on Microelectronics*, ISHM Reston, VA, 189-95 (1988)

She86 R-S Sheu, "Rheology of Sol-Gel Materials," M S Thesis, University of Florida (1986)

Shi83 Y Shimada, K. Utsumi, M Suzuki, H Takamizawa, M Nitta, and T Watari, "Low Firing Temperature Multilayer Glass-Ceramic Substrate," *IEEE Trans Components Hybrids Manufacturing Technol* **6**[4] 382-88 (1983).

Shi87 Y Shimada, Y Yamashita, Y Shiozawa, M Suzuki, and H Takamizawa, "Low Dielectric Constant Multilayer Glass-Ceramic Substrate with Ag-Pd Wiring for VLSI Package," pp 398-405 in IEEE 37th Electronics Componeneta Conference Proceedings, IEEE, Washington, DC (1987)

Shi90 Y Shimada, Y Kobayashi, K. Kata, M Kurano and H Takamizawa, "Large Scale Multilayer Glass-Ceramic Substrate For Supercomputer" *IEEE Trans Components Hybrids Manufacturing Technol* **13**[4] 751-58 (1990)

Shy95 J-J Shyu and Y-C Chen, "Mullite-ZrO_2 Ceramics Made From Al_2O_3 and ZrO_2/$ZrSiO_4$ Particles Coated with Amorphous Silica," *J Mater Sci Lett.*, **14**, 609-12 (1995)

Sto68 W Stober, A. Fink, and E Bohn, "Controlled Growth of Monodisperse Silica Spheres in the Micron Size Range," *J Colloid Interface Sci*, **26**, 62-69 (1968)

Sun96 H-T Sun, C Cantalini, M Faccio, and M. Pelino, "Porous Silica-Coated α Fe_2O_3 Ceramics for Humidity Measurement at Elevated Temperature" *J Am Ceram Soc.*, **79**[4] 927-37 (1996)

Tho91 J S Thorp, M Akhtaruzzaman, E.A Logan, and D Holland, "The Dielectric Properties of Glass-Ceramic-on-Metal Substrates for Microelectronics Packaging," *J Mater Sci* **26** 5367-73 (1991)

Tim70 S.P. Timoshenko and J.N. Goodier, Theory of Elasticity, 3rd ed. McGraw-Hill, New York (1970)

Tum91 R.R. Tummala, "Ceramics and Glass-Ceramic Packaging in the 1990s," *J. Am. Ceram. Soc.*, **74**[5] 895-908 (1991)

Ult88 Ultrastructure Processing of Advanced Ceramics, edited by J.D. Mackenzie and D.R. Ulrich, John Wiley and Sons, New York, NY, 1988

Ver85 H. Verweij, G.De With, and D. Veeneman, "Hollow Glass Microsphere Composites: Preparation and Properties," *J. Mater. Sci.* **20** 1069-78 (1985)

Vor90 S.D. Vora, "Effect of Green Microstructure on the Sintering of Model Silica Compacts," Ph.D. Dissertation, University of Florida (1990)

Wha90 P.J. Whalen, C.J. Gadsaska, and R.D. Silvers, "The Effect of Microstructure on the High-Temperature Deformation Behavior of Sintered Silicon Nitride," *Ceram. Eng. Sci. Proc.*, **11**[7-8] 633-49 (1990)

Woo70 M.E. Woods and I.M. Krieger, "Rheological Studies on Dispersions of Uniform Colloidal Spheres, II. Dispersions in Non-Aqueous Media," *J. Colloid. Interface Sci.*, **34**[1] 126-30 (1970).

Wus90 R. Wusirika, "Reaction of Ammonia with Fused Silica," *J. Am. Ceram. Soc.*, **73**[10] 2926-29 (1990)

Yeh84 O. Yeheskel, Y. Gefen, and M. Talianker, "Hot Isostatic Pressing of Si_3N_4 With Y_2O_3 Additions," *J. Mater. Sci.* **19** 745-52 (1984)

Yeh88 T.-S. Yeh and M.D. Sacks, "Low Temperature Sintering of Aluminum Oxide," *J. Am. Ceram. Soc.*, **71**[10] 841-44 (1988)

Yoo96 S.Y. Yoon, T. Akisu, and Eiichi Yasuda, "The Microstructure and Creep Deformation of Hot-Pressed Si_3N_4 with Different Amounts of Sintering Additives," *J. Mater. Res.*, **11**[1] 120-26 (1996)

Zal83 R. Zallen, *The Physics of Amorphous Solids*, Wiley, New York (1983)

Zar91 J. Zarzycki, *Glasses and the Vitreous State*, Cambridge University Press, Cambridge, UK (1991)

Zen92 J. Zeng, I. Tanaka, Y. Miyamoto, O. Yamada, and K. Nuhara, "High-Temperature Strength and Cavitation Threshold of Silicon Nitride-Silica Ceramics," *J. Am. Ceram. Soc.*, **75**[1] 195-200 (1992)

Zhe92 J Zheng and J S Reed, "Study of Bimodal Pore Structure of Ceramic Powder Compacts by Mercury Porosimetry," *J Am Ceram Soc*, **75**[12] 3498 500 (1992)

BIOGRAPHICAL SKETCH

Ramesh Raghunathan was born on June 21, 1968, in Tamil Nadu, India. He completed his elementary and middle school education at Kendriya Vidyalaya, Bombay, India, and his high school education at S.I.E.S. Junior College, Bombay, India. He received B. Tech. in metallurgical engineering from the Indian Institute of Technology, Bombay, India, in May 1989 and M.S. in materials science and engineering from the University of Florida, Gainesville, Florida, in April 1993.

I certify that I have read this study and that in my opinion it conforms to acceptable standards of scholarly presentation and is fully adequate, in scope and quality, as a dissertation for the degree of Doctor of Philosophy

Michael D. Sacks, Chairman
Professor of Materials Science and Engineering

I certify that I have read this study and that in my opinion it conforms to acceptable standards of scholarly presentation and is fully adequate, in scope and quality, as a dissertation for the degree of Doctor of Philosophy

Joseph H. Simmons
Professor of Materials Science and Engineering

I certify that I have read this study and that in my opinion it conforms to acceptable standards of scholarly presentation and is fully adequate in scope and quality, as a dissertation for the degree of Doctor of Philosophy

Robert T. DeHoff
Professor of Materials Science and Engineering

I certify that I have read this study and that in my opinion it conforms to acceptable standards of scholarly presentation and is fully adequate in scope and quality, as a dissertation for the degree of Doctor of Philosophy

E. Dow Whitney
Professor of Materials Science and Engineering

I certify that I have read this study and that in my opinion it conforms to acceptable standards of scholarly presentation and is fully adequate, in scope and quality, as a dissertation for the degree of Doctor of Philosophy

Bhavani V. Sankar
Professor of Aerospace Engineering Mechanics, and Engineering Science

This dissertation was submitted to the Graduate Faculty of the College of Engineering and to the Graduate School and was accepted as partial fulfillment of the requirements for the degree of Doctor of Philosophy

May 1997

Winfred M. Phillips
Dean, College of Engineering

Karen A. Holbrook
Dean, Graduate School